UNIVERSITAT POLITÈCNICA DE CATALUNYA

DOCTORAL THESIS

Classical and Quantum simulation of quantum matter beyond symmetry breaking

Author:
Niccolò BALDELLI

Supervisor:
Prof. Dr. Maciej LEWENSTEIN
Co-supervisor:
Dr. Luca BARBIERO

A thesis submitted in fulfillment of the requirements for the degree of Doctor of Philosophy

in the

Quantum Optics Theory group
Institut de Ciències Fotòniques (ICFO)

May 30, 2024

Declaration of Authorship

This thesis is based on the following papers, which are referred to in the text by their Roman numerals.

Peer-reviewed papers

- [I] T. Graß, B. Juliá-Díaz, **N. Baldelli**, U. Bhattacharya, and M. Lewenstein. "Fractional Angular Momentum and Anyon Statistics of Impurities in Laughlin Liquids", *Phys. Rev. Lett. 125.13, 136801* (2020), will be discussed in Chapter 3.

- [II] **N. Baldelli**, B. Juliá-Díaz, U. Bhattacharya, M. Lewenstein, and T. Graß. "Tracing Non-Abelian Anyons via Impurity Particles", *Phys. Rev. B 104.3, 035133* (2021), will be discussed in Chapter 3.

- [III] **N. Baldelli**, U. Bhattacharya, D. González-Cuadra, M. Lewenstein, and T. Graß. "Detecting Majorana Zero Modes via Strong Field Dynamics". *ACS Omega 7.50, 47424–47430* (2022), will be discussed in Chapter 4.

- [IV] **N. Baldelli**, C. R. Cabrera, S. Julià-Farré, M. Aidelsburger, and L. Barbiero. "Frustrated Extended Bose-Hubbard Model and Deconfined Quantum Critical Points with Optical Lattices at the Anti-Magic Wavelength", accepted in *Phys. Rev. Lett.*, will be discussed in Chapter 5.

Pre-prints

- [V] **N. Baldelli**, S. Julià-Farré, A. Montorsi, M. Lewenstein, M. Oshikawa and L. Barbiero. *(In Preparation)*, will be discussed in Chapter 5.

- [VI] **N. Baldelli**, B. Kloss, M. Fishman, and A. Wietek. "Fragmented Superconductivity in the Hubbard Model as Solitons in Ginzburg-Landau Theory". *arXiv:2307.11820* (2023), under review in *npj Quantum Materials*, will be discussed in Chapter 6.

Other publications not included in this thesis

- [VII] K. Kottmann, F. Metz, J. Fraxanet, and **N. Baldelli**. "Variational Quantum Anomaly Detection: Unsupervised Mapping of Phase Diagrams on a Phys- ical Quantum Computer". *Phys. Rev. Research 3.4, p. 043184* (2021).

- [VIII] M. Lewenstein et al. "Attosecond Physics and Quantum Information Science". (2022)

Abstract

When matter is cooled to temperatures near absolute zero, its quantum nature begins to emerge. The interactions between its microscopic constituents can then lead to the emergence of fascinating physical properties. While the framework of spontaneous symmetry breaking has been incredibly successful in describing how a macroscopic number of particles cooperate to give a system its properties, there are many situations where this is not sufficient to describe quantum systems. This is especially true for strongly interacting many-body systems.

In recent years, multiple techniques have been developed to address this problem. On the one hand, the incredible advances in classical computing hardware and algorithms, have made it possible to study systems with a number of elementary components that were unimaginable just a few decades ago. In particular, the development of techniques such as *tensor networks* has unified the framework of quantum information with condensed matter physics, making it possible to optimize the computational complexity of simulating a system, based on its entanglement content.

On the other hand, the development of platforms to directly perform simulations on quantum systems is a highly sought objective. While a hypothetical universal quantum computer could dramatically increase our understanding of the quantum nature of matter, its difficult development makes it essential to study analog platforms where specific many-body models can be studied directly in a controlled environment. In these *quantum simulators*, novel quantum phenomena can be studied in an environment free of disorder, with excellent control over parameters and measurement capabilities.

In this thesis, we aim to explore these two paths to study some of the most relevant active topics in physics beyond the symmetry breaking paradigm. In the first part, devoted to *topology*, we propose and analyze new techniques for the detection of topological excitations. We start by proposing a protocol to detect *anyons*, quasiparticles that do not behave either as bosons or fermions, in Fractional Quantum Hall Effect systems through measuring the angular momentum of impurities binding to the anyons. We then show how similar excitations can be identified in topological superconductors through an interaction between the electromagnetic field of a strong laser pulse and the system in a process called *High Harmonic Generation*

In the second part, we move to the study of quantum *frustration*. This phenomenon, which describes a situation in which various constraints of the system cannot be satisfied simultaneously, can lead to the emergence of unexpected phases of matter. In particular, we study how frustrated phases and a particular class of quantum critical points, called *deconfined* can emerge in one-dimensional frustrated systems, potentially realizable in quantum simulators. We then study how frustration could explain the onset of superconductivity mixed with charge density modulations in two-dimensional strongly-correlated systems.

Resum

Quan la matèria es refreda a temperatures prop del zero absolut, la seva naturalesa quàntica emergeix. En aquest règim, les interaccions entre els seus constituents microscòpics poden conduir a l'aparició de propietats físiques fascinants. Encara que el marc de la ruptura espontània de simetria ha estat remarcablement reeixit en descriure com un nombre macroscòpic de partícules cooperen per dotar a un sistema de les seves propietats, això no és sempre suficient per descriure els sistemes quàntics. Això és especialment cert per sistemes de molts cossos que interactuen fortament.

En els darrers anys, s'han desenvolupat múltiples tècniques per abordar aquest problema. D'una banda, els increïbles avenços en computació clàssica i el desenvolupament de nous algorismes han fet possible estudiar sistemes amb un nombre de constituents fonamentals que eren inimaginables fa tan sols unes dècades. En particular, el desenvolupament de tècniques com les xarxes de tensors ha unificat els marcs de la informació quàntica amb la matèria condensada, el que permet optimitzar els recursos computacionals per simular un sistema en funció del seu entrellaçament.

D'altra banda, el desenvolupament de plataformes per realitzar simulacions directament sobre sistemes quàntics és un objectiu molt buscat. Encara que un hipotètic ordinador quàntic universal podria augmentar dramàticament la nostra comprensió de la naturalesa quàntica de la matèria, el seu difícil desenvolupament fa essencial la realització de plataformes analògiques on es poden estudiar directament models específics de molts cossos en entorns altament controlats. En aquests simuladors quàntics, es poden observar fenòmens quàntics nous en un entorn lliure de desordre i amb un excel·lent control sobre els paràmetres i capacitats de mesura.

En aquesta tesi, explorem aquestes dues vies per estudiar alguns dels temes més rellevants i actius de la física més enllà del paradigma de la ruptura espontània de simetria. En la primera part, dedicada a la topologia, proposem i analitzem noves tècniques per a la detecció d'excitacions topològiques. Comencem proposant un protocol per detectar anyons, quasi-partícules que no es comporten ni com bosons ni com fermions, en sistemes d'efecte Hall quàntic fraccional per mitjà de la mesura del moment angular d'impureses que s'enllacen als anyons. Després mostrem com excitacions similars poden ser identificades en superconductors topològics a través de la interacció entre el camp electromagnètic d'un fort pols làser amb el sistema en un procés anomenat generació d'alts harmònics.

En la segona part, passem a l'estudi de la frustració quàntica. Aquest fenomen, que descriu una situació en la qual diverses restriccions del sistema no poden ser satisfetes simultàniament, pot conduir a l'aparició de fases inesperades de la matèria. Concretament, estudiem l'emergència de fases frustrades i una classe particular de punts crítics quàntics, anomenats desconfiats, en sistemes frustrats unidimensionals potencialment realitzables en simuladors quàntics. Finalment, estudiem com la frustració podria explicar l'aparició de la superconductivitat barrejada amb modulacions de densitat de càrrega en sistemes bidimensionals fortament correlacionats.

Acknowledgements

After this long journey, there are many people that I would like to thank for walking together with me to arrive where I am today. Many more than I was expecting when I first started.

First, my supervisor Maciej, for giving me full support and the freedom I needed to explore my passions. Tobi and Utso, for working with me in the first difficult years when I was embarking on the adventure of doing a PhD during a pandemic. And my co-supervisor Luca, for helping me in these last years, pushing me when I thought what I was doing was too difficult to achieve, and supporting me way beyond science. I am also extremely grateful to all the collaborators I worked with during these years, especially Alex and Matt for warmly hosting and supporting me during my stay in New York and, remotely, in the last two years. From all of you, I learned something invaluable. Finally, I would like to thank the past and present members of QOT, especially Dani, Alex, and Sergi, for always being much more than simple colleagues.

Ringrazio tutti gli amici italiani che mi hanno circondato in questi anni. Da buona tradizione nostrana, sono cominciati in pochi (ma buoni) e sono cresciuti a dismisura. Paolo, Costi, Egle, Giulia, Carmen, Sabri, gli scalatori, Els Napolitans e tutti gli altri. Scusate se non vi menziono tutti uno per uno, non entrereste nella pagina. Ringrazio i miei amici di Pontedera, Pisa, Parigi e in giro per il mondo, che nonostante tutti questi anni mi fanno sentire come se non fosse passato un giorno ogni volta che li vedo. Alla mia famiglia, che mi ha sempre supportato e sopportato nonostante le mie chiamate col contagocce.

Tots els catalans que he pogut conèixer, sobretot la Joana, el Borja, la Natàlia, l'Esteve i el Miquelito. Amb la vostra ajuda vaig poder moltes vegades trobar la llum en la foscor. M'agradaria dir que després de tants anys jo també he après com és viure aquí, i poder dir que aquesta també és la meva casa.

Para acabar, agradezco a todas las personas que en un momento u otro hayan cruzado mi camino en estos años, de aquí o de fuera, y me hayan hecho crecer mucho más de lo que habría podido pasar si no hubiera intentado nunca salir de mi zona de confort. Mis compañeros de piso, los que han llegado y se han ido, los de Nueva York y de Okinawa, todas las personas que conocí en estos años en Barcelona y alrededor del mundo. Gracias por haber compartido conmigo este largo viaje.

Contents

Introduction

The discovery of quantum mechanics at the beginning of the last century completely changed our understanding of the nature. Microscopic phenomena such as the spectra of atomic gases, the photoelectric effect, and the electric resistance in metals could finally be described by a unified framework. While these discoveries revolutionized both science and technology, one issue was evident from the beginning: the quantum properties of matter are extremely delicate and difficult to control. Indeed, the susceptibility of quantum states to decoherence induced by external perturbations, and the consequent difficulty to isolate them from the environment, made it extremely challenging to go beyond single-particle physics and exploit the full potential of quantum mechanics.

However, already at the beginning of last century, the discovery of superconductivity and superfluidity [1, 2] hinted at the presence of an unexplored world of collective quantum phenomena with potentially revolutionary applications. This goal however, required that the matter was cooled enough to suppress external disturbances to let the quantum properties free to emerge. A first step towards the understanding of these phenomena was the development of the theory of phase transitions by Ginzburg and Landau [3, 4], that made it possible to classify an enormous quantity of systems, both classical and quantum, in terms of their symmetries. Nevertheless, the increasing experimental achievements in creating quantum systems shielded from external noise, with the discovery of phenomena like the Quantum Hall Effect [5, 6] or high-Tc superconductivity [7, 8], made it clear that this paradigm was not sufficient. The theoretical effort to understand these new phases led to the opening of completely new fields, like the theory of topological order [9–11] and quantum spin liquids [12–15], that in turn inspired a great deal of experimental work. In the following years indeed, the development of new platforms like 2D materials [16], Moiré materials [17], quantum dots and wells [18, 19], and the possibility to induce quantum phases through light-matter interaction [16, 20], provided an experimental realization to these exotic phases.

At the same time, the last fifty years there have seen an impressive development of the capabilities of manipulating quantum matter at the atomic level. Famously, Schrödinger once said: *"In the first place it is fair to state that we are not experimenting with single particles, any more than we can raise Ichthyosauria in the zoo"* [21]. Contrary to this prediction, single-atom manipulation was achieved: the discovery of the laser [22] made it possible in the 70s to develop techniques to cool ions [23, 24] and neutral atoms [25] near to the absolute zero, and even trap and move them singularly using optical tweezers[26, 27]. This was rapidly stepped up to many-body control schemes thanks to magneto-optic trapping [28] and evaporative cooling [29], leading to the milestone of realizing of the first Bose-Einstein condensate in the 90s [30, 31]. As technology progressed, it was then possible to develop platforms to implement complex quantum Hamiltonians in an environment whose properties are readily tunable and accessible, while keeping the same quantum properties of real materials [32]. The opportunity to shield the system from the environment and almost cool it near-zero temperatures makes it then possible to observe quantum phenomena

that would be otherwise hidden by disorder and thermal fluctuation. In particular, the development of optical lattices for ultracold atoms [33] meant that band structures typical of solid state systems could be realized in the regime of strong particle-particle interaction, leading to the realization of a plethora of many-body phases only theoretically conjectured up to that point, starting from the emblematic Mott insulator - superfluid transition in the Bose-Hubbard model [34]. These techniques have evolved since to include effects like synthetic classical [35–37] and dynamical gauge fields [38], topological bands [39] and quantum chemistry models [40]. Moreover, the introduction of new detection techniques made it possible to image atoms in lattice up to single-site resolution [41, 42]. These kinds of developments, and similar advances in other platforms like trapped ions, Rydberg atoms in optical tweezer and photonic waveguides made it possible to explore landmark phenomena peculiar of many-body quantum physics. Examples include many-body localization [43], lattice gauge theory [38, 44], Fermi-Hubbard physics [45, 46], topology [47–49], non-integrable dynamics [50], and quantum spin liquids [51].

During all this time, a guiding approach for the development of feasible experimental platforms has been the use of numerical simulations to investigate how various phase can be realized. While impressive work has been done in the development of algorithms like Variational and Quantum Monte Carlo and Exact Diagonalization [52], these techniques were always limited respectively by the representation power of the variational ansatz, the sign problem, and the exponential scaling of the Hilbert space dimension. For these reasons, the understanding of strongly-correlated phases has seen a dramatic acceleration since the introduction of Tensor Network techniques, that efficiently represent the relevant physics while being unaffected by the sign problem [53–55]. Starting from the discovery of the Density Matrix Renormalization group [56, 57] and its interpretation in terms of Matrix Product States (MPS) [58], the physics of one-dimensional quantum systems has become a reachable task. MPS based techniques have rapidly evolved to encompass the study of 2D hamiltonians [59], dynamics [60–62], infinite systems [63, 64] and thermal states [65, 66]. The subsequent interpretation of these states in terms of entanglement using the tools of quantum information theory made it possible to generalize their construction [60, 65, 67], creating new networks suited for application in higher-dimensional systems [68], critical systems [69], and graphs with more general entanglement structure [70], among others. Lately, Tensor Network techniques have been used to benchmark the capabilities of early quantum computers [71, 72], pushing forward the limits of classical simulation of quantum systems. It is then of fundamental importance to understand what advantages and limitations new platforms like quantum simulators can bring to the study of condensed matter physics compared to state-of-the-art classical methods.

Motivation

In this thesis, motivated by the recent achievements in computational techniques and quantum simulators as resumed above, we aim to explore the possibility of realizing and controlling new quantum phases of matter. From one side, we develop new protocols to implement in quantum simulators and related platforms, models whose realization in real materials has been so far elusive. On the other, we leverage the power of modern classical numerical simulations to investigate the properties of these new phases. In this way, our goal is to exploit the strengths of these two

complementary approaches, to provide a comprehensive understanding of two very relevant topics in modern condensed matter physics: *topology* and *frustration*.

Topology. The birth of topology in condensed matter physics is conventionally dated back to the discovery of the Quantum Hall Effect in the 80s [5, 6]. In these systems, the electrical conductivity of samples assume discrete values proportional to an integer or a rational number, depending on the magnitude of a background magnetic field. While initial attempts focused on trying to explain this phenomenon in terms of symmetry breaking [73], it was soon realized that this was an impossible task, as states with drastically different physics share the same symmetries.

For the Integer Quantum Hall effect, a breakthrough arrived when the conductivity plateaus were linked to an integer quantity deeply connected to the geometry of the band structure of the system, a *topological invariant* [74]. Subsequently, it was discovered that this number is the same as the number of conducting modes at the boundary of the systems, or *edge states* [75]. The field rapidly developed: first it was discovered that Quantum Hall physics was possible without a background magnetic field [76], creating the field of Chern insulators [77]. Later, the description of Quantum Spin Hall Effect [78, 79], where topological edge states carry spin, but zero net charge, launched the field of *topological insulators* [80]. These systems are unified by the fact that they are described by a bulk band structure with a topological invariant, connected to the presence of edge states by a property called *bulk-boundary correspondence* [81]. This theoretical work culminated with the complete classification of topological systems described by single particle physics [82, 83]. However, already starting from the works of Haldane in the 80s [84, 85] it was evident that topological phases can survive in presence of interactions, and even be induced by them [86]. In this case, the lack of a clear band structure makes a full classification in terms of topological invariants highly challenging, leading to the development of new metrics based on entanglement [87]. The unification between interacting and non-interacting models led to the concept of *symmetry protected topological phases* [88], meaning short-entangled phases whose topological properties depend on the presence of a particular symmetry. A great amount of these phases found an experimental realization both in real materials and quantum simulators, like Chern insulators [89], lattice quantum hall states [47, 48, 90] and one-dimensional topological insulators [91]. For the interacting case, recent breakthroughs led to the realization of Haldane phases [92, 93]. However, for more complex models, there is still need to look for experimental and theoretical signatures [86]. Recent numerical works suggest the presence of interacting topological phases in lattice models [94, 95], but the fragile nature of the interacting physics and the difficulty to perform numerical simulations makes a challenging task engineering systems to observe these phases.

The other precursor of topological matter, the Fractional Quantum Hall Effect, has drastically different properties. In this case the system is *topologically ordered* [10, 11], showing long-range entanglement, degenerate ground states on closed manifolds, and topological properties independent of any symmetry. The most striking characteristic however, is the presence of bulk excitations that carry a fraction of the charge of electrons and a statistics that interpolates between fermions and bosons, called *anyons*[96]. The localized nature of these particles, the degeneracy of the states associated to them, and their topological protection have been put forward for the realization of intrinsically fault-tolerant topological quantum computation [97]. Theoretical proposals for the realization of anyons have been ubiquitous in the last 20 years from lattice models [98], $\nu = 5/2$ Fractional Quantum Hall Effect [99], and Majorana modes in topological superconductors [100–102]. However, their physical realization is still elusive due to difficulties in detecting their statistics [103].

While prototypes of this kind of topologically ordered states are starting to appear in quantum simulators [51, 104–107], there is still need for new protocols to detect their presence.

Frustration. The breaking of the time reversal symmetry required for the onset of Quantum Hall physics can be induced by different mechanisms. While the most straightforward is the insertion of a background magnetic field, another driving mechanism can be the presence of frustration. In physics, the concept of frustration refers to a situation in which competing forces cannot be satisfied at the same time, leading to a suboptimal equilibrium configuration of a state [14]. The causes of this competition can be multiple, like geometrical, kinetic [108, 109] or interaction [110] based constraints. The most striking consequence is that equilibrium states of frustrated systems are usually hugely degenerate, and as the system explores this degenerate manifold, the onset of order is suppressed. While this concept is well known in classical physics, where systems like spin ices do not develop magnetic order well below their Curie temperature [111], in quantum systems the concept of frustration is more elusive. This is because the interplay between frustration and quantum fluctuations needed to identify quantum frustration is usually hidden by thermal noise. Here, the impossibility to obtain conventional ordering can lead to unexpected phases like *quantum spin liquids* [14, 15]. One of the first proposed examples was the *resonating valence bond solid* [12], a quantum spin liquid state initially proposed to describe high-Temperature superconductor [13]. While it was later discovered that this picture does not match with the experiments [112], frustration is still thought to play a fundamental role in this phenomenon. This has been the subject of extensive numerical investigation, that concluded that a minimal model of interacting fermions with frustrated hopping could stabilize superconductivity [113–115]. Moreover, the study of quantum spin liquids had a remarkable development by itself [15]. However, the implementation of the interaction required for the realization of quantum frustration is extremely complex. In optical lattices for example, the required procedures can lead to heating of the systems destroying quantum fluctuations [116, 117]. Only in recent years the first quantum spin liquid was implemented in Rydberg quantum simulators [51]. Still, the question of where to realize these phases and the study of their properties is still open.

Content

The thesis is divided in three parts. The first part is devoted to briefly reviewing the theoretical and experimental background necessary for the comprehension of the original results. In particular, I discuss the physics of relevant systems not described by the symmetry breaking paradigm, and discuss the tools of classical and quantum simulations. In the second part we propose new tools and platforms for the realization of topological phases of matter, with an outlook on both quantum simulators and real materials. In part three we discuss frustrated quantum systems, and how they show properties compatible with deconfined quantum criticality and high-temperature superconductivity. Lastly, I added some relevant details on the numerical and analytical procedures used to obtain the results of the thesis in three separate Appendices.

Part I

In Chapter 1 we give a brief introduction of physical systems whose classification goes beyond the Ginzburg-Landau symmetry breaking description. We start by describing *Symmetry protected topological phases* as the simplest example of topology in quantum physics, listing some paradigmatic models that serve as a starting point for the original point of this thesis. We then introduce *topological order*, and particularly the Fractional Quantum Hall Effect, as a more complex example of highly-entangled topological phase. Finally, we review some results on *Deconfined Quantum Criticality*.

In Chapter 2 we introduce the main numerical techniques used to obtain the results of the thesis: *Exact Diagonalization* and *Tensor Networks*. We also describe how strongly interacting lattice models can be engineered in quantum simulators, particularly *ultracold atoms* in optical lattices. For this system we also briefly introduce the most relevant measurement and detection techniques.

Part II

In Chapter 3 we propose a protocol to detect anyons in FQHE systems through measuring the angular momentum binding to the anyons. We characterize the angular momentum of a single and multiple impurities, and show that this scheme is applicable to the detection of both Abelian and non-Abelian anyons.

In Chapter 4 we show another protocol for the detection of quasi-particles expected to show non-Abelian anyonic statistics. In this case the anyons in exam are Majorana modes localized at the end of a topological superconducting chain. By starting from a realistic model, we show that the interaction between the electromagnetic field of a strong laser pulse and the chain can lead to *High Harmonic Generation*. In this process, harmonics of the order of up to hundreds of time the driving frequency are re-emitted. In this way we can map the full band structure of the system and recognize the presence of sub-bandgap topological modes.

Part III

In Chapter 5 we study the effect of frustration in two paradigmatic one-dimensional lattice models. In the bosonic case we recover a phase diagram with the presence of states of matter typical of frustrated quantum magnets like Bond Order Waves. Moreover, in presence of nearest-neighbor interactions we find a third phase with spontaneous symmetry breaking, connected to the Bond Order Wave by a Deconfined Quantum Critical Point. For this model we also design a realistic experimental setup with ultracold atoms in optical lattices. In the fermionic case, we revisit the phase diagram of the Extended Hubbard model, and find that the competition behind the contact and nearest-neighbor interactions can lead to two symmetry broken phases, also connected by a deconfined quantum critical point. We also find that by adding an antiferromagnetic spin-spin interaction another transition of this type appear. Most importantly, we find that these two latter transitions are characterized by the long-range order of non-local order parameters. This in turn, means that these DQCP are qualitatively different from the ones found in the bosonic case.

In Chapter 6 we study the onset of superconductivity in the two-dimensional Hubbard model in presence of a frustrated hopping. By means of 2D DMRG calculations, we confirm previous results on the presence of superconducting pairing at small hole-doping and strong contact interaction, and give another interpretation of such phase in terms of the formation of a *fragmented* Condensate of cooper pairs. This

allows us to describe the behavior of this condensate through an effective Ginzburg-Landau theory, and expand the predictions in presence of the magnetic field. The validity of the theory is then confirmed by the comparison with the results of the DMRG simulations.

Part I

Preliminaries

Chapter 1

Quantum matter beyond symmetry breaking

The behavior of quantum matter is usually captured by how electron and nuclei behave. However, materials composed by a macroscopic number of these elements show a richness of properties and behaviors that cannot be traced back to the properties of the underlying elementary particles. Condensed matter physics is a field devoted to the study of these *emergent* properties, that do not come from the simple mechanical properties of the particles, but from the complex way they interact and organize between themselves [118]. The macroscopic properties of a material, either classical or quantum, are then determined by how the microscopic constituents are organized, or by different *orders*: to every different order corresponds a different *phase* of matter. A change of phase, or *phase transition*, is a sudden change in this order.

In the last century, the most successful description of phase transitions has been the one introduced by Landau and Ginzburg [3, 4]. In this celebrated framework different phases are labeled by their symmetry. A phase transition amounts then to a change of behavior of the system under one of these symmetries. To be more specific, consider a system described by a Hamiltonian invariant under a certain symmetry group G. There might be a choice of parameters (either the temperature for classical systems, or a Hamiltonian parameter for quantum systems), for which the equilibrium state is no longer invariant under the action of G, but only under a subgroup $H \subset G$. In this case, we say that the symmetry G is *spontaneously broken*. This can be quantified by a local quantity called *order parameter*, invariant under the action of H but not under the action of G. For a particular symmetry we then say that the system is *disordered* if the symmetry is not broken, and *ordered* if the symmetry is broken.

The Ginzburg-Landau description has been incredibly successful in describing phase transitions in all fields of physics, both classical and quantum, ranging from the superfluid transition in matter close to the absolute zero temperature, to the Higgs mechanism in high-energy physics. For a long time, it was believed that any kind of phase behavior could be traced back to the breaking of some symmetry, and that the Ginzburg-Landau paradigm was the ultimate description of phase transitions.

However, starting from the 70s, it became increasingly clear that many phenomena avoid this classification [119]. In particular, after the discovery of the Integer Quantum Hall Effect [5] and its fractional counterparts [6] it was evident how systems that do not break any symmetry can have dramatically different phenomenology depending on the choice of the Hamiltonian's parameters. These states define new phases of matter in the sense that their fundamental properties are insensitive to local perturbation of the system unless they cross a quantum phase transition and

a gap closing. Because of this robustness, and owing to the mathematical framework behind their classification, this kind of order is called *topological* [74, 120].

From a mathematical perspective, topology is the study of the properties of objects that do not change under continuous deformations. For example, it is impossible to change the number of holes or handles of an object without breaking it. These quantities that globally characterize something and are immune to local changes are called *topological invariants*. In the same way, if two objects have a different value of their topological invariants, they cannot be transformed one in the other by only stretching and deforming them. How can this concept be applied to quantum mechanics?

To make this point clear, in the following Chapter we will introduce some paradigmatic examples of systems eluding the Ginzburg-Landau paradigm, starting from the simplest case of *Symmetry Protected Topological* phases [88] in Section 1.1. These are the simplest states of matter that can be considered topological and comprehend the IQHE. Most importantly, they are the only allowed topological phases in one-dimension, and for this reason particularly relevant for the results of Chapters 4 and 5 of this thesis. We will then move to the concept of *Topological Order* [10, 120] in section 1.2. A prime example of this type of order is the Fractional Quantum Hall Effect (FQHE). This will be the starting theoretical background for Chapter 3. Compared to SPT topologically ordered phases can only arise in presence of strong interactions and can exist for dimensionality greater or equal than two. Finally, we will describe a more modern approach to phase transitions that go beyond the Ginzburg-Landau theory, the so called *deconfined quantum critical points* [**senthil2023a**, 121]. While these points show topological features in two dimensions, their most striking property is that they connect two-symmetry broken phases by restoring both symmetries in correspondence of a single point, a possibility excluded in standard Ginzburg-Landau theory. We will study some systems showing deconfined quantum criticality in Chapter 5.

1.1 Symmetry Protected Topological phases

Symmetry Protected Topological (SPT) phases comprehend a plethora of different effects, that only years after their discovery were unified under the same framework [88]. The most notorious representative of this class is the Integer Quantum Hall Effect (IQHE) [5], that was also the first one for which the role of topology was highlighted [74].

After the discovery of the IQHE, it was thought that the presence of a background magnetic field was necessary for the appearance of topological phases. However, Haldane showed that similar physics can appear in 2D models without the presence of a magnetic field, only by breaking time-reversal invariance [76], a phenomenon called *Quantum Anomalous Hall Effect*. This in turn led to discovery of a new family of materials called *Chern insulators* [80]. In the last 20 years, a new state of matter not breaking the time-reversal symmetry has also been discovered, called *Quantum Spin Hall Effect* or *Topological Insulator* [78, 79]. The ideas developed to understand topological insulators were then extended to study *Topological Superconductors* [80].

While all these states are described by single-particle physics, it was discovered that interacting systems can also show a non-trivial topology, but in this case the topological properties are better understood by looking at the entanglement properties of their ground states [84, 122, 123]. The search for interacting phases with

topological characteristics is currently a very active field of research [86], and is going to be the main topic of Chapter 5.

All these seemingly unrelated systems share several properties that justify their common classification: (i) they are all short-range entangled (ii) they have non-degenerate ground states when put on a closed manifold (iii) when on an open manifold gapless modes appear on the boundary of the system, called *edge modes*. Most importantly, the presence and the number of edge states can be inferred from a bulk topological invariant computed with periodic boundary conditions, a property called *bulk-boundary correspondence* [80, 81]. Finally, the name "Symmetry Protected", comes from the fact that their edge states and bulk topological invariants are protected from external perturbations, but only if this perturbation respects the protecting symmetries.

In the rest of the section we will describe some paradigmatic examples of SPT phases, starting from the Integer Quantum Hall Effect, and then moving to examples of a topological insulator, a topological superconductor and an interaction-induced topological phase. All of these examples are fundamental starting points for the results of the rest of the thesis.

1.1.1 Berry phase and Chern Number

To explain how topology can appear in the band structure of a single-particle spectrum, we will work our way from the concept of *Berry phase* [124] and see how it is related to the geometry of the bands. That, in turn, will quantify the presence of non-trivial topology.

As we said topology is the study of properties of objects insensitive to continuous deformations: in our case the objects will be the eigenstates of gapped Hamiltonians, and the stretches and deformations the adiabatic transformations of these Hamiltonians that do not close the gap. The topological invariants are then defined in a space of the possible quantum states, spanned by the possible choices of the Hamiltonian parameters. If two states have two different values of these invariants, they can only be transformed one in the other by "breaking" them, meaning by performing a gap-closing transformation.

The reasoning starts from a simple consequence of the *adiabatic theorem* [125]: this theorem states that if we prepare a quantum system in an eigenstate $|\psi(t=0)\rangle$ of a Hamiltonian $H(t=0)$, and we change the parameters of the Hamiltonian slow enough with respect to the energy gap, the system will stay in the evolved eigenstate $|\psi(t=T)\rangle$, without any transition to higher or lower energy states. What if we consider a closed path in parameter space such that $H(t=0) = H(t=T)$? In this case the state can only acquire a phase factor

$$|\psi(t=T)\rangle = e^{i\gamma}|\psi(t=0)\rangle. \tag{1.1}$$

One part of this phase is the usual dynamical factor that we can always remove shifting the zero of the energy. The remaining part is deeply linked to the geometry of the parameter space, and is called Berry Phase. Notably, this is a phase *difference*, meaning that it can be measured, for example in interferometry experiments [126].

To obtain an expression for this phase, we compute a generic adiabatic evolution of the state under the Schrödinger equation. For simplicity, we restrict to the evolution of a non-degenerate ground state $|g(\lambda)\rangle$ of a system with a single parameter $\lambda(t)$, such that at any moment in the adiabatic evolution we can set $H(t)|g(t)\rangle = 0$.

In this case, the state after the evolution can be written as

$$|\psi(T)\rangle = U(T)|g(T)\rangle, \tag{1.2}$$

with U a phase. The unitary operator $U(T)$ can then be computed by inserting this ansatz in the Schrödinger equation

$$i\frac{\mathrm{d}}{\mathrm{d}t}U(t)|g(t)\rangle = H(t)|\psi(t)\rangle = 0. \tag{1.3}$$

By taking the scalar product with $\langle\psi(t)|$ and expanding the total derivative we finally obtain an equation for U

$$\frac{\mathrm{d}U}{\mathrm{d}t} = -\langle g(t)|\partial_\lambda|g(t)\rangle\frac{\mathrm{d}\lambda}{\mathrm{d}t}U. \tag{1.4}$$

Here we can identify the quantity $A = -i\langle g(t)|\partial_\lambda|g(t)\rangle$ called the *Berry connection*, such that by integrating (1.4) we obtain the expression for the Berry phase U

$$U(T) = e^{-i\int_0^T \mathrm{d}t A(t)\frac{\mathrm{d}\lambda}{\mathrm{d}t}}. \tag{1.5}$$

If we finally consider a closed path $\lambda(T) = \lambda(0)$, we obtain an expression for γ in (1.1) in terms of the Berry connection

$$\gamma = -\oint \mathrm{d}\lambda A(\lambda). \tag{1.6}$$

This quantity does not depend on the time taken to complete the loop, but only on the geometry of the path in parameter space. The reason why the quantity A is called connection is because of its properties under gauge transformations. If we consider a transformation $A \to A + \partial_\lambda\omega$, the quantity γ is invariant as expected, being a measurable quantity. Notably, this only happens if the path in parameter space is closed, otherwise the phase can be reabsorbed by the gauge transformation.

This property already hints at similarities between the Berry connection A and the gauge potential of electromagnetism. Starting from this analogy we can construct the gauge-invariant *Berry Curvature* $\mathcal{F}_{\mu\nu}$, defined as the curl of the Berry connection

$$\mathcal{F}_{\mu\nu} = \partial_\mu A_\nu - \partial_\nu A_\mu, \tag{1.7}$$

equivalent to the field strength in electromagnetism. In this case we assumed a multivariate connection over a manifold of multiple parameters: $A_\mu(\lambda_\mu)$. We can then recast the expression of γ in terms of the curvature by using the Stokes theorem

$$\gamma = -\oint \mathrm{d}\lambda^\mu A_\mu(\lambda) = -\int \mathrm{d}S^{\mu\nu}\mathcal{F}_{\mu\nu}, \tag{1.8}$$

where S is the surface in parameter space enclosed by the path. If this surface is closed, however, the Gauss-Bonnet theorem implies that this quantity is quantized in units of 2π

$$\gamma = -\int \mathrm{d}S^{\mu\nu}\mathcal{F}_{\mu\nu} = 2\pi C, \tag{1.9}$$

where $C \in \mathcal{Z}$. The quantity C is a topological invariant linked to the *genus*, or the "number of holes" of the surface S. As we will see in the following, this quantity and others obtained in an analogous way, can be used to characterize topological band structures. It will then be the starting point to classify SPT phases.

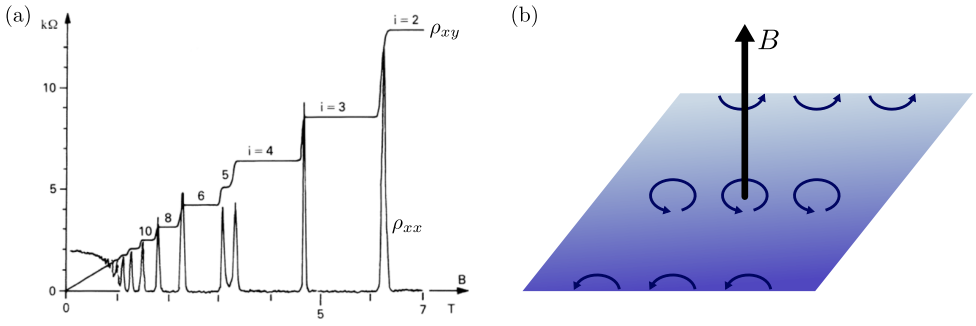

FIGURE 1.1: The Integer Quantum Hall effect. (a) The longitudinal (ρ_{xx}) and the longitudinal (ρ_{xy}) resistivity as a function of the magnetic field B. A change in the Hall plateau corresponds to a finite ρ_{xx}. For low magnetic fields the relation is the one expected classically. Data taken from [127]. (b) Schematics of the IQHE system. Intuitively, the electrons in the bulk are insulating because they go along cyclotron orbits, while the edges are metallic because the electrons can hop along the boundary of the system.

1.1.2 Integer Quantum Hall Effect

The Integer Quantum Hall Effect (IQHE) can be considered the precursor of all the topological states of matter. Firstly discovered in 1980 by von Klitzing [5], it describes the behavior of electrons confined in two dimensions, under the effect of a magnetic field orthogonal to the plane.

Classically, when applying a potential difference in the direction x, the magnetic field would cause a drift of the electrons in the direction y. This creates an effective transversal current $J_y = \sigma_{xy} E_x$, with σ_{xy} called the *Hall conductivity*. One would expect for the transverse resistivity $\rho_{xy} = \sigma_{xy}^{-1}$ to increase linearly with the background magnetic field B. However, experimental measurements [5] showed that, for B strong enough, the Hall resistivity remains perfectly constant for a wide range of magnetic fields, with sudden jumps to another of these *plateaus*, when B crosses some value. In correspondence of these points, the longitudinal resistivity ρ_{xx} also becomes finite, and the system is metallic. This behavior is shown in Figure 1.1(a). The plateaus were measured to be characterized by a perfectly quantized resistivity

$$\rho_{xy} = \frac{h}{e^2} \frac{1}{\nu}, \tag{1.10}$$

where ν is an integer.

This remarkable result can be intuitively explained by considering the band structure of the system: when subject to a magnetic field B, free electrons in two dimensions of charge e and mass m form highly degenerate flat bands called *Landau Levels* [128]. Each band can host $N_\phi = \Phi/\Phi_0$ electrons, where $\Phi = BL_xL_y$ is the flux threading a system of size $L_x \times L_y$, and $\Phi_0 = h/e$ is called *flux quantum*. Each pair of levels is separated by an energy gap $\hbar eB/m$. If the Fermi energy lies between two of this levels, and $k_bT \ll \hbar eB/m$, the levels above stay empty, and the electrons have nowhere to scatter when applying an electric field, resulting in a vanishing longitudinal conductivity. As the magnetic field is increased the degeneracy of the levels N_ϕ increases, and the Fermi energy lowers. When the Fermi energy crosses one of the levels, the system becomes metallic and $\rho_{xx} \neq 0$, while ρ_{xy} jumps to a new plateau, with a value given by (1.10).

The IQHE is then a bulk band insulator, but it shows a finite transverse resistivity.

How is this possible? This is due to the presence of gapless edge states that appear as chiral currents on the boundaries of the system. As we have seen this hints at a topological structure. This was confirmed by Thouless, Kohmoto, Nightingale and deNijs (TKNN) [74]. Using the Kubo formula [129] to compute the Hall response to a weak electric field, they showed that it is indeed quantized in terms of a bulk topological invariant C called *Chern number*:

$$\sigma_{xy} = \frac{e^2}{h} C, \tag{1.11}$$

We can then conclude that the IQHE can be described by single particle physics and its properties are topological. It can then be classified as an SPT phase. However, it has a particular property: no symmetry has to be preserved for the system to show a non-trivial topology[1].

Particles on a lattice

The TKNN invariant is better understood if we put the system on a lattice: in this case the IQHE can be extracted from the *Harper-Hofstadter* Hamiltonian [130, 131]

$$H = -t \sum_{\langle i,j \rangle} \left(e^{i\phi} c_i^\dagger c_j + h.c. \right), \tag{1.12}$$

This Hamiltonian describes spinless fermions hopping on a square lattice with a magnetic flux ϕ per plaquette, expressed in the Landau gauge. In this case the spectrum forms electronic bands in the Brillouin zone and the Chern number can be computed directly from the band structure of the system as in Eq. (1.11), by using the momentum $\mathbf{k}$ as the adiabatic parameter. This gives a total conductivity

$$\sigma_{xy} = \frac{e^2}{h} \sum_n \int_{BZ} \frac{\mathrm{d}^2 k}{2\pi} \mathcal{F}_{\mu\nu,n}(\boldsymbol{k}), \tag{1.13}$$

with $\mathcal{F}_{\mu\nu,n}(\boldsymbol{k})$ the Berry curvature of the n-th band and the sum performed on the n occupied bands. This model was experimentally realized in ultracold atoms in an optical lattice [47, 90], and its Chern number measured in the same setup [48]. It will be relevant for the investigation of Chapter 6.

1.1.3 Topological Insulators: the Su-Schrieffer-Heeger model

We will now introduce one of the simplest topological insulators in one-dimension: the *Su-Schrieffer-Heeger* (SSH) model [132, 133]. This model is a convenient starting point to introduce some phenomena that will appear with a different origin in Chapter 5. Initially introduced to model polyacetylene chains [132, 134], it became one of the stable platform to study topology and *fractionalization* in 1D systems [135], for example in cold atoms platforms [91].

The SSH model describes spinless fermions hopping on a one dimensional lattice, with a modulated hopping, described by the Hamiltonian

$$H = -\sum_i \left(v c_{i,A}^\dagger c_{i,B} + w c_{i,B}^\dagger c_{i+1,A} + h.c. \right). \tag{1.14}$$

[1] To be more precise, the presence of the $U(1)$ symmetry corresponding to charge conservation is needed for the quantization of conductivity, but not for the presence of edge states

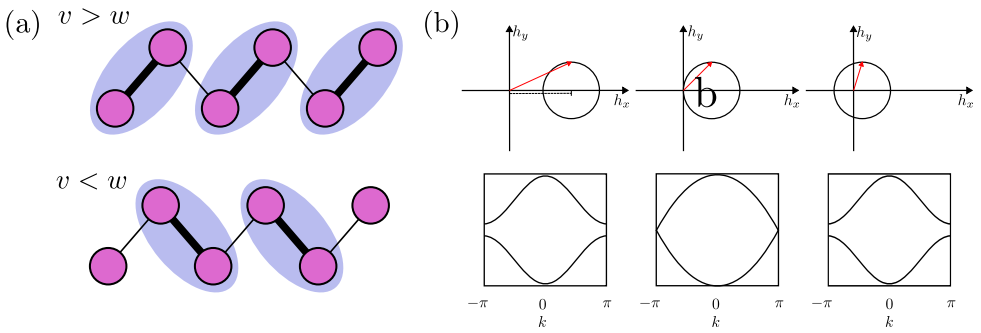

FIGURE 1.2: The SSH model. (a) Depending on the phase the dimerization leaves two sites unpaired, leading to a 4-fold degenerate ground state and the formation of edge states. (b) These two situations correspond to topologically different band structure as seen by computing the winding of $\mathbf{h}(k)$ in (1.16) around the origin.

This Hamiltonian models for example the dimerization in a monoatomic chain, due to a *Peierls Instability* [136] of the lattice. In this case the system can be thought of being composed by a repeating unit cell with two sites A and B, and v denotes the hopping inside the unit cell, while w denotes the hopping between neighboring cells. For $v = w$ the system is translationally invariant, representing free fermions on a lattice, and the spectrum is gapless. However, for $v \neq w$, the physics is drastically different depending on if $|v| > |w|$ or $|v| < |w|$, as can be realized by considering the chain with open boundary conditions. For $|v| > |w|$, every electron can form a dimer with a neighboring one, while for $|v| < |w|$ the two electrons at the boundaries are left unpaired. This situation is schematically shown in Fig. 1.2(a). This leads to a degeneracy in the ground state and the formation of edge states that, as we saw, is a standard signature of topological properties.

To unveil these properties, we can investigate the bulk of the chain in momentum space: as the translational invariance is explicitly broken for $v \neq w$, the Hamiltonian decomposes in 2×2 blocks that can be written in terms of the Pauli matrices $\boldsymbol{\sigma}$ as

$$H(k) = \begin{pmatrix} 0 & v + we^{-ik} \\ v + we^{ik} & 0 \end{pmatrix} = \mathbf{h}(k) \cdot \boldsymbol{\sigma}, \tag{1.15}$$

with

$$\mathbf{h}(k) = (v + w\cos k, w \sin k, 0). \tag{1.16}$$

The spectrum of decomposes then in two bands with energy

$$E_{\pm}(k) = \pm\sqrt{v^2 + w^2 + 2vw\cos k}. \tag{1.17}$$

As shown in Fig. 1.2, the spectrum is gapless for $v = w$ at momentum $k = \pm\pi$, while the gap opens for $v \neq w$. In the other extreme limits $(v = 0, w \neq 0)$ and $(w = 0, v \neq 0)$ the spectrum forms two flat bands and the system is totally dimerized.

The phase diagram of the model is composed then by two insulating phases connected by one metallic transition point. However, the two gapped phases are not topologically equivalent: if we compute the Berry phase of the lower, fully occupied band $|E_-(\boldsymbol{k})\rangle$, we obtain

$$A_-(k) = -i\langle E_-(\boldsymbol{k})|\partial_k|E_-(\boldsymbol{k})\rangle = -\frac{1}{2}\frac{\mathrm{d}\phi}{\mathrm{d}k}, \qquad \phi(k) = \arctan\left(\frac{w\sin k}{v + w\cos k}\right).$$

This expression of the connection as a derivative of an angle is particularly representative of the topological nature of the model: if we compute the Berry phase integrating over the Brillouin zone, we can obtain two different integers depending on the values of v and w

$$-\frac{1}{\pi}\int_{-\pi}^{\pi} \mathrm{d}k A_-(k) = -\frac{1}{2\pi}\left(\phi(\pi)-\phi(-\pi)\right) = \begin{cases} 0 & v > w \\ 1 & v < w \end{cases} . \tag{1.18}$$

For one dimensional systems this is also sometimes called *Zak phase* [137]. Due to the gauge invariance of A_-, the Zak phase is only defined modulo 2. The same result can be obtained by computing the *winding number*, that is the number of times the vector $\mathbf{h}(k)$ winds around the origin as k goes from $-\pi$ to π:

$$\nu = \frac{1}{2\pi}\int_{-\pi}^{\pi} \mathrm{d}k \frac{\partial_k \mathbf{h}(k)}{|\mathbf{h}(k)|} = \begin{cases} 0 & v > w \\ 1 & v < w \end{cases} .$$

In this picture the topological nature of the model is even more evident, by representing the vector $\mathbf{h}(k)$ as a vector in the plane, as shown in Fig. 1.2(b).

It is worth noting that the winding number is not in general constrained to be an integer. What it represents is indeed the solid angle spanned by the vector $\mathbf{h}(k)$ as changing k. It is however constrained to the plane h_x, h_y due to the condition $h_z = 0$ in Eq. 1.16. This results in the quantization condition $\nu \in \mathbf{Z}$.

The condition $h_z = 0$ is indeed the core of the topological properties of the SSH chain: if we add a perturbation $\propto \sigma_z$ the transition point $v = w$ becomes gapped and the system is a trivial insulator. This condition is in turn enforced by the *chiral symmetry* of the SSH Hamiltonian:

$$\sigma_z H(k) \sigma_z^{-1} = -H(k). \tag{1.19}$$

The chiral phase is then the symmetry protecting the topological phase.

The two phases are more evident with open boundary conditions thanks to the bulk-boundary correspondence: in the topological phase the two edge states that appear at the boundary in the fully dimerized survive the change of parameters until the gap closing, while in the trivial phase they are absent.

1.1.4 Topological superconductors: the Kitaev chain

The classification of SPT phases can be extended to systems with a non-trivial superconducting pairing as prescribed by BCS theory [138]. Although their Hamiltonians are not describing free particles, their quadratic structure makes it possible to diagonalize them and extract topological invariants analytically from the band structure. In this case though, the bands are not labeling free electrons, but free *Bogoliubov quasiparticles*.

The most relevant example of a topological superconductor for the scope of this thesis is the *Kitaev chain* [102]. This model describes spinless fermions hopping on a one-dimensional lattice, with an extra term describing p-wave superconductivity, as described by the Hamiltonian.

$$H = -\frac{1}{2}\sum_i \left(t c_i^\dagger c_{i+1} + \Delta c_i^\dagger c_{i+1}^\dagger + h.c. \right) - \mu \sum_i c_i^\dagger c_i, \tag{1.20}$$

where t is the hopping amplitude, Δ is a mean-field p-wave superconducting pairing and μ is the chemical potential.

The main interest of this system is the possibility of using its edge states as building blocks to realize intrinsically fault-tolerant topological qubits [139, 140]. For this reason its experimental realization has been the object of intense investigation in the last decade [103]. We will discuss this aspect in more detail in Chapter 4.

As for the SSH model, we can extract the bulk topological properties by going to momentum space. To do so we have to introduce the *Nambu spinor* $\Psi_k = \left(c_k^\dagger, c_{-k}\right)^T$, such that the Hamiltonian can be written as a quadratic form

$$H = \frac{1}{2}\sum_k \Psi_k^\dagger H_{BdG}(k)\Psi_k, \qquad H_{BdG}(k) = \begin{pmatrix} \mathcal{H}_0 & \mathcal{H}_\Delta \\ \mathcal{H}_\Delta^* & -\mathcal{H}_0 \end{pmatrix}, \tag{1.21}$$

with

$$\mathcal{H}_0 = -\mu - t\cos(k), \qquad \mathcal{H}_\Delta = -i\Delta\sin k. \tag{1.22}$$

The matrix H_{BdG} is called *Bogoliubov-de Gennes* (BdG) Hamiltonian. To obtain it we promoted the fermionic destruction operators c_k to new degrees of freedom: creation operators for *holes*. To counterbalance this artificial doubling of the degrees of freedom we had to introduce a new particle-hole symmetry in the system $C = \sigma_x K$, where K is the complex conjugation operator and τ_x is the Pauli matrix acting on the particle-hole space. It is easy to see that $CH_{BdG}C^{-1} = -H_{BdG}$: as a consequence the spectrum of H_{BdG} is composed by two bands symmetric around zero energy.

We can now proceed as we did for the SSH model. We express the Hamiltonian in momentum space and in terms of 2×2 blocks by using the Pauli matrices in particle-hole space $\boldsymbol{\tau}$ as

$$H_{BdG}(k) = \mathbf{h}(k)\cdot\boldsymbol{\tau}, \qquad \mathbf{h}(k) = (0, -\Delta\sin k, -\mu - t\cos k,). \tag{1.23}$$

The final diagonalization of the 2×2 blocks is called a *Bogoliubov transformation*, and results in a spectrum

$$H_{BdG}(k) = \sum_{BZ} E_\pm(k) a_k^\dagger a_k, \qquad E_\pm(k) = \pm\sqrt{(-\mu - t\cos k)^2 + \Delta^2\sin^2 k}. \tag{1.24}$$

The elementary degrees of freedom $a_k = \sum_i \left(u_{ik}c_i + v_{ik}c_i^\dagger\right)$, with u_i and v_i the eigenvectors of the BdG Hamiltonian, are a superposition of a particle and a hole, called *Bogoliubov quasiparticles*. As for the case of the SSH chain, for a finite Δ the spectrum is gapped for any value of k, expect in a particular point in parameter space. In this case, when $|\mu| = t$, the gap closes for $k = 0, \pi$.

To compute the topological invariant we can proceed as before by computing the winding number of $\mathbf{h}(k)$. In this case however, the symmetry protecting the topological phase is the particle-hole symmetry C. It turns out that an easier way to express the resulting invariant is

$$Q = \text{sign}\left(Pf(\mathcal{H}(k=0))Pf(\mathcal{H}(k=\pi))\right), \tag{1.25}$$

where Pf denotes the *Pfaffian* of the matrix $\mathcal{H}$. This quantity is defined only for antisymmetric matrices, and is related to the determinant by $Pf(\mathcal{H})^2 = \det(\mathcal{H})$ [100]. It will be relevant in the next section for the study of the Fractional Quantum Hall Effect.

Majorana Fermions

The edge states of the Kitaev chain appearing in the topological phase when $|\mu| < t$, are particularly interesting. This can be shown by diagonalizing the Hamiltonian in real space in the extreme limits $\mu = 0, t \neq 0$ and $\mu \neq 0, t = 0$, that as we know are adiabatically connected to all the states in the trivial and topological phases respectively.

In both case we are going to express the fermionic operators in terms of "half-fermions"

$$\gamma_{2i-1} = \frac{1}{2}\left(c_i + c_i^\dagger\right), \qquad \gamma_{2i} = \frac{1}{2i}\left(c_i - c_i^\dagger\right), \tag{1.26}$$

The operators γ_i create *Majorana fermions* [141]. They are special in the sense that they are their own antiparticles:

$$\gamma_i = \gamma_i^\dagger, \qquad \{\gamma_i, \gamma_j\} = 2\delta_{ij}. \tag{1.27}$$

There are currently no experimental realization of Majorana fermions as elementary particles, but as in this case they can be realized as emergent excitations in condensed matter systems [100, 102, 142]. By expressing the Hamiltonian in terms Majoranas we obtain (putting $\Delta = \mu$ for simplicity)

$$H = i\frac{\mu}{2}\sum_i \gamma_{2i-1}\gamma_{2i} + \frac{t}{2}\sum_i \gamma_{2i}\gamma_{2i+1}. \tag{1.28}$$

In the extreme (trivial) limit $t = 0$ the γ on the same site $(2i-1, i)$ can be paired again in the original fermions c_k, and the ground state corresponds to localized fermions without hopping. In the other extreme (topological) limit $\mu = 0$ the γ can be seen as paired on adjacent sites, and the Hamiltonian is diagonal on a basis of non-local fermions $d_i = (\gamma_{2i} + i\gamma_{2i+1})$.

There are, however two Majoranas γ_1 and γ_{2N} that do not appear in the diagonal Hamiltonian and are left unpaired at the boundaries of the chain. These are the edge states of the system. As Majoranas are not physical excitations, they can be combined to create an *extremely non-local* excitation

$$f = \frac{1}{2}\left(\gamma_1 + i\gamma_{2N}\right). \tag{1.29}$$

The zero-energy mode f lies in the middle of the spectrum of the system, symmetric due to the particle-hole symmetry. Being a zero-energy fermion, its presence or absence in the system makes the ground state doubly degenerate.

1.1.5 The periodic table of topological insulators of superconductors

The similarity between the various models we encountered so far hints at a unifying framework that can describe all the topological phases of matter described by a single-particle bands. The complete characterization of all the topological insulators and superconductors was indeed performed starting from three possible symmetries that can be preserved [82, 143]:

- Time-reversal symmetry T (anti-unitary): $TH(k)T^{-1} = H(-k)$,
- Particle-hole symmetry C (anti-unitary): $CH(k)C^{-1} = -H(-k)$,
- Chiral symmetry S (unitary): $SH(k)S^{-1} = -H(k)$.

Class	T	C	S	$d=1$	$d=2$	$d=3$
A	0	0	0	0	$\mathbb{Z}$	0
AIII	0	0	1	$\mathbb{Z}$	0	$\mathbb{Z}$
AI	1	0	0	0	0	0
BDI	1	1	1	$\mathbb{Z}$	0	0
D	0	1	0	$\mathbb{Z}2$	$\mathbb{Z}$	0
DIII	-1	1	1	$\mathbb{Z}2$	$\mathbb{Z}2$	$\mathbb{Z}2$
AII	-1	0	0	0	$\mathbb{Z}2$	$\mathbb{Z}2$
CII	-1	-1	1	$2\mathbb{Z}$	0	$\mathbb{Z}2$
C	0	-1	0	0	$2\mathbb{Z}$	0
CI	1	-1	1	0	0	$2\mathbb{Z}$

TABLE 1.1: The periodic table of topological insulators and superconductors for different dimensionalities. The IQHE belongs to class A, the Kitaev chain to class D, and the SSH model to class BDI.

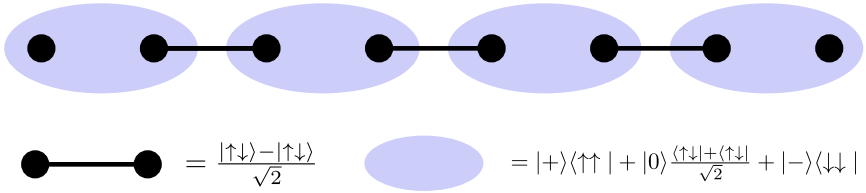

FIGURE 1.3: The AKLT state with 4 sites. The black dots represent "artificial" spin-1/2 at the boundaries, forming singlets with the neighbors (black lines). The blue ovals are projectors on the physical, spin-1 degrees of freedom. It is possible to see the unpaired spin-1/2 at the boundaries.

This led to a full classification called the 10-fold way [144, 145] or the *periodic table of topological insulators and superconductors* [83], shown in Table 1.1. In this classification the IQHE belongs to class A, the Kitaev chain to class D, and the SSH model to class BDI (there are indeed several ways to protect the topological phase).

1.1.6 Topology induced by interactions: the Haldane phase

The classification of the periodic table completed the theoretical understanding of topological band structures. However, the presence of interactions opens a completely new avenue to stabilize SPT phases [86, 88]. In this case the computation of quantities like the Berry phase and the Chern number is impractical due to the lack of a clear band structure. For this reason, the identification of topological phases is mainly based on the impossibility to adiabatically connect them to a trivial product state without closing the gap.

To introduce some quantities used for the purpose, we will explore the famous example of the spin-1 antiferromagnetic Heisenberg spin chain [84]:

$$H = J \sum_i \mathbf{S}_i \cdot \mathbf{S}_{i+1}. \tag{1.30}$$

For classical spins $S = 1/2$, the ground state of this model is the Néel state $(\uparrow\downarrow\uparrow\downarrow \dots)$. For quantum spins, however, this order gets destroyed by quantum fluctuations and the ground state is gapless with only polynomial quasi-long range order.

This was expected to hold for higher values of S. However, Haldane suggested that, while for half-integer S this actually is the case, for an integer S the system is

gapped. This remained a conjecture until a generalized model was solved numerically in presence of a quadratic interaction term [123]

$$H_{HB} = J \sum_i \left(\mathbf{S}_i \cdot \mathbf{S}_{i+1} + D \left(S_i \right)^2 \right). \tag{1.31}$$

It was found that this model is gapped for every value of D except for $D = 1$. For $D \to \infty$ one can easily see that the ground state is the state $|000\ldots\rangle$, so any state with $D > 1$ can be connected adiabatically to a trivial product state. The situation for $D < 1$, comprising the model in (1.30), is drastically different: for a related model

$$H_{AKLT} = J \sum_i \left(\mathbf{S}_i \cdot \mathbf{S}_{i+1} + \frac{1}{3} \left(\mathbf{S}_i \cdot \mathbf{S}_{i+1} \right)^2 \right), \tag{1.32}$$

the ground state was computed exactly by Affleck, Kennedy, Lieb and Tasaki (AKLT) [85, 122] and shown to be gapped. This *AKLT state* can be constructed by "breaking" each spin-1 to two spin$-1/2$ and coupling them in a singlet state with a spin-1/2 on a neighboring site. The state is then brought back to the spin 1 representation by applying a projector from the space of two spin-1/2 to one spin-1. A picture of this construction is shown in Fig. 1.3. The resulting state with periodic boundary conditions, expressed in a spin configuration basis $|s_1, \ldots, s_N\rangle$ can be written as

$$|\Psi_{AKLT}\rangle = \sum_{\{s\}} \mathrm{Tr} \left[A^{s_1} \ldots A^{s_N} \right] |s_1, s_2, \ldots, s_N\rangle, \tag{1.33}$$

with $s_i \in \{+, 0, -\}$ and the matrices A^{s_i} acting on site i defined as

$$A^+ = \sqrt{\frac{2}{3}} \sigma^+, \quad A^- = -\sqrt{\frac{2}{3}} \sigma^-, \quad A^0 = -\sqrt{\frac{1}{3}} \sigma^z, \tag{1.34}$$

This is an example of a *Matrix Product State*, a concept we will explore more deeply in the next chapter.

The AKLT state has several intriguing properties. It is gapped but does not break the symmetries of the Hamiltonian, eluding then the Ginzburg-Landau classification. It is short-range entangled due to his nature as a Matrix Product State. Most importantly, it is the unique ground state for $D = 1/3$ on the circle, but four-fold degenerate when on open boundary conditions. This degeneracy is linked to the presence of two decoupled "artificial" spins-1/2 at the boundary of the systems that can take any combination of values without changing the energy of the systems.

These properties, that extend to all the ground states of the model for $D < 1$ [146], already suggest the possible identification of an SPT phase, called in this case *Haldane phase*. To certify the topological nature of this phase, however, we need a global quantity reminiscent of the topological invariants that can be found for topological bands.

Pollmann et al. [147] discovered that the Haldane phase can be protected by three different symmetries: (i) the dihedral group $D_2 = \mathbb{Z}_2 \times \mathbb{Z}_2$ representing all the rotation of π along the three axis [148], (ii) time-reversal symmetry (iii) reflection symmetry along one bond [123]. Depending on the symmetries respected by the Hamiltonian different "order parameters" can be defined. For example in presence of the D_2 symmetry we can define the *string order parameter* [148, 149]

$$O_{ij} = \lim_{|i-j| \to \infty} \langle S_i^\alpha \exp \left(i\pi \sum_{k=i+1}^{j-1} S_k^\alpha \right) S_j^\alpha \rangle, \tag{1.35}$$

that can be extracted by mapping the Haldane model to a model with spontaneous symmetry breaking. The string order parameter is then a non-local quantity that detects the spontaneous breaking of a "hidden" symmetry. However, the only quantity that can identify the topological phase in presence either of the three symmetries is the *entanglement spectrum* [87, 150]. This is defined as the values $-\log(\lambda_i)$, where λ_i are the *Schmidt values* of a bipartition of the state. For a definition of the Schmidt values we refer to the next chapter. In presence of a topological phase, all the values in the entanglement spectrum are even-fold degenerate.

1.2 Topological Order

The examples we discussed up to this point owe the name of topological phases either due to their single particle band structure or, in the case of interacting systems, to the presence of a degeneracy in the entanglement spectrum. In all of these cases, it was possible to define an integer quantity or a topological invariant that characterizes the phase, and link it to the presence of edge states for the system with open boundary condition. However, both the edge states and the topological nature of the bulk can be destroyed if a perturbation breaking the protecting symmetry is introduced.

Nevertheless, there is a class of quantum systems that have more robust topological characteristics, not relying on any particular protecting symmetry. These are called *topologically ordered* phases [11]. Compared to SPT they have long-range entanglement and their ground states are degenerate even if put on closed manifolds with non-trivial topology. However, their most striking peculiarity is the presence of bulk excitations that have *fractional charge* with *fractional statistics*[2].

Some notable theoretical examples of topologically ordered phases are the Kitaev toric code [51, 98], the chiral spin liquids [151] and the 2D $p+ip$-wave superconductor [100]. However, the most famous example is the *Fractional Quantum Hall Effect* (FQHE) [6, 152]. This was the phase for which the concept of topological order was created [10].

In this section we will focus on this latter example, as it will be the system under study in Chapter 3. We will see in what sense it is drastically different from the more trivial IQHE, and describe in more detail the properties of the fractional excitations.

1.2.1 Fractional Quantum Hall Effect

The main approximation we introduced when talking about the IQHE in Section 1.1.2 was neglecting the electron-electron interaction. This let us describe the system in terms of single-particle physics, and use the techniques and terminology of topological bands to extract the Chern number and the quantized Hall conductivity. While the assumption is well justified in the case of completely filled bands, it is not the case when the Fermi energy lies in the middle of a band. In this case, the quenched kinetic energy of the electrons makes the coulomb interaction

$$V_c(\mathbf{r_i} - \mathbf{r_j}) = \frac{e^2}{4\pi\epsilon_0|\mathbf{r_i} - \mathbf{r_j}|}, \tag{1.36}$$

relevant.

[2] SPT phases can have fractional excitations, but only as edge states

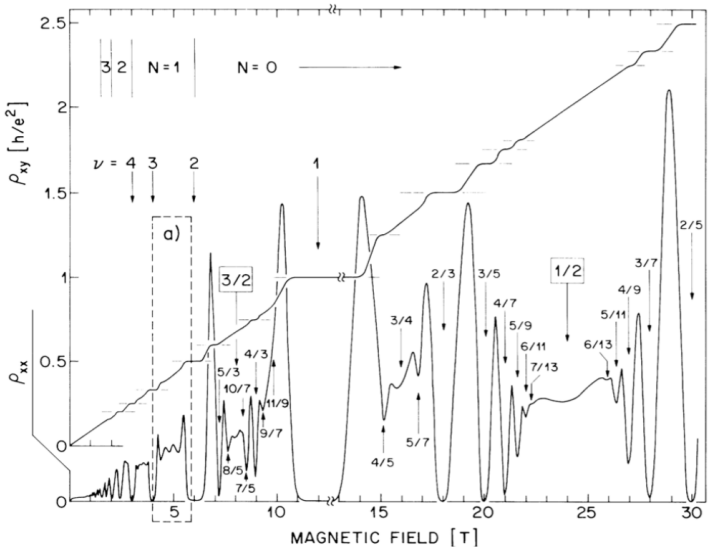

FIGURE 1.4: Experimental evidence of FQHE resistivity plateaus in an electronic system. Data taken from [153]. Fractional resistivity plateaus are visible for high magnetic fields on the right of filling $\nu = 1$.

Intuitively, the potential V_c lifts the degeneracy of the Landau levels splitting it into a band of width $\sim V_c$. Gaps can then form inside these bands in correspondence of a fractionally filled Landau Level. As in the case of the IQHE these gaps would then correspond to plateaus in the Hall conductance, but with a quantized value that is a fraction of the one in the IQHE. An exact solution of the full Hamiltonian

$$H_{FQHE} = \sum_i \frac{1}{2m}\left(\mathbf{p}_i - \frac{e}{c}\mathbf{A}(\mathbf{r}_i)\right)^2 + \sum_{i<j} V_c(\mathbf{r_i} - \mathbf{r_j}), \tag{1.37}$$

in presence of the Coulomb interaction is not possible. Moreover, the flat-bands structure of the non-interacting problem makes it impossible to treat V_c perturbatively. Numerical solutions are possible, as we will see in Chapter 3, but are limited to at most a dozen particles. Nevertheless, this model was studied with great success. The reason is that the phenomenology of FQHE can be captured with great accuracy by some special ansatz wavefunctions [152, 154–156]. Here we will introduce the two most famous examples, the Laughlin wavefunction [152] and the Moore-Read wavefunction [155], and explain how they describe states at different filling fractions, and how their excitations behave in a subtly different way.

1.2.2 Laughlin state

The Laughlin wavefunction [152] was proposed to describe FQHE state at filling fraction $\nu = 1/m$[3], and has the form

$$\Psi_\nu(z_1, \ldots, z_N) = \prod_{i<j}(z_i - z_j)^m \, e^{-\sum_i |z_i|^2/4l_B^2}, \tag{1.38}$$

[3]The filling is defined as $\nu = N/N_\phi$, where N is the number of particles and the previously defined N_ϕ is the degeneracy of the lowest Landau level.

where $z_i = x_i + iy_i$ is the complex coordinate of the i-th particle and $l_B = \sqrt{\hbar c/eB}$ is the magnetic length. It describes fermions for m odd, and bosons trial ansatz wavefunctions were discovered for the ground state that describe with great accuracy for m even. It was constructed on the grounds that it has to reproduce the correct filling fraction, and it has to be expressed in terms of wavefunctions of the lowest Landau level. Macroscopically, it represents an incompressible liquid, as the wavefunction vanishes if the particles are brought together, or if they are too far from the origin.

The correctness of this assumption can be shown by computing the overlap of the ground state of the Hamiltonian H_{FQHE} with the Laughlin wavefunction, which is found to be extremely high for a variety of interaction potentials and a couple of dozen of particles, as we will show in Chapter 3. We can then assume that even if the Laughlin wavefunction and the ground state of (1.37) are not exactly the same, they belong to the same *class of universality*. Nevertheless, a toy Hamiltonian can be constructed whose ground state is exactly (1.38) by using the *Haldane pseudopotentials* [157]: these so-called *parent Hamiltonians* are the starting point to add the effects of impurities or perturbation over the FQHE state, as we will see in Chapter 3.

Quasi-holes and quasi-particles

One of the most intriguing properties of the Laughlin state is the presence of bulk excitations called *quasi-holes* and *quasi-particles*. These are zero-energy localized bulk excitations that take their name from the fact that they only carry a *fraction* of the charge of an electron. In particular, for the Laughlin wavefunction at filling $\nu = 1/m$, the quasi-particles have charge e/m and the quasi-holes have charge $-e/m$.

The wavefunction for quasi-holes can be obtained by multiplying (1.38) by a factor $\prod_{i=1}^{m}(z_i - \zeta)$, where ζ is the position of the quasi-hole:

$$\Psi_{qh}(z_1, \dots, z_N) = \prod_{i=1}^{N}(z_i - \zeta)\prod_{i<j}\left(z_i - z_j\right)^m e^{-\sum_i |z_i|^2/4l_B^2}. \tag{1.39}$$

The charge of the quasi-hole is readily obtained from this expression: if we were to insert m quasi-holes at position ζ, the wavefunction would get multiplied by a factor $\prod_{i=1}^{m}(z_i - \zeta)^m$, corresponding to a Laughlin state with one more electron at position ζ. But since ζ is not a dynamical variable, that would represent a deficit of charge $-e$ at that position. Hence, the negative charge $-e/m$.

Quasi-particle states, on the other hand, cannot be constructed in the same way as to insert a charge in the same fashion would amount to dividing for a factor $\prod_{i=1}^{m}(z_i - \zeta)^m$, instead of multiplying, introducing a singularity in the wavefunction. However, as the prefactor of the Laughlin state is a polynomial, another way to decrease its degree would be to act with a derivative, leading to the formulation for quasi-particles

$$\Psi_{qp}(z_1, \dots, z_N) = \left[\prod_{i=1}^{N}(\partial_{z_i} - \eta)\prod_{i<j}\left(z_i - z_j\right)^m\right] e^{-\sum_i |z_i|^2/4l_B^2}. \tag{1.40}$$

Note that the derivative does not act on the exponential.

The fractional charge is only one of the striking characteristics of quasi-holes and particles. A thing that will have much more repercussion is the fact that they have fractional *statistics*, meaning that they do not believe neither as fermion nor bosons, but as a sort of in-between called *anyons*. We will discuss this in more detail in the

following. Before that, however, we will introduce the Moore-Read wavefunction, and see how anyons arise differently in this case.

1.2.3 Moore-Read states

As the Laughlin wavefunction was describing fermions for m odd, the Moore-Read (MR) wavefunction [155] aims to describe fermionic FQHE states with m even, and bosonic with m odd. In particular, it was proposed to describe the $\nu = 5/2$[4] state [153, 158]. This is one of the most promising candidates for the implementation of topological quantum computing [97]. It has the form

$$\Psi_{MR}(z_1, \dots, z_N) = Pf\left(\frac{1}{z_i - z_j}\right) \prod_{i<j} (z_i - z_j)^m \, e^{-\sum_i |z_i|^2/4l_B^2}, \tag{1.41}$$

where Pf is the Pfaffian of the antisymmetric matrix $\frac{1}{z_i - z_j}$, as defined in (1.25).

As in the case of the Laughlin wavefunction, the Moore-Read wavefunction is not the exact ground state of H_{FQHE} at filling $\nu = 1/m$. However, effective Hamiltonians can be constructed whose ground state is exactly (1.41). The most evident case is the $\nu = 1$ state: in this case the Moore-Read wavefunction vanishes only when three particles are brought in the same position, meaning that is the exact ground state of the three-boy contact Hamiltonian

$$H_3 = \sum_{i<j<k} \delta^2(z_i - z_j)\delta^2(z_i - z_k), \tag{1.42}$$

when projected on the lowest Landau Level.

Quasi-holes in the Moore-Read wavefunction

The quasi-holes of the MR state have a very different nature from the ones of the Laughlin state. In particular, each quasi-hole added as in Eq. (1.39) by multiplying the MR state by a factor $\prod_{i=1}^{m} (z_i - \zeta)$, can be split in two *half* quasi-holes by relying on the properties of the Pfaffian.

For example, by adding two quasi-holes at positions ζ_1 and ζ_2 we can write

$$\Psi_{MR}(z_1, \dots, z_N) = \prod_{i=1}^{N} Pf\left(\frac{(z_i - \eta_1)(z_j - \eta_2) + (z_j - \eta_1)(z_i - \eta_2)}{z_i - z_j}\right) \Psi_{MR}(z_1, \dots, z_N). \tag{1.43}$$

We can then repeat the previous argument to confirm that we obtain a full missing electron when adding $2m$ quasi-holes, meaning that the quasi-holes charge is $-e/2m$. However, the situation is more interesting if we consider the case of an even number of quasi-holes $2n > 4$. in this case there are multiple, degenerate states with the same number of quasi-holes. It was shown that this degeneracy is 2^{n-1} for $2n$ quasi-holes [159]. This degeneracy in turn impacts the statistics of quasi-holes, that behave as *non-abelian anyons* [155].

1.2.4 Anyons

We now introduce the concept of *anyons* and *fractional statistics* [160]. Our discussion starts from some subtle consequences of the concept of indistinguishable particles

[4] Intended as a state with filling $\nu = 1/2$ on top of two fully filled Landau Levels

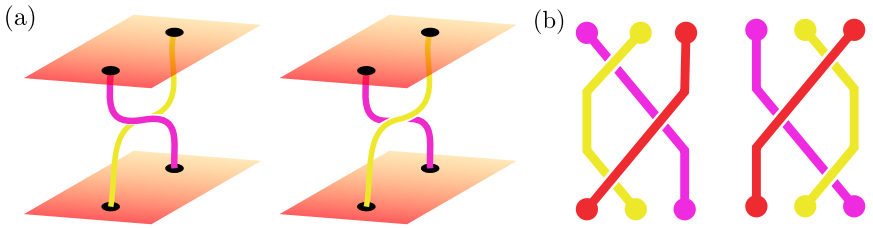

FIGURE 1.5: The braiding of two anyons. (a) Two non-equivalent (clock- and counter-clockwise) cannot be deformed one in the other without a crossing in their paths. (b) The Yang-Baxter relations: the two different ways to braid three anyons are equivalent.

in quantum mechanics. Consider for example a system of two identical particles placed in $\mathbf{q}_1, \mathbf{q}_2$ and exchanging them. This process can be described by a permutation P. If we perform two exchanges we must end up with the initial state, so that $P^2 = 1$. This means that the state of the system can be classified in terms of the eigenvalues of P, that is by either antisymmetric or symmetric wavefunctions under particle exchange:

$$P\psi_A(\mathbf{q}_1, \mathbf{q}_2) = -\psi_A(\mathbf{q}_2, \mathbf{q}_1), \qquad P\psi_S(\mathbf{q}_1, \mathbf{q}_2) = \psi_S(\mathbf{q}_1, \mathbf{q}_2). \tag{1.44}$$

However, all the operators of this system are symmetric under this exchange, meaning that it is not possible to have a superposition of an antisymmetric and a symmetric wavefunction: for any generic operator O, $\langle\psi_A|O|\psi_S\rangle = 0$, a *superselection rule*. That means that the system must be described by either a symmetric or antisymmetric wavefunction. This notion generalizes to any number of particles as long as they are identical. This approach, based on the (anti-)symmetrization of the wavefunction, leads to the standard distinction between Fermi-Dirac and Bose-Einstein statistics, and explains effects like the Pauli exclusion principle and Bose-Einstein condensation. On top of that, the spin-statistics theorem gives us a tool to assign the correct statistic to different kind of particles [161].

This picture can be enriched and generalized if we base our definition of statistics on a more physically motivated adiabatic exchange of the particles instead of an instantaneous permutation. The quantum statistics in this case will be related to the phase that appears during this exchange process.

While in three and more dimensions this approach gives the same results of the (anti-)symmetrization procedure [162], this is drastically different in two dimensions [163, 164]. This can already be realized by the consequences of the spin-statistics theorem in 2D. The quantization of spin relies on the non-commutative algebra of the generators $[S_j, S_k] = i\hbar\varepsilon_{jkl}S_l$. In two dimensions this algebra is trivial since there is only one allowed rotation, hence just one generator. That means that there is no quantization of angular momentum, suggesting that in two dimensions particles may interpolate between bosons and fermions [96], showing fractional statistics.

1.2.5 Braiding

To quantify the concept of fractional statistics, we have to explicitly perform the adiabatic exchange of two particles, also called *braiding*. In three or more dimensions, this is quite straightforward. After an exchange of particles their joint probability density must remain the same, meaning that the wavefunction just acquires a phase:

$$|\psi(\mathbf{r}_1, \mathbf{r}_2)|^2 = |\psi(\mathbf{r}_2, \mathbf{r}_1)|^2 \qquad \Rightarrow \qquad \psi(\mathbf{r}_2, \mathbf{r}_1) = e^{i\pi\alpha}\psi(\mathbf{r}_1, \mathbf{r}_2), \tag{1.45}$$

and after two exchanges, enforcing the fact that the wavefunction must be the same at the beginning and the end:

$$\psi(\mathbf{r}_1, \mathbf{r}_2) = e^{i2\pi\alpha}\psi(\mathbf{r}_1, \mathbf{r}_2) \qquad \Rightarrow \qquad e^{i\pi\alpha} = \pm 1. \tag{1.46}$$

The exchange is thus implemented by a permutation P, and the states lie in an irreducible representation of this group. If $\alpha = 0$ the particles are bosons, if $\alpha = 1$ they are fermions. In this case, the statement that the wavefunction must not change after an exchange between two particles is based on the fact that there is always a way to contract the exchange path to a point.

For $d = 2$ instead, not all the particle exchanges can be contracted to a point. That means that in principle there is no prescription for the wavefunction at the end of the exchange to be the same as the beginning. Let us picture the exchange process as pictured in Fig. 1.5(a): we start with two particles on a plane and follow their evolution under an adiabatic exchange. In this case the third dimension will represent time. As we can see the worldlines of a clockwise or a counter-clockwise exchange cannot be continuously deformed one in the other without a crossing. It is possible to classify all these different and not continuously connectable paths in topological classes forming elements of the so-called *braid group*. What then happens in $d = 2$ is that particle exchanges are represented by a representation of this group instead that by one of the permutation group.

The braid group can be constructed starting from a set of generators of exchanges which obey particular relations. Imagine putting n particles on a line and that σ_1 exchanges counter-clockwise particles 1 and 2, σ_2 exchanges particles 2 and 3 and so on. Any kind of exchange of the n particles can be built by repeatedly applying the σ operators, generating the group.

As a first condition these generators must satisfy

$$[\sigma_j, \sigma_k] = 0 \qquad \text{if } |j - k| \geq 2, \tag{1.47}$$

meaning that exchange of disjoint pairs of particles do not affect each other. The other, more subtle, relation is the so called Yang-Baxter relations [165]:

$$\sigma_j\sigma_{j+1}\sigma_j = \sigma_{j+1}\sigma_j\sigma_{j+1}, \qquad j = 1, 2, \ldots, n-2, \tag{1.48}$$

that can be more easily understood via a graphic representation like the one in Fig. 1.5(b).

In the simplest one dimensional representation of this group every generator is simply a phase: $\sigma_j = e^{i\pi\alpha_j}$. While this generator trivially satisfy (1.47) we must impose:

$$e^{i\pi\alpha_j}e^{i\pi\alpha_{j+1}}e^{i\pi\alpha_j} = e^{i\pi\alpha_{j+1}}e^{i\pi\alpha_j}e^{i\pi\alpha_{j+1}} \quad \rightarrow \quad \sigma_j = e^{i\pi\alpha}\ \forall j. \tag{1.49}$$

Particles that exhibit this kind of behaviour under exchange, i.e. for whose 2-particles wavefunction $\psi(\mathbf{r_1}, \mathbf{r_2})$ holds

$$\psi(\mathbf{r_2}, \mathbf{r_1}) = e^{i\pi\alpha}\psi(\mathbf{r_1}, \mathbf{r_2}), \tag{1.50}$$

are called *Abelian anyons*. The particular value of θ is explicitly dependent on the Hamiltonian of the exchange process, and it can be retrieved by computing the Berry phase of the adiabatic time dependent process. We can then understand the concept of fractional statistics as a value of α that interpolates between the fermionic ($\alpha = 1$) and bosonic ($\alpha = 0$) statistics.

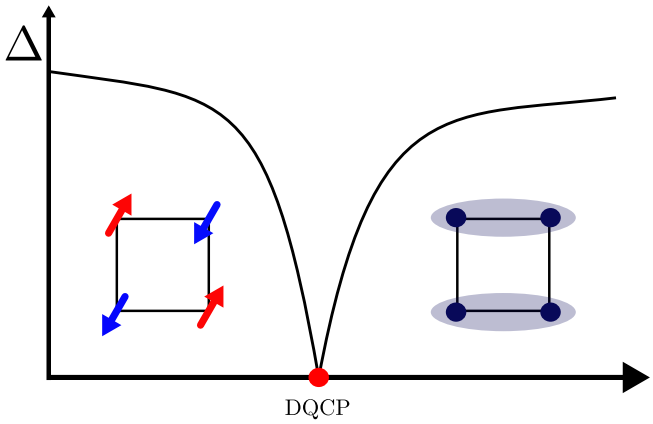

FIGURE 1.6: Sketch of DQCP. The transition between two symmetry broken phases is second order with a closing of the gap Δ. Here exemplified the Néel and VBS phases of the Heisenberg model on a square.

As the quasi-hole state in the Laughlin state is not degenerate, quasi-holes are an example of Abelian anyons with $\alpha = 1/m$ [166]. It is possible to build higher dimensional representations of the braiding group: that happens when the states of the particles to be exchanged are described by vectors in a degenerate ground state. The exchange process can then rotate the vectors in this space. In this case the generators σ are represented by matrices and the simple 2-particles exchanges do not in general commute with each other. Particles that transform under this representation are then called *non-abelian anyons*. The quasi-holes in the Moore Read state are an example of this [159, 167].

1.3 Deconfined Quantum Criticality

The last example of phenomenon eluding the Ginzburg-Landau paradigm is the so called *deconfined quantum criticality* [**senthil2023a**]. While in the rest of the chapter we considered *phases* going beyond symmetry breaking, in this section we will focus on only phase *transitions* not captured by the Landau framework.

As we stated in the introduction, in the Landau theory a second-order transition happens when we cross the boundary between two phases characterized by symmetries G and H such that $H \in G$. In this case we can describe the low-energy physics around the transition through a functional (such as the free energy in statistical physics) of the order parameter, that is invariant under the action of H: from that we can extract the transition point and characterize it through properties like Goldstone modes, correlation functions, critical exponents and so on.

Notably, this framework only works at a boundary connecting a trivial phase with a spontaneously broken one. It breaks down when considering boundaries between two non-trivial states, as for example the topological ones considered in the previous sections. In particular, in the case of transition between two symmetry broken phases with different symmetries H and H', the Landau theory predicts a first-order transition.

However, there are situations where two symmetry-broken phases can be connected by a second-order transition point, with a restoring of both symmetries and the appearance of a gapless phase. This is called a *deconfined quantum critical point* (DQCP) [121, 168]. The name comes from the fact that the low-energy physics at the transition is described by a *deconfined* gauge theory, and its excitations are not the

usual Goldstone modes, but *fractionalized* excitations. Notably, similar transitions can also be connected with the physics of SPT phases [169].

Firstly introduced by Senthil et al. in 2004 [168] in the context of two-dimensional antiferromagnets, they consider the Heisenberg model on a square lattice

$$\hat{H} = J \sum_{\langle ij \rangle} \boldsymbol{S}_i \cdot \boldsymbol{S}_j + \dots, \tag{1.51}$$

where the dots represent further-neighbor interactions and J is the antiferromagnetic coupling. The model is invariant under the action of the $SU(2)$ group of spin rotations, and the ground state is a Néel state with long-range antiferromagnetic order, breaking this symmetry. However, depending on the nature of further-range interactions the ground state can be a *valence bond solid* (VBS) state, where the spins are paired in singlets. This is reminiscent of the dimerization of the SSH model, but in this case the dimers are formed by two spins-1/2. This phase breaks translational invariance and lattice rotations, but preserves the $SU(2)$ symmetry. In [168] the authors show how these two phases can be connected by a second-order transition, gapless transition, as showed in Fig. 1.6.

This opened a search for this new class of critical points, that were discovered notably in systems like the previously mentioned spin Hall insulators [170], and various SPT-trivial insulator transitions [169, 171, 172]. Lately, several works hinted at the presence of DQCP in one-dimensional systems [**roberts2019a**, 173–175], mainly in spin systems. The search for this exotic critical points in one-dimensional fermionic and bosonic systems will be one of the main goal of Chapter 5.

Chapter 2

From classical to quantum simulation of quantum many-body systems

The simulation of quantum many-body systems is a central problem in modern physics: reliably simulating quantum systems in a controlled environment is a crucial step in understanding the physics of exotic phases of matter like the ones discussed in the previous chapter, and to guide the development of new materials with desired properties. However, this task is extremely challenging due to the exponential growth of the complexity of the problem with the number of particles present in the system. While this problem can sometimes be circumvented for weakly interacting systems, for example by using mean-field theory or perturbative approaches, like Fermi liquid theory for highly dimensional systems [176] and bosonization for one-dimensional systems [177], these pictures often fail to capture the physics of strongly correlated systems.

In those cases the most viable approach is to use numerical simulations to complement experimental results. In the years several methods have been developed to tackle this task, like variational and quantum Monte Carlo, Exact Diagonalization and Tensor Networks [54, 55]. Each one of these techniques has its own advantages and drawbacks: while quantum Monte Carlo techniques can deal with large systems, they are limited in the study of fermionic and frustrated systems due to the sign problem [178, 179]. Exact diagonalization, on the other hand, can deal with any kind of quantum system but are limited to small sizes due to the exponential growth of the Hilbert space. Tensor networks, finally, can be used to simulate impressively large system sizes but are currently limited to one and small two-dimensional systems due to the growing complexity of the involved calculations [180].

In the last twenty years more direct approaches to the simulation of quantum systems have been explored, based on the experimental realization of artificial quantum systems that directly reproduce the properties of the system under study in a controlled setting. These platforms are called *quantum simulators* and have been realized in a broad range of physical systems like photonic waveguides [181], trapped ions [182, 183], Rydberg atoms [184], and ultracold atoms in optical lattices [185, 186]. The main advantage of this platform is the possibility to reproduce the behavior of complex quantum systems, like solid state materials, in a controlled environment that allows for better tunability of the relevant parameters and a more direct access to the observables of interest. On the other side, compared to classical numerical simulations, quantum simulators can potentially reach a larger number of interacting particles and can be used to probe the dynamics of the system [187].

In this Chapter we will explore both the classical and quantum approaches relevant to the simulation of the phenomena discussed in the rest of the thesis. In the first section we will introduce the basic concepts of Exact Diagonalization and discuss its advantages and limitations. We will continue in the second section by introducing the concept of Tensor Networks and the related algorithms for the extraction of ground states of quasi-one dimensional systems, both in finite and infinite systems. We will also give an outline of more complex Tensor Network architectures. Finally, in the last section we will introduce the concept of quantum simulation using ultracold atoms in optical lattices, showing how various many-body Hamiltonians can be engineered by leveraging the interaction between confined neutral atoms and laser light, and how various measurements can be performed on the resulting systems.

2.1 Exact diagonalization

The Exact Diagonalization (ED) technique implies directly solving numerically the Schrödinger equation

$$H|\Psi\rangle = E|\Psi\rangle, \tag{2.1}$$

by expressing the Hamiltonian H as a matrix in an appropriate basis.

This technique has been successfully used to study the properties of systems such as fermionic and bosonic lattice models, quantum magnets and FQHE states [188, 189]. The main advantage of ED is that it does not involve approximations further than a truncation of the basis on which the Hamiltonian is expressed. Moreover, it can be used to study any kind of quantum system with arbitrary interaction ranges and dimensionality. However, the exponential scaling of the size of H with the number of degrees of freedom of the system, greatly limits the number of interacting particles we can consider: in the case of lattice systems the dimension of the full Hilbert space grows with the number of sites L as d^L, where d is the dimension of the local Hilbert space of the species in consideration, for example $d = 2$ for spin-1/2 particles or $d = 4$ for spinful fermions. Depending on the complexity of the local degrees of freedom the number of simulable particle can range from ~ 18 for fermionic systems to ~ 50 for quantum magnets [190].

While at first glance this approach may seem straightforward to implement, the choice of the basis and the efficient implementation of the symmetry constraints of the Hamiltonian can dramatically affect the performance of this method. In particular, choosing a basis that reflects the symmetries of H makes it possible to write the Hamiltonian matrix in a block-diagonal form, with each block corresponding to a different symmetry sector. The blocks can in turn be diagonalized independently, vastly reducing the computational cost and potentially opening the possibility to run the simulations in parallel [190].

Moreover, due to the extremely large size that the Hamiltonian can reach, particular care has to be taken to avoid resource bottlenecks in both memory and CPU. While physically relevant Hamiltonians usually have a sparse structure, with only a few non-zero elements in each row, modern algorithms directly compute matrix-vector multiplications without ever storing the matrix in memory. Finally, usually we are interested only in the lowest energy states of the system, so that we can use iterative methods to find the ground state without ever computing the full eigenvalue decomposition of the Hamiltonian. These precautions are at the basis of the Lanczos method [191], whose details we are discussing in Appendix A.

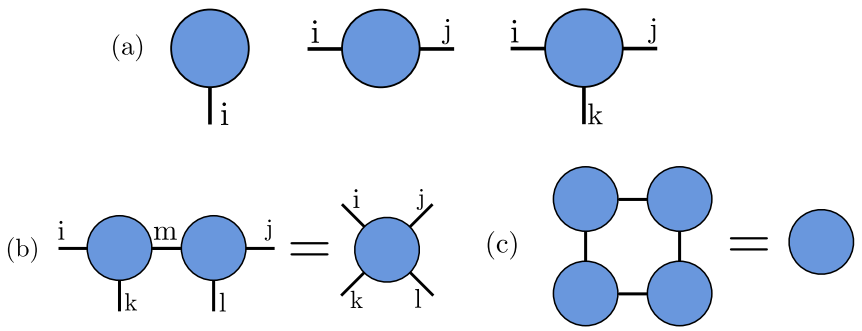

FIGURE 2.1: (a) Tensor Notation where each leg coming out of the circle represents an index of a tensor. An example of a tensor of rank 1 v_i (vector), a tensor of rank 2 (matrix) M_{ij}, and a tensor of rank 3 T_{ijk}. (b) Tensor contraction. Sum over repeated indices is represented as two legs of two tensors being connected. The result of the contraction is a tensor with the remaining indices. In this example we draw the contraction $A_{ikm}B_{mlj} = C_{iklj}$. (c) When fully contracting a network, the result is a scalar represented by a circle with no legs.

2.2 Tensor Networks

As we saw in the previous section, the power of ED techniques is strongly limited by the size of the system under study. Many numerical techniques have then been developed with the goal of overcoming this limitation. One typical way to circumvent this problem is to encode the state of the system in a parametrized function, called *ansatz*, with a number of parameters that is much smaller than d^L. The numerical value of the parameters is then variationally optimized in order to minimize a chosen goal function, usually the expectation value of the Hamiltonian. The crucial point is how to choose an appropriate ansatz that can appropriately capture the physics of the system under study while keeping a small enough number of parameters [52].

This is the idea behind several classes of numerical and analytical techniques called *Variational Methods*, that differ on the choice of physical ansätze and the processes of optimization of the variational parameters. Techniques belonging to variational methods are, for example, mean-field theory, Hartree-Fock theory, Variational Monte Carlo, Neural Network quantum states and the subject of this section, Tensor Networks.

The name Tensor Networks (TN) comes from the way to compactly represent various quantities. As shown in Fig. 2.1(a), relying on the linear structure of quantum mechanics, all the relevant quantities are expressed in terms of multidimensional arrays, or tensors, which are represented by nodes with a number of legs equal to their rank. Scalar product over shared indices, more commonly called *contraction* is represented as a connection between two legs, as shown in Fig. 2.1(b), whose result is another tensor with the remaining legs.

The field of Tensor Networks in quantum physics can be traced back to the ground state of the AKLT model as described in Chapter 1 [85], whose structure was lately extended to more complex models, leading to the concept of Matrix Product State [192, 193]. At the same time, a fundamental milestone was set by White with the development of the Density Matrix Renormalization Group (DMRG) algorithm [56, 57] to study one-dimensional quantum lattice systems. While the connection between the fixed point of the DMRG procedure and MPS was soon made [58, 194], the potential of Tensor Network was fully realized when it was shown the connection

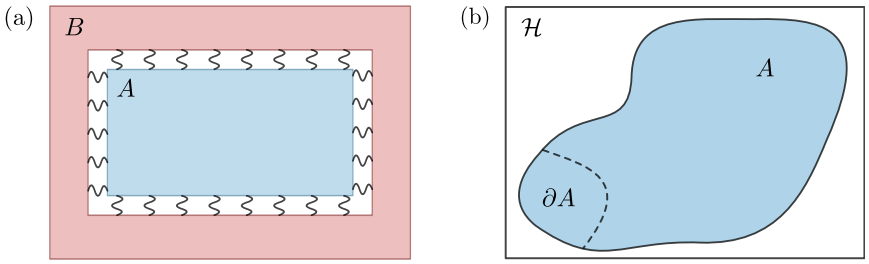

FIGURE 2.2: (a) In states following the area law all the entanglement between two subregions A and B is localized on their boundary. (b) The state following the area law are a small corner of the available Hilbert space but are the most physically relevant ones.

between the entanglement structure of one such state and its computational complexity. This led to a unified framework to study condensed matter physics with the tools of quantum information theory [60, 67, 195]. Starting from this point, the field of Tensor Networks has developed rapidly to other kind of systems like systems in two dimensions [68] or at criticality [69], and extensions to the study of dynamical [61] and thermal properties [65].

The Area Law

To develop the idea behind the power of Tensor Networks it is useful to start from a concept that links the entanglement structure of a quantum state to its computational complexity, as this connection will give us a powerful tool to efficiently compress these states [196].

Consider the (exponentially large) Hilbert space $\mathcal{H}$ of a generic many-body system. To each state $|\Psi\rangle \in \mathcal{H}$ we can associate a density matrix $\rho = |\Psi\rangle\langle\Psi|$, that can be used to define the bipartite *entanglement entropy* of the state as

$$S = -\mathrm{Tr}\left[\rho_A \log \rho_A\right], \tag{2.2}$$

where $\rho_A = \mathrm{Tr}_B\left[\rho\right]$ is the reduced density matrix of a subsystem A obtained by tracing out the degrees of freedom of the subsystem B. For a generic state in $\mathcal{H}$ the value of S is roughly proportional to the size of the subregion A, a property called *volume law*:

$$S \propto A \sim L^d. \tag{2.3}$$

This is in contrast to the ground states of gapped, local Hamiltonians, that are characterized by an entropy proportional to the boundary of subregion A, thus following the so-called *area law*:

$$S \propto \partial A \sim L^{d-1}. \tag{2.4}$$

This can be restated as saying that for the ground state of this type of Hamiltonians, all the correlations between the subregions A and B are localized at the boundary between the two. The area law states are only a small corner of the Hilbert space, but are the ones that are most relevant to the study of gapped systems.

The fundamental idea behind Tensor Networks is then to construct ansatzë to represent states in this corner of the Hilbert space, and in this way reducing the number of parameters needed to describe them. In the following we will focus on the type of Tensor Networks that are most relevant to the study of quasi-one dimensional systems and the ones used to obtain the results of this thesis: the *Matrix Product States* (MPS).

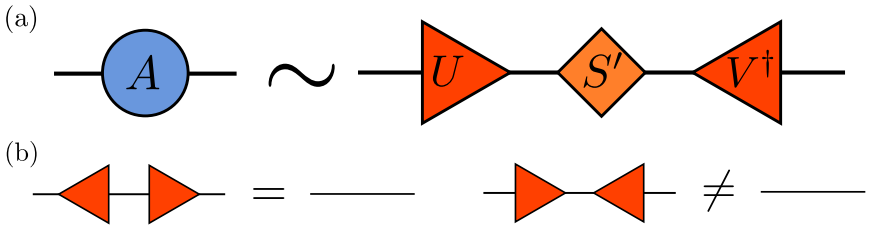

FIGURE 2.3: (a) Singular Value Decomposition written in Tensor Networks notation. In this representation isometries are drawn as triangles while diagonal matrices as rhombuses. (b) Properties of isometries: contraction of an isometry with its complex conjugate yields the identity (straight line). If the converse is true as well the isometry becomes a unitary transformation.

2.2.1 Matrix product states

For one-dimensional systems, the area law assumes a particularly simple form as the size of the boundary of a subregion A of length L with another subregion B does not depend on L, and is bounded by a constant:

$$S \propto L^{d-1} = c. \tag{2.5}$$

The aim is then to construct a variational ansatz respecting this property. As we will see this will result in a dramatic reduction of the number of parameters necessary for an accurate description of the ground states of local Hamiltonians. In particular, this number scales linearly with the size of the system, instead of exponentially. To this end we first have to introduce the concept of *Singular Value Decomposition*.

Singular Value Decomposition and Schmidt decomposition

The Singular Value Decomposition (SVD) is a particular way to express a generic rectangular matrix A of dimension $m \times n$:

$$A = USV^\dagger, \tag{2.6}$$

where U and V are respectively *left and right isometries* of dimensions $m \times d$ and $d \times n$, that is matrices that respect the properties $U^\dagger U = \mathbb{1}$ and $V^\dagger V = \mathbb{1}$. If A is square $m = n = d$ and the isometries become unitary transformations also obeying $UU^\dagger = \mathbb{1}$ and $VV^\dagger = \mathbb{1}$. The matrix S is instead a rectangular diagonal matrix of dimension $d \times d$ where $d = \min(m, n)$, with non-negative entries called *singular or Schmidt values*. The number of non-zero singular values is called the Schmidt *rank* of the matrix A. The SVD and the isometry matrices are represented using the Tensor Networks notation in Fig. 2.3.

Let us now see how the SVD is linked to another decomposition called *Schmidt decomposition* which, in turn, makes explicit the connection between the singular values and the entanglement entropy of a bipartite quantum state. For any bipartite state $|\Psi\rangle \in \mathcal{H}_A \otimes \mathcal{H}_B$ we can in general write

$$|\Psi\rangle = \sum_{i,j=1}^{d} c_{ij} |a_i\rangle |b_j\rangle, \tag{2.7}$$

where $\{|a_i\rangle\}$ and $\{|b_j\rangle\}$ are orthonormal bases of $\mathcal{H}_A$ and $\mathcal{H}_B$ respectively, and d was defined above. The Schmidt decomposition of the state is obtained by performing

an SVD on the matrix c_{ij}:

$$|\Psi\rangle = \sum_{i,j=1}^{d} U_{is} S_{ss'} V^{\dagger}_{s'j} |a_i\rangle |b_j\rangle = \sum_{s=1}^{d} \lambda_s |\tilde{a}_s\rangle |\tilde{b}_s\rangle, \tag{2.8}$$

where $|\tilde{a}_s\rangle$ and $|\tilde{b}_s\rangle$ are the rotated basis of the two subsystems and λ_s are the singular values of the matrix c_{ij}. From this expression, recalling that the full density matrix of the system is $\rho = |\Psi\rangle\langle\Psi|$, it is straightforward to extract the entanglement entropy of the bipartition $A|B$ as

$$S = -\mathrm{Tr}\left[\rho_A \log \rho_A\right] = -\sum_{s=1}^{d} \lambda_s^2 \log \lambda_s^2. \tag{2.9}$$

It is important to note that as the λ_s^2 are the eigenvalues of a density matrix, they are all positive and sum up to one. We get minimum entanglement for a product state $|\tilde{a}_1\rangle|\tilde{b}_1\rangle$ with $\lambda_s^2 = 1$ for $s = 1$ and $\lambda_s^2 = 0$ for all the others, and maximum entanglement for a fully entangled state with uniform $\lambda_s^2 = 1/d$ for all s. We can then see that the Schmidt spectrum of a bipartition is a measure of its entanglement: the faster the Schmidt values decrease with s, the smaller the entanglement entropy and the closer the state is to a product state. Moreover, the Eckart-Young-Mirsky theorem [197, 198] states that the truncation of the SVD to a finite rank s' is the best approximation of the state in the sense of the Frobenius norm $\||\Psi\rangle\| = \mathrm{Tr}\left[\rho^2\right]$:

$$\||\Psi\rangle - |\Psi_{s'}\rangle\| = \min_{|\Psi'\rangle \in \mathcal{H}_{s'}} \||\Psi\rangle - |\Psi'\rangle\|, \tag{2.10}$$

where $\mathcal{H}_{s'}$ is the space of states with Schmidt rank s'. We can then conclude that for a bipartite state the most efficient approximation is the one that keeps only the most relevant degrees of entanglement at the boundary between the two subsystems: if the state is close to a product state this compression will be very efficient, getting worse as the entanglement grows.

We will now repeatedly apply this idea to a one dimensional quantum state to construct an MPS, making explicit the amount of entanglement encoded in each bipartition. To do such we will introduce the tensor notation for states: a state describing a lattice of L sites $\{s_1, \ldots, s_L\}$ with local Hilbert space d written as

$$|\Psi\rangle = \sum_{s_1,\ldots,s_L} T_{s_1,\ldots,s_L} |s_1, \ldots, s_L\rangle, \tag{2.11}$$

is identified by a set of d^L coefficients $T_{s_1,\ldots,s_L}$ that can be seen as a tensor of rank L as represented in Fig. 2.4. We can now create a matrix out of T by grouping all the indexes together except the first one and then decompose it using an SVD:

$$T_{s_1,(s_2,\ldots,s_L)} = A^{s_1}_{j} T'_{j,(s_2,\ldots,s_L)}, \tag{2.12}$$

obtaining a contraction between to tensors of rank 1 and $L-1$ respectively. We can then repeat the process by grouping the first two indices of T and decomposing again, and continue iteratively until we reach the last two indices. The final result is a state

$$|\Psi\rangle = \sum_{s_1,\ldots,s_L} A^{s_1}_1 A^{s_2}_2 \ldots A^{s_L}_L |s_1, \ldots, s_L\rangle, \tag{2.13}$$

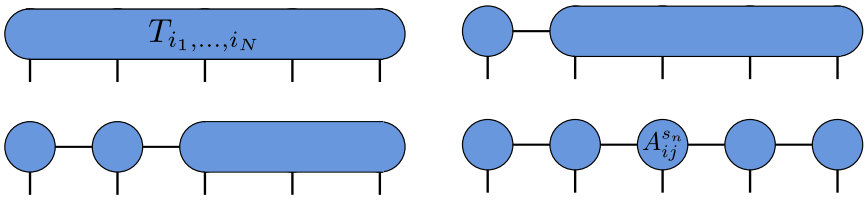

FIGURE 2.4: From a full quantum state to an MPS. Starting from the full tensor of coefficients $T_{s_1,\ldots,s_L}$ we can repeatedly perform an SVD on each bond by grouping the indices on the two sides of the partition to obtain an MPS.

where the tensor T was decomposed in a product of L matrices A, from which the MPS take their name. The graphical representation of this process is shown in Fig. 2.4.

At this point no approximation has been made, and the state is still described by d^L coefficients. Indeed, by construction the matrix A_n has dimension $d^{n-1} \times d^n$ for $n = 1, \ldots, L/2$ and $d^{L-n} \times d^{L-n+1}$ for $n = L/2+1, \ldots, L$. However, by recalling the approximation properties of the SVD we can truncate the dimension of the matrices A to a maximum value χ without losing too much accuracy. The quantity χ is called in this framework the *bond dimension* of the MPS and is a measure of the entanglement of the state. We can readily check the maximum amount of entanglement that can be encoded in an MPS at fixed bond dimension: for a fixed bond dimension χ, the maximally entangled state has uniform entries on the diagonal of the reduced density matrix $\lambda_s^2 = 1/\chi$ for $s = 1, \ldots, \chi$. The corresponding entanglement entropy is then

$$S = -\sum_{s=1}^{\chi} \frac{1}{\chi} \log \frac{1}{\chi} = \log \chi < c. \tag{2.14}$$

We can then conclude that an MPS at fixed bond dimension correctly encodes the entanglement structure of an area law state in one dimension, and in particular the ground states of local, gapped Hamiltonians. By directly checking Eq. (2.13) we can see that the number of parameters describing such MPS is $Ld\chi^2$, thus scaling linearly instead than exponentially with the size of the system.

2.2.2 Properties of Matrix Product States

On top of the dramatic reduction of the number of parameters necessary to describe the state, MPS have several properties that make them ideal candidates to perform efficient numerical simulations. In the following section we will discuss some of them particularly important for the results of this thesis.

Efficient contractions

For a variational ansatz to be useful, there must be an efficient way to compute quantities like expectation values of operators or overlaps with other states. This corresponds in the TN language in fully contracting a network. While for generic TN the problem of finding the optimal contraction is non-trivial, for MPS this can be done optimally with a number of operations of order $\mathcal{O}(Ld\chi^3)$ by following an algorithm as shown in Fig. 2.5. Another order of contractions can produce a worse scaling that can drastically affect the employability of the ansatz. For example, a naive contraction of the state with its complex conjugate produces a scaling of $\mathcal{O}(\chi^4)$, that makes computations intractable for large bond dimensions.

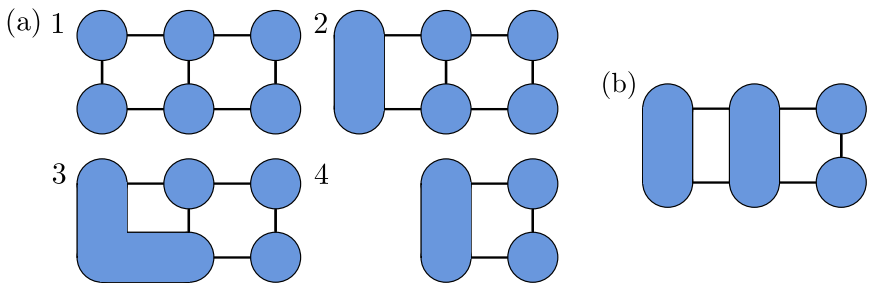

FIGURE 2.5: Example of computation of the expectation value $\langle\Psi|\Psi\rangle$. (a) The optimal contraction with scaling $\mathcal{O}(Ld\chi^3)$ by following a "zip up" algorithm. (b) An example of an inefficient contraction with scaling $\mathcal{O}(\chi^4)$.

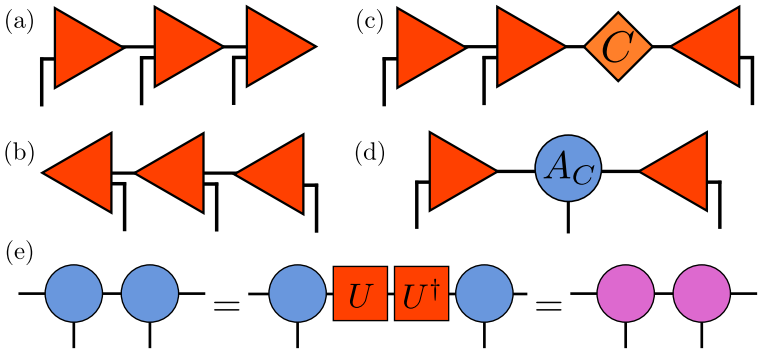

FIGURE 2.6: Canonical forms of an MPS. (a) Left canonical form. (b) Right canonical form. (c) Mixed bond canonical form. (d) Mixed site canonical form. (e) A generic gauge transformation acting on a bond.

Gauge transformations and canonical forms

In many circumstances it is not necessary at all to contract MPS to obtain some quantities of interest. This is due to the highly non-unique way to represent a state as an MPS. In particular, it is always possible to perform a local gauge transformation on each one of the bonds without changing the final state. Indeed, for any generic unitary matrix U_n acting on a bond n we can write

$$\ldots A^{s_n} A^{s_{n+1}} \cdots = \ldots A^{s_n} U_n U_n^\dagger A^{s_{n+1}} \cdots = \ldots \tilde{A}^{s_n} \tilde{A}^{s_{n+1}} \ldots, \tag{2.15}$$

changing two matrices in the MPS without changing the physical state. It can be proven that this is the most general gauge transformation acting on the space of MPS [53]. Gauge freedom is central to the flexibility of MPS as a computational tool as it drastically simplifies the operations required to contract the full network.

In particular gauge transformations can be used to rewrite an MPS in one of four different *canonical forms* by using an SVD: left, right, mixed bond or mixed site canonical. This amounts to writing the state in terms of left or right isometries, possibly changing the direction of the isometries in correspondence of a particular site called *center*. In this way we can exploit the properties of isometries to reduce the majority of contractions in the state to identities, only having to compute the contraction in correspondence to the center site.

2.2.3 Matrix product operators

It is useful to extend the concept of MPS to operators acting on them. This allows us to write the Hamiltonian of the system and the observables in a form that is suited for

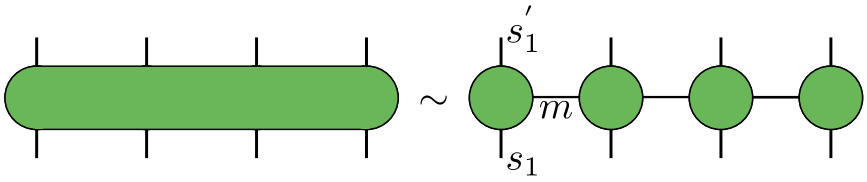

FIGURE 2.7: An operator in Tensor Networks notation and its decomposition in an MPO. The bond dimension is called m and is usually of order ~ 10.

the optimization process, and for which we can use the same efficient contractions as for the state.

For a generic operator acting on the space of MPS we can expand it in terms of the same basis of the state:

$$O = \sum_{\{s\},\{s'\}} O^{s_1',\ldots,s_L'}_{s_1,\ldots,s_L} |s_1,\ldots,s_L\rangle\langle s_1',\ldots,s_L'|. \tag{2.16}$$

At this point we can proceed as we did for MPS and perform an SVD on each bond to obtain a local decomposition of the coefficient of the operators in terms of rank-4 tensors:

$$O = \sum_{\{s\},\{s'\}} M_1^{s_1,s_1'} M_2^{s_2,s_2'} \ldots M_L^{s_L,s_L'} |s_1,\ldots,s_L\rangle\langle s_1',\ldots,s_L'|. \tag{2.17}$$

Coherently with the denomination for states, this for decomposition is called *Matrix Product Operator* (MPO). The graphical representation of this decomposition is shown in Fig. 2.7. Each tensor M has two sites indices corresponding to the physical degrees of freedom and two bond indices with associated bond dimension m. For local Hamiltonians this decomposition is usually exact with bond dimension $m \sim 10$. For example in the case of the Heisenberg model the bond dimension is $m = 4$ as the Hamiltonian is a sum of four terms, each one acting on two sites.

The decomposition of an operator in an MPO is crucial to the performance of several algorithms like DMRG that rely on projecting global operations (like the computation of eigenvalues of the Hamiltonian) over local degrees of freedom. However, performing the SVD for such large matrices can prove to be a bottleneck in the calculations. For this reason, it is often useful to obtain the MPO decomposition by using *finite-state machines* [199, 200].

2.2.4 Density Matrix Renormalization Group

We now have all the necessary ingredients to introduce the Density Matrix Renormalization Group (DMRG) [56, 57]. As with all the variational methods we need three basic building blocks: (i) an ansatz to be optimized, represented in our case as an MPS; (ii) an objective function to be minimized, the expectation value of the Hamiltonian, written as an MPO; (iii) and an optimization algorithm, the DMRG.

Compared to other methods that could be used to optimize the parameters of an MPS, like gradient descent or its generalizations, the DMRG has the crucial advantage of always choosing the optimal update of the parameters at each step, as it is based on the exact diagonalization of the Hamiltonian in a projected subspace. The basic idea of DMRG is to map the global optimization problem of minimizing the energy over the full Hilbert space, to a local one, by projecting the Hamiltonian in a subspace of the Hilbert space spanned by a base defined on a few physical sites. In its modern formulation the DMRG sequentially optimizes the parameters of a small

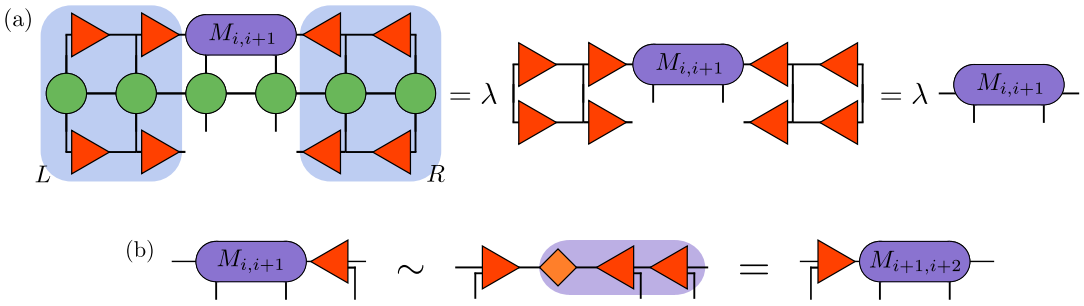

FIGURE 2.8: The DMRG algorithm. (a) Starting from a trial MPS $|\Psi_0\rangle$ and the Hamiltonian H_{MPO}, we optimize the tensor $M_{i,i+1}$ by solving the generalized eigenvalue problem (2.19). (b) We then substitute the optimized tensor in the MPS and split it using an SVD to obtain the new tensors A_i and A_{i+1}. (c) We then move the center to the next bond and repeat the process until convergence.

subset of Tensors of an MPS while keeping the rest of the state fixed. The optimization process then sweeps along the tensors of the chain until a convergence to a fixed point in the value of the energy is reached. The most common schemes involve the optimization of one (1DMRG) or 2 (2DMRG) tensors at the same time. While the 1DMRG is computationally lighter, the two-site version allows for a dynamical increasing of the bond dimension χ during the optimization process, by performing an SVD after every optimization. We will focus on the latter version to describe in depth the algorithm.

To initialize the optimization process we start with a trial MPS $|\Psi_0\rangle$ of the form (2.13) and the Hamiltonian of the system H_{MPO} expressed as in (2.17). The entries of the tensors A in $|\Psi_0\rangle$ can be chosen randomly or following some criteria: the choice of the starting MPS is fundamental to the performance and the convergence properties of the algorithm. In general, we should choose a state as close as possible to the target one, for example by considering the symmetries of the ground state we expect to find.

In the 2DMRG we aim to optimize two tensors at the same time, we then focus on a four-legs tensor $M_{i,i+1} = A_i^{s_i} A_{i+1}^{s_{i+1}}$ obtained by contracting two single-site matrices. To minimize the expectation value of H_{MPO} over the entries of $M_{i,i+1}$ we can take the gradient over their complex conjugate $M^\dagger_{i,i+1}$ and set it to zero:

$$\frac{\partial}{\partial M^\dagger_{i,i+1}} \left[\langle\Psi|H_{MPO}|\Psi\rangle - \lambda\left(\langle\Psi|\Psi\rangle - 1\right)\right] = 0, \tag{2.18}$$

where we added λ as a Lagrange multiplier that enforces the normalization of the state. By expanding the gradient we obtain the generalized eigenvalue equation:

$$H^{i,i+1}_{MPO} M_{i,i+1} = \lambda G^{i,i+1} M_{i,i+1}. \tag{2.19}$$

Here $H^{i,i+1}_{MPO}$ is the projection of H_{MPO} in the basis of sites i and $i+1$, obtained by contracting the MPO with $|\Psi_0\rangle$ and $\langle\Psi_o|$ *excluding* the sites s_i, s_{i+1}. This results in an eight-rank tensor with dimensions $d^4 \times \chi^4$. Operationally however, $H^{i,i+1}_{MPO}$ never has to be explicitly calculated, as we can directly compute the smaller tensor $H^{i,i+1}_{MPO} M_{i,i+1}$ of dimension $d^2 \times \chi^2$ instead. The tensor $G^{i,i+1}$, similarly, is the contraction of the whole MPS with its complex conjugate except the tensors on sites $i, i+1$. The stability of the solutions of Eq. (2.19) generally depends on the matrix G, however the possibility of casting $|\Psi\rangle$ in a canonical form means that we can choose the center to

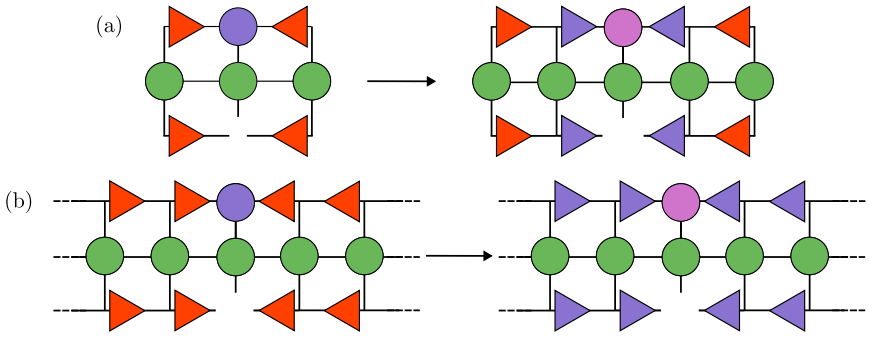

FIGURE 2.9: Sketch of the main difference between the iDMRG and the VUMPS algorithms. (a) Starting from a trial unit cell $|\Psi_0\rangle$ and the Hamiltonian H_{MPO}, we optimize the tensor $M_{i,i+1}$ by solving the generalized eigenvalue problem (2.19). (b) We then substitute the optimized tensor in the unit cell and optimize it again. (c) We continue in this way until convergence.

be on site s_i, and as a consequence we can always choose $G^{i,i+1}$ to be the identity. In this way, on top of avoiding the need for computing G, we reduce the optimization of the tensor $M_{i,i+1}$ to the solution of a standard eigenvalue problem of dimension $d^2 \times \chi^2$, that can be solved efficiently using the Lanczos method we explained in the previous section.

The optimization of the full state proceeds then as follows: we start by optimizing the tensors $M_{1,2}$, putting the gauge center on site s_1 and solving (2.19). We then substitute the solution $\tilde{M}_{1,2}$ in the MPS by creating the new tensors $\tilde{A}_1, \tilde{A}_2$ splitting $\tilde{M}_{1,2}$ using an SVD. The power of the 2DMRG relies on this step, as we can dynamically choose the new bond dimension between the two tensors after the SVD, for example by a targeting a fixed truncation error. We then repeat this process by moving the center to s_2 and creating the new tensor $M_{2,3} = \tilde{A}_2 A_3$ to be optimized. We continue in this way sweeping back and forth along the chain until a desired precision in the energy of the state is reached. At any step of the process, the (contracted) tensors of the MPS and MPO on the two sides of the tensor to be optimized are respectfully called the *left and right environments* of the tensor $M_{i,i+1}$ and intuitively represent a "bath" over which the remaining tensors are optimized. These environments do not have to be fully recomputed at each step, as they can be updated by contracting them with the resulting tensors of the previous optimization. The fundamental steps of the DMRG algorithm are summarized in Fig. 2.8.

2.2.5 Infinite systems

The DMRG, as we described it, is designed to study finite systems with open boundary conditions. Enforcing periodic boundary condition creates some problems as we introduce long range entanglement that increases the required bond dimension to reach a given accuracy to χ^2, with χ being the bond dimension of the open boundary system. On the other hand, the generalization to the case of an infinite chain composed by repeating a small set of tensors, called a *unit cell* is quite straightforward and is called *Infinite DMRG* (iDMRG) [63]. In this section we will briefly describe it then introduce a more modern algorithm called *Variational Uniform Matrix Product States* (VUMPS) [64, 201] that solves some pitfalls in the application of iDMRG that need to be avoided to obtain the results of this thesis.

Infinite Density Matrix Renormalization group

The iDMRG procedure starts by choosing a unit cell of an appropriate size. Usually this should reflect the periodicity of the infinite Hamiltonian (expressed appropriately as an Infinite MPO) or, if we expect the appearance of some order breaking the symmetry under lattice translations, the periodicity of the order parameter. The first step of the optimization is then to perform the usual DMRG on the unit cell using identities as the left and right environments. We then use the optimized tensors to construct the left and right environment of a new enlarged system and optimize the unit cell again. We continue in this way until the energy density of the unit cell converges to a fixed point. As we only optimize a few tensors per sweep (usually 1-2) and the environment is formed by already optimized tensors, the system sizes that can be reached are extremely large (usually of the order of 10^4). The infinite system can then be approximated by the last unit cell optimized, infinitely repeated.

While this technique has been extremely successful in the study of bulk properties of countless one-dimensional systems, it suffers from some problems that can be particularly severe in the study of systems around criticality. The first is that the state keeps memory of the previously optimized unit cells as they are used to construct the environments, meaning that the optimization is skewed towards the ground state of short chains, slowing the convergence to the thermodynamic limit and being prone to get stuck in local minima. The second is that while the resulting state is very large compared to usual finite DMRG, it is not really translationally invariant, and a scaling with the effective dimension of the chain is needed in order to extract a reliable bulk state. In situations where the presence of boundaries cannot be neglected, like the cases we are going to study in Chapter 5, this can result in serious stability and convergence problem to the true ground state.

Variational Uniform Matrix Product States (VUMPS)

For the reasons outlined in the last paragraph, VUMPS was introduced as an algorithm that directly works with states in the thermodynamic limit, replacing the *entire* infinite state at each step of the optimization process. In this way the environment never breaks the translational invariance of the state and the memory of the presence of previous unit cells in the environment is lost. For a unit cell of one tensor A, the building blocks of the algorithm are the tensor in the three possible gauges: left, right, and center, that we will call A_L, A_R, A_C respectively, and the bond center matrix C. These quantities are related by the gauge transformations rule

$$A_C = A_L C = C A_R. \tag{2.20}$$

The VUMPS update procedure consists then in solving the eigenvalue problem both for the matrix C and the tensor A_C:

$$H_{A_C} A_C = E_{A_C} A_C, \qquad H_C C = E_C C. \tag{2.21}$$

The two updated matrices $\tilde{A}_C$ and $\tilde{C}$ can then be plugged in (2.20) to obtain the updated tensors $\tilde{A}_L$ and $\tilde{A}_R$ to update the full environment without breaking the translational invariance of the state. Crucially, the two effective Hamiltonians projected in the basis of the site H_{A_C} and the bond H_C, can be computed efficiently at any step for an infinite environment [64]. The convergence of the algorithm is then checked by ensuring that both the tensors in the left and right change do not change

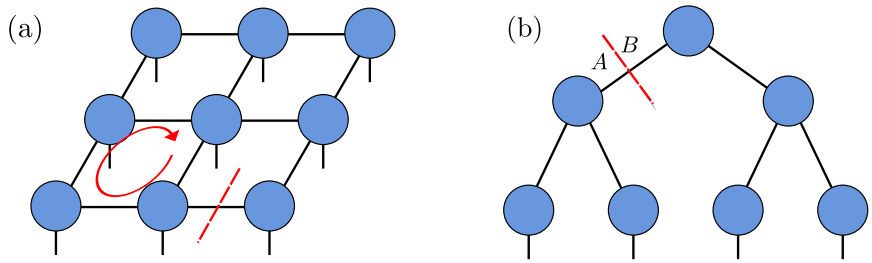

FIGURE 2.10: The network structure of a PEPS. The tensors are placed on the sites of a square lattice and are connected by bonds.

after the optimization step by setting a threshold for the two quantities

$$\epsilon_L = \|\tilde{A}_C - A_L\tilde{C}\|, \qquad \epsilon_R = \|\tilde{A}_C - \tilde{C}A_R\|. \tag{2.22}$$

While VUMPS requires the solution of two eigenvalue problems at each step, compared to one in the case of iDMRG, the full substitution of the state massively speeds up the algorithm, requiring noticeably fewer sweeps to reach convergence.

In the case of a multi-tensor unit cell we can proceed in two different ways: in both cases we sweep through the unit cell optimizing one tensor at time, but we can either replace the environment after each optimization (sequential approach), or after the optimization of the whole unit cell (parallel approach). Both approaches have their advantages and drawbacks. Finally, it is worth mentioning that at no point in the application of VUMPS we perform an SVD: this means that we cannot dynamically increase the bond dimension of the state. This can be done instead by performing a *subspace expansion* [202] when needed, to "artificially" increase χ.

2.2.6 Beyond Matrix product states

MPS, paired with optimization algorithms such as DMRG are powerful tools to study one-dimensional systems. However, as we will see in more detail in Chapters 5 and 6, they are severely limited when applied to systems around criticality, higher dimensionality systems or, equivalently, long range interactions. MPS are indeed constructed to satisfy the area law for ground states of gapped local Hamiltonians in one-dimension and are unable to fully encode the entanglement structure in other circumstances.

For this reason several other architectures have been developed to adapt to different geometries and symmetries. The most direct generalization of MPS to two-dimension are *Projected Entangled Pair States* (PEPS) [68], whose network structure for a square lattice is shown in Fig. 2.10. While by construction they capture the area law in two-dimension they suffer from severe computational problems that have been limiting their range of applications and are still object of active research. In particular, the presence of *loops*, closed between tensors connected by bonds, in a tensor network architecture makes it impossible to perform most the operations that make computations with MPS efficient. First, cutting the state along a bond does no longer produce a bipartition of the system, meaning that it is impossible to use SVD to efficiently compress the state and to create canonical forms that simplify calculations. In turn, this makes it extremely complex to implement an algorithm like DMRG for PEPS. Second, the contraction of the network to compute expectation values or overlaps is no longer efficient, as it is not possible to find an optimal order of

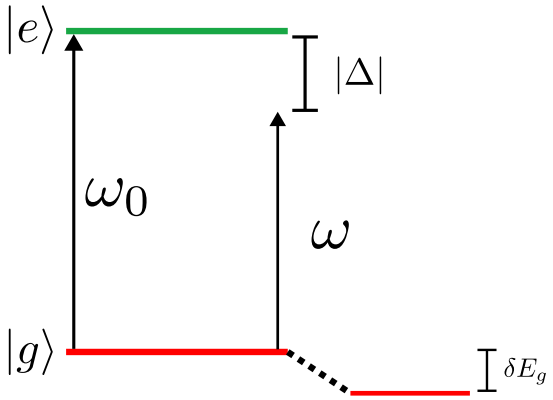

FIGURE 2.11: Schematic of the transitions involved in the laser-atom interaction in a quantum simulator. For a small detuning Δ the transitions to the excited state can be neglected and the net effect is a position-dependent shift of the ground state energy.

contractions that does not depend on the size of the system. This effectively makes it impossible to exactly contract PEPS for systems larger than a few sites.

A possible workaround that has been employed successfully is the use of small unit cells to construct *infinite* PEPS (iPEPS) [203] that can capture bulk properties of various systems. However, the size unit cell is severely restricted (usually not more than 2×2 or 3×3). To solve the problem of contraction instead, several algorithms have been proposed that perform the contraction using controlled approximations [204, 205]

An alternative architecture that does not suffer the problems of loops while capturing longer range entanglement are *Tree Tensor Networks* (TTN) [70]. These are constructed by layering tensors on top of each other like in Fig. 2.10(b) avoiding contractions that would create loops. Each layer then represents a different scale in the entanglement structure of the state, making it possible to capture longer range correlations than MPS. Moreover, the absence of loops makes it possible to perform SVD on bipartitions, creating canonical forms, efficiently contracting the network and eventually writing DMRG-like algorithms adapted to the particular geometry of the system in exam. This is particularly useful when studying one-dimensional systems with long range interactions or periodic boundary conditions. The main drawback of TTN is that they are not able to capture the area law, meaning that the encoding of entanglement is not optimal, limiting their applicability. Nevertheless, there have been several successful applications for example in the study of FQHE [206], and even small systems in three dimensions [207].

Finally, we briefly mention the class of *Multi-scale Entanglement Renormalization Ansatz* (MERA) [69]. These are generalizations of TTN that add some intermediate tensors called *disentanglers* that are used to capture the entanglement structure necessary for the area law. While these states correctly reproduce the area law for critical systems, the insertion of disentanglers introduces loops in the network making the optimization process severely more complex than for TTN.

2.3 Quantum simulation with ultracold atoms

While classical simulation techniques like the ones we described above have reached impressive results in reproducing ground state physics, they are severely limited in

the reachable size of quantum systems, and in the study of their dynamical properties. For instance, as we saw in the previous section, the efficacy of Tensor Networks is severely limited in two dimensions, even for ground state problems, and almost completely impractical to use in three dimensions.

For these reasons in the last decades, experimental apparatuses called quantum simulators were developed in order to reproduce directly in a quantum platform the properties of system hardly approachable classically. While simulators are not universal as they only reproduce a particular model, they can be used to mimic the properties of complex quantum system in a controlled environment that allows a better tunability of the parameters and ease of measurements [187].

In this section we will describe the basis of quantum simulation using ultracold atoms. As a feasible platform where to realize strongly-correlated phenomena like FQHE and frustrated magnetism, it will be relevant for the result of this thesis.

2.3.1 Ultracold atoms in optical lattices

The starting point is the cooling and trapping of atoms in order to be able to control them. This is usually done through laser [25] and evaporative cooling [29], and the use of a magneto-optic trap that confines the atoms in a harmonic potential[28]. The next step is the creation of an *optical lattice* [185, 186] for the trapped atoms that can mimic the periodic potential typical of solids. In this way, it is possible to engineer for neutral atoms potentials reproducing the ones that nuclei exert on electrons in materials. In experiments, we usually consider alkali atoms, for which only one electron occupies a partially filled band. The Hamiltonian for the atom can then be written (setting $\hbar = 1$) as

$$H_0 = \omega_i \sum_i |e_i\rangle\langle e_i|, \tag{2.23}$$

where $|e_i\rangle$ are the internal states of the valence electron and ω_i are the corresponding energies, setting the energy of the ground state $|e_0\rangle = |g\rangle$ to zero for simplicity. We are neglecting the kinetic energy of the atoms as we are interested in how the effect of the interaction of the atom with an external electric field shifts its internal levels.

The coupling of the atom with an electric field can be modeled as a dipole interaction, assuming that the wavelength of the field is much larger than the size of the wavefunction of the atom. In this case the interaction can be written as

$$H_I = -\mathbf{d} \cdot \mathbf{E}(\mathbf{r}, t). \tag{2.24}$$

Here $\mathbf{d} = e\mathbf{r}$ denotes the vector dipole moment operator associated to the valence electron, while $\mathbf{E}(\mathbf{r}, t) = \mathbf{E}(\mathbf{r})e^{i\omega t}$ is a classical electric field generated by a monochromatic laser. As it is widely known, the expectation value of the dipole operator on the ground state is zero $\langle g|\mathbf{d}|g\rangle = 0$, so that we will consider the coupling to the excited states to study the effects of the atom-radiation interaction. By only considering the first excited state $|e_1\rangle = |e\rangle$ we can write the complete Hamiltonian in the interaction picture as

$$H_I = \left(|e\rangle\langle g|e^{i\omega_0 t} + |g\rangle\langle e|e^{-i\omega_0 t}\right)\left(\frac{\Omega}{2}(\mathbf{r})e^{i\omega t} + \frac{\Omega^*}{2}(\mathbf{r})e^{-i\omega t}\right), \tag{2.25}$$

where we defined the *Rabi frequency* $\Omega(\mathbf{r}) = -2\langle e|\mathbf{d} \cdot \mathbf{E}(\mathbf{r})|g\rangle$ as the frequency of oscillations between the two internal states. Assuming a small *detuning* between the atomic and laser frequency $|\Delta| = \omega - \omega_0 \ll \omega_0$, we can neglect the fast oscillating terms containing $\pm i(\omega_0 + \omega)t$ (the *Rotating Wave Approximation*) and obtain the

effective Hamiltonian

$$H_I \sim \frac{\Omega(\mathbf{r})}{2}|g\rangle\langle e|e^{i\Delta t} + \frac{\Omega^*(\mathbf{r})}{2}|e\rangle\langle g|e^{-i\Delta t}. \tag{2.26}$$

Now we can perturbatively calculate the effects of this light-matter coupling on the energy of the ground state of the atom. For $\Omega << \Delta$ the transitions to the excited state can be neglected, and we can employ a second order perturbation theory to obtain the energy shift of the ground state, the so called ac-Stark shift:

$$\delta E_g = \frac{|\langle g|H_I|E\rangle|^2}{4\Delta} = \frac{|\Omega(\mathbf{r})|^2}{4\Delta}. \tag{2.27}$$

As the Rabi frequency is proportional to the spatial profile of the electric field, this creates an effective position-dependent potential for the atoms to move in. If the laser is red-shifted ($\Delta > 0$) the atoms are attracted to the minima of the laser, while for a blue-shifted laser ($\Delta < 0$) to the maxima.

We will now focus on the simple case of one-dimensional systems. If we consider a standing wave field obtained by two monochromatic counter-propagating laser beams with the same frequency and polarization

$$E(x) = E_0 \sin(\frac{2\pi}{\lambda}x), \tag{2.28}$$

the atoms are subject to a periodic potential of the form

$$V(x) = V_0 \sin^2(\frac{2\pi}{\lambda}x), \tag{2.29}$$

where $V_0 = |E_0\langle e|d|g\rangle|^2/\Delta$ is usually expressed in terms of the recoil energy $E_r = k^2/2m$. The atoms are then confined in a periodic potential with period $d = \lambda/2$. The eigenfunctions of the atomic Hamiltonians in this potential are delocalized Bloch waves of the form

$$\psi_{nk}(x) = e^{ikx}u_{nk}(x), \tag{2.30}$$

where $u_{nk}(x)$ is a periodic function with the same periodicity of the potential $V(x)$: $u_{nk}(x+d) = u_{nk}(x)$. The momentum k is defined in the first Brillouin zone, while n represent instead the band index, as it is standard in the study of the spectra of periodic potential.

2.3.2 Tight-Binding approximation

In the case of deep lattices, when $V_0 \sim 5E_r \gg E_r$, the lowest band in the spectrum becomes almost flat, and we can assume the atoms to be localized around the minima of the potential, in analogy to atomic potentials in the case of electrons. If the system is cooled at a temperature lower than the gap between the first and the second band, we can assume that all the atoms occupy the lowest band. In this case an orthogonal basis more suited to describe the system is given by Wannier functions

$$w_{n=0}(x - X_i) = \frac{1}{\sqrt{L}}\sum_k e^{-ikX_i}\psi_{n=0,k}(x), \tag{2.31}$$

where L is the size of the system, X_i are the positions of the potential minima, and we set $n = 0$ to restrict to the lowest band. This basis is the starting point to describe the physics of the system in the *tight-binding* approximation, that is the situation where

the atoms are assumed to be localized in the minima of the potential and to move only by hopping between neighboring sites.

If the generic Hamiltonian of free atoms (supposed to be bosons for simplicity) of mass m in a periodic potential $V(x)$ and a generic trapping potential $V_{ext}(x)$ is written as

$$H = \int dx \Psi^\dagger(x) \left(\frac{p^2}{2m} + V(x) + V_{ext}(x) \right) \Psi(x), \tag{2.32}$$

we can express the bosonic destruction operator in terms of operators defined on the sites of the lattice via de Wannier basis as

$$\Psi(x) = \sum_i w_0(x - X_i) b_i. \tag{2.33}$$

The kinetic energy can then be rewritten as

$$H_K = -\sum_{i,j} t_{ij} b_i^\dagger b_j, \qquad t_{ij} = \int dx w_0^*(x - X_i) \left(-\frac{\partial_x^2}{2m} \right) w_0(x - X_j). \tag{2.34}$$

If the lattice is deep enough the overlap between Wannier functions centered in sites further than nearest neighbor is negligible, and we can approximate $t_{ij} = 0$ for $j \neq i \pm 1$. The potential $V_{ext}(x)$ represents instead other external potentials to be applied to the system on top of the lattice, like a harmonic trap or a magnetic field to prevent the atoms to escape the system. This can be rewritten as a local chemical potential

$$H_{ext} = \sum_i \mu_i b_i^\dagger b_i, \qquad \mu_i = \int dx |w_0^*(x - X_i)|^2 V_{ext}(x). \tag{2.35}$$

2.3.3 Adding interactions

Having described the single particle physics of atoms in an optical lattice, we now turn to the study of how to tune and engineer interactions between them. The generic atom-atom interaction can be written as

$$H_{int} = \frac{1}{2} \int dx dx' \Psi^\dagger(x) \Psi^\dagger(x') V_{int}(x - x') \Psi(x') \Psi(x), \tag{2.36}$$

where $V_{int}(x - x')$ can in general be a complicated function. For neutral atoms usually the typical two-body interaction is given by the van der Waals potential. However, for atoms in the so-called *ultracold limit* as the ones we are considering the only relevant interaction happens in the s-wave channel and, neglecting the corrections in [208], the interaction potential can be approximated by a contact potential

$$V_{int}(x - x') = \frac{2\pi a_s}{m} \delta(x - x'). \tag{2.37}$$

Here the quantity a_s is called *scattering length* and, in the case of alkali atoms, can be tuned by means of a Feshbach resonance. In this case, and by using the expression of Eq. (2.33), the interaction Hamiltonian can be written as

$$H_{int} = \frac{U}{2} \sum_i b_i^\dagger b_i^\dagger b_i b_i = \frac{U}{2} \sum_i n_i(n_i - 1), \qquad U = \frac{4\pi a}{m} \int dx |w_0(x)|^4, \tag{2.38}$$

with $n_i = b_i^\dagger b_i$ the number operator on site i.

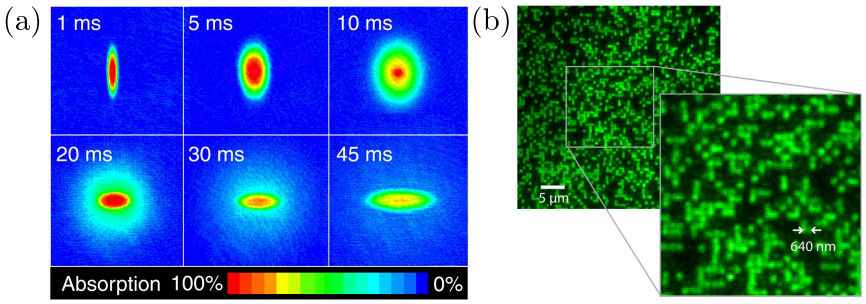

FIGURE 2.12: Measurement techniques. (a) Time-of-flight expansion snapshots of a suddenly released BEC cloud. By measuring the ballistic expansion after the release from the trap it is possible to reconstruct the momentum distribution of the initial state. Image adapted from [209]. (b) Quantum gas microscopy allows for imaging of optical lattices at the single atom level, allowing to explicitly measure local quantities like density and spin patterns. Image adapted from [41].

By adding all the terms we obtain for the effective physics of the lowest band of atoms in the optical lattice the *Bose-Hubbard* Hamiltonian

$$H_{BH} = -\sum_{i,j} t_{ij} b_i^\dagger b_j + \frac{U}{2}\sum_i n_i(n_i - 1) + \sum_i \mu_i n_i. \tag{2.39}$$

The parameters of the Hamiltonian only depend on two readily tunable parameters: the lattice depth V_0 and the scattering length a. Moreover, by using different standing wave pattern different geometries of the lattice with different periodicities can be engineered. This allows to study a wide range of models, with results on the phase diagram of this model starting from the Mott insulator-superfluid transition [34]. More details on the phases of this model will be given in Chapter 5. While we performed the derivation of the model in the case of bosons, also fermionic atoms can be studied in the same way: in this case the s-wave scattering between two equal fermions is suppressed by the Pauli principle, and the relevant interaction is the one between two fermions of opposite spin. This can be modeled by adding a spin degree of freedom, obtaining the Hamiltonian

$$H_{FH} = -\sum_{i,j,\sigma} t_{ij} c_{i\sigma}^\dagger c_{j\sigma} + \frac{U}{2}\sum_i n_{i\uparrow} n_{i\downarrow} + \sum_i \mu_i \sum_\sigma n_{i\sigma}, \tag{2.40}$$

called the *Fermi-Hubbard* model. This Hamiltonian represents a key minimal model for the study of interacting electrons in solids, and it will be described in more details in Chapters 5 and 6. Notably, its classical simulation is severely limited by the sign problem when using Monte Carlo approaches and the large local Hilbert space dimension (4 states per site) when using Tensor Networks, making it a prime candidate for quantum simulation.

2.3.4 Measurement techniques

The power of cold atoms simulators resides not only in the possibility of tuning the parameters of the many-body Hamiltonian with precision, but also on a wide array of detection techniques that makes it possible to measure the properties of the system with high precision. One of the most important is the *time-of-flight method* [210]: in this technique the atoms get suddenly released from the optical lattice (and any eventual confining potential), and are let to expand in a ballistic way for some

time t. At this point the atomic cloud can be photographed using standard imaging techniques: as the distance traveled by the particles depends on their momentum, this is an efficient way to measure the momentum distribution of the atoms. This can be used for example to detect superfluidity in the system [34], but also to map the topological properties of a system, like the Berry phase of a band structure [211, 212]. An example of the time-of-flight evolution of a Bose-Einstein condensate is shown in Fig. 2.12(a).

Another, more recent technique is the *quantum gas microscopy* [32, 41] that allows to directly image the configurations of atoms in the lattice, with a resolution up to the single atom. This led for example, to the direct, real space identification of the Mott insulator-superfluid transition in the Bose-Hubbard model [42], and the detection of antiferromagnetic correlations in the Fermi-Hubbard one [45]. This technique is also particularly suited to probe properties encoded in non-local correlators, like the ones we are going to study in Chapter 5. For example, quantum gas microscopy was employed to study chiral currents[49], and string order correlators [213]. A snapshot of a bosonic configuration in an optical lattice captured with quantum gas microscopy is shown in Fig. 2.12(b).

Part II

Novel techniques for detection of topology

Chapter 3

Tracing of anyons in FQHE via impurity particles

As we introduced in Chapter 1, one of the most striking characteristics of topological order is the presence of excitations that exhibit fractional charge and fractional statistics, with a behavior dramatically different from the one of the elementary constituents of the system. A paradigmatic example of this phenomenon are the quasi-holes and quasi-particles in Fractional Quantum Hall (FQHE) liquids: the liquid is made of interacting electrons, but its excitations appear as fractional electrons. By having fractional charge and fractional statistics they are neither bosons nor fermions, but anyons. [152, 163, 164, 166]. Even if the concept of anyons has been known for several decades [163, 164], the search for this quasi-particles has seen an unprecedented rise in the last year due to the possibility of using the intrinsic topological protection of anyons to perform *topological quantum computation* [97, 98]. In FQHE, this behavior is perfectly captured theoretically by various ansatz wavefunctions like the ones discussed in Section 1.2.1. However, it may be hard to determine whether such phenomenology is indeed realized in a real-world FQHE system.

In the case of *Abelian* quasi-holes, for examples the ones present in the $\nu = 1/3$ Laughlin state presented in 1.2.1, the nature of the FQHE phase is well established through theoretical considerations but also experimentally, by directly measuring the fractional charge, most notably via shot noise measurements [214]. The measurement of the fractional statistics, however, is much more challenging as it would have to be performed through the braiding of the quasi-holes. This is extremely nontrivial as the quasi-holes have to be exchanged adiabatically without introducing excitations in the system. The most successful attempts up to this moment have been focusing on beamsplitter experiments [215] and Fabry-Perot interferometry [216–219].

The task of detecting and engineering *non-abelian* states, is even more complex. As we saw in Section 1.2.1, the most promising candidate to describe the half-filled $\nu = 5/2$ FQHE phase, the most relevant for quantum computation [99], is the Moore-Read or Pfaffian wavefunction [155, 220, 221]. This was indeed heavily suggested by several experimental signatures, including spin polarization [222], $e/4$ quasi-particle charge [158, 223], or half-integer thermal conductance [224]. Nevertheless, other experiments suggest an Abelian phase [225]. Interferometric measurements to determine the non-Abelian nature of the quasi-particles have not been conclusive, as they are also compatible with the presence of Abelian quasi-holes [217].

From this perspective, great work has been put in the implementation of FQHE physics in highly controllable quantum systems, boosting the search for this kind of states in quantum simulators, for example in cold atoms [226, 227] or photonic

systems [105]. Advances towards the simulation of FQHE physics include the generation of artificial magnetic fields and detection of topological properties, such as chiral edge states [228, 229], topological quantum numbers [48, 230–233], topological transport [234, 235]. In the last five years, even the creation of a Laughlin-like state of two photons [105] and two atoms [104, 236] have been achieved. In the context of non-Abelian states, one feature of quantum simulators seems particularly promising: They can operate also with bosonic species, for which often a simple two-body contact potential appears to be sufficient to produce non-Abelian ground states [237–239]. Recently, a non-Abelian state has been observed in a trapped ions quantum simulator [107].

In addition to the engineering, synthetic quantum Hall systems in quantum simulators also provide new detection opportunities: light-matter interactions can be used to create, trap, and braid quasi-particles [240–244]. The total angular momentum of a FQHE system, which for atoms can be measured by time-of-flight imaging, carries signatures of fractional statistics [245]. Spectroscopic signatures have been described for atomic systems [246], graphene [247], or magnetic materials [248]. Several works have suggested to bind impurities to fractional quasi-particles [249–254], which can then be used to trace or manipulate the anyons.

In this chapter, following the results in [I] and [II], we take up the idea of binding impurities to quasi-holes in a FQHE liquid to obtain their statistics. First, we consider a single impurity and show that its angular momentum is fractional (in units $\hbar \equiv 1$). Then, by adding more impurities, taken as non-interacting fermions, we observe how their behavior changes. Specifically, we show that the total angular momentum of the impurities matches neither the value from a fermionic construction, nor the value of bosonic condensate. Instead, the total angular momentum is reproduced by a linear interpolation between fermionic and bosonic distribution, proportional to $\alpha = 1 - \phi$. Here, ϕ depends on the filling factor of the FQHE liquid and the fractional charge of the quasi-hole, and α equals the anyons' statistical parameter. These results are valid for both Abelian and non-Abelian anyons states. In this latter case, the non-Abelian nature of the anyons is reflected on a dependence of the impurity angular momentum on the even or odd number of particles in the system.

The results are obtained numerically either by performing exact diagonalization of the underlying quantum Hall Hamiltonian, or by Monte Carlo sampling of the ansatz wavefunction. They can also be understood from a mean field theoretical construction, by relying on the parallel between fractional statistics and flux-matter attachment [152, 164]. While this reasoning has already been employed to explain the fractional relative angular momentum between two anyons [249], we demonstrate that the properties of the anyon vacuum and fractional angular momentum can even be probed with a single excitation. Moreover, the fractionalization of angular momentum can directly be inferred from the density of impurities bound to quasi-holes, making it easily accessible in experiment. This gives a new avenue to measure fractional statistics without having to rely on the difficult task of braiding quasi-holes.

The chapter is structured in this way: after having reviewed the concept of Haldane pseudopotentials and parent Hamiltonians in Section 3.1, we will describe the system with impurities in Section 3.2. In Section 3.3 we will then discuss the statistics of one or multiple impurities in a Laughlin liquid, and the results of the numerical simulations. Finally, in Section 1.2.3 we will do the same for Moore-Read liquids.

3.1 FQHE from parent Hamiltonians

In this section we will introduce some technical details required for the understanding the rest of the Chapter. As we mentioned in Section 1.2.1, a way to effectively retrieve the Laughlin state is to construct parent Hamiltonians using the *Haldane pseudopotentials* [157]. Here, following [127], we will be more specific about this construction. We will use units in which $\hbar = 1$.

We consider a system of N particles (either bosons or fermions) on a plane, interacting with each other through a generic central potential V, and subject to a perpendicular magnetic field B. In this case the states in the Lowest Landau Level can be labeled by their angular momentum m and written as

$$\varphi_m(z) = \frac{1}{\sqrt{2\pi m!}} z^m e^{-|z|^2/4l_B^2}, \tag{3.1}$$

sometimes called *Fock-Darwin* [255] states. Here l_B is the magnetic length $l_B = \sqrt{1/eB}$. If we now consider only two of these particles, we can write their joint state as

$$\psi_{Mm}(z_1, z_2) = (z_1 + z_2)^M (z_1 - z_2) e^{-(|z_1|^2+|z_2|^2)/4l_B^2}, \tag{3.2}$$

where M is the center of mass angular momentum and m is the relative angular momentum. These wavefunctions are peaked at a distance $r\sqrt{2m}l_B$ from the origin. Notably, if we avoid mixing with higher Landau Levels, these are the eigenstates of the interaction V for *any* choice of the potential, with eigenvalues

$$v_m = \frac{\langle \psi_{Mm}|V|\psi_{Mm}\rangle}{\langle \psi_{Mm}|\psi_{Mm}\rangle} \tag{3.3}$$

independent on M. The v_m are the celebrated Haldane pseudopotentials (for two particles).

For any central potential we can then write the interaction Hamiltonian on the Lowest Landau Level as

$$H_{\text{int}} = \frac{1}{2} \sum_{m,m'} v_{m'} P_{m'}, \tag{3.4}$$

with $P_{m'}$ the projector onto the subspace of states with relative angular momentum m'. As the v_ms usually decrease for larger angular momenta, the repulsive interaction then translates in the requirement that the two particles have to maximize their relative angular momentum. The reasoning can be extended for the full system of N particles, resulting in a Hamiltonian

$$H_{\text{int}} = \sum_{m'} \sum_{i,j} v_{m'} P_{m',ij} \tag{3.5}$$

where now there is a different projector P for any possible pair of particles i, j. If we cut the sum over the angular momenta at a value q, such that $m' = 0, \forall m' \geq q$, the degenerate wavefunctions minimizing the energy are of the form

$$\Psi_q(z_1, \ldots, z_N) = s(z_i) \prod_{i<j} (z_i - z_j)^q e^{-\sum_i |z_i|^2/4l_B^2}, \tag{3.6}$$

where $s(z_i)$ is a generic symmetric polynomial. However, the case $s(z_i) = 1$, corresponding to the Laughlin wavefunction [152], is the *most compact* one, with an

average radius of $r \sim \sqrt{2qN} l_B$[1]. As the polynomial $s(z_i)$ increases the total angular momentum, all the other states are more extended in space.

This is particularly relevant if we add a harmonic trapping potential as customary in experiments. In terms of the angular momentum operator L this potential is

$$V_{trap} = \omega L, \tag{3.7}$$

with ω the trapping frequency. In this case the degeneracy is broken and the compact Laughlin state is the non-degenerate ground state of the system with energy $E_0 = \frac{1}{2}\omega q N(N-1)$. We can then conclude that Eq. (3.4), with a sum running for $m' < q$, is the parent Hamiltonian for the Laughlin state at filling $\nu = 1/q$ in presence of a harmonic trap.

3.1.1 Edge states and quasi-holes

What is the role of the $s(z_i)$ term? If we expand the polynomial in terms of a basis of symmetric polynomials, we can write

$$s(z_i) = \sum_n = s_n(z_i)^{d_n}, \quad s_n(z_i) = \sum_i z_i^n. \tag{3.8}$$

Here d_n is an exponent to obtain a polynomial of rank $n + d_n$ starting from a basis element s_n. As each polynomial s_n adds an angular momentum n, the energy increases as

$$E_s = E_0 + \sum_n d_n E_n, \qquad E_n = \omega n. \tag{3.9}$$

This can be seen as the linear dispersion of the edge states of the system. In absence of the confining potential they are degenerate with the Laughlin state, but they become gapped because of the harmonic trap.

To each level in the spectrum (3.9) we can associate a degeneracy. We already know that for $n = 0$, $s(z_i) = 1$ and there is no degeneracy. The first excited state has $E = E_0 + \omega$. To obtain it we need to set $d_1 = 1$ and $d_n = 0$ for $n > 1$. This corresponds to $s(z_i) = \sum_i z_i$, and the level has degeneracy 1. The state with $E = E_0 + 2\omega$ can be obtained by putting either $d_2 = 1$ or $d_1 = 2$, corresponding respectively to $s(z_i) = \sum_i z_i^2$ and $s(z_i) = (\sum_i z_i)^2$. It has then degeneracy 2. Turns out that the degeneracy of a state with energy $E = E_0 + d\omega$ is equal to $\mathcal{N}_d$, the number of ways to *partition* the integer d in a sum of integers. This is shown for some values of d in Table 3.1.

However, if we add an angular momentum N equal to the number of particles, there is another way to construct a corresponding state. If we put $d_N = 1$ and the rest to zero, corresponding to an energy $E = E_0 + N\omega$, we can write

$$s(z_i) = \prod_i (z_i - \zeta). \tag{3.10}$$

This corresponds to adding a quasi-hole at position ζ. In absence of the harmonic potential, all these states are degenerate ground state of the Haldane pseudopotential Hamiltonian (3.4), together with the Laughlin state, only differing in their angular momentum. For this reason we will call the *zero interaction energy* states.

[1] This can be confirmed by noting that each term in the polynomial adds an angular momentum m and $N-1$ such terms are present for each particle.

d	0	1	2	3	4	5	6
$\mathcal{N}_d$	1	1	2	3	5	7	11
$\mathcal{N}_{d,\text{imp}}$	1	2	4	7	12	19	30

TABLE 3.1: Number $\mathcal{N}_d$ of edge modes in the Laughlin liquid of degree d, and number $\mathcal{N}_{d,\text{imp}}$ of zero-energy modes of degree d in the presence of an impurity.

3.2 Impurities in a FQHE bath

To set the physical framework of this chapter, we now extend this construction to the case of two different species of particles a and b: Majority particles a form a FQHE liquid with filling fraction $\nu = 1/q$, in which *impurity* particles b are immersed. For simplicity, we assume similar single-particle physics for both species: They have equal mass M, are trapped in the xy-plane by harmonic potentials of frequencies ω_a and ω_b, and are brought into the lowest Landau level by a sufficiently strong potential $\mathbf{A} = \frac{B}{2}(-y, x, 0)$ written in Landau gauge. In this gauge, as we saw in the previous section, the single-particle wavefunctions can be written in terms of their angular momentum m using Fock-Darwin wavefunctions. The corresponding single-particle energies are

$$E_{m,s} = m\Omega_s, s \in \{a, b\}, \qquad \Omega_s \equiv \sqrt{\omega_B^2 + \omega_s^2} - \omega_B. \tag{3.11}$$

Here, $\omega_B = eB/M$ is the *cyclotron frequency*, with e the electric charge of the particles (or synthetic charge in the case of a quantum simulator). The coordinates $z = (x + iy)/l_B$ are given in units of the oscillator length $l_B = \sqrt{1/M\Omega_s}$, which depends on the trapping frequency. We assume $\omega_a \approx \omega_b \ll \omega_B$, such that $\Omega_a \approx \Omega_b$, and the length scale l_B takes the same value for both a and b.

The a particles are either bosons or fermions. To make them form a FQHE liquid, we consider repulsive interactions expressed by Haldane pseudopotentials. We truncate the pseudopotential expansion at $m' = q$, obtaining a parent Hamiltonian for the Laughlin state Ψ_q, $s(z_i) = 1$ in Eq. (3.6). The total angular momentum of the Laughlin ground state is then

$$L_q = \frac{q}{2} N_a (N_a - 1), \tag{3.12}$$

with N_a the number of a particles, and if $L_a = L_q$ it is non-degenerate. By checking the parent Hamiltonian, no zero-interaction energy states are allowed for $L_a < L_q$. Following the previous section, if we increase the angular momentum of the system $L_a = L_q + d$ with $d > 0$, the liquid can accommodate $\mathcal{N}_d$ edge modes, or a bulk quasi-hole if $L_a = L_q + N_a$.

The b species are taken as non-interacting fermions. To bind to quasi-holes of the Laughlin liquid, we consider a sufficiently strong repulsive contact interaction between a and b particles. This interaction allows for exchange of angular momentum between the species, but the joint angular momentum L remains a conserved quantity. For the case of a single impurity, we can write its lowest-energy wavefunction as

$$\Psi_{q,\text{imp}} \sim \prod_i (w - z_i)\Psi_q \tag{3.13}$$

where the quasi-hole position w was "upgraded" to represent a dynamical variable representing the position of the impurity. This state is non-degenerate at $L = L_q +$

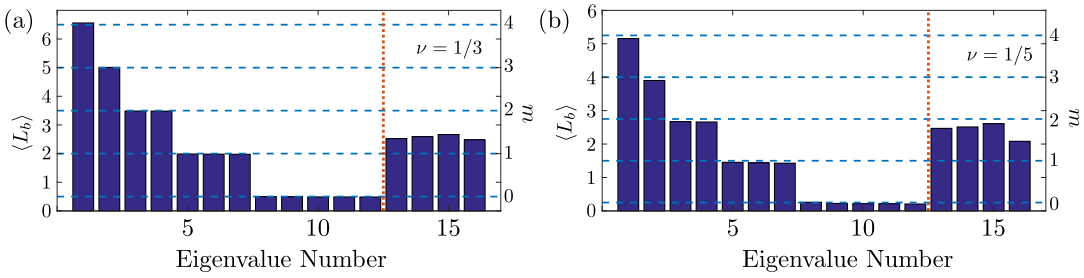

FIGURE 3.1: We plot the angular momentum $\langle L_b \rangle$ of an impurity in a Laughlin liquid at (a) $\nu = 1/3$ ($N_a = 8$ particles at $L = L_3 + N_a + 4 = 96$), and at (b) $\nu = 1/5$ ($N_a = 6$ particles at $L = L_5 + N_a + 4 = 85$). The twelve lowest states (on the left to the red-dotted line) are states of zero interaction energy. On average, the impurity takes fractionally quantized values $\langle L_b \rangle = \frac{m+\nu}{1-\nu}$ (indicated through the blue-dashed lines).

N_a, and no zero-interaction states exist at $L < L_q + N_a$. However, it is still possible to create edge states on top of $\psi_{q,\text{imp}}$ with angular momentum $L = L_q + N_a + d$ with $d > 0$, of the form

$$\Psi_{q,m_1,m_2} \sim w^{m_1} s_{m_2}(z_i) \prod_i (w - z_i) \Psi_q, \tag{3.14}$$

where m_1 and m_2 are positive integers with $m_1 + m_2 = d$. Here $s_{m_2}(z_i)$ are all the allowed polynomials of degree m_2. Thus, the number of zero-energy modes at $L = L_q + N_a + d$ is given by $\mathcal{N}_{d,\text{imp}} = \sum_{m_2=0}^{d} \mathcal{N}_{m_2}$. This increases the degeneracy of the zero-interaction modes, as shown in the second row of Table 3.1.

3.3 Statistics of impurities in a Laughlin state

The Laughlin state Ψ_q can be seen as an effective impurity vacuum, and the states $\Psi_{q,\text{imp}}$ and Ψ_{q,m_1,m_2} define the ground state and excited states of a single impurity. These states have total angular momentum $L = L_q + N_a$ and $L = L_q + N_a + m_1 + m_2$, but it is not immediately clear how the angular momentum is distributed between the two species. Let L_b^0 denote the average angular momentum of the impurity in its ground state, i.e.

$$L_b^0 \equiv \langle \Psi_{q,\text{imp}} | L_b | \Psi_{q,\text{imp}} \rangle, \tag{3.15}$$

with L_b the angular momentum operator for the b particle. Naively, one may expect that the angular momentum L_b^m of an impurity in its mth excited state, i.e. in $L_b^m \equiv \langle \Psi_{q,m,d-m} | L_b | \Psi_{q,m,d-m} \rangle$, is given by $L_b^m = L_b^0 + m$. However, as we show below, this is not the case. Instead, the angular momenta of impurity levels differ by multiples of a fractional value, suggesting the interpretation of fractional quantization.

Analytical arguments for this behavior are based on the notion that the impurity at w "sees" the majority particles at z_i as fluxes, reducing the effective magnetic field for the impurity to

$$B^* = B - 2\pi l_B^2 \rho_a B = B(1 - \nu), \tag{3.16}$$

where ρ_a is the density of the majority particles [249]. This leads to an increased magnetic length scale $l_B^* = l_B / \sqrt{1-\nu}$. Thus, the renormalized wavefunctions for a

single impurity are given by

$$\tilde{\varphi}_m(w) = \sqrt{\frac{(1-\nu)^{m+1}}{2\pi 2^m m!}} w^m e^{-(1-\nu)|w|^2/4}. \tag{3.17}$$

In the limit of $\nu = 0$, this wave function is identical to the un-renormalized Fock-Darwin state $\varphi_m(w)$ in Eq. (3.1). The density corresponding to $\tilde{\varphi}_m$ is given by

$$\begin{aligned}\tilde{\rho}_m(w) &= |\tilde{\varphi}_m(w)|^2 = \frac{(1-\nu)^{m+1}}{2\pi 2^m m!}|w|^{2m} e^{-(1-\nu)|w|^2/2} \\ &= \sum_{n=0}^{\infty} \rho_{m+n}(w)\nu^n(1-\nu)^{m+1}\frac{(m+n)!}{m!n!}.\end{aligned} \tag{3.18}$$

In the second line, we have expanded the renormalized density $\tilde{\rho}_m$ in terms of un-renormalized densities $\rho_{n+m} = |\varphi_{n+m}|^2$, corresponding to angular momentum $n+m$. Thus, the average angular momentum L_b^m of an impurity in level m is given by

$$L_b^m = \sum_{n=0}^{\infty}(n+m)\nu^n(1-\nu)^{m+1}\frac{(m+n)!}{m!n!} = \frac{m+\nu}{1-\nu}. \tag{3.19}$$

In its ground state ($m = 0$), the impurity has average angular momentum value $L_b^0 = \nu/(1-\nu)$, and exciting the impurity by one unit (from m to $m+1$) changes the average angular momentum by $\Delta L_b = 1/(1-\nu) > 1$. The standard deviation is $\delta L_b^m = \sqrt{\nu(m+1)}/(1-\nu)$, so the relative error $\delta L_b^m / L_b^m \to 0$ for large m.

To confirm this analytical prediciton we used various numerical approaches: First, we applied exact diagonalization (see Section 2.1) to the pseudopotential Hamiltonian (3.4) at fixed total angular momentum L to verify the analytical construction of the zero-energy modes, and in particular the counting of Table 3.1. We lift the ground state degeneracy $\mathcal{N}_{d,\mathrm{imp}}$ at $L = L_q + N_a + d$ by choosing the trap frequency ω_a slightly larger than ω_b. The states within the quasi-degenerate manifold are then energetically ordered decreasingly with the excitation level m of the impurity. The corresponding impurity angular momentum $\langle L_b \rangle$ can be directly obtained from the numerical solution, and for each $m \leq d$, we find $\mathcal{N}_{d-m}$ degenerate states, in which the impurity's angular momentum matches very well with the theoretically expected value $L_b^m = L_b^0 + m\Delta L_b$. This behavior is shown in Fig. 3.1 for two cases corresponding to Laughlin filling factors $\nu = 1/3$ and $\nu = 1/5$. In this example, we have chosen $d = 4$ yielding twelve quasi-degenerate states (left of the red-dotted vertical line).

Eq. (3.19) can also be verified by directly evaluating the impurity angular momentum from the wavefunction in (3.14), either by symbolical operations [256], or numerically via Monte Carlo integration method. This allowed to obtain much larger system sizes compared to ED. We used the latter method to determine the impurity angular momentum of $\Psi_{q,1,0}$ for $2 \leq q \leq 6$ for $N_a \sim 40$, which is accurately given by L_b^0.

The fractional "quantization" of angular momentum is reflected by the impurity density, plotted in Fig. 3.2(a). Higher orbitals correspond to larger angular momenta and are characterized by broader density profiles. More quantitatively, there is a linear relation between the mean square of the radial position, $\langle r^2 \rangle$, and the angular momentum m. In the absence of a liquid (i.e. for $\nu = 0$), we have $\langle r^2 \rangle_m \equiv \int_0^\infty dr r^3 |\varphi_m(r)|^2 = 2m + 2$. As we find numerically, the slope of this curve

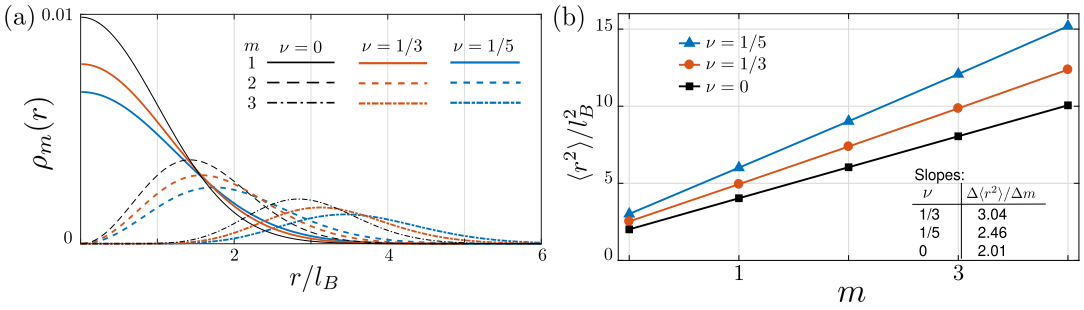

FIGURE 3.2: (a) We plot the radial density $\rho_b^{m,q}(|w|)$ of an impurity, which is excited to the mth level ($m = 0, 1, 4$), and which is immersed in a FQHE liquid at $\nu = 1/q$ (for $q = 3$ and $q = 5$). For concreteness, we have assumed a liquid of $N_a = 8$ particles at $L = L_3 + N_a + 4 = 96$ for $\nu = 1/3$, and a liquid of $N_a = 6$ particles at $L = L_5 + N_a + 4 = 85$ at $\nu = 1/5$, and different m levels correspond to different edge modes. We also plot the density $\rho_m(|w|) = |\varphi_m(w)|^2$ of a single impurity in the absence of a liquid ($\nu = 0$). (b) For different levels m, we plot the mean square $\langle r^2\rangle_m$ of the radial position of the impurity in the presence of a liquid at $\nu = 1/3$, $\nu = 1/5$, and in the absence of the liquid. The slope of the linear relation between m and $\langle r^2\rangle_m$ characterizes the quantization of angular momentum.

changes at finite ν, see Fig. 3.2(b). In this case,

$$\langle r^2\rangle_{m,q} \equiv \int_0^\infty dr r^3 \rho_b^{m,q}(r), \tag{3.20}$$

where the impurity density $\rho_b^{m,q}(r)$, corresponds to a many-body state $\Psi_{q,m,d-m}$, and is essentially independent of the choice of d. Specifically, at $\nu = 0$, the slope of value 2 corresponds to integer quantization of angular momentum, whereas at $\nu = 1/3$ and $\nu = 1/5$, the slopes are increased by factors $3/2$ and $5/4$, in full accordance with the expected "quantization" of angular momentum.

3.3.1 Breakdown of the mean-field theory

There are different scenarios in which the mean-field result (3.19) ceases to describe the behavior of an impurity bound to a quasi-hole: for example, the effect of the majority particles on the impurities cannot be completely described by a renormalization of the effective magnetic field when the filling is too high. Alternatively, in the limit of large excitation index m, the impurity reaches the edge of the system, and we can expect deviations from the behavior of an impurity deeply embedded in the bulk. In the following, we discuss these two breakdown scenarios in more detail.

Breakdown at $\nu = 1$

The mean-field picture assumes a screening of the magnetic field due to the liquid particles. In this picture, a liquid at $\nu = 1$ would entirely screen the magnetic field, and the assumption of our model that both liquid and impurity are subject to the Lowest Landau Level breaks down. This restricts (3.19) to FQHE liquids at $\nu < 1$.

Thus, it is interesting to ask how an impurity in an integer quantum Hall liquid at $\nu = 1$ behaves. Therefore, let us write down the wave function which describes

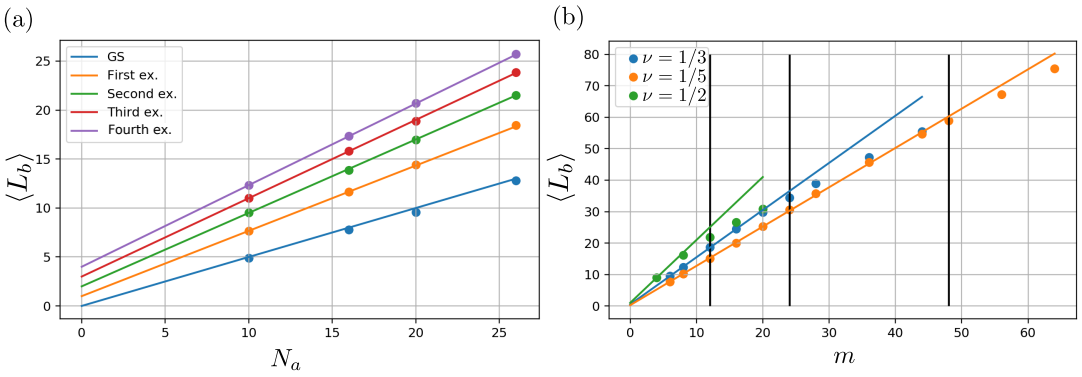

FIGURE 3.3: Breakdown of the mean field construction. (a) Breakdown at filling $\nu = 1$, illustrated by impurity angular momentum vs. N_a for different impurity levels m. The impurity angular momentum has become an extensive quantity, and scales according to Eq. (3.22) represented by the solid lines. (b) Breakdown at large m, illustrated by impurity angular momentum vs. m for three different fillings. The solid vertical lines represent the value $(q-1)N$ for the three fillings, at which the impurity should be at the edge of the liquid.

such scenario:

$$\Psi_m = w^m \prod_{1\leq i\leq N_a} (w - z_i) \prod_{1\leq i<j\leq N_a} (z_i - z_j). \tag{3.21}$$

In the impurity ground state, $m = 0$, both the impurity coordinates and the liquid coordinates are on equal footing, thus we can immediately conclude that the impurity angular momentum must be equal to the angular momentum per particle, $L_b^0 = N_a/2$. This establishes a stark contrast to the fractional case: While in the fractional scenario the average angular momentum of the impurity is independent of the number of liquid particles, in the integer case the average impurity angular momentum becomes an extensive quantity.

We may further ask what happens for excited impurity states, i.e. for $m > 0$. To address this scenario, we have computed the average angular momentum of the impurity by Monte Carlo integration applied to the wavefunction in Eq. (3.21). In Fig. 3.3(a), the average impurity angular momentum is plotted vs. the number of liquid particles N_a, for different m. Formally, these results can very well be captured by the following expression:

$$L_b^m = N_a \frac{m+1}{m+2} \tag{3.22}$$

Thus, the extensive character of L_b^m holds for all m. This establishes a clear difference between the fractional and the integer scenario. In particular, in the integer case, m cannot be interpreted as a quantity only linked to the impurities.

Breakdown for large m

The previous subsection demonstrates that, in the FQHE liquid at $\nu < 1$, the non-extensive nature of the impurity angular momentum is a striking and non-trivial feature. This feature keeps an impurity with small m away from the edge. Nevertheless, it is still possible to make the impurity particle explore the full size of the system, if it is excited to large values of m. To determine the value of m at which such breakdown is expected, let us first estimate the size of the liquid: the highest orbital

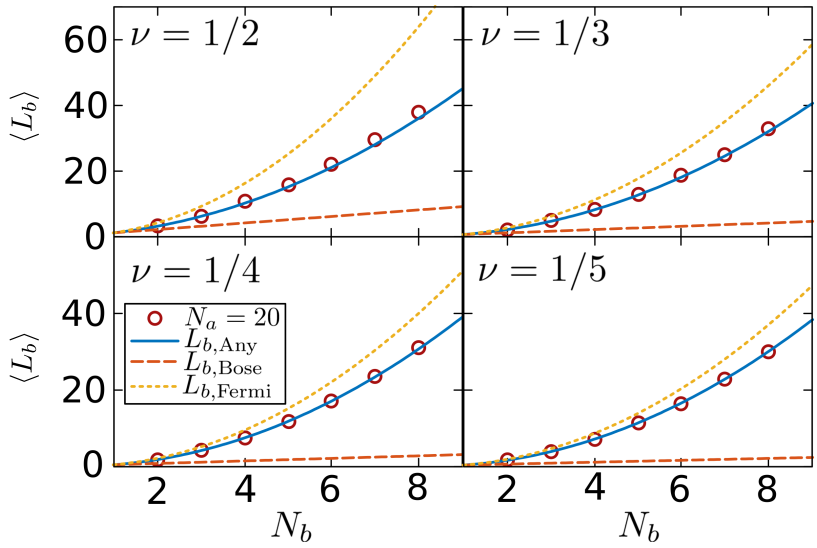

FIGURE 3.4: The impurity angular momentum $\langle L_b \rangle$ is plotted as a function of impurity number N_b, for different filling factors ν of the majority liquid in the Laughlin state. The numerical results are obtained from Monte Carlo sampling in the wave function Eq. (3.27) for $N_a = 20$ majority particles. We also plot $L_{Bose}(N_b, \nu)$ and $L_{Fermi}(N_b, \nu)$, the values expected if free bosons or fermions would fill the effective single-particle levels for impurities bound to quasi-holes, as well as the anyonic interpolation between both curves, $L_{Any}(N_b, \nu)$, defined in Eq. (3.30). The numerical data is found to match very well the anyonic prediction.

which is occupied in the Laughlin wave function at filling $\nu = 1/q$ is $M = q(N_a - 1)$, thus the system size is on order of

$$R \sim \sqrt{2M}\, l_B = \sqrt{2q(N_a - 1)}\, l_B. \tag{3.23}$$

On the other hand, an impurity in level m has a density peak at

$$W = \sqrt{2(qm + 1)/(q - 1)}\, l_B. \tag{3.24}$$

Accordingly, we expect a breakdown of our predictions for

$$m \sim (q - 1)N_a. \tag{3.25}$$

By performing an explicit Monte Carlo integration, we confirm that the breakdown indeed happens near this expected value of m. The results are shown in the right panel of Fig. 3.3: For a fixed liquid size ($N_a = 12$), we plot the average value of the impurity angular momentum as a function of m at different filling fractions $1/q$. The solid lines indicate the behavior expected from the mean-field formula. The vertical black lines indicate where, according to the above estimate, the deviations from this formula are expected (for the different values of q). Indeed, we find that around these values of m the impurity angular momentum deviates from the analytical expectations.

3.3.2 Multiple impurities

Having established the angular momentum levels of a single impurity, we now ask how is the behavior in the presence of N_b impurities. To obtain states of zero interaction energy, the total angular momentum needs to accommodate the anticorrelations of the majority liquid, the presence of N_b quasi-holes, and, for fermionic impurities, a *Vandermonde determinant* [257] $\prod_{i<j}(w_i - w_j)$ to introduce the right statistics. Thus, the zero-energy ground state occurs at

$$L = L_q + N_b N_a + \frac{1}{2} N_b (N_b - 1), \tag{3.26}$$

and its wave function reads:

$$\Psi_{f,qhs} \sim \left[\prod_{i<j}^{N_b} (w_i - w_j) \right] \cdot \left[\prod_{i=1}^{N_a} \prod_{j=1}^{N_b} (z_i - w_j) \right] \Psi_q. \tag{3.27}$$

Naively, one might expect that the total angular momentum of the impurities is equal to the value obtained from filling the single-particle levels,

$$L_{b,Fermi}(N_b, \nu) = \sum_{m=0}^{N_b - 1} \frac{m + \nu}{1 - \nu} = \frac{1}{q-1} [\frac{q}{2} N_b (N_b - 1) + N_b]. \tag{3.28}$$

However, this expectation is not correct: Fig. 3.4 shows our numerical results for $\langle L_b \rangle$ as a function of the number N_b of fermionic impurities, interacting with a bosonic or fermionic liquid ($N_a = 20$) at different filling factors ν. For comparison, we also plot $L_{b,\mathrm{Fermi}}(N_b, \nu)$ as well as the angular momentum expected for Bose condensation in the lowest impurity level,

$$L_{b,Bose}(N_b, \nu) = N_b L_b^0 = N_b \frac{\nu}{1 - \nu}. \tag{3.29}$$

The numerical value is intermediate, $L_{b,\mathrm{Bose}} < \langle L_b \rangle < L_{b,\mathrm{Fermi}}$. More precisely, it matches extremely well with the following interpolation formula:

$$L_{b,Any}(N_b, \nu) = (1 - \nu) L_{Fermi}(N_b, \nu) + \nu L_{Bose}(N_b, \nu). \tag{3.30}$$

This formula suggests that the statistical parameter α, which interpolates from Bose statistics ($\alpha = 0$) to Fermi statistics ($\alpha = 1$), is given by $\alpha = 1 - \nu$. This is in agreement with the effective Hamiltonian derived in Ref. [251] for impurities coupled to fractional quasi-holes (see also Refs. [258, 259]), and with the general expectation for a Laughlin quasi-hole ($\alpha = -\nu$) bound to a fermion ($\alpha = 1$). Importantly, we note that similar results as shown in Fig. 3.4 (with $N_a = 20$) can already be obtained for quite small Laughlin liquids ($N_a < 10$), enabling the detection of anyonic statistics in microscopic quantum simulators.

3.3.3 Increasing the range of interactions

The Laughlin wave function at filling $\nu = 1/q$ is an exact solution of a system of particles in the lowest Landau level which interact via Haldane pseudopotentials v_m with $m < q$. Strikingly, Laughlin liquids can also be formed in systems with long-range interactions. Specifically, the $\nu = 1/3$ state turns out to be a strongly gapped

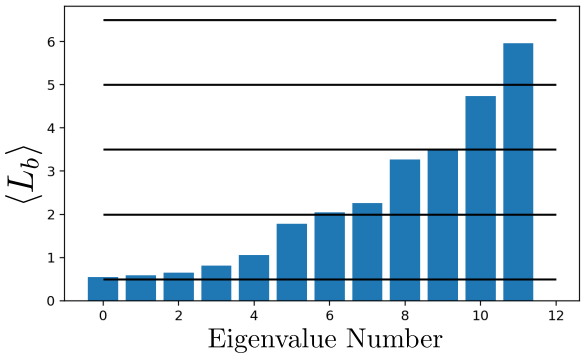

FIGURE 3.5: Angular momentum of one impurity interacting via contact interaction with a screened Coulomb liquid of $N_a = 6$ electrons, for the twelve quasi-degenerate ground states which exist at total angular momentum $L = L_{\text{Laughlin}} + N_a + 4$. The degenerate states typical of a pseudopotential construction disappear but the zero-energy manifold is not affected.

FQHE phase described by the Laughlin wave function for a variety of systems interacting with screened or unscreened Coulomb potentials, or dipolar potentials.

Here we address whether such long-ranged systems exhibit the same angular momentum behavior for impurities bound to quasi-holes that we derived for the pseudopotential model. Specifically, we will look at systems interacting with a screened or unscreened coulomb potential described by [260]:

$$V(r) = \frac{e^2}{\epsilon r} + \alpha \frac{e^2}{\epsilon \sqrt{r^2 + r_0^2}}, \tag{3.31}$$

where the first term accounts for the unscreened Coulomb interactions in a medium of dielectric constant ϵ, while the second term provides a potential screening via a dielectric plate at distance $r_0/2$ with dielectric constant ϵ', and $\alpha = \frac{\epsilon - \epsilon'}{\epsilon + \epsilon'}$.

First, we consider the case of unscreened Coulomb interactions within the liquid, and a contact impurity-liquid interaction of strength V_0, as it may for instance apply to an impurity given by a charge-neutral exciton without dipole moment [261]. In contrast to the pseudopotential model, the liquid now possesses a finite amount of interaction energy even in its Laughlin-like ground state. This means that, when the angular momentum of the liquid is increased, the system may either form a quasi-hole and reduce the interactions between liquid and impurity, or it may decrease the interaction energy of the liquid via high-order edge deformations. From this perspective, it is not in principle clear how the angular momentum of the impurity will behave when changing the value of the contact interaction V_0.

Interestingly, considering the average angular momentum $\langle L_b \rangle$ of an impurity in its ground state ($m = 0$) as a function of V_0, we find significant deviations from the expectation $L_b^0 = \frac{1}{2}$ (for $\nu = \frac{1}{3}$), but these deviations decrease, when V_0 is increased. For instance, in a system of five electrons

$$\langle L_b \rangle = 0.28, \quad \text{when } V_0 = v_1, \tag{3.32}$$

but converges to the value

$$\langle L_b \rangle = 0.39, \quad \text{when } V_0 > 10 v_1, \tag{3.33}$$

with v_1 being the $m = 1$ pseudopotential of the Coulomb interactions. These numbers further converge to the value expected from (3.19) when the system size is increased: For seven and eight electrons, we have obtained values $\langle L_b \rangle = 0.49$ and $\langle L_b \rangle = 0.52$. This suggests that our findings accurately describe also systems with unscreened Coulomb interaction in the liquid and contact interaction between liquid and impurity.

However, the condition $V_0 \gg v_1$ can be rather restrictive. Let us therefore also look at systems with screened Coulomb potentials. For concreteness, we choose $\alpha = -1$ and $d = 2\sqrt{2}l_B$ in Eq. (3.31). This choice dramatically relaxes the requirements on the strength of V_0. More importantly, we may now allow for liquid-impurity interactions and liquid-liquid interactions to be given by the same long-ranged potential $V(r)$. Such scenario could apply to impurities given by charged excitons (trions) or electronic impurities (e.g. with spin polarization opposite to the fractional quantum Hall liquid). In this case, $\langle L_b \rangle$ takes the value 0.5 in a system for seven electrons.

Finally, we further investigate the case of short-range impurity-liquid interactions with screened liquid-liquid Coulomb interactions, corresponding to charge-neutral impurities. If Fig. 3.5 we plot the angular momentum of one impurity in the twelve quasi-degenerate ground states which occur when, $L = L_{\text{Laughlin}} + N_a + 4$. This twelve-fold manifold is expected to contain five states with $\langle L_b \rangle = 0.5$, three states with $\langle L_b \rangle = 2$, two states with $\langle L_b \rangle = 3.5$, one state at $\langle L_b \rangle = 5$, and one state at $\langle L_b \rangle = 6.5$. Most significant deviations from this "quantization" are seen for the latter states at largest $\langle L_b \rangle$, where $\langle L_b \rangle$ remains significantly below the expected values. For the other states at smaller $\langle L_b \rangle$, in contrast, we observe the tendency to exhibit values slightly above the expected values. This is due to the fact that the long-ranged potential lifts the degeneracy of the edge excitations, and thus splits the degeneracy of this low-energy manifold.

The low-energy manifold as a whole, however, is unchanged. Accordingly, if we average $\langle L_b \rangle$ over the full low-energy manifold, we obtain exactly the value 2.25 as obtained by averaging over the twelve ground states in the degenerated model. Therefore, although the degeneracy lifting makes it more difficult or even impossible to determine the "quantized" angular momentum values from excited eigenstates, it does not impede our task of measuring the angular momentum of multiple impurities in a non-degenerate ground state. To this end, we assume that the impurity levels in the long-ranged liquid are still characterized by the same "quantization" scheme, i.e. $L_b^m = L_b^0 + \frac{3}{2}m$. This then also defines the value $L_{b,\text{Any}}$ for anyonic filling of these levels, as given by Eq. (3.30). Accordingly, anyonic filling of the impurity levels should be reflected by $\langle L_b \rangle = L_{b,\text{Any}} = 2$ for two impurities, or $\langle L_b \rangle = L_{b,\text{Any}} = 4.5$ for three impurities. Strikingly, our numerical results for the (unique) ground state of two or three impurities at total angular momentum $L = L_{\text{Laughlin}} + N_b N_a + N_b(N_b - 1)/2$ exhibit values which are very close to the expected value $L_{b,\text{Any}}$. The precise numbers are given in Table 3.2.

Hence, our scheme applies also to systems with long-range interactions, provided a sufficiently strong screening of the liquid, and/or sufficiently strong liquid-impurity interactions.

3.3.4 Other types of impurities

In all the cases discussed so far the impurity particles were always taken as non-interacting fermions. In all cases, we minimally included the fermionic statistics by multiplying the quasihole wavefunction by a Vandermonde determinatnt $\prod_{i<j}(w_i -$

N_b	N_a	L	$L_{b,Any}$	$\langle L_b \rangle$
2	4	27	2	**2.04**
2	5	41	2	**1.87**
2	6	58	2	**1.91**
3	6	48	4.5	**4.41**
3	6	66	4.5	**4.41**

TABLE 3.2: Filling the anyon sea: N_b impurities interact (via contact interaction, $V_0 = 1$ with N_a electrons in a screened Coulomb liquid ($\alpha = -1$ and $d = 2\sqrt{2}l_B$ in Eq. 3.31), at Landau filling $\nu = 1/3$. The total angular momentum L is chosen such that there is a unique ground state in which the impurities can bind to N_b quasi-holes. The angular momentum $\langle L_b \rangle$ of the impurities matches well with L_{Any}, the expected value for non-interacting anyons defined by Eq. (5) in the main text.

w_j). However, one may ask what would happen in the case of non-interacting bosonic impurities or interacting impurities, either bosonic or fermionic. In the present section, we will study these cases, and we will show how anticorrelations between the impurities reflect in the total impurity angular momentum.

Non-interacting bosonic impurities

To obtain an appropriate wave function for non-interacting bosonic impurities bound to quasi-holes it is simply sufficient to omit the Vandermonde determinant from Eq. (3.27), obtaining

$$\Psi(\{w_i\}) = \prod_{i,j}(w_i - z_j)\Psi_q. \tag{3.34}$$

The values for the angular momentum of the impurity $\langle L_b \rangle$, found by Monte Carlo sampling of this wave function, are given in Table 3.3 for some values of q, N (number of particles in the liquid), and N_b (number of impurities), and contrasted to the analog values obtained in the case of fermionic impurities. Interestingly, for a given q, the value obtained for the bosonic impurities is approximately constant, i.e. it depends neither on the number of particles in the liquid (which is true also in the case of fermionic impurities), nor on the number of impurities (in stark contrast to the case of fermionic impurities). The value of total angular momentum for the bosonic impurities appears to be proportional to the average angular momentum of a single impurity in its ground state, $L_0 = \frac{1}{q-1}$, as given by Eq. (3.19). In fact, for all cases shown in Table 3.3, we approximately have $\langle L_b \rangle \approx 1.4 L_0$.

An explanation for this behavior could be the following: The bosonic impurities form a condensate (in which the individual impurities fluctuate around the condensate center of mass), and all quasi-holes bind to this condensate, just as if there was only a single quasi-hole and a single impurity. In this picture, the (small) difference between $\langle L_b \rangle$ and L_0 would then be due to the fluctuations of impurities within the impurity condensate, although the picture does not necessarily imply that $\langle L_b \rangle$ is independent of N_b.

What appears to be clear, though, is the fact that non-interacting bosons as impurity particles are not suited for probing the anyonic properties of quasi-holes. In the following subsection, we are going to investigate whether and how the situation changes if the bosonic impurities are interacting.

q	N_b	N	$\langle L_b\rangle^B$	$\langle L_b\rangle^F$	$\langle L_b\rangle^F$(th.)
3	2	10	0.70	2.03	2
3	3	10	0.73	4.55	4.5
3	4	10	0.72	8.11	8
5	2	7	0.33	1.47	1.5
5	3	7	0.32	3.65	3.75
2	2	7	1.39	3.11	3
2	3	7	1.43	6.31	6

TABLE 3.3: For different filling $\nu = 1/q$ of a Laughlin liquid with N particles, we numerically obtain the average angular momentum $\langle L_b\rangle^B$ ($\langle L_b\rangle^F$) of N_b bosonic (fermionic) non-interacting impurities. We also show the values for fermionic impurities computed by means of Eq. (3.43) for reference.

Interacting impurities

We restrict to the simplest and most relevant case of bosonic impurities with repulsive contact interaction. With the impurities being subject to Landau quantization, this implies that the zero-energy ground state of the impurities itself is a bosonic Laughlin state, $\sim \prod_{i<j}(w_i - w_j)^2$. Therefore, in this case, the Vandermonde determinant in the wave function of fermionic impurities, has to be replaced by these bosonic Laughlin-like correlations. Evaluating again the average impurity angular momentum value numerically, we find that it matches very well with the following pattern:

$$\langle L_b\rangle(N_b, q) = \frac{N_b + \frac{2q-1}{2}N_b(N_b-1)}{q-1}. \tag{3.35}$$

This observation leads to the question of how this expression connects to the effective single-impurity levels L^m in Eq. (3.19). A simple guess would be that each impurity pair enters a state in which their relative angular momentum is given by L_b^2, as the impurities are forming a $q = 2$ Laughlin state, leading to a total angular momentum $\langle L_b\rangle = \frac{2q+1}{2(q-1)}N_b(N_b-1)$. This guess, though, does not match with the observed pattern. However, two more things should be considered: First, the Laughlin liquid also has a center-of-mass angular momentum L_{com} which comes from N_b particles condensing into L_0. Thus,

$$L_{\text{com}} = N_b/(q-1). \tag{3.36}$$

Moreover, one has to consider screening effects for the relative angular momentum, because in the vicinity of one impurity/quasi-hole the majority density is lowered. Following [249], we first note that a wave function of a pair at relative angular momentum M has an amplitude peak at radial distance $R_M = (2M)^{1/2}l_B$ in the absence of any screening. The screening due to the majority liquid effectively leads to a redefinition of the magnetic length, $l_B \to l_B^* = l_B/\sqrt{1-\nu}$. The screening which one impurity experiences due to the presence of the other impurity is captured by $M \to M^* = M - \nu$. Thus, for a pair at $M = 2$, the effective size of the wave function is given by

$$R^* = [2(M-\nu)]^{1/2}l_B^* = \left[\frac{2(M-\nu)}{1-\nu}\right]^{1/2} l_B \tag{3.37}$$

corresponding to an effective relative angular momentum

$$L^* = \frac{1}{2}(R^*/l_B)^2 = \frac{M-\nu}{1-\nu} = \frac{Mq-1}{q-1}. \tag{3.38}$$

Thus, for $N_b(N_b-1)/2$ pairs at $M=2$, the relative angular momentum becomes in total:

$$L_{\text{rel}} = \frac{1}{2}N_b(N_b-1)\frac{2q-1}{q-1} \tag{3.39}$$

With this, the sum, $L_{\text{rel}} + L_{\text{com}}$ exactly matches the pattern in Eq. (3.35) found numerically.

Another way of understanding Eq. (3.35) is in the light of hierarchy states [154, 157]. This construction builds upon the Laughlin states at filling $1/q$ (or their hole-conjugate at filling $1-1/q$). It then argues that FQHE states at other (odd-denominator) filling factors can appear when quasi-holes or quasi-particles in the parent liquid themselves form a Laughlin-like state. Noting the relation between filling factor ν, angular momentum L, and particle number N, $\nu = \lim_{N\to\infty}\frac{N^2}{2L}$ [262], we find that the angular momentum of Eq. (3.35) corresponds to a fractional quantum Hall state at $\nu = \frac{q-1}{2q-1}$, which matches the filling factor of the first state in the hierarchical construction. This observation suggests a feasible way of exploring hierarchical fractional quantum Hall states using bosonic impurities with repulsive contact interactions.

3.4 Moore-Read state

The fractionalization of impurity angular momentum, as described by Eq. (3.19), does not only apply to impurities in a Laughlin liquid, but also in the non-Abelian Moore-Read liquid incorporating the pairing of particles. The wave function describing the Moore-Read (MR) state for filling $\nu = 1/m$, as introduced in Section 1.2.1, is

$$\psi_{\text{MR}}(z) = Pf\left(\frac{1}{z_i - z_j}\right)\prod_{i<j}(z_i - z_j)^m e^{-\sum_i |z|^2/4}, \tag{3.40}$$

where Pf denotes the Pfaffian. The total angular momentum of the state can be read from the polynomial part of the wave function, being equal to the degree of the polynomial in z_i. It is given by

$$L = \frac{m}{2}N_a(N_a-1) - \frac{N_a}{2} \tag{3.41}$$

for N_a particles. The contribution $N_a/2$ is due to the Pfaffian which removes $N_a/2$ zeros from the wave function.

As outlined in Section 1.2.1, such liquid allows for two types of quasi-holes [263]: a "Laughlin"-like quasi-holes, of charge νe, and a "Pfaffian"-like quasi-hole, of charge $\nu e/2$. To obtain the renormalized angular momentum of the impurities bound to these quasi-holes, we can repeat the same reasoning as in the case of the Laughlin liquid. In this case, however, the effective flux felt by the impurity depends on the type of quasi-hole, such that

$$L_b^m = \frac{m+\varphi}{1-\varphi}, \tag{3.42}$$

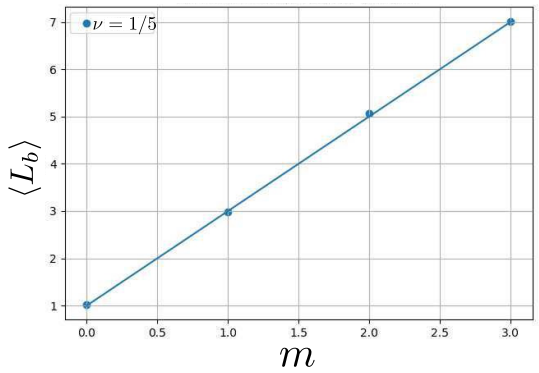

FIGURE 3.6: Average angular momentum of one impurity bound to a full quasi-hole in a Moore-Read liquid ($\nu = 1/2$), as a function of the excitation index m, computed by Monte-Carlo sampling of the Moore-Read wavefunction with 26 particles. The solid line represents the expectation from the mean-field formula.

with $\varphi = \nu$ for the Laughlin-like quasi-hole, and $\varphi = \nu/2$ for the Pfaffian-like quasi-hole. For multiple impurities one might again expect to obtain the total angular momentum by filling the available states, such as $L_{b,Fermi} = \sum_{m=0}^{N_b-1} \frac{m+\varphi}{1-\varphi} = \frac{1}{1-\varphi}\left[N_b(N_b-1)/2 + N_b\varphi\right]$ for fermionic impurities, or $L_{b,Bose} = N_b\varphi/(1-\varphi)$ for bosonic impurities. Instead, as for the Laughlin liquid, we numerically find that the total angular momentum of the impurities is given by

$$L_{b,Any} = (1-\alpha)L_{b,Fermi} + \alpha L_{b,Bose}. \tag{3.43}$$

Here the anyonic statistical parameter α is different for the two types of holes.

Therefore, by computing $L_{b,Fermi}$ and $L_{b,Bose}$ from the effective single-impurity levels, and computing L_{Any} from the many-body wave function, we can determine the statistical parameter of the quasi-holes:

$$\alpha = \frac{L_{b,Fermi} - L_{b,Any}}{L_{b,Fermi} - L_{b,Bose}}, \tag{3.44}$$

to determine their nature. We will now discuss the results for the two different cases.

3.4.1 Impurities bound to Laughlin-like quasi-holes

In the simplest case, a quasi-hole can be described as in the Laughlin state by multiplying ψ_{MR} by a polynomial term. Explicitly, the wave function reads

$$\psi_{\mathrm{LQH}}(z,w) = \prod_k (z_k - w)\mathrm{Pf}\left(\frac{1}{z_i - z_j}\right)\prod_{i<j}(z_i - z_j)^m, \tag{3.45}$$

where w is the position of the quasi-hole, and we have omitted the exponential factor. The addition of the prefactor implies that the total angular momentum is

$$L = \frac{m}{2}N_a(N_a-1) + \frac{N_a}{2}. \tag{3.46}$$

This quasi-hole, as in the Laughlin case, has fractional charge e/m and Abelian statistical parameter $\alpha = 1/m$ [263].

We verify that Eq. (3.42) holds for a Moore-Read liquid at filling $\nu = 1/2$ by Monte-Carlo integration of its wave functions. The results are shown in Fig. 3.6(a). Not surprisingly, the impurity bound to a full quasi-hole behaves in exactly the same way as in the $\nu = 1/2$ Laughlin liquid, e.g. $L_b^m = \frac{m+\nu}{1-\nu}$. However, as in the case of the Laughlin liquid, for the bosonic Moore-Read liquid at $\nu = 1$ the mean-field formula is not applicable, and the impurity angular momentum becomes a quantity which scales extensively with the number of liquid particles.

3.4.2 Impurities bound to half quasi-holes

More interesting is the fact that in this system each quasi-hole can "split in two", resulting in a state with the same angular momentum L, but with two "half" quasi-holes (HQH), described by a wave function

$$\psi_{\mathrm{HQH}}(z, w_1, w_2) = \mathrm{Pf}(W) \prod_{i<j} (z_i - z_j)^m. \tag{3.47}$$

Here W is a matrix that depends on the parity P of the number of particles N_a. If N_a is even, we have

$$W = \frac{(z_i - w_1)(z_i - w_2) + (i \leftrightarrow j)}{z_i - z_j}. \tag{3.48}$$

If N_a is odd, this definition would lead to an odd-dimensional matrix, for which the Pfaffian is not defined. Therefore, to obtain W for N_a odd, we have to construct a $N_a + 1 \times N_a + 1$ matrix by adding to the previously defined matrix W a row (column) of 1 (-1), and 0 in the lower right corner [264].

Similar to the Laughlin case, half quasi-holes are characterized by fractional charge $e/2m$ and fractional statistics. Crucially, the statistical parameter of the two quasi-holes depends on the parity of N_a. In particular, we have that [167, 264]

$$\alpha = \frac{1}{4m} - \frac{1}{8} + \frac{P}{2}, \tag{3.49}$$

where $P = 0(1)$ for an even (odd) number of particles.

Notably, the statistical parameter α for Pfaffian quasi-holes exhibits filling-independent terms, and the P-dependence serves as a proof of the non-Abelian statistics of the quasi-holes [101]. Specifically, the P-dependence reflects the existence of two different fusion channels for the anyons, which, by invoking a conformal field theory description, can be related to the parity of the particle number [167]. Alternatively, the P-dependence can also be explained by the theory of p-wave superconductors [100]. From this viewpoint, the two parity sectors correspond to two degenerate ground states of a p-wave superconductor with two half vortices. The analogy between Pfaffian FQHE states and p-wave superconductors becomes evident in the composite fermions framework for the state at $\nu = 1/2$: in this picture the composite fermions are subjected to a zero effective magnetic field, the state then represents a Fermi liquid that undergoes a BCS instability to a p-wave superconducting state [100].

An even richer picture appears in the presence of $2n$ HQHs, with $n > 1$. The state can still be described by Eq. (3.47), if we replace W by the matrix

$$\frac{(z_i - w_1)\dots(z_i - w_n)(z_j - w_{n+1})\dots(z_j - w_{2n}) + (i \leftrightarrow j)}{z_i - z_j}. \tag{3.50}$$

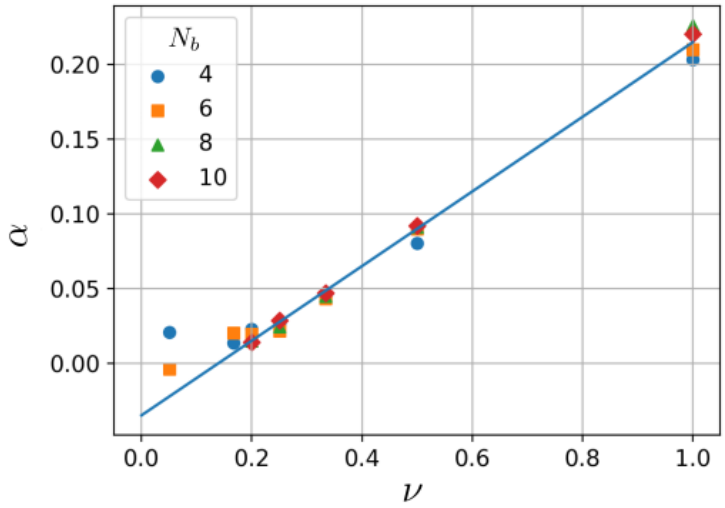

FIGURE 3.7: Statistical parameter α of HQHs as a function of filling ν, obtained for different numbers of impurities. For lower fillings (below $1/5$) the HQHs becomes bosonic, and the prediction (3.43) does not hold, i.e. see the two points at filling $1/20$. Solid line is a fit $\alpha = \nu/4 - 1/8 + 0.09$.

It can be seen from Eq. (3.50) that there is an arbitrary choice involved when the $2n$ quasi-holes are split in two groups, each of n elements. This means that it is possible to write more than one such states with $2n$ HQHs. There are $\frac{1}{2}\frac{(2n)!}{n!n!}$ possible ways to group $2n$ elements in two groups, but these states are not orthogonal. Instead, it can be shown that the dimension of the Hilbert space spanned by these degenerate ground states is 2^{n-1}. Strikingly, an exchange of two quasi-holes can mix one state with one of the others, one of the most direct manifestations of the non-Abelian statistics of the HQHs [159].

Finally, it is also possible to construct a state that contains a single half quasi-hole by setting

$$W = \frac{(z_i - w_1) + (z_j - w_1)}{z_i - z_j}. \tag{3.51}$$

The angular momentum of this wave function is $L = \frac{m}{2}N_a(N_a - 1)$. In presence of an impurity this state can be retrieved by exact diagonalization of the three-body contact Hamiltonian and a repulsive majority-impurity contact potential [263].

Numerical results

If impurities in the lowest Landau level bind to the HQHs of the FQHE liquid, the many-body system can still be described by the HQH wave function, Eq. (3.47), but the quasi-hole parameters w_i now become dynamical quantities. In the case of multiple fermionic impurities the state also has to be multiplied by the Vandermonde factor $\prod_{i<j}(w_i - w_j)$ that enforces the Pauli principle. The resulting wave function is then

$$\psi(z, w) = \mathrm{Pf}(W) \prod_{k<l, i<j} (w_k - w_l)(z_i - z_j) e^{-\frac{1}{4}\sum_{i,j} |w_i|^2 + |z_j|^2}, \tag{3.52}$$

with W chosen appropriately depending on the number of impurities. We have used this wave function as a probability distribution for the Monte Carlo calculations,

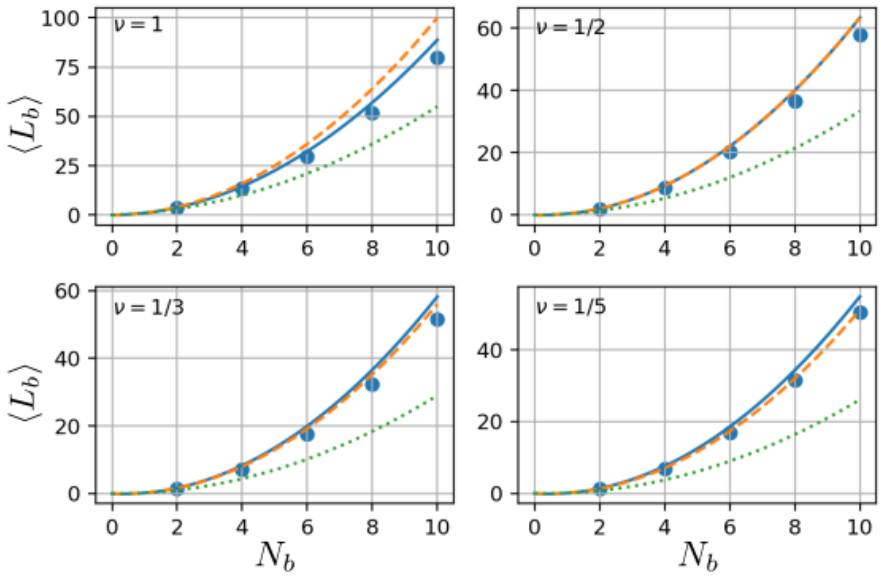

FIGURE 3.8: Impurities angular momentum as a function of number of impurities, compared to Eq. (3.43) (solid line), value for pure bosonic (dotted line) or fermionic (dashed line) impurities. For low fillings, the impurities behave as free fermions and prediction (3.43) breaks down.

computing the expected value of both the impurity angular momentum and, as a crosscheck, the total system angular momenta.

First, we have studied the single impurity angular momentum by setting W as in (3.51). For $N_a = 30$ with a total angular momentum $L = 435/\nu$, the results match well with Eq. (3.42) for $m = 0$ for a wide range of fillings, as shown in Fig. 3.9(a). The agreement holds also for $m > 0$, as shown in Fig. 3.9(b) or three different fillings and $N_a = 26$.

Second, we considered the case of two impurity particles, to show that the impurities angular momentum can be used to track the two different parity sectors. Specifically, we computed $L_{b,Any}$ for N_a from 30 to 49. The expected values of $\langle L_b \rangle$ are 3.75 for N_a even and 2.75 for N_a odd. We show in Fig. 3.10 that for filling $\nu = 1$ the jump in angular momentum for even and odd parity is compatible with Eq. (3.43),

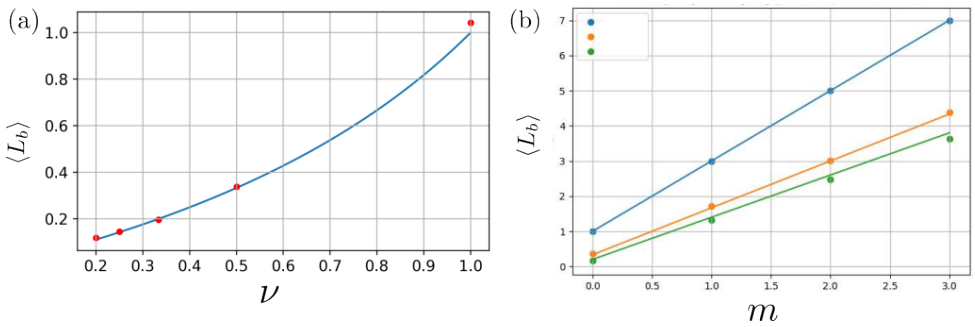

FIGURE 3.9: Angular momentum of a single impurity bound to a HQH for states at different fillings compared to the mean-field formula Eq. (3.42). (a) Single impurity at $m = 0$ for different fillings $\nu = 1, 1/2, 1/3, 1/4, 1/5$. The solid line represents the expectation from the mean-field formula. (b) Single impurity at different fillings for various values of m.

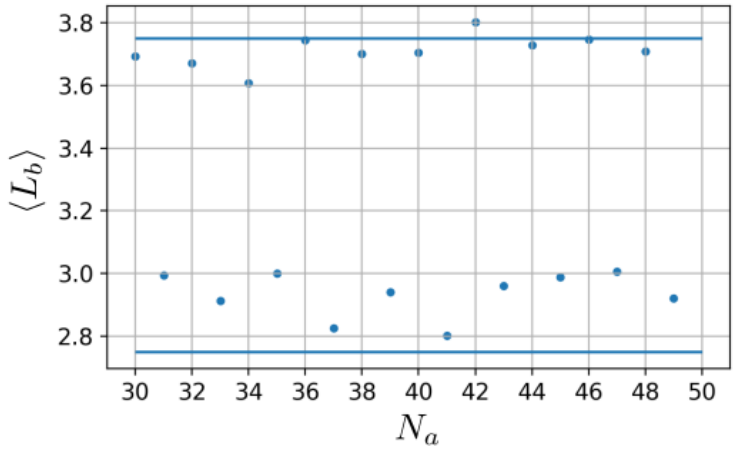

FIGURE 3.10: Angular momentum of two impurities bound to HQH for an even/odd number of majority particles at filling $\nu = 1$. The jump can be explained considering the different statistical parameter α for the two parity sectors, as described in Eq. (3.49). The solid lines represent the value of $\langle L_b \rangle = L_{b,Any}$ predicted in Eq. (3.43) for $P = 0, 1$.

except for a correction that can be explained by finite size effects, as we will show below.

In order to quantify the statistical parameter α of the anyons, we also studied a larger (even) number of impurities for different filling factors. From each of the numerically computed impurity angular momentum values $\langle L_b \rangle$ we extracted the corresponding α, via Eq. 3.44. The results for $N_a = 30$ for fillings from 1 to 1/6 are shown in Fig. 3.7, plotting α as a function of filling ν. From the slope of this curve, we see that the filling-dependent part of α perfectly agrees with the expectation, i.e. $\alpha \propto \nu/4$. However, the constant contribution is not exactly $-1/8$, as one would expect, but it has a correction of order 10^{-2}. We account this deviation to the overlapping size of the impurity wave functions. For lower fillings, the prediction (3.43) breaks down, and the impurities bound to quasi-holes behave effectively as free fermions, and the statistical parameter α of the quasi-holes goes to the bosonic limit (zero).

We also note that the computation of $\langle L_b \rangle$ does not lead to any different behavior for the different 2^{n-1} degenerate ground states. Thus, the behavior of the HQHs under braiding cannot be extracted from this impurity angular momentum.

Our data of $\langle L_b \rangle$ for multiple impurities at different ν is also illustrated in Fig. 3.8, plotting $\langle L_b \rangle$ vs. the number of impurities in the system at a given ν. We compare this curve with $L_{b,Fermi}$ and $L_{b,Bose}$, i.e. with the expectation for fermionic or bosonic particles. At all $\nu \leq 1/2$, the impurity behave very similar to fermions.

3.4.3 Analysis of fluctuations of the Berry phase

Eq. (3.49) holds in a regime where the quasi-holes are sufficiently far apart to be considered effectively non-interacting. This in turn influences the validity of Eq. (3.43). For finite distances, the quasi-holes will hybridize and lead to a fluctuation of the exchange statistical phase. This dependence of the statistical parameter on the quasi-hole distance has been evaluated for MR states in a spherical geometry in [265, 266].

In order to estimate this effect in our system, we first need to determine the impurity distance. In our case, this becomes a dynamical variable which we can estimate from the combined wave function. For two fermionic impurities with coordinates

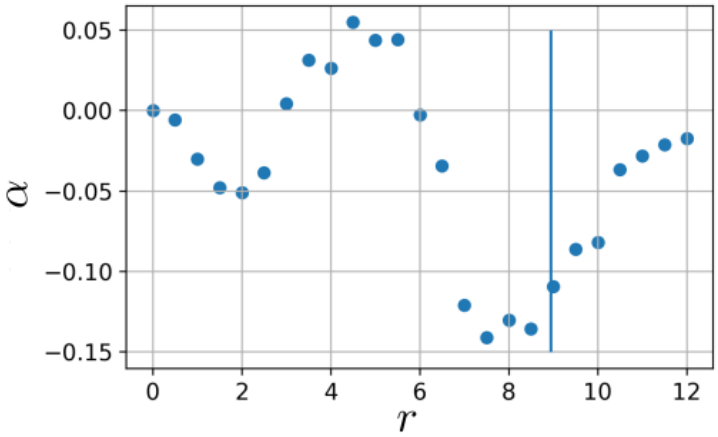

FIGURE 3.11: Statistical parameter α computed by explicitly evaluating the Berry phase of a braiding of two quasi-holes at a distance r in an MR state with $\nu = 1/2$. For distances of order $r \sim 3$ the finite size deviation from the expected value $\alpha = 0$ is of order 0.05, compatible with what obtained in Fig. 3.7. The fluctuations for large distances can be explained by finite size effects: for $N_a = 20$ the radius of the MR state is ~ 8.9.

w_1, w_2 the combined wave function in terms of renormalized Fock-Darwin wave functions is

$$\phi(w_1, w_2) = \frac{\tilde{\phi}_0(w_1)\tilde{\phi}_1(w_2) - \tilde{\phi}_0(w_2)\tilde{\phi}_1(w_2)}{\sqrt{2}}, \tag{3.53}$$

that can be re-expressed in terms of center of mass and relative coordinates $R = (w_1 + w_2)/2$, $r = w_1 - w_2$ as

$$\tilde{\phi}(r, R) = -\frac{\sqrt{1 - \frac{\nu}{2}}(\nu - 2)}{8\pi} r e^{\frac{(\nu-2)}{16}(|r|^2 + 4R^2)}, \tag{3.54}$$

with ν the previously defined filling. This function is peaked at $r \sim 3$. Monte Carlo computations for the average distance between two impurities in the state (3.52) recover roughly the same values for different fillings.

It is then interesting to evaluate directly the statistical phase for two fixed quasi-holes and its dependence on the relative distance. To do so, we considered a configuration with two HQH, one at the center of the system and the other at a fixed radius R from the center. The system is then described by Eq. (3.47) with $w_1 = 0$, $w_2 = Re^{i\theta}$. We then compute the Berry phase associated with the state Eq. (3.52) under a rotation of the second hole around the first, for an adiabatic change of the parameter θ at fixed R:

$$\gamma = i \oint \mathrm{d}\theta \langle \frac{\psi^*}{\mathcal{N}} \frac{\mathrm{d}}{\mathrm{d}\theta} \frac{\psi}{\mathcal{N}} \rangle, \tag{3.55}$$

where $\mathcal{N} = \sqrt{\langle \psi^* \psi \rangle}$ is the normalization of the wave function. As this normalization is explicitly dependent on the value of θ we have to explicitly consider it in the computation of the derivative obtaining

$$\gamma = i \oint \mathrm{d}\theta \, \mathrm{Im} \left(\frac{1}{\mathcal{N}^2} \langle \psi^* \frac{\mathrm{d}}{\mathrm{d}\theta} \psi \rangle \right) = i 2\pi \mathrm{Im} \left(\frac{1}{\mathcal{N}^2} \langle \psi^* \frac{\mathrm{d}}{\mathrm{d}\theta} \psi \rangle \right), \tag{3.56}$$

where the last step is justified by the rotational invariance of the system. There is left

to evaluate the derivative in the round brackets. The only dependence on θ in the state (3.47) is in the Pfaffian term. We then can use the identities

$$\frac{\mathrm{d}}{\mathrm{d}\theta}\mathrm{det}W = \frac{\mathrm{d}}{\mathrm{d}\theta}[\mathrm{Pf}(W)]^2, \tag{3.57}$$

$$\frac{\mathrm{d}}{\mathrm{d}\theta}\mathrm{det}(W) = \mathrm{det}(W)\mathrm{Tr}\left(W^{-1}\frac{\mathrm{d}W}{\mathrm{d}\theta}\right), \tag{3.58}$$

to show that

$$\frac{\mathrm{d}\psi}{\mathrm{d}\theta} = \frac{1}{2}\mathrm{Tr}\left(W^{-1}\frac{\mathrm{d}W}{\mathrm{d}\theta}\right)\psi. \tag{3.59}$$

We then obtain

$$\gamma = i\pi\mathrm{Im}\left(\frac{1}{\mathcal{N}^2}\left\langle\psi^*\mathrm{Tr}\left(W^{-1}\frac{\mathrm{d}W}{\mathrm{d}\theta}\right)\psi\right\rangle\right). \tag{3.60}$$

The quantity inside the round bracket can then be computed by Monte Carlo. To retrieve the statistical phase we have to subtract the Aharonov-Bohm phase that the state accumulates because of the background magnetic field. We can do that by recomputing the Berry phase, removing the w_1 quasi-hole: this corresponds to substituting W, ψ in Eq. (3.60) with the appropriate ones for a single HQH. Finally the statistical parameter is $\alpha = \gamma/(2\pi)$.

As an example, we show the results for the most relevant filling fraction $\nu = 1/2$ in Fig. 3.11. At this filling, one would expect fermionic quasi-holes, i.e. impurities with $\alpha = 0$. However, at (small) distances, the statistical phase oscillates around zero, with an amplitude on the order of 0.05. This order of magnitude for fluctuations is compatible with the results of section 3.4.2.

3.5 Impurities bound to quasi-particles

So far we have only considered impurities which, through repulsive interactions, bind to quasi-holes. It is interesting to ask what happens if we have impurities which attract the liquid particles. Can they bind to quasi-particle and exhibit a behavior similar to the one of impurities bond to quasi-holes? The task is numerically non-trivial due to the more complicated trial wave functions for quasi-particles as explained in Section 1.2.1, but we can provide a brief perspective on this subject.

To accommodate a Laughlin-like quasi-hole the angular momentum of the liquid has to be increased by N_a, whereas the formation of a quasi-particle requires to reduce the angular momentum by the same amount. This suggests that an impurity particle bound to a quasi-particle shall carry negative angular momentum. Mathematically, this is possible if the Landau level basis of the impurity is the complex conjugate of the Landau levels for the liquid. Physically, this is possible if the coupling to the gauge field (charge $\times$ magnetic field) is reversed. Indeed, it seems natural that such reversal occurs for an impurity which binds to a quasi-particle: In this case, the impurity shall carry a charge which is opposite to the charge of the liquid particles, and with this, the impurity will be subject to opposite magnetic fluxes. This leads to the following ansatz for a single impurity in a Laughlin state, bound to a quasi-particle at position w, in the mth effective impurity state:

$$\Psi_{m,\mathrm{qp}}(w) = w^{*m}\prod_{i=1}^{N_a}(\partial_i - w^*)\Psi_{\mathrm{Laughlin}}, \tag{3.61}$$

where the asterisk denotes the conjugate of the complex position. In this wave function, the impurity "sees" the liquid particles as conjugated fluxes, in close analogy to the quasi-hole case. Thus, we expect that the same re-definition of magnetic length applies also to the effective impurity Landau level. This implies that the effective impurity Landau levels for quasi-particles are the conjugate of those for quasi-holes, and accordingly, the impurity angular momentum is given by Eq. (3.19) of the main text, with opposite sign.

The same reasoning can be extended to Moore-Read state, for both Laughlin-like quasi-particles and Pfaffian-like ones. In this latter case, the effective impurity wavefunction would be given by Eq. (3.47) by replacing W with

$$W = \frac{(\partial_i - w_1^*) + (\partial_j - w_1^*)}{z_i - z_j}. \tag{3.62}$$

3.6 Summary

In this Chapter, we studied the angular momentum of non-interacting fermionic impurities, bound to quasi-holes in FQHE states constrained to the lowest Landau levels. We represented them either by Laughlin or Moore-Read wave functions, and determined the fractional statistics of their quasi-hole excitations. We showed that in this situation the quantum statistics of quasi-holes can be directly read from the impurity angular momentum. The impurity particles see a renormalized magnetic field in the presence of majority particles, which in turn depends on the charge of the quasi-hole. It should be possible to determine the angular momentum of many impurities by taking into account the renormalization of the magnetic field for a single impurity, and by filling the single impurity angular momentum levels, assuming them to be either fermions or bosons. Instead, we showed through Exact Diagonalization of the parent Hamiltonians and Monte Carlo sampling of the many-body wave function, that the angular momentum of many impurities actually interpolates between the two limits, capturing the anyonic statistics. We show for Laughlin liquids that this picture also holds for longer-range interactions and interacting impurities. The interpolation parameter depends on the charge of the quasi-holes, and, for half quasi-holes in the Moore-Read state on the parity of the number of particles. This is a signature of the non-Abelian nature of these excitations. There are, however, some fluctuations in the estimation of this parameter due to finite size effects, that can be well understood by studying the Berry phase in a finite system, upon exchange of impurities.

If instead of considering non-interacting fermionic impurities we look at non-interacting bosonic impurities as tracer particles, we demonstrated that total angular momenta for such bosonic impurities appear to be proportional to the average angular momentum of a single impurity in its ground state. This happens because, confined to the lowest Landau level, such bosons form a condensate. Therefore, bosonic impurities are not suitable to trace the quasi-hole statistical behavior. However, if the bosons can repulsively interact with each other, they are appropriately explained by considering the total center of mass angular momentum and the screened (due to other impurities) relative angular momentum. Intriguingly, the total angular momentum corresponds to a FQHE state which matches the filling factor of the first state in the hierarchical construction of odd denominator FQHE states. Such odd denominator states arise from quasi-particles in the parent Laughlin liquid, forming their own FQHE states.

The implementation of our ideas could be possible either in quantum simulators using atoms or photons [105, 226], or in macroscopic electronic samples with optically created impurities such as excitons or trions. Signatures of excitons bound to fractional quasi-particles have been reported in [267], and the exciton density can be detected via scanning-transmission-electron microscopy [268]. It also opens the possibility of studies beyond the system studied here, and to address other types of fractional quantum Hall systems. This might include other members of the Read-Rezayi series, which in contrast to the Moore-Read state may support a type of anyons where universal quantum computation could be implemented. Another interesting subject could be the use of tracer particles in lattice fractional quantum Hall systems, for which a lattice version of the Moore-Read state and relative parent Hamiltonians have been derived [269].

Chapter 4

Detection of Majorana fermions through High Harmonic Generation

As we introduced in Chapter 1, the search for Majorana Fermions [141] is one of the most active topics in condensed matter research, both from a fundamental interest and for their potential applications in quantum technologies. Indeed, two-dimensional Majorana Fermions are expected to exhibit non-Abelian anyonic statistics [270] making them very interesting candidates for topological qubits, thanks to their capability of robustly storing and processing quantum information [98, 139, 271]. Although it is well established theoretically that Majorana Fermions can emerge as quasiparticles in condensed matter [142], clear experimental evidence is still lacking. A paradigmatic system expected to host these excitations at the edges is the Kitaev chain [102] introduced in Chapter 1. In the topological superconducting state, they appear as zero-energy modes in the middle of the superconducting gap, and are therefore also called Majorana zero modes (MZMs). In this way we also avoid the misleading name of "Fermions" being rather, as we said, non-Abelian anyons.

Despite the design of several experimental setups that effectively realize the Kitaev chain model [272–281], the detection of MZMs remains challenging. In nanowire setups, MZMs are expected to appear as zero-energy states in the tunneling density-of-states (DOS), manifested through a quantized zero-bias peak of height $2e^2/h$ in the differential conductance [282–284]. Even if several works show compatible results [103, 285, 286], there is still no conclusive evidence of the predicted robust quantization of the conductance [287]. Specifically, the zero-bias peaks are found at heights significantly smaller than $2e^2/h$, challenging their interpretation. Moreover, the observed nearly perfect conductance quantization may also stem from non-topological states, for example the so-called *Andreev Bound States* [288–291].

In this Chapter, that revisits the results reported in [III], we explain an alternative approach to uncovering MZMs, showing that the topological nature of the edge states can be revealed by analyzing the non-linear response of the chain to strong electromagnetic fields [292], via the process of *High Harmonic Generation* (HHG). We thus propose an optical method to independently check for the presence of MZMs, with a spatial resolution limited only by the wavelength of the light, and a temporal resolution which enables to probe the higher part of the excitation spectrum, with the goal of complementing transport-based detection techniques [282].

The structure of the chapter is the following. We start by introducing the concept of HHG in condensed matter, its successful applications in condensed matter physics, and the intuition behind its use for the detection of topological phases in Section 4.1. We then describe the model object of study in Section 4.2: we consider

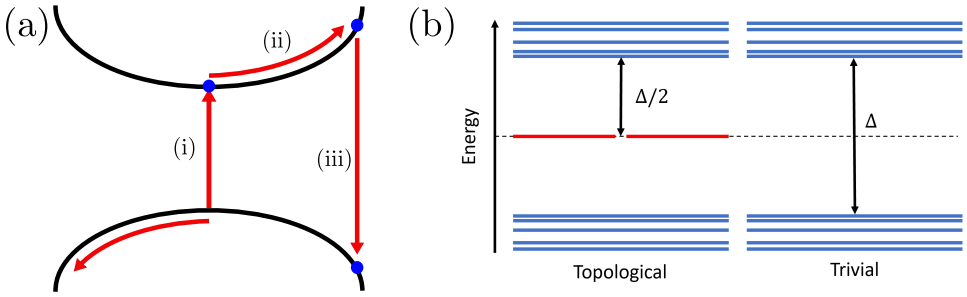

FIGURE 4.1: HHG in condensed matter (a) Schematics of the three-steps model (i) An electron is excited from the valence to the conduction band. (2) The electron moves driven by the field of the pulse, emitting a radiation dependent on the curvature of the conduction band. A similar dynamics happens for the hole left behind in the valence band. (3) The electron gets reabsorbed, emitting a high-energy photon, whose energy is bounded by the bandwidth. (b) The presence of zero energy edge states in the topological phase means that intraband transitions are allowed starting from a frequency of half of the bandgap of the system.

a realistic system with *p*-wave superconductivity obtained via proximity effect, instead of studying the idealized Kitaev chain. This choice allows us to address the coupling between the EM field and the electrons at a microscopic level, overcoming the ambiguity coming from the lack of gauge invariance of the Kitaev chain under minimal coupling with an EM field.

We then show the main results of this Chapter in Section 4.3: the use the HHG response of the system to map its density of states, and thus, the width of its energy bands and energy gaps. This gives rise to a scheme that distinguishes the topological from the trivial phase. Specifically, we introduce a measurable quantity, obtained from the HHG spectrum, that allows us to chart out the whole phase diagram. Finally, we explain how this difference in the spectrum can be traced back to topologically protected edge states. By focusing the radiation source to the edge, we are able to discern bulk from edge excitations, clearly isolating the contribution from the topological MZMs. Moreover, we show how the spectrum is robust to perturbation that do not break the symmetries of the system and do not close the gap.

4.1 High Harmonic Generation in Condensed Matter

High Harmonic Generation (HHG) is a non-linear light-matter interaction process in which a material, when illuminated by a laser pulse of high intensity, re-emits light with a frequency several times higher than the incoming one (even of a magnitude hundreds of times larger). In the past, HHG has been used to track the dynamics of excitations at femtosecond timescales, yielding ultrafast imaging methods in atomic and molecular gases [293–296] and, more recently, in solid-state systems [297–299]. Lately, there has been a rising interest in using HHG to detect topological properties of matter [300–305], including MZMs in Kitaev chains [306], and edge states in generalized SSH chains [307].

To explain the mechanism behind HHG, we will employ the *strong field approximation* [293, 294, 308]. This approximation, widely employed in the study of atomic and molecular physics, is based on a semi-classical picture of the non-linear process of emission and reabsorption of electrons in atoms subjected by a strong electromagnetic field. This process can be split in three fundamental steps [308]: (i) The incoming pulse lowers the Coulomb potential barrier enough that the electron can

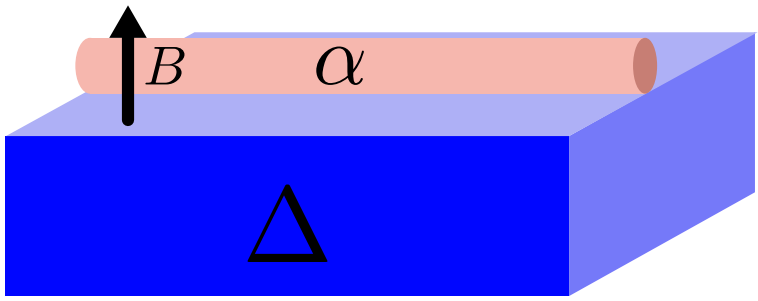

FIGURE 4.2: Sketch of the system under study. A semiconducting nanowire with strong spin-orbit coupling α (red) is in proximity to a superconducting substrate with s-wave superconducting pairing Δ (blue). The system is subjected to an external magnetic field B.

tunnel out of the atom; (ii) The free electron is accelerated by the pulse and moves away from the atom, emitting radiation during this process due to its acceleration; (iii) The electron re-collides with the atom and is reabsorbed, emitting a photon with energy equal to the difference between the energy of the electron in the continuum and the energy of the electron in the atom. The frequency of this re-emitted photon can be several times higher (order of $10^2 - 10^3$) than the frequency of the incoming pulse.

In the case of solids the intuition is similar [309], as sketched in Fig. 4.1(a): in this case an electron from the valence band is excited to the conduction band and its dynamic under the pulse is constrained by the dispersion of the conduction band. Moreover, the dynamics of the leftover hole in the valence band has also to be taken into account. Due to the band structure, the energy of the re-emitted photons after the absorption process is bounded by the bandgap of the two bands from one side, and their bandwidth from the other. This, in turn, means that the emitted spectrum is a direct probe of the band structure of the system.

We will exploit the last property to detect topology: as we know from Chapter 1, in the topological phase of the Kitaev chain there are zero-energy states in the middle of the gap. This means that the lowest possible interband transition is at half the bandgap, thus is the lowest frequency at which we can expect to see emission. In the trivial phase, instead, the lowest transition corresponds to the bandgap, meaning that we can recover the phase by looking at the lowest frequency for which we see a re-emission. This is schematically shown in Fig. 4.1(b).

4.2 From a Semiconducting Nanowire to the Kitaev Chain

As we have seen in Chapter 1, the 1D p-wave superconducting Kitaev chain [102] described by Eq. 1.20 exhibits two phases, a trivial one and a topological one, with a topological phase transition at $|\mu| = t$. In the topological phase, for open boundary conditions, the spectrum is characterized by two degenerate ground states, corresponding to MZMs localized at the two edges of the chain.

To study the response of this model to a strong field, it is crucial to correctly represent the coupling of the fermions to the electromagnetic field. The most straightforward way to couple a classical vector potential $A(t)$ to particles on a lattice is via the so called *Peierls substitution*

$$c_j^\dagger \to e^{iA(t)j} c_{j\sigma}^\dagger. \tag{4.1}$$

However, this creates an ambiguity in the definition of the superconducting coupling. As the Hamiltonian must remain gauge invariant, this transformation would require a corresponding time-depending change in the superconducting gap Δ. While this is possible, we make the approximation that the value of Δ remains fixed throughout.

Therefore, and to be more consistent with experimental efforts, we focus on a particular system [274, 275], which has been the main focus of several experimental investigations and whose low energy behavior is governed by the Kitaev chain Hamiltonian: a heterostructure between a semiconducting chain with strong spin-orbit coupling and a regular s-wave superconductor, additionally subjected to an external Zeeman field. A sketch of the system is shown in Figure 4.2.

To obtain the effective model we start from the continuum Hamiltonian of the semiconducting chain, whose electrons are described by a fermionic field $\psi_s(x)$, where s is the spin index and x is the position along the chain:

$$H_0 = \sum_s \int \mathrm{d}x \psi_s^\dagger(x) \left(\frac{p^2}{2m} - \mu + V(x) - \alpha E_\perp p \sigma_y + \frac{1}{2} g \mu_B B \sigma_z \right) \psi_s(x) \tag{4.2}$$

Here σ are Pauli matrices acting on the spin degree of freedom, B is a Zeeman field in the z direction, $g\mu_B$ is the gyromagnetic factor of the electron in units of the Bohr magneton, and $\alpha E_\perp$ is the spin-orbit coupling. $V(x)$ is the lattice potential that the electrons are subjected to. On the other hand, the underlying s-wave superconductor introduces a proximity-induced pairing term modeled as [310]

$$H_{sc} = \int \mathrm{d}x \psi_\downarrow(x) \Delta \psi_\uparrow(x) + h.c., \tag{4.3}$$

where the electrons are locally paired in space. At this point we can write the coupling to the electromagnetic field of the external pulse $A(x,t)$ (that we assumed to point in the x direction) by using minimal coupling $\vec{p} \to \vec{p} - e\vec{A}(x,t)$. We can then write the full Hamiltonian as

$$H_0 = \sum_s \int \mathrm{d}x \psi_s^\dagger(x) \left(\frac{(p - eA)^2}{2m} - \mu + V(x) - \alpha E_\perp (p - eA) \sigma_y + \frac{1}{2} B \sigma_z \right) \psi_s(x). \tag{4.4}$$

Note how the spin-orbit coupling, being proportional to the momentum, is also affected by the coupling to the electromagnetic field. As we have seen in Section 2.3.2, if the local potential $V(x)$ is periodic and deep enough, the Hamiltonian in the lowest band is better expressed in a Wannier function basis

$$\psi_s^\dagger(x) = \sum_n e^{-i\lambda_n(x,t)} \phi_n^*(x) c_{ns}^\dagger(t), \qquad \lambda_n = e \int_{X_n}^x \mathrm{d}x A(x,t), \tag{4.5}$$

where $\phi_n(x)$ are generalized Wannier function centered on the lattice sites at X_n and $c_{ns}^\dagger$ are the related creation operators. The multiplication by a factor proportional to the factor λ_n is a gauge transformation implemented to simplify the computation of the terms involving the field $A(x,t)$. Finally, under the assumption that the EM field wavelength is much larger than the lattice spacing we can employ the dipole approximation and set

$$A(x,t) \sim A(t), \qquad \lambda_n \sim eA(t)(x - X_n). \tag{4.6}$$

Regarding the proximity-induced superconducting term instead, it only contains operators acting on the same site (two of which are "hidden" in the order parameter Δ), and does not couple with the electromagnetic field. The resulting total Hamiltonian can then be written in the tight-binding formulation as

$$H = \sum_{m,n,s} J_{mn}(t) c^\dagger_{ms} c_{ns} + \sum_{m,n,s,s'} U_{mn,s's}(t) c^\dagger_{ms'} c_{ns} + \sum_i (c_{\downarrow i} \Delta c_{\uparrow i} + h.c.), \tag{4.7}$$

where

$$J_{mn}(t) = J e^{-iA(t)(X_m - X_n)} [\delta_{m+1,n} + \delta_{m-1,n}] - \mu(t)\delta_{m,n}, \tag{4.8}$$

$$U_{mn,s's}(t) = -i\tilde{\alpha}\sigma_{y,s's} e^{-iA(t)(X_m - X_n)} [\delta_{m+1,n} - \delta_{m-1,n}] + \frac{1}{2} B \sigma_{z,s's} \delta_{m,n}. \tag{4.9}$$

For quadratic superconducting Hamiltonians, we can express 4.7 for a chain of length N in a Bogoliubov-de Gennes basis:

$$H = \Psi^\dagger H_{BdG} \Psi, \qquad H_{BdG}(t) = \begin{pmatrix} J + I\frac{B}{2} & U^\dagger(t) & I\Delta^* & 0 \\ U(t) & J - I\frac{B}{2} & 0 & I\Delta^* \\ I\Delta & 0 & -J + I\frac{B}{2} & -U^\dagger(t) \\ 0 & I\Delta & -U(t) & -J - I\frac{B}{2} \end{pmatrix}. \tag{4.10}$$

Here, I is the $N \times N$ identity matrix, and J and U are $N \times N$ matrices defined as

$$J_{l,m} = -\mu\delta_{l,m} + (\delta_{l,m-1} J e^{iA(t)} + \text{H.c.}), \quad U_{l,m}(t) = \delta_{l,m-1} \alpha e^{iA(t)} + \text{H.c.}. \tag{4.11}$$

The operator $\Psi = (c_\uparrow, c_\downarrow, c^\dagger_\downarrow, -c^\dagger_\uparrow)$ is a "compressed" Nambu spinor, where $c_\sigma \equiv c_{1\sigma}, \ldots, c_{N\sigma}$, with $\sigma \in \{\uparrow, \downarrow\}$. The Hamiltonian's parameters are the hopping J, the chemical potential μ, the effective spin-orbit coupling α, the Zeeman field B and the proximity-induced superconducting s-wave coupling Δ. In contrast to the Kitaev chain, this Hamiltonian lacks an explicit p-wave pairing term, and therefore, the gauge-invariant coupling to the external field can straightforwardly be described via a Peierls substitution.

4.2.1 Analysis of the Bogoliubov-de Gennes Hamiltonian

We will now show how to recover Majorana physics from (4.10). Using the same notation as the previous $H = \Psi^\dagger H_{BdG} \Psi$ where $\Psi = (c_{i\uparrow}, c_{i\downarrow}, c^\dagger_{i\downarrow}, -c^\dagger_{i\uparrow})^T$ is a Nambu spinor, we can write the Hamiltonian as

$$H_{BdG}(t) = \begin{pmatrix} H_0 & \Delta^* I_{2N} \\ \Delta I_{2N} & -\sigma_y H_0^* \sigma_y \end{pmatrix}, \quad H_0 = \begin{pmatrix} J + I\frac{B}{2} & U^\dagger(t) \\ U(t) & J - I\frac{B}{2} \end{pmatrix}, \tag{4.12}$$

where $-\sigma_y H_0^* \sigma_y$ is the time-reversed of H_0 and I_{2N} is the $2N \times 2N$ identity. In momentum space, the Hamiltonian can be exactly diagonalized leading to a 4-band spectrum. For momentum $k = 0$, the energy levels are located at

$$E = \pm B \pm \sqrt{\mu^2 + \Delta^2}. \tag{4.13}$$

The artificial doubling of the Hilbert space occurring by casting the Hamiltonian in a Bogoliubov-de Gennes form introduces a particle-hole symmetry in the system to account for the new non-physical degree of freedom. This symmetry is implemented

by the operator $P = \tau_y \otimes \sigma_y K$ where τ_y is a Pauli matrix in electron-hole space and K is the complex conjugation, acting on the Hamiltonian as

$$PH_{BdG}P^\dagger = -H_{BdG}. \tag{4.14}$$

This implies that for every state with energy E_i with associated creation operator $\psi_i^\dagger$ there is a corresponding one with energy $-E_j$ whose operator is $\psi_j^\dagger = \psi_i$. This means that if a Majorana quasi-particle obeying the relation $\gamma_0 = \psi_i = \psi_i^\dagger$ exists, it has to be a zero-energy excitation, and it can only appear in pair with another zero-energy Majorana mode. However, if the system's Hamiltonian is also invariant under time-reversal symmetry, these two Majoranas are one the Kramer partner of the other. This in turn means that they have the same probability density, leading to a splitting of the zero-energy level [311]. The addition of the magnetic field B is then fundamental to break this symmetry if we want to create spatially isolated Majoranas.

We can now intuitively understand how the different terms in the Hamiltonian contribute to the physics of the Kitaev chain, starting from the parabolic dispersion of free electrons: (1) adding the Zeeman term B breaks the spin degeneracy necessary to have a spinless model; (2) the chemical potential μ can be used to set the Fermi energy in the middle of the two resulting bands; (3) the spin-orbit coupling α makes the spin in the lower band momentum-dependent, and (4) the proximity-induced s-wave superconducting term Δ pairs the two electrons at spin k and $-k$. We can then project the system on the two inner bands to obtain an effective Kitaev chain [139]. When the gap closes at $k = 0$, by changing one of these parameters, we can expect a quantum phase transition, whose topological nature can be confirmed by computing the Pfaffian invariant of the bands in the two phases, leading to the topological criterion

$$B^2 > \mu^2 + \Delta^2. \tag{4.15}$$

In the topological phase, for open boundary conditions, the system supports two localized Majorana Zero Modes on the boundaries.

To obtain the expectation value of the observables on the ground state of the system we can remember that H_{BdG} can be diagonalized in a basis of Bogoliubov quasiparticles $(\gamma_{1i}^\dagger, \gamma_{2i}^\dagger, \gamma_{2i}, \gamma_{1i})$

$$H = \sum_i E_{1i}\gamma_{1i}^\dagger\gamma_{1i} + E_{2i}\gamma_{2i}^\dagger\gamma_{2i} - E_{1i}\gamma_{1i}\gamma_{1i}^\dagger - E_{2i}\gamma_{2i}\gamma_{2i}^\dagger \tag{4.16}$$

where $i = 1, \dots, N$. Here the two different species of Bogoliubov quasiparticles γ_1, γ_2 appear because of the 4-band structure of H_{BdG}. The Hamiltonian is diagonalized by a matrix U, such that

$$U^\dagger H U = \text{diag}\{-E_1, -E_2, E_2, E_1\},\ (c_{i\uparrow}, c_{i\downarrow}, c_{i\downarrow}^\dagger, -c_{i\uparrow}^\dagger)^T = U(\gamma_{1j}^\dagger, \gamma_{2j}^\dagger, \gamma_{2,N-j-1}, \gamma_{1,N-j-1})^T. \tag{4.17}$$

As the ground state of the system is defined as the state annihilated by all γ operators, we can write the expectation value of any fermionic operator by expressing it in terms of the γs and using the appropriate commutation relations. For example, the position operator (that will be useful in the following) can be computed as

$$\langle GS|x|GS\rangle = \langle GS|\sum_i i(c_{i\uparrow}^\dagger c_{i\uparrow} + c_{i\downarrow}^\dagger c_{i\downarrow})|GS\rangle = \sum_{ij}^{2N} iU_{ij}^2. \tag{4.18}$$

The observables of a time evolved state can then be retrieved by evolving the eigenvectors U of the H_{BdG} and computing the quantity as in (4.18).

4.2.2 Coupling of the nanowire with an EM pulse

We now explain how we chose the incoming electromagnetic pulse $A(t)$ for the purpose of simulating the HHG process. For convenience, we choose units of $A(t)$ such that the coupling constant $ea/\hbar$, with a the unit cell size, is 1. The time-dependence of the vector potential is of the form

$$A(t) = A_0 \sin(\omega t) \sin^2\left(\frac{\omega t}{2n_c}\right) - \varepsilon_c t, \quad 0 \leq t \leq 2\pi n_c/\omega \tag{4.19}$$

describing a pulse of n_c cycles with frequency ω, and a constant electric field with ε_c, explicitly breaking time inversion symmetry in the system, such that both even and odd harmonics of the driving frequency can be generated [312]. Measuring energies in units of J, we choose $\omega = 0.0025$, such that it corresponds roughly to $1/50$ of the bandgap of the system. Specifically, to be able to discern the superconducting phase from a metallic one, the driving frequency needs to be sufficiently smaller than the bandgap. The symmetry-breaking DC field is very weak, $\varepsilon_c = 10^{-5}$, whereas the amplitude of the vector potential has to be strong enough to produce high harmonics and is taken to be $A_0 = 1.2$, which for $a = 0.5$ nm corresponds to 1.6×10^{-6} Vs/m.

We note that our treatment makes the assumption that the light field only couples to the electrons of the semiconducting wire, whereas the pairing Δ from the surrounding superconductor is taken as a static parameter. This assumption is only justified if the superconductor is shielded from the incoming light.

For the static Hamiltonian at $t = 0$, the topological phase appears for $B > \sqrt{\Delta^2 + \mu^2}$ [311]. For lower values of B, the system is in a trivial gapped superconducting state with no topological edge modes. Although in realistic semiconductor/superconductor heterostructures, the energy scales J, α, Δ widely differ, in the following we choose them to be of the same order of magnitude (specifically, $\alpha = \Delta = 3/4$). The reason for this choice is to achieve clear Majorana modes for system sizes that are sufficiently small to numerically perform simulations of the full dynamics. In particular, the parameters were tuned according to the prescription from Alicea [140] in order to assure the presence of a topological phase. For the purpose of detecting MZM from the high harmonic spectrum, it is important that the ratio between the bandgap (usually of the order of Δ) and the frequency ω of the incoming pulse is much larger than 1. For InAs nanowires, the bandgap is on the order of 1 meV (with $J \sim 3000$ meV, $\alpha \sim 25$ meV, $\Delta \sim B \sim \mu \sim 1$ meV, see for example [284]), but also much larger gaps have been reported, of 4 meV for β-Bi_2Pd films [313], or even 15 meV for iron-based superconductors [314]. Depending on the size of the gap, our scheme requires strong microwave to THz sources [292], with pulse duration on the order of 1-100 ps, which is potentially much shorter than typical relaxation time scales.

4.3 Analysis of the High Harmonic Spectrum

The key quantity that captures the non-linear optical response of the system is the transmitted HHG spectrum, that is, the normalized spectrum of emission obtained

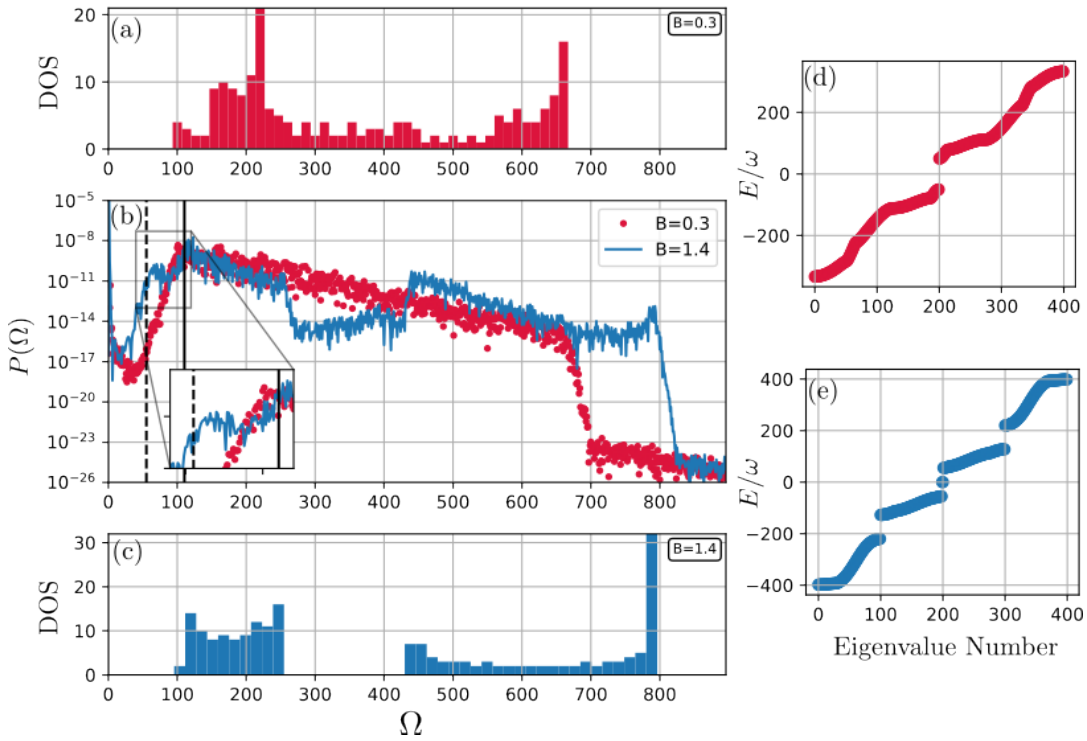

FIGURE 4.3: Comparison of the emitted power spectra deep in the topological ($B = 1.4$) and trivial phases ($B = 0.3$) for a spatially uniform field and $\mu = 0$. The emission spectra shown in (b) follow the density of state of the Hamiltonian at time $t = 0$ both in (a) the trivial and (c) topological phases. For the topological phase, an emission below the bandgap of the system (zoomed inset in (b)) can be related to the presence of zero energy edge states. The density of states can be compared with the band structure in the trivial (d) and topological (e) phases. Simulations performed by using parameters $N = 100$, $\omega = 0.0025$, $j = -0.3$, $\alpha = \Delta = 0.4$, $A_0 = 1.2$.

from the time-dependent dipole moment of the chain $x(t)$:

$$P(\Omega) \propto |\int \mathrm{d}t e^{-i\Omega t}\langle \dot{x}\rangle|^2/P_0, \tag{4.20}$$

where Ω is the frequency of the re-emitted light in terms of the driving frequency ω, and $P_0 = \max|\int \mathrm{d}t e^{-i\Omega t}[\partial_t A(t)]|^2$ is the maximum of the spectrum of the free incoming field, set to $P_0 \sim 1.3 \cdot 10^{10}\ \mathrm{V}^2/\mathrm{m}^2$ with our choice of parameters [315]. Here, the time derivative of the average dipole moment $e\langle x(t)\rangle$ yields the electric current, which is Fourier transformed into the frequency domain. The dipole moment was computed by numerically integrating the time-dependent Schrödinger equation (TDSE) from the initial ground state of the Hamiltonian up to a time $T = 2\pi n_c/\omega$, using Exact Diagonalization techniques.

By analyzing this quantity, we recovered several signatures of the presence of topological edge states: a density of states compatible with the presence of zero modes, a half-bandgap emission only with light focused on the edges, and a robustness to perturbations that do not close the gap. We will now show these results in detail.

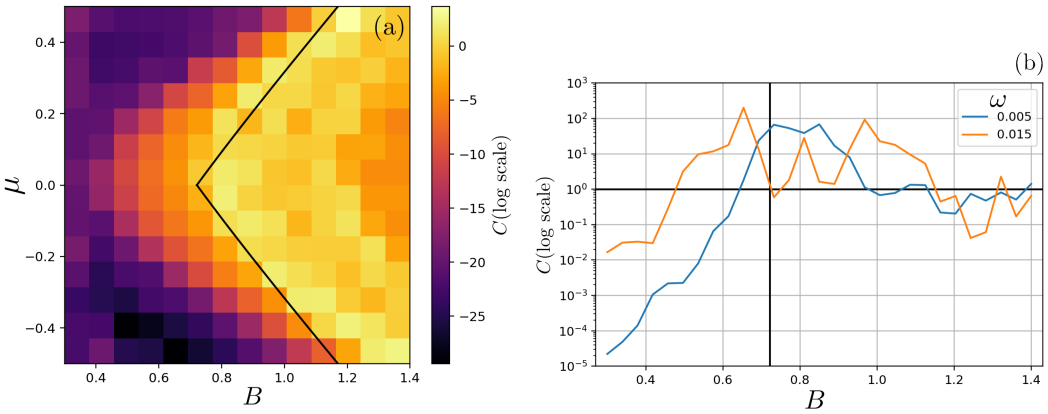

FIGURE 4.4: Contrast C as a function of magnetic field and chemical potential. In the topological phase $C \sim 1$, while in the trivial one $C \sim 0$. The black line represents the phase separation boundary for a system in the thermodynamic limit. Simulations performed by using parameters $N = 100$, $\omega = 0.0025, j = -0.3, \alpha = \Delta = 0.4, A_0 = 1.2$. (b) Contrast order parameter as a function of magnetic field (at $\mu = 0$) for two values of the driving frequency. For the smaller frequency, the order parameter is peaked at the phase boundary (indicated by the vertical black line), and quickly drops below 1 (indicated by the horizontal black line) in the trivial phase. For the larger frequency, the distinction between the phases is less sharp, and the order parameter over-estimates the topological regime.

4.3.1 Band structure and density of states

In Figure 4.3(b) we plot the emission spectrum, obtained from Eq. (4.20), as a function of the frequency of the emission in units of the driving frequency ω. We consider two points in parameter space, one deep in the trivial phase at $B = 0.3$, and the other one in the topological one at $B = 1.4$. Interestingly, we observe that, in both cases, the spectrum echoes the band structure of the Bogoliubov Hamiltonian, plotted in Figure 4.3(d) and (e), with two or four bands symmetric around the Fermi energy due to particle-hole symmetry [140]. In particular, the density of states in the two phases, shown in Figure 4.3(a) and (c), clearly determines the emission. In particular, there is no emission above the bandwidth and below the bandgap (defined as the difference between the highest valence band and the lowest conduction band excluding edge modes) in the trivial phase. In stark contrast, in the topological phase, the radiation plateau starts from half-bandgap, which is related to the presence of radiating edge modes at zero energy.

This confirms the applicability of the three-step interpretation. In particular, the harmonics with a frequency above the bandgap are due to the interband transitions, the ones between half of the bandgap and the bandgap are due to the presence of zero-energy edge states, and the ones below are caused by intraband motion (Bloch oscillations). This is already a clear signature of a topological phase for the right choice of parameters.

4.3.2 Phase Diagram

We now propose a measurable diagnostic, called contrast, defined as the ratio between the emission at half the bandgap P_{half} over the emission at the bandgap P_{gap},

$$C = \frac{\log(P_{\text{half}})}{\log(P_{\text{gap}})}, \tag{4.21}$$

which is of order one in the topological phase and zero in the trivial phase. The choice of this quantity is dictated by the different behavior of the emission at these special points in the two phases. The bandgap is defined as the minimum energy difference between the valence and the conduction band, thus the minimum frequency at which emission can be produced by interband transitions in the trivial phase. The half-bandgap emission P_{half} instead is due to the presence of the zero-energy state, and is supposed to be present only in the topological phase, when it is of the order of P_{gap}. The contrast is then a measure of the presence of these zero-energy states.

The topological phase diagram of the system is computed in Figure 4.4 in the $\mu - B$ plane using the proposed signature. Exactly at the boundary where the gap closes the system behaves as a metal, resulting in a contrast greater than one. The choice of the frequency of the incident light pulse is crucial to localizing the phase boundary, as a lower frequency provides a sharper criterion for distinguishing topological and trivial phases. From this point of view, choosing a small driving frequency is favorable, as long as the pulse remains short compared to relaxation times. As the system approaches the transition the gap closes and when the driving frequency ω is of the order of the bandgap $\sim \Delta$ the response of the system becomes metallic. In this regime, the contrast order parameter is higher than 1 and generally not stable as shown in Figure 4.4(b), where the bandgap deep in the trivial phase is $\sim \Delta = 0.4$. Therefore, a better resolution for detecting the phase transition is obtained when a lower driving frequency is chosen.

4.3.3 Identification of edge states

So far, the devised scheme distinguishes between topological and trivial phases by measuring the full bandstructure of the system, but yet it does not capture one of the most relevant properties of the MZMs: their localization at the edge and topological protection. However, with the spatial resolution of the radiation being limited only by the wavelength, it becomes possible to demonstrate that the sub-bandgap emission is due to edge modes by focusing the electromagnetic field either on the edge or the bulk of the sample. In Figure 4.5, we show how in the trivial phase the emitted spectrum is qualitatively the same for a pulse focused on the edge or on the bulk. On the other hand, in the topological phase there is a strong sub-bandgap emission, but only if the light is focused on the edge. This shows that this contribution to the emission spectrum is solely due to edge states. We have used a Gaussian envelope, cut in half for the edge radiation, and the amplitude of the envelopes is normalized in order to have the same total energy of the electromagnetic field for all cases (edge, bulk, and uniform field).

Finally, to illustrate the topological nature of the edge modes, we add a local perturbation to the system that does not break the particle-hole symmetry of the Hamiltonian. Such local potentials (acting on three sites on the left and right edges) can be added by applying gate voltages at the edges and are modeled by adding a local potential term to the Hamiltonian $\propto \sum_{i,\sigma} c^\dagger_{i\sigma} c_{i\sigma}$ for $i = 1, 2, 3, N-2, N-1, N$. We observe that increasing the value of this potential does not affect the shape of the

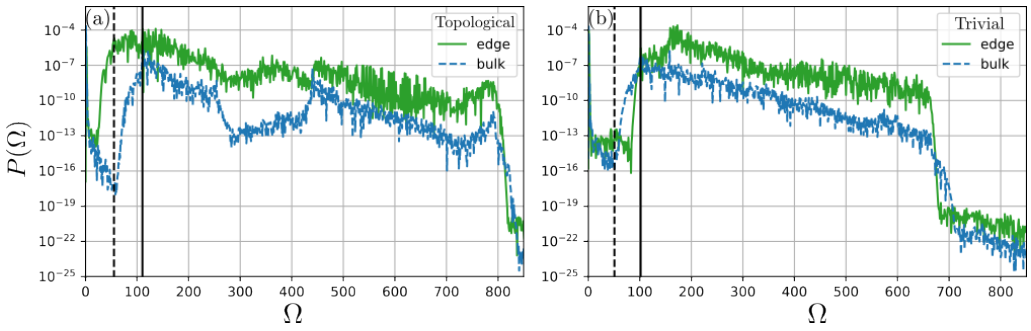

FIGURE 4.5: Emission for a pulse focused on the edge or on the bulk of the sample in the topological (a) and trivial (b) phases. The spacial envelope is normalized to have constant energy of the EM field. In the topological phase, the spectra differ depending on where the pulse is focused, showing emission from sub-band-gap states only when it is focused on the edge. This is not the case, however, in the trivial phase, where both spectra are qualitatively similar. Simulations performed by using parameters $N = 100$, $\omega = 0.0025$, $j = -0.3$, $\alpha = \Delta = 0.4$, $A_0 = 1.2$.

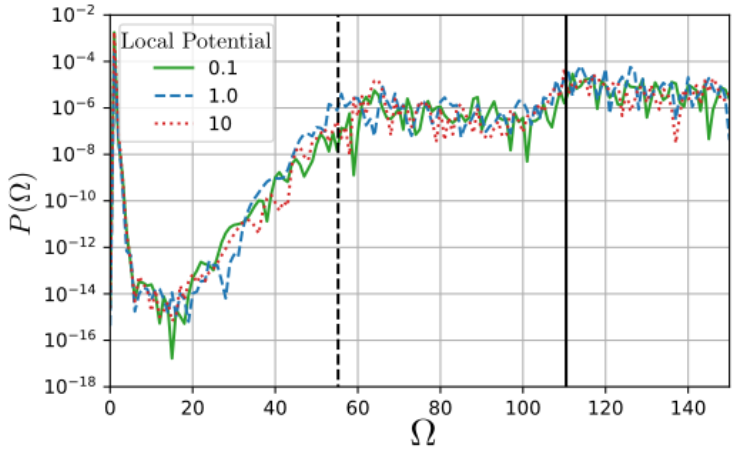

FIGURE 4.6: Emission spectra with the addition of a local potential on the edges of the chain (in units of J). The local potential acts on the first and last 3 sites and does not break the symmetry responsible for the topological protection. The qualitative behavior of the emission of the edge states does not change with an increasing value of this potential. The black lines indicate half bandgap and the bandgap in order of the driving frequency. Simulations performed by using parameters $N = 100$, $\omega = 0.0025$, $j = -0.3$, $\alpha = \Delta = 0.4$, $A_0 = 1.2$.

emission spectrum. Specifically, the sub-bandgap edge state emission only appears in the topological phase and remains present precisely between half bandgap and the bandgap, as can be seen in Figure 4.6. The different curves in this figure, corresponding to different edge potentials, lie on top of each other for lower harmonics (until the bandgap of the system), indicating that the edge modes do not shift in energy upon the application of edge potentials, clearly demonstrating the topological robustness of the radiating edge modes.

4.4 Summary

In this Chapter, we presented a protocol to detect topological edge modes in an experimentally realizable platform reproducing the Kitaev chain model. This detection was performed via the electromagnetic emission spectrum in the non-linear regime. In this way, we were able to map the band structure and the density of states of the system. We also proposed an experimentally observable quantity, the contrast, in order to map the phase diagram of the system. To confirm the topological nature of the radiating modes, we showed that the system can be probed locally to see what portions of it are responsible for the sub-bandgap emission. The emission spectrum is also shown to be robust under local perturbations that do not break the symmetry protecting the topological phase. Thus, our protocol complements other established methods in the search of MZMs. Moreover, the reconstruction of the bandstructure from HHG has been successfully used in recent years to study topology in SSH systems [307], and properties of quasi-crystals [316].

A major experimental challenge for the detection of MZMs is to distinguish them from trivial sub-bandgap states that can appear in the material, that is, Andreev bound states [317–320]. These states can appear because of regions in the semiconducting chain where the proximity-induced superconductivity fails (i.e. near the edges), creating zones of normal metal where scattering effects can lead to the creation of localized states [288]. A straightforward extension of these results is the use of a spatially dependent superconducting order parameter to study the formation of these states and their influence on the emission spectrum. Another interesting application of our technique is the study of Majorana physics in two dimensions, where MZMs can arise as vortices in p-wave superconductors [100]. Compared to 1D models, the dependence of the emission spectrum on the field polarization states will make the two-dimensional scenario very rich. Recent studies have shown that left-right polarized drives can shed light on the presence of topological chiral states [232, 321], both in the perturbative and ultra-strong regime [303, 304], but a study of the effect on Majoranas is still missing. Finally, a possible application of this technique would be in the framework of quantum simulation with ultracold atoms, where the possibility to engineer dynamics similar to the one described in this Chapter has been recently proposed [322].

Part III

Frustration and Deconfined Quantum criticality

Chapter 5

Frustration and Deconfined Quantum Criticality

In physics, the concept of *frustration* describes situations where competing constraints prevent a system to minimize the energy for all its microscopic constituents. Imagine for example three classical, antiferromagnetic spins on a triangular plaquette: whatever the choice of the three spins, they can never minimize their mutual interaction energy. This is an example of *geometrical frustration*, where the competition is between the interactions and the geometry of the system. Frustration can also be driven by competing interaction terms or different ways in which the particles can minimize their kinetic energy. This leads to a large ground state degeneracy and an impossibility to develop order up to very low temperatures [14].

In many-body quantum systems, geometrical frustration leads to the onset of a plethora of exotic quantum phases, including the ones studied in the previous chapters [323, 324]. Paradigmatic examples are different topological insulators [78, 325–327] and superconductors [328, 329], spin liquids [14, 94, 330], and valence bond solids [12, 331, 332]. Nevertheless, because of the complexity generated by competing interactions, frustration, and quantum fluctuations, several scenarios are still poorly understood. In particular, numerical efforts are highly demanding and often affected by finite size effects [333]. At the same time, possible sample imperfections and limited detection probes narrow the efficiency of solid-state experimental platforms [334, 335].

The tunability and control offered by quantum simulation experiments based on ultracold atoms in optical lattices [336] provide a promising alternative for understanding the behavior of a large variety of physical systems [185]. However, theoretical proposals to engineer ultracold frustrated synthetic materials are mainly based on direct implementations of specific geometries [116, 337–340] and alternative approaches are scarce [341–343]. Moreover, experimental realizations of frustrated quantum systems relying on optical lattice engineering successfully achieved weakly interacting [326, 344–346], classical [117, 347, 348] or kinetically frustrated [108, 109, 349–351] regimes. Noticeably, these experiments investigated configurations with purely local couplings, while realizations of geometrically frustrated systems with beyond-contact interactions have not yet been achieved.

Interactions with an extended range are a key ingredient to create spontaneous-symmetry-broken (SSB) states of matter with broken translational symmetry. The occurrence of these phases in various physical systems [352–354] has sparked significant experimental interest leading to their observation in atomic frustration-free atom-cavity [355, 356] setups, continuum- [357–359] and lattice-dipolar [360] systems, as well as in out-of-equilibrium configurations [361, 362]. While Rydberg

atoms in optical tweezer arrays allow engineering long-range couplings also in frustrated geometries [51, 363] and polar molecules in optical lattices represent a promising platform in this direction [364], their effectiveness remains limited to the study of spin-1/2 systems. In this respect, proposals to investigate Hamiltonians with an enlarged Hilbert space, where beyond-contact repulsion and geometric frustration strongly compete are absent.

The interplay between quantum frustration and longer-range interactions can also give rise to deconfined quantum critical point (DQCP) [**senthil2023a**, 121, 168]. Because of their deep quantum nature combined with possible exotic properties like fractional excitations and emergent gauge fields, an exceptional theoretical effort has unveiled the presence of DQCPs in a large variety of 2D spin [365–376] and fermionic [377–380] models as well as in 3D [381, 382], 1D [**roberts2019a**, 173, 174, 383–385], and 0D [386] two-level systems. Moreover, unique evidence of their possible existence has been provided in recent solid-state experiments [387–390].

In this chapter, based on the results obtained in [IV] and [V], we study the physics of frustration-induced phases and phase transitions in paradigmatic one-dimensional models of interacting bosons and fermions, that we will briefly review in Section 5.1. To do so we study the ground state of systems using VUMPS techniques [64, 201, 391]. In this way we work directly in the thermodynamic limit, to better identify lowest-energy states in phase diagrams with several symmetry broken phases.

For bosons [IV], we show in Section 5.2 that it is possible to stabilize a dimerized Bond Order Wave (BOW) and a time-reversal symmetry broken Chiral Superfluid (CSF) phase when introducing frustrated nearest-neighbor hoppings in a triangular ladder geometry. Remarkably, in the presence of only local repulsion we recover the phases predicted to occur in frustrated triangular quantum magnets [392–397]. Furthermore, we show that in the presence of beyond-contact interaction a phase transition between the BOW and a Density Wave (DW) appears, showing the properties of a Deconfined Quantum Critical point. Finally, we propose an experimental implementation with ultracold Cesium atoms in an optical lattice that allows to engineer the desired Hamiltonian. For this latter point, we describe how the relevant requirements (namely frustration, extended interactions, and efficient readout techniques) can be efficiently implemented, overcoming pitfalls that make it non-trivial to insert frustration in such platforms [116, 117].

For the fermionic case instead [V], we focus in Section 5.3 on the one dimensional Fermi Hubbard model with extended interactions. While this model with only contact interactions can be solved analytically [398], longer-range interactions introduce new phases that have been the object of intense theoretical [399–401] and experimental investigation in cold-atoms systems [402–404]. In this case, the competition between contact and nearest-neighbor interactions, gives rise to a dimerized Bond Order Wave (BOW) and a Charge Density Wave. Here, we revisit its phase diagram and show that the second order transitions connecting the BOW and the CDW can either be first order or deconfined depending on the strength of the contact potential. Moreover, when adding a magnetic spin-spin coupling, a new symmetry broken phase Antiferromagnetic (AF) phase opens up. We show that the transition between the BOW and the AF spontaneously broken phases also shows the properties of a DQCP. A bosonization analysis confirming these results is presented in Appendix C.

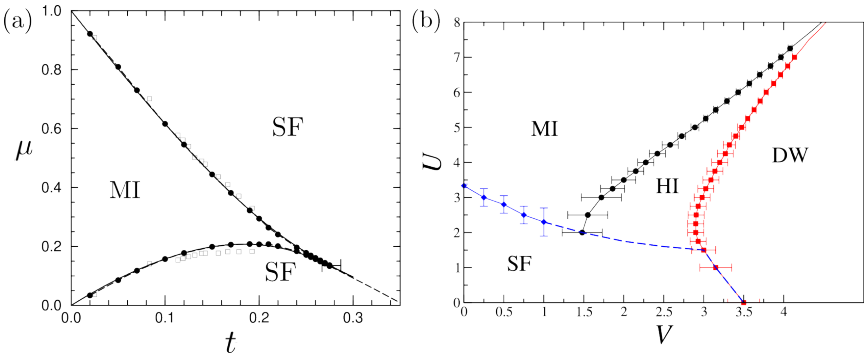

FIGURE 5.1: Phase diagram of the 1D Bose-Hubbard model. (a) $V = 0$; It is possible to observe a transition between a Mott Insulator (MI) and a superfluid (SF). Image taken from [405] (b) $V \neq 0$, at half-filling. In this case a Density wave (DW) and a topological Haldane Insulator (HI) phase appear. Image taken from [406]

5.1 The 1D Hubbard model

In this section we will describe the physics of the one-dimensional Hubbard model, either bosonic or fermionic. After giving a general overview of their phases in the simplest case of contact interaction, we will show how the introduction of extended interactions can lead to the appearance of a much richer phase diagram.

5.1.1 Bosons

As we introduced in Chapter 1, the Bose-Hubbard model [407] describes bosons hopping on a lattice, interacting between each other through a contact potential. Although it is not naturally realized in nature[1], it is particularly relevant for the physics of neutral atoms trapped in an optical lattice [33], in the limit of strong localization of the atoms on lattice sites (tight binding). It is then a fundamental building block in the design of quantum simulators. The minimal Hamiltonian for the model in a general dimensionality, in the grand-canonical ensemble is

$$H_{BH} = -\sum_{i,j\in\Lambda} t_{ij} b_i^\dagger b_j + U\sum_i n_i(n_i-1) - \mu\sum_i n_i, \tag{5.1}$$

where Λ is a lattice composed of M sites, t_{ij} is the hopping amplitude between sites i and j, U is the on-site interaction, and μ is the chemical potential. The operators $b_i^\dagger$ are the creation operators on site i, and $n_i = b_i^\dagger b_i$ is the number operator. In the case of a homogeneous lattice, as the one produced by counter-propagating lasers, the hopping amplitude can be set to be uniform $t_{ij} = t$.

To have an intuitive view of the physics of this model, it is instructive to consider the two extreme limits of strong and weak interactions. This in turn will give us an idea of the phases of the system.

Weak coupling: Superfluid

In the weak coupling limit $U/t \ll 1$, the system is well described by the non-interacting Hamiltonian. In this case, the Hamiltonian can be diagonalized in momentum basis, and the bosons are allowed to condense in the lowest-momentum

[1] It however models systems like arrays of Josephson junctions, were the Cooper pairs can be considered bosons

eigenstate

$$|g\rangle_{SF} = \prod_N b^\dagger_{k=0}|0\rangle, \tag{5.2}$$

where $|0\rangle$ is the vacuum state and N is the number of bosons in the system. As we are working in the grand-canonical ensemble, the number of bosons is fixed only on average $\langle n_i\rangle = N/M$ and the state is better expressed as a superposition of all the possible states at fixed N, or as a coherent state

$$|g\rangle_{SF} = \prod_i e^{\sqrt{\nu} b_i^\dagger}|0\rangle, \tag{5.3}$$

where we exploited the relation $b^\dagger_{k=0} = \sum_i b_i^\dagger$. Here $\nu = N/M$ is the *filling* of the system. This state is completely delocalized in real space; however, it is interesting to note that it can be expressed as a product state in position space.

This picture holds for a finite value of the interactions U as can be seen from mean field theory. In this case, we say that the system is in the *superfluid* phase. The mean field construction is only exact for infinite dimensions [408] and reasonable for dimensions down to 2, but this behavior can be numerically retrieved also in one dimension.

This phase is associated to a spontaneous breaking of the $U(1)$ charge conservation symmetry, and it is associated to an order parameter

$$\psi = \langle b_i\rangle \sim \sqrt{\nu} e^{\imath\theta}, \tag{5.4}$$

where we explicitly wrote the superfluid order parameter in terms of the density ν and a phase θ. The superfluid phase is gapless, with phase fluctuations as the associated Goldstone modes of the spontaneously broken symmetry. It also possesses gapped amplitude excitations, corresponding to the Higgs modes of the model.

Strong coupling: Mott insulator

In the other extreme limit $U/t \gg 1$, the sites of the lattice are decoupled and the Hamiltonian can be diagonalized in a basis of the local number operator n_i

$$H = \sum_i \left[-\mu n_i + \frac{U}{2} n_i(n_i - 1) \right]. \tag{5.5}$$

This in turn means that the ground state is also a product state in position space, with a fixed number of particles per site

$$n_i|g\rangle_{MI} = n|g\rangle_{MI}. \tag{5.6}$$

The value of n, however, depends on the ratio μ/U: as the chemical potential is increased it is energetically favorable to insert more particles in the system; on the other hand, the on-site interaction U penalizes the presence of more than one particle per site. Turns out that $|g\rangle_{MI}$ contains n particles if

$$(n-1) < \frac{\mu}{U} < n. \tag{5.7}$$

This phase is called *Mott insulator*. It is a gapped and incompressible phase, as $\partial\langle n\rangle/\partial\mu =$, and it does not break any symmetry. In correspondence of the points where a new particle gets added to the system $\mu/N \in \mathbf{N}$, the gap closes, and the

system is superfluid even for $t = 0$. The Mott phase extends for intermediate values of U/t in the so-called Mott lobes.

Phase diagram

The phase diagram of the Bose-Hubbard model for various spatial dimension is shown in Fig. 5.1(a). In one dimension, our case of interest, the spontaneous breaking of the $U(1)$ symmetry leading to the superfluid phase is forbidden by the Mermin-Wagner theorem [409]. However, a superfluid phase is still present separated from the Mott side by a Kosterlitz-Thouless transition (BKT) [405]. In this case, while the order parameter $\langle b_i \rangle \equiv 0$, the ordered phase can be detected by the presence of quasi-long range order in the superfluid correlator

$$g^1(|i-j|) = \langle b_i^\dagger b_j \rangle. \tag{5.8}$$

This correlator is expected to decay exponentially in the disordered phase and algebraically in the ordered one.

Extended Interactions

If we add nearest-neighbor interactions to the 1D system, the phase diagram shows several new interesting phases. This can be achieved by introducing in the Hamiltonian 5.1 the term

$$H_V = V \sum_i n_i n_{i+1}. \tag{5.9}$$

Intuitively, for strong values of V the system will tend to avoid inserting particles in neighboring sites, forming instead a *density wave* (DW). However, for intermediate couplings, a more interesting phase can appear, characterized by a gap and a topological invariant. This is called *Haldane phase* in parallel to the Haldane phase of the spin models, and is an SPT phase. As in the case of spins it can be detected by the long-range behavior of an approximate string order parameter [406]

$$\mathcal{O}_s = \lim_{|i-j|\to\infty} \langle \delta n_i e^{t \sum_{k=i+1}^{j} \delta n_k} \delta n_j \rangle, \tag{5.10}$$

where $\delta n_i = n_i - \nu$ is the fluctuations from the average density. The topological nature of the Haldane insulating phase has also been confirmed by the presence of edge states in the open boundary system [410]. In Fig. 5.1(b) we show the phase diagram of the model for filling $\nu = 1$ as a function of V/U and t/U.

5.1.2 Fermions

The phenomenology of the fermionic Hubbard model is drastically different from the bosonic case. Here we will focus on the physics of the 1D model, leaving the discussion of the 2D model to Chapter 6. The Hamiltonian is

$$H_{FH} = -\sum_{i,j\in\Lambda,\sigma} t_{ij} c_{i,\sigma}^\dagger c_{j,\sigma} + U \sum_i \hat{n}_{i,\uparrow} \hat{n}_{i,\downarrow}, \tag{5.11}$$

where $c_{i,\sigma}^\dagger$ is the creation operator of a fermion with spin σ on site i and U is the on-site interaction. In this case, the Pauli exclusion principle forbids the presence of more than two fermions per site. It is then more suitable to work in the canonical ensemble at fixed filling $\nu = N/M$.

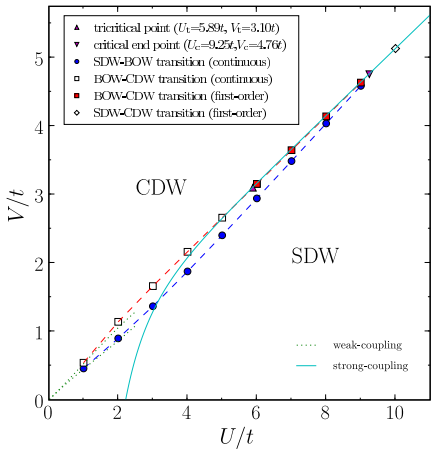

FIGURE 5.2: Phase diagram of the extended 1D Hubbard model as a function of U/t and ν. A small Bond Order Wave (BOW) region appear between the Charge Density Wave (CDW) and the Haldane insulator (or Spin Density Wave, SDW). Image taken from [400]

Remarkably, this model can be solved exactly at half-filling $\nu = 1$[2][398] via the *Bethe ansatz*. In particular, the case of $U/t > 0$ is a Mott insulator characterized by gapped charge excitations and gapless spin excitations. For this reason this phase is also sometimes called *Spin Density Wave* (SDW). On the other hand, for $U/t < 0$ the system is a *Luther-Emery* liquid (LL), with gapped spin excitations and gapless charge ones. For the case $U = 0$ the system stays in a *Luttinger Liquid* phase, characterized by spin-charge separation [177, 411]. In all of these cases, in accordance with the Mermin-Wagner theorem, the symmetries of the Hamiltonian are unbroken, and the different phases can be classified by their gaps in different sectors and non-local order parameters.

Extended interactions

As for the bosonic case, adding extended interactions can lead to the appearance of new phases. In particular, the addition of nearest-neighbor repulsion V of the form

$$H_V = V \sum_{i\sigma} n_{i\sigma} n_{i+1,\sigma}, \tag{5.12}$$

makes it possibly to have phases with spontaneous symmetry breaking. In this case, for strong V the particles will tend to avoid sitting on neighboring sites, forming a *charge density wave* (CDW). For intermediate values of V however, a *bond order wave* (BOW) phase can appear, characterized by a dimerization of the lattice [400]. This phase, in turn, can be shown to possess topological properties [412]. The phase diagram of the extended Hubbard model is shown in Fig. 5.2.

5.2 Frustrated Extended Bose-Hubbard model

We will move on to the discussion of the results of [IV]. In this first section, we will explain how adding geometrical frustration to the Extended Bose-Hubbard model leads to the appearance of new phases. In particular, by engineering an effective

[2]For fermions, the fact that each momentum or position state can accommodate two spins means that a fully filled band has $\nu = 2$

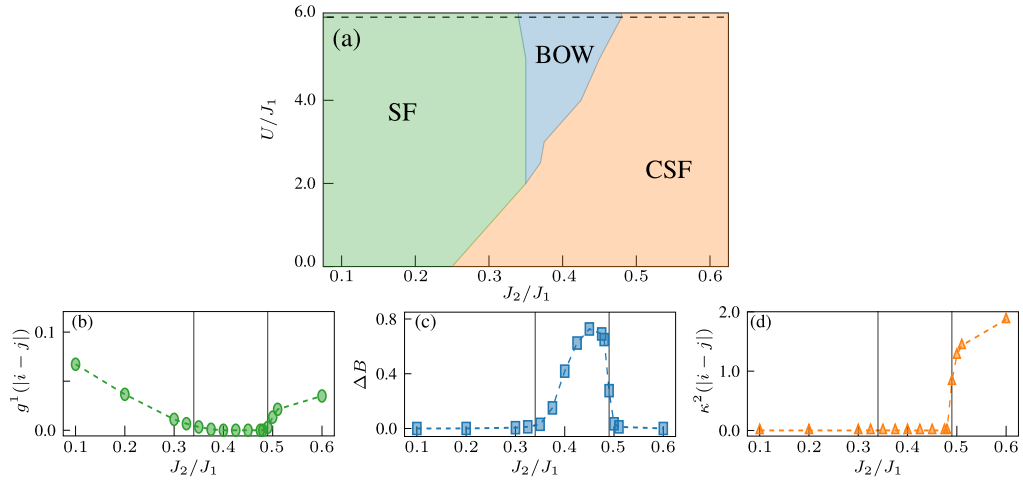

FIGURE 5.3: (a) Phase diagram of H_{FEBH} Eq. (5.13) as a function of J_2/J_1 and U/J_1, showing the superfluid (SF), bond-order-wave (BOW) and chiral superfluid (CSF) phases; (b) superfluid correlator $g^1(|i-j|)$ for $|i-j|=100$; (c) bond-order-wave order parameter ΔB; (d) chiral superfluid correlator $\kappa^2(|i-j|)$ for $|i-j|=100$; The vertical continuous lines in (b)-(d) are the estimated transition points for $U/J_1=6$ [dashed line in (a)]. All the figures refer to the configuration where the total density $\bar{n}=0.5$ and the nearest-neighbor repulsion $V=0$. The VUMPS simulation have been performed by using a bond dimension χ=400

triangular geometry, we will be able to find a phase reminiscent of a Valence Bond Solid (the Bond Order Wave), a chiral superfluid, a Density Wave and, strikingly, evidence of Deconfined Quantum Criticality. The Hamiltonian under study is

$$H_{\text{FEBH}} = -\sum_j \left[J_2(a_j^\dagger a_{j+2} + h.c.) + J_1(-1)^j(a_j^\dagger a_{j+1} + h.c.)\right] + \frac{U}{2}\sum_j n_j(n_j-1) + V\sum_j n_j n_{j+1}, \tag{5.13}$$

with $J_1, J_2 > 0$. We will study this model at half-filling $\nu = 1/2$. As shown in Fig. 5.6 (b), Eq. (5.13) describes a frustrated extended Bose-Hubbard model in a triangular ladder, where the staggered nature of J_1 gives rise to the effective geometrical frustration, U accounts for the contact interactions and V for the nearest-neighbor ones. Although various versions and regimes of similar models have been theoretically studied [410, 413–420], we focus on the previously not approached cases of staggered nearest-neighbor tunneling both with and without nearest-neighbor interactions.

5.2.1 Phase diagram for $V = 0$

We start by studying the phase diagram of the Hamiltonian described in Eq. (5.13) for finite values of U and $V = 0$, in order to see onset of the physics induced by geometrical frustration. We do so by means of VUMPS simulations [391, 421], varying the parameters U/J_1 and J_2/J_1. As already mentioned in Sec. 2.2.5, this method allows to study the ground state properties of the 1D system directly in the thermodynamic to avoid boundary effects that can interfere in the localization of the phases.

As shown in Fig. 5.3(a), in the regime $V = 0$, H_{FEBH} hosts three different phases. For weak frustration, meaning for small J_2/J_1, we detect a gapless superfluid (SF),

captured by the quasi long-range-order (LRO) of the correlator defined as

$$g^1(|i-j|) = \langle b_i^\dagger b_j \rangle, \tag{5.14}$$

see Fig. 5.3(b).

On the other hand, $g^1(|i-j|)$ vanishes exponentially for strong enough U and larger J_2/J_1. This behavior signals the appearance of a gapped phase [177] which, as shown in Fig. 5.3(c), is characterized by a finite value of the local order parameter[3]

$$\Delta B = \frac{1}{L}\sum_j \langle B_j + B_{j+1} \rangle, \tag{5.15}$$

where

$$B_j = (b_j^\dagger b_{j+1} + b_{j+1}^\dagger b_j). \tag{5.16}$$

Specifically, $\Delta B \neq 0$ demonstrates the presence of a BOW phase with broken site-inversion symmetry similar to the one we introduced for the Fermi-Hubbard model. This lattice dimerization bears a striking resemblance to the Peierls instability [136], like the one responsible for the onset of dimerization in the SSH model. In particular, while in real materials the effective dimerization is generated by the electron-phonon coupling, here it is induced by the combination of finite interaction, quantum fluctuation and geometrical frustration. These BOW phases are potentially SPTs, as recently discovered in 1D [412] and 2D [422] systems.

In the strongly frustrated regime of large J_2/J_1, the BOW gives way to a new gapless state where $g^1(|i-j|)$ exhibits quasi LRO. The findings in Fig. 5.3(d) illustrate that this regime can be classified as a CSF captured by the LRO of the correlator defined as

$$\kappa^2(|i-j|) = \langle \kappa_i \kappa_j \rangle, \tag{5.17}$$

where

$$\kappa_j = -\frac{\imath}{2}(b_j^\dagger b_{j+1} - b_{j+1}^\dagger b_j) \tag{5.18}$$

is the vector chiral order parameter [415, 416]. This point shows this CSF to be characterized by alternated finite currents between nearest-neighbor sites, thus resembling an effective vortex-antivortex antiferromagnetic crystal with staggered loop currents around each effective triangular plaquette.

Strong coupling limit

To give an intuition of the physics of the model in terms of quantum magnets, we discuss the hardcore-boson limit $U \to \infty$, with $V = 0$. In this case, the system can be mapped into a spin-1/2 XY model using the Holstein-Primakoff [423] transformation for $S = 1/2$

$$S_i^+ \equiv S_i^x + \imath S_i^y = b^\dagger \quad S_i^- \equiv S_i^x - \imath S_i^y = b, \quad S_i^z = b_i^\dagger b_i - 1/2, \tag{5.19}$$

[3]Notice that the $+$ between the two operators is required because of the specific gauge constraint in which we are working, namely by the staggered J_1.

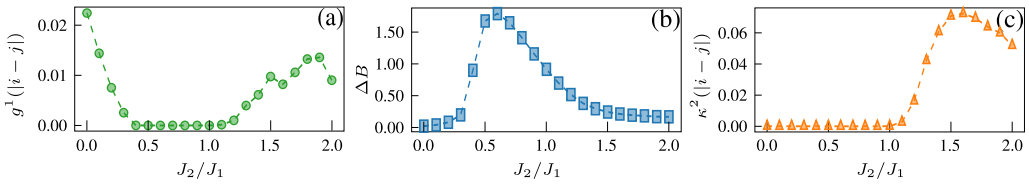

FIGURE 5.4: Phase diagram of (Eq. 5.20) corresponding to H_{FEHB} with $U = \infty$ and $\bar{n} = 0.5$ where we show in (a) superfluid correlator $g^1(|i-j|)$ for $|i-j| = 100$; (b) bond-order-wave order parameter ΔB; (c) chiral superfluid correlator $\kappa^2(|i-j|)$ for $|i-j| = 100$; The VUMPS simulation have been performed by using a bond dimension χ=400

Under this transformation the Hamiltonian becomes

$$\begin{aligned} H = &-2J_2 \sum_j (S_i^x S_{j+2}^x + S_j^y S_{j+2}^y) - \\ &-2J_1 \sum_j (-1)^j (S_j^x S_{j+1}^x + S_j^y S_{j+1}^y). \end{aligned} \tag{5.20}$$

Within a different gauge sector [393, 394], this Heisenberg model accurately describes triangular frustrated quantum magnets [392, 395–397]. For this model we reconstructed the phase diagram as a function of the frustration strength J_2/J_1. Analogously to the bosonic case, for this quantum magnet we can recover the three phases SF, BOW and CSF, as shown in Fig. 5.4. This proves that the system with hardcore-bosons to be highly suitable to investigate the properties of frustrated quantum magnets.

Notably, in this limit the vector chiral Order Parameter κ_i gets a form that is particularly intuitive to understand [393]:

$$\kappa_i^z = (\boldsymbol{S}_i \times \boldsymbol{S}_{i+1}) \cdot \hat{z}. \tag{5.21}$$

The spatial average of this quantity is a measure of the times a spin winds around the origin when going around a plaquette.

5.2.2 $V \neq 0$ and Deconfined quantum critical points.

We now turn to the study of the phase diagram for $V \neq 0$. To match the experimentally realizable regimes (as we will explain in the next Section), we keep $V/U < 0.3$. In order to be able to reach relatively large values of V, we fix $U/J_1 = 6$ [see the dashed line in Fig. 5.3(a)] and we concentrate on the regime of weak and intermediate frustration[4].

Our VUMPS analysis in Fig. 5.5(a) finds the SF stable with respect to the addition of moderate V. On the contrary, for a gradual increase of the nearest-neighbor repulsion the system undergoes a phase transition from the BOW to a different SSB insulator identified by the local order parameter

$$\delta N = \frac{1}{L} \sum_j (-1)^j (n_j - \bar{n}). \tag{5.22}$$

[4]We checked that the CSF is not affected by the presence of V.

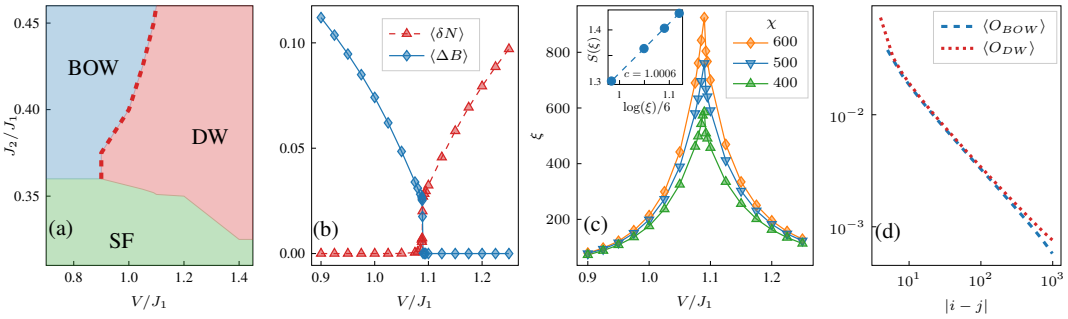

FIGURE 5.5: Effect of the nearest-neighbor repulsion V in the Hamiltonian (5.13). For all the panels, we fix $U/J_1 = 6$ and $\bar{n} = 0.5$. (a) Phase diagram of H_{EFBH} in the $V/J_1 - J_2/J_1$ plane, using $\chi = 400$. (b) ΔB and δN as a function of V/J_1 for $J_2/J_1 = 0.45$ and $\chi = 600$. (c) The correlation length ξ as a function of V/J_1 for different bond-dimension χ and fixed $J_2/J_1 = 0.45$. Inset: scaling of the entanglement entropy $S(\xi)$ as a function of ξ at the critical point for bond dimensions $\chi = 400, 500, 600$ showing the extrapolated central charge $c = 1$. (d) Decay of O_{DW} and O_{BOW} at the critical point for fixed $J_2/J_1 = 0.45$.

A finite δN, which can be accurately probed through quantum gas microscopy [424], reflects the spatial alternation between empty and singly occupied sites, thus revealing the appearance of a DW characterized by broken translational symmetry. Phase transitions between two gapped SSB phases are usually described by the Ginzburg-Landau theory [3, 425]. The latter predicts the existence of a first-order transition where the gap never vanishes, and it exhibits a discontinuity between two finite values. Quantum fluctuations can instead give rise to continuous phase transitions between different SSB states, where the gap vanishes only at a single point: a Deconfined Quantum Critical Point (DQCP) [121, 168].

The numerical detection of DQCPs is highly challenging. On the one hand, their complete characterization requires algorithms directly mimicking the thermodynamic limit and, on the other hand, the diverging correlation length ξ occurring at criticality requires a specific entanglement scaling [**pollmann2009a**]. In this respect, VUMPS are particularly suitable. This advantage stems from the fact that the variational optimization is performed on a unit cell directly in the thermodynamic limit. In this way it is possible to avoid the slower and non-monotonous convergence to the variational optimum [391] peculiar to algorithms involving a gradual growth of the system size.

Thanks to this technique, our results in Figs. 5.5(b)-(d) clearly demonstrate the BOW-DW transition to be continuous and therefore the presence of 1D DQCPs. Specifically, we find that ΔB and δN vanish continuously exactly at the same V/J_1, see Fig. 5.5(b). In order to rule out the presence of a weakly first-order phase transition, we extract the correlation length ξ through the relation

$$\xi = -N/\log(\lambda_2), \tag{5.23}$$

where N is the number of sites of a unit cell and λ_2 is second-highest eigenvalue of the transfer matrix. Within an MPS formalism, ξ must not depend on the bond dimension χ in the presence of a finite gap. On the other hand, a χ-dependence in the form of a cusp should be observed only at the critical point [**roberts2019a**, 174, 385]. Fig. 5.5(c) accurately confirms this behavior. In the inset of Fig. 5.5(c) we

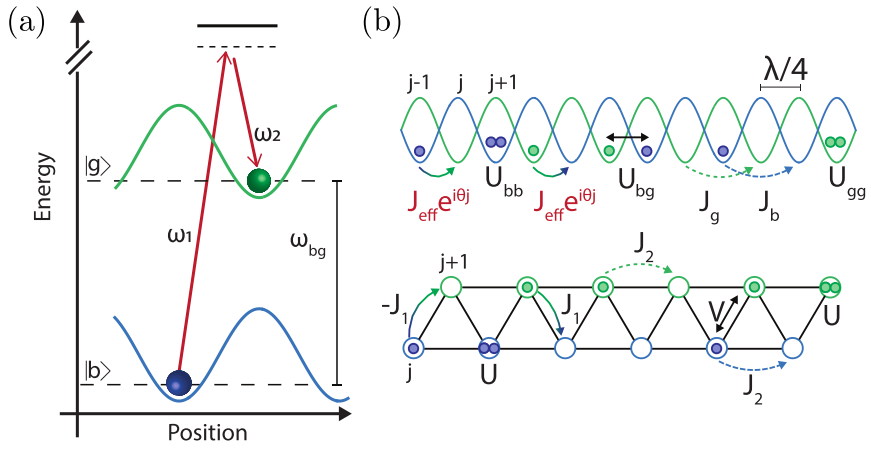

FIGURE 5.6: Experimental scheme to realize Eq. (5.28). (a) State-dependent optical lattice at the anti-magic-wavelength λ. Due to the opposite polarizability, both states experience a trapping potential with opposite strength. Raman-assisted tunneling between neighboring sites is induced using a two-photon Raman transition between states $|b\rangle$ and $|g\rangle$ for $\omega_{bg} = \omega_1 - \omega_2$ the energy difference between the two states on neighboring lattice sites. (b) The state-dependent lattice can be seen as two shifted sub-lattices with an effective lattice spacing of $\lambda/4$ (for a retro-reflected configuration), intra/interspecies tunneling $J_b, J_g/J_{\text{eff}}e^{i\theta j}$ and interaction $U_{bb}, U_{gg}/U_{bg}$ (upper panel). (c) Choosing $J_b = J_g = J_2$, $J_{\text{eff}} = J_1$, $\theta = \pi$, $U_{bb} = U_{gg} = U$ and $U_{bg} = V$ this scheme is modeled by the frustrated extended Bose-Hubbard model defined in Eq. (5.13).

further extract the central charge c through the relation

$$S(\xi) = \frac{c}{6}\log(\xi) + \text{const.}, \tag{5.24}$$

where for MPS around a critical point it is proven that [**pollmann2009a**]

$$\xi(\chi) \sim \chi^{\kappa}, \quad \kappa/6 = (c(\sqrt{12/c}+1))^{-1}. \tag{5.25}$$

Conformal field theories rigorously demonstrate that the extracted $c = 1$ implies indeed the presence of a critical regime which, in this case, is further characterized by an emergent $U(1)$ symmetry. In order to enforce our results, we calculate the decay of the correlations functions

$$O_{\text{BOW}}(|i-j|) = \langle (B_i + B_{i+1})(B_j + B_{j+1})\rangle, \tag{5.26}$$

$$O_{\text{DW}}(|i-j|) = \langle (n_i - \bar{n})(n_j - \bar{n})\rangle. \tag{5.27}$$

Here, we expect LRO of $O_{\text{BOW}}/O_{\text{DW}}$ uniquely in the BOW/DW phase while both should vanish algebraically at criticality. Fig. 5.5(d) precisely shows the expected power-law decay. This point, that we have been able to demonstrate thanks to the fact that VUMPS mimic the thermodynamic limit, unambiguously proves the critical nature of this transition point. Finally, we point out that, as imposed in DQCPs [**roberts2019a**], the two correlation functions clearly vanish in the thermodynamic limit with the same exponent.

5.2.3 Experimental implementation

To give a physical realization to our predictions, we design a realistic experimental setup as illustrated schematically in Fig. 5.6. Here, the Hamiltonian (5.13) is realized using a two-components atomic mixture in a one-dimensional (1D) lattice at the *anti-magic wavelength* [341, 426, 427]. In this setting, the two different components have the same polarizability with opposite sign, meaning that when one species is experiencing a minimum in the potential the other is experiencing a maximum, and vice versa. While this technique can be employed with several atomic species [428–434] with minimal heating, we focus on an implementation with Cesium atoms. Here, convenient inter- and intraspecies Feshbach resonances [435] enable the engineering of frustrated quantum systems with tunable contact and nearest-neighbor interactions without requiring large electric or magnetic dipole moments.

As shown in Fig. 5.6 (a), in this regime the two atomic species, hereafter defined as $|b\rangle$ and $|g\rangle$, remain localized in two sub-lattices formed respectively by the intensity maxima and minima of the optical periodic potential with L sites. This configuration thus mimics an effective discrete geometry with $\tilde{L} = 2L$ sites and lattice spacing $\lambda/4$ (for retro-reflected lattices), see Fig. 5.6 (b). Since the two sub-lattices have by definition the same depth, the $|b\rangle$- and $|g\rangle$-bosons experience the same direct hopping amplitude $J_b = J_g = J$. On the other hand, intra- U_{bb}, U_{gg} and interspecies U_{bg} interactions are potentially different and tunable. Furthermore, tunable Raman-assisted tunneling processes $J_{\text{eff}}e^{\imath\theta j}$ (j is the $\tilde{L}$-lattice site index) connect consecutive sites of different sub-lattices; as a consequence, one tunneling event is accompanied by converting one internal state into the other, as shown in Fig. 5.6(a). Here J_{eff} and θ are given by the intensity and wavevector of the Raman coupling [436, 437]. This setup is accurately modeled by the Hamiltonian

$$\begin{aligned} H = &- \sum_j \left[J(a_j^\dagger a_{j+2} + h.c.) + J_{\text{eff}} e^{\imath\theta j} (a_j^\dagger a_{j+1} + h.c.) \right] \\ &+ \sum_j \left[\frac{U_{bb}}{2} n_{2j-1}(n_{2j-1} - 1) + \frac{U_{gg}}{2} n_{2j}(n_{2j} - 1) \right] \\ &+ U_{bg} \sum_i n_i n_{i+1}, \end{aligned} \tag{5.28}$$

where $a_j^\dagger / a_j$ is a bosonic creation/annihilation operator. To provide a more concrete implementation, we focus on two internal states of Cesium $|b\rangle \equiv |F = 3, m_F = 3\rangle$ and $|g\rangle \equiv |F = 3, m_F = 2\rangle$ where the interactions are tunable. For this system, the "anti-magic" wavelength occurs in the vicinity of $\lambda = 871$ nm for σ^+ polarized light.

A further essential aspect of the proposed configuration is its reliance on adiabatic state preparation. For instance, it is possible to prepare an initial state with N bosons in the $|b\rangle$ state forming a Mott insulator with $N = N_b = L$. By subsequently introducing $J_{\text{eff}}e^{\imath\theta j}$, it becomes possible to populate the $|g\rangle$ state and therefore reach the regime of half-filling $\bar{n} = N/\tilde{L} = 0.5$, with $N = N_b + N_g$, which is particularly suitable to explore SSB phases [360]. Finally, an adiabatic lowering of the lattice depth gives rise to a finite direct tunneling J. Finally, we fix $U_{gg} = U_{bb} = U$ and $\theta = \pi$ so that, after renaming $J = J_2$, $J_{\text{eff}} = J_1$ and $U_{bg} = V$, Eq. (5.28) becomes Eq. (5.13).

The realizable values of U and V can be computed by following the lattice configuration in the Cs quantum gas microscope presented in [438], in the presence of a state-dependent potential. The on-site U and nearest-neighbor interaction V are computed by the overlap of the Wannier functions $w_0(x)$ on each lattice site [341]:

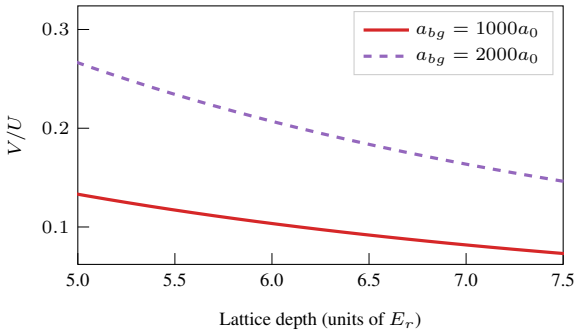

FIGURE 5.7: Ratio of nearest-neighbor V and on-site U interactions for two different interspecies scattering length a_{bg}. This is shown as a function of the lattice depth in units of the recoil energy E_R. The intraspecies scattering lengths a_{bb}, a_{gg} were set to $1000a_0$.

$$U = \frac{4\pi\hbar^2 a}{m} \int |w_0(x)|^4 \, dx, \tag{5.29}$$

$$V = \frac{4\pi\hbar^2 a_{bg}}{m} \int |w_0(x+\lambda/4)|^2 \, |w_0(x)|^2 \, dx. \tag{5.30}$$

Here a and a_{bg} are the intra- and interspecies scattering lengths: to achieve a large and nearly symmetric interaction, we operate at a magnetic field strength of approximately 56 G. At this field strength, the background scattering length of the three Feshbach resonances (inter- and intraspecies) is $a \sim 1000a_0$ [435, 439]. Additionally, a narrow resonance located at approximately 56.9 G provides additional flexibility in tuning the interspecies interaction strength a_{bg}, allowing the control of the nearest-neighbor interaction.

The ratio of nearest-neighbor and on-site interactions can then be tuned and is shown in Fig. 5.7. This allows us to choose $V/U < 0.3$ and $U/J_1 = 6$, and to explore the space of parameters necessary for the appearance of a DQCP.

Detection scheme and probes

The experimental detection of the DW phase can be performed in a very accurate way. Indeed, the measurement of the DW local order parameter δN requires resolving the local density n_j. Quantum gas microscopy allows for an impressive precision in measuring the bosonic occupation and therefore to accurately unveil the presence of the DW regime. On the other hand, the detection of the SF, BOW and CSF phases would require measurements of nearest-neighbor correlations and local currents. While this is indeed possible [49, 440], we provide an alternative way to characterize the mentioned regimes. Following the results in [412], we reveal the BOW via the string correlator

$$\mathcal{O}(|i-j|) = \langle \delta n_{2i} e^{\imath\pi \sum_{k=2i+1}^{2j-2} \delta n_k} \delta n_{2j-1} \rangle, \tag{5.31}$$

where $\delta n_j = (n_j - \bar{n})$. Note that this string correlator is not the same as in Eq. (5.10). The results reported in Fig. 5.8 prove this quantity to be highly suitable to detect the BOW. In particular, this strategy offers the fundamental advantage that Eq. (5.31) depends uniquely on the local occupation n_j which, as mentioned, can be accurately measured with a quantum gas microscope. Moreover, we find that the asymptotic value of $\mathcal{O}(|i-j|)$ perfectly reflects the behavior of ΔB and thus making this strategy realistic also to detect the DQCPs.

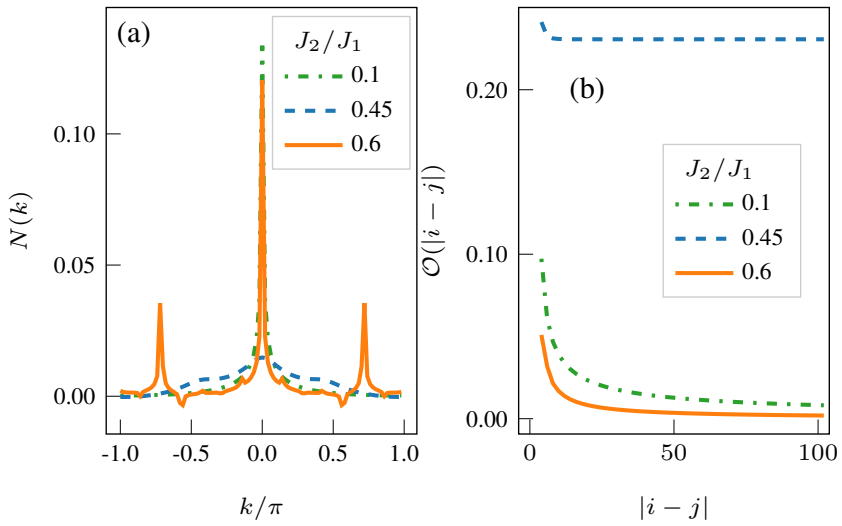

FIGURE 5.8: Momentum distribution $N(k)$ (a) and $\mathcal{O}(|i-j|)$ (b) for $U/J_1 = 6$, $\bar{n} = 0.5$, and $J_2/J_1 = 0.1, 0.4, 0.8$ corresponding to the SF, BOW and CSF respectively.

In order to distinguish between the two gapless phases, we can make use of the structure of the dispersion relation. In particular, while in the SF regime the dispersion relation has one minimum at the momentum $k = 0$, in the CSF regime two minima at incommensurate k occur. The structure of the dispersion relation can be accurately probed by the momentum distribution

$$N(k) = \frac{1}{L^2} \sum_{i,j} e^{\imath |i-j| k} g^1(|i-j|). \tag{5.32}$$

Our numerical analysis in Fig. 5.8 reveals specifically this behavior as we find one $k = 0$ peak in the SF and two peaks at different ks, when in the CSF. To access the momentum distribution $N(k)$, we propose using a matter wave focusing technique. Here, the momentum-space is mapped into real space after a quarter period (T) evolution in a harmonic trap [441, 442]. In the presence of an optical lattice, the experimental protocol would consist of mapping the band population and the quasi-momentum states into real-space momentum components, followed by the expansion in the harmonic potential for a time $T/4$. Finally, the atomic distribution is frozen in a deep optical lattice for single-site imaging. Similar protocols have been proposed and implemented in [443, 444]. Although not yet proved in optical lattice at the anti-magic wavelength, a possible alternative protocol would consist in extracting the local current κ_i following the scheme derived in [49]. In this way the CSF phase could be easily distinguished from the normal SF phase

5.3 Deconfined quantum critical points in the Fermi-Hubbard model

The phases of the paradigmatic Extended Fermi-Hubbard model (EFHM) have been extensively studied in the last decades. The most established results for its zero-temperature phase diagram with repulsive interactions [400] recover three different phases: a Mott insulator (MI), a charge density wave (CDW) and a bond order wave (BOW), depending on the relative strength of the on-site repulsion U/t and the nearest-neighbor repulsion V/t. Remarkably, this study finds a second-order transition between the two symmetry-broken CDW and BOW for moderate values of U/t.

Motivated by the results of previous section, we then aim to revisit the phase diagram of the EFHM, focusing on the BOW-CDW transition, to show that this phase transition is indeed of second-order and compatible with the presence of a DQCP. Indeed, by using VUMPS we can reach an accuracy in the identification of the critical point and the nature of the transition not achievable with less refined methods. Moreover, we will show that by adding a magnetic coupling J_z to the EFHM, an antiferromagnetic phase (AF) can be stabilized, leading to another DQCP at the boundary AF-BOW.

The complete model in study is then

$$\begin{aligned} H_{\text{EFHM}} = &- t\sum_{j,\sigma}(c^\dagger_{j\sigma}c_{j+1\sigma} + h.c.) + U\sum_j n_{j\uparrow}n_{j\downarrow} \\ &+ V\sum_j n_j n_{j+1} + J_z\sum_j S^z_j S^z_{j+1}, \end{aligned} \tag{5.33}$$

where $c^\dagger_{j\sigma}$ creates a fermion with spin σ on site j, $n_{j\sigma} = c^\dagger_{j\sigma}c_{j\sigma}$, and $S^z_j = c^\dagger_{j\uparrow}c_{j\uparrow} - c^\dagger_{j\downarrow}c_{j\downarrow}$ is the z-component of the spin operator. Finally, as the transition happen for low enough values of U/t, V/t, and J_z/t, we will give an interpretation in terms of bosonization in Appendix C.

5.3.1 Analysis of BOW-CDW transition

We start by performing a numerical analysis of the BOW-CDW phase transitions of the model in Eq. (5.33), restricting to the case $J_z = 0$. Previous finite size DMRG studies [400] and Montecarlo [399] showed that this transition is of second order for moderate values of U, while it becomes of first order for $U > 5.19t$. For $U \simeq 9.25t$, the BOW phase is absent, and there is a direct first-order phase transition between the Mott Insulator and CDW phases. In the following we will show that for moderate values of $U = 4t$ the phase transition is indeed second-order and compatible with the presence of a DQCP.

We emphasize that, for spinful fermionic systems, both charge and spin degrees of freedom must be considered. More precisely, we refer to a gapped charge or spin sector when the system has to pay a finite energy for adding/removing an up-down pair, or flipping a single fermion, respectively.

To capture the phase transitions we consider the three order parameters

$$\Delta S_z = \frac{S^z_1 - S^z_2}{2}, \quad \Delta B = \frac{B_1 - B_2}{3}, \quad \delta n = \frac{n_1 - n_2}{2}, \tag{5.34}$$

where $B_j = \sum_\sigma c^\dagger_{j\sigma}c_{j+1\sigma} + h.c.$. The three parameters identify respectively the AF, the BOW, and the CDW phase. As we are working with uniform MPS the average

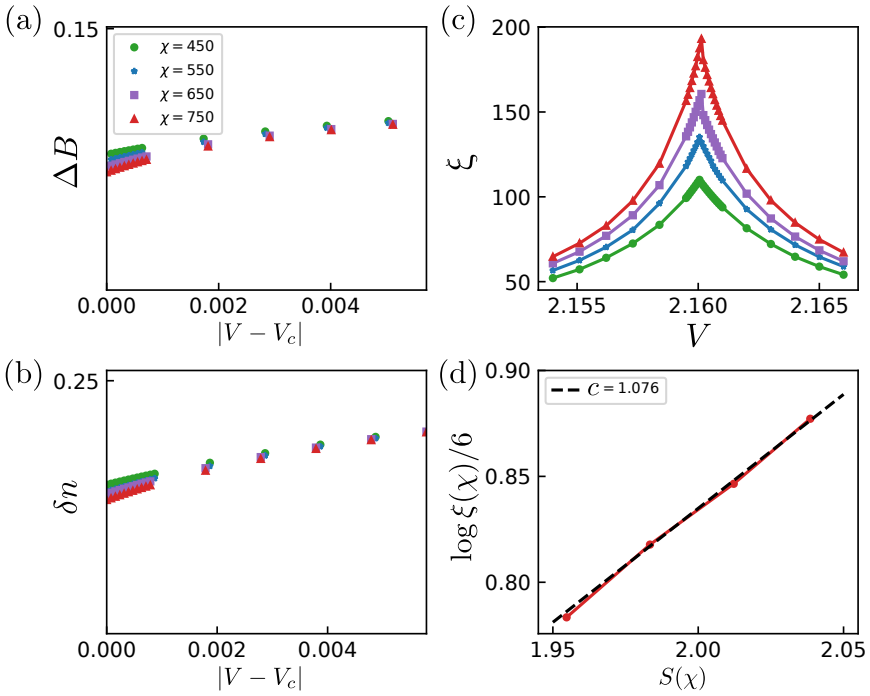

FIGURE 5.9: Results for $U = 4t$ obtained with the VUMPS optimization method. We show relevant quantities across the BOW-CDW transition as a function of the nearest-neighbor interaction V. (a)-(b) Show, respectively, the BOW and CDW order parameters around the critical point $V_c = 2.1601$. We observe how they both tend to zero with increasing bond dimension when approaching the critical point. (c) Correlation length showing a χ-dependent cusp at the critical point, characteristic of continuous phase transitions. (d) The relation $S(\chi) = c \log(\xi(\chi))/6$ suggests a transition with central charge $c = 1$.

is performed over a unit cell of length $L = 2$. The denominator in ΔB is 3 as the dimerization order parameter involves three sites instead than two.

In Fig. 5.9(a),(b) we characterize the BOW-CDW transition as a function of the bond dimension χ. By increasing χ, we see that ΔB and δn scale to zero at the transition point as expected for a DQCP [**roberts2019a**]. As in the case of the frustrated Bose-Hubbard model, we can then perform a scaling of the correlation length ξ as a function of the bond dimension χ at the critical point, as shown in Fig. 5.9(c). In such a way, the central charge c can be inferred by Eq. (5.24). The results in Fig. 5.9(d) allow extracting the value $c = 1$, a clear sign of a critical regime and therefore of a DQCP.

Finally, it is important to consider the decay of long-range correlators of the order parameters defined above at or close to the transition point. Consistently with the order parameters we define the correlators as

$$\begin{aligned} O_{\mathrm{AF}}(i,j) &= (-1)^{i+j} \hat{S}^z_i \hat{S}^z_j \\ O_{\mathrm{BOW}}(i,j) &= (-1)^{i+j} (\hat{B}_i - \hat{B}_{i+1})(\hat{B}_j - \hat{B}_{j+1}) \\ O_{\mathrm{CDW}}(i,j) &= (-1)^{i+j} (n_i - 1)(n_j - 1) \end{aligned} \tag{5.35}$$

which have to display long-range order in AF, BOW or CDW respectively. The results in Fig. 5.10 confirm the expected algebraic decay with the same critical exponent of two correlators corresponding to the two different orders at the two sides of the transition. Furthermore, this decay shows the appearance of an emergent $SU(2)$

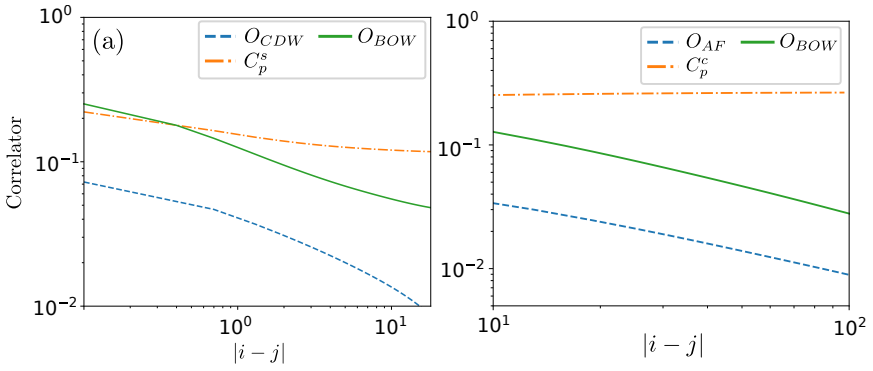

FIGURE 5.10: Decays of correlators at the critical point. (a) BOW-CDW transition. Results for $U = 4t$ obtained with the VUMPS optimization method with $\chi = 750$. We show the decay of the BOW, CDW and spin parity long-range correlators at critical point for $V_c = 2.1601$. (b) AF-BOW transition. Results for $U = 4t$ and $J_z = 1$ obtained with with $\chi = 700$. We show the decay of the BOW and AF long-range correlators at critical point for $V_c = 2.2632$. In both cases the correlators decay with a power law with the same exponent, a characteristic of DQCPs.

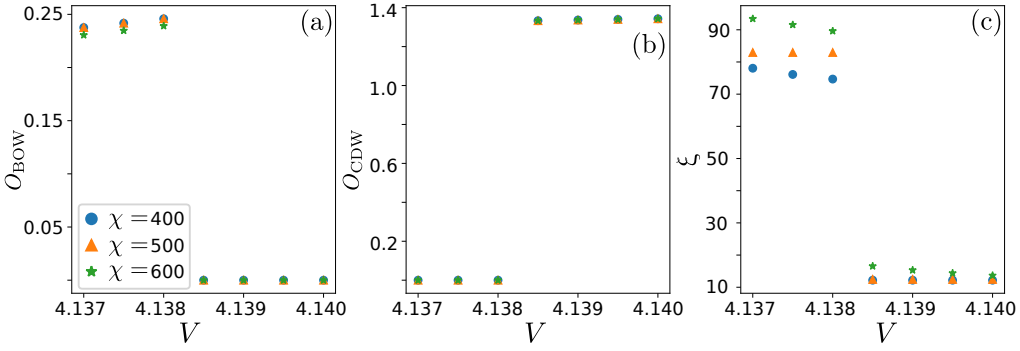

FIGURE 5.11: Results for $U = 8t$ obtained with the VUMPS optimization method. We show relevant quantities across the BOW-CDW transition as a function of the nearest-neighbor interaction V, for bond dimensions $\chi = 400, 500, 600$. (a)-(b) Show, respectively, the BOW and CDW order parameters around the critical point. We observe how these observables barely depend on the bond dimension when approaching the transition, and thus they do not tend to zero at the critical point with increasing bond dimension. (c) Correlation length exhibiting a jump characteristic of a first order phase transition.

symmetry occurring exactly at the transition point. Based on this fact, at this DQCPs we expect long-range behavior of non-local order parameters of the form of parity operators [411, 445]. Specifically, at the BOW-CDW transition where the charge gap vanishes and the spin sector remains gapped, we expect the emergence of a Luther-Emery phase captured by the long-range order of

$$C_P^{(s)}(r) = \langle \prod_{j \leq r} e^{i\pi(n_{j\uparrow} - n_{j\downarrow})} \rangle, \tag{5.36}$$

called the *spin-parity* correlator. In Fig. 5.10(a) we show that this correlator has indeed long range order.

Finally, we checked the case of strong interaction $U = 8t$. Here our results show the BOW-CDW transition becomes first order with a sharp jump of the order parameters at criticality and a non-diverging correlation length around the transition point, coherent with the results in [400]. This is shown in Fig. 5.11. In particular,

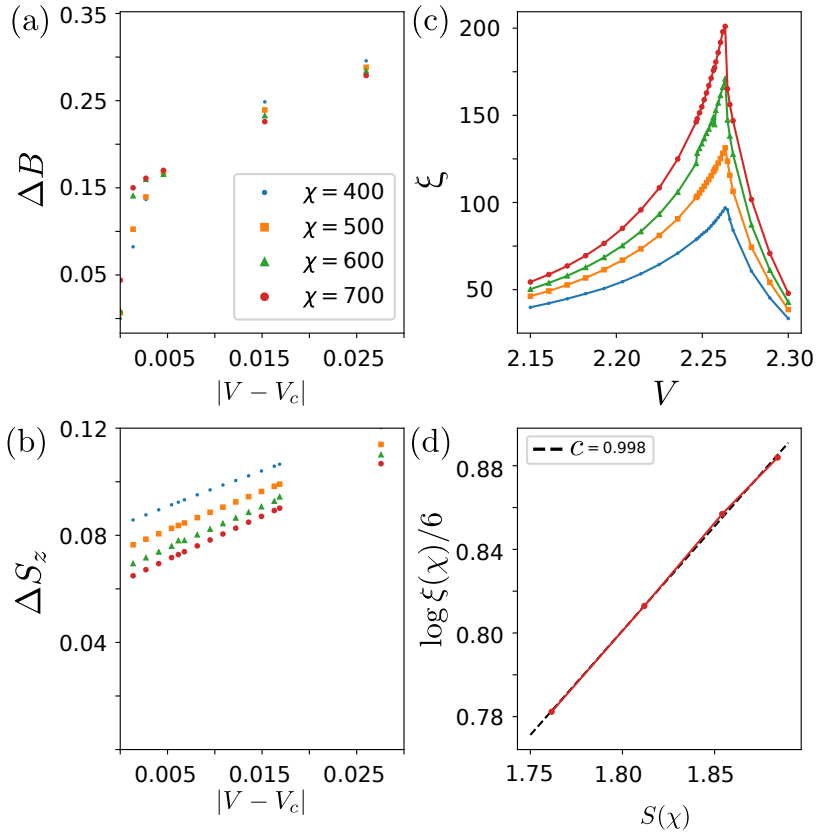

FIGURE 5.12: Results for $U = 4t$ and $J_z = 1$ obtained with the VUMPS optimization method. We show relevant quantities across the AF-BOW transition as a function of the intersite interaction V. (a)-(b) Show, respectively, the BOW and AF order parameters around the critical point $V_c = 2.2632$. We observe how they both tend to zero with increasing bond dimension when approaching the critical point. (c) Correlation length showing a χ-dependent cusp at the critical point, characteristic of continuous phase transitions. (d) The relation $S(\chi) = c \log(\xi(\chi))/6$ suggests a transition with central charge $c = 1$.

in Fig. 5.11(a),(b) we show that the value of the order parameters around the phase transition are independent on the bond dimension, and in Fig. 5.11(c) we show that the correlation length jumps always stays finite at the transition, independently of the bond dimension. This is coherent with the fact that the quantum fluctuations driving the continuous phase transition are weaker in the presence of strong interactions.

5.3.2 Analysis of AF-BOW transition

For a strong enough antiferromagnetic coupling J_z in Eq. (5.33) the Mott insulating ground state can become unstable to the formation of antiferromagnetic ordering AF breaking the spin $SU(2)$ symmetry. In this situation, there is a new transition line between AF and BOW order that can show the properties of a DQCP. We identify deconfined quantum criticality for the AF-BOW transition setting $U/t = 4$ and $J_z/t = 1$ when $V/t \sim 2.2632$, see Fig. 5.12. As in the case of the BOW-CDW transition we identify the properties of the deconfined transitions: a diverging correlation length associated with a finite central charge $c = 0.998 \sim 1$, and decaying correlators with the same power law. As for the CDW-BOW transition, this DQCP is characterized by an emergent $SU(2)$ symmetry, this time associated with a charge gapped

Mott insulator captured by the long-range behavior of the parity charge operator

$$C_P^{(c)}(r) = \langle \prod_{j \leq r} e^{i\pi(n_j - 1)} \rangle. \tag{5.37}$$

This behaviour is shown in Fig. 5.10(b). The different type of non-local order at the DQCP confirms that the two transitions are indeed associated to a different phase at criticality.

5.4 Summary

In this Chapter, we studied two paradigmatic models, the Extended Bose-Hubbard model and the Extended Fermi-Hubbard model, showing how frustration can lead to the appearance of exotic phases and, in particular, deconfined quantum criticality at the transition between them. For bosons, by only considering contact interaction we demonstrated that states of matter peculiar to frustrated quantum magnets, namely chiral superfluids and spontaneously-symmetry-broken Bond Order Wave insulators, can be created and accurately probed. By adding strong nearest-neighbour repulsion, a new spontaneously-symmetry-broken Density Wave insulator occurs. We proved that the phase transition between the two spontaneously-symmetry-broken phases is continuous, thus representing a one-dimensional deconfined quantum critical points not captured by the Landau–Ginzburg-Wilson symmetry-breaking paradigm. For this system, we designed an experimental scheme based on two-component bosonic atoms in an optical lattice at the anti-magic wavelength. In this setup all the fundamental properties of the model, namely frustrated hoppings and contact and nearest-neighbour interactions, can be efficiently controlled and probed. This allows us to perform experiments in a regime where geometrical frustration and quantum fluctuation strongly compete. For fermions, we showed how by using of cutting-edge VUMPS simulations we can better characterize the transition between a Bond Order Wave and a Charge Density Wave already identified in previous works [400]. In this case, frustration induced by the competition between the contact and nearest-neighbor interaction can result in two symmetry broken phases connected by a DQCP. Moreover, we show how adding an antiferromagnetic nearest-neighbor spin-spin interaction can lead to the stabilization of a spontaneously broken Antiferromagnetic phase, also connected to the Bond Order Wave by a DQCP. Strikingly, these two phase transitions, Bond Order Wave-Charge Density Wave and Bond Order Wave-Antiferromagnet, are associated to the emergence of two different $SU(2)$ symmetries at the critical point. We confirmed that by computing two non-local order parameters, the spin and charge parity correlators. We used the long range of these correlators to show that in one case the transition is associated to the emergence of a Luther-Emery phase with zero charge gap and finite spin gap, while in the other case is associated to the emergence of a Mott insulator with zero spin gap and finite charge gap [411, 445]. Importantly, the presence of this long-range order makes this DQCP qualitatively different from the one found in the Bose-Hubbard model, where all the correlators exhibit a power-law decay.

Chapter 6

Fragmented superconductivity in the Hubbard model

The two-dimensional Hubbard model is a cornerstone of modern condensed matter physics. Initially introduced as a minimal model of interacting electrons in a lattice to describe itinerant ferromagnetism and metal-insulator transition [446, 447], it has found particular relevance in the description of the physics of Cuprates [13, 448], to try to describe their high-temperature superconducting properties. Despite its apparent simplicity, this system shows an extremely rich physics and a thorough study of its phase diagram is still an open problem. Different phases have been targeted by numerical and experimental investigations, such as antiferromagnetic, striped and pseudo-metal regions, but often with incompatible results. Strikingly, studies at finite and zero-temperature of the model have proven inconsistent with each other. Lately, it has been studied in the context of quantum simulators, and some regimes have been realized experimentally in cold atoms systems like the antiferromagnetic phase [45] and even pairing in narrow ladders [449]. It is however pivotal to investigate ways to confirm the structure of different phases. Indeed, the complex structure of the model means that often the system forms *intertwined orders* [450], in which several mechanisms cooperate to form a complex phase.

Intertwined orders come in many flavors in strongly correlated electron systems [450–452]. Continuous and discrete symmetries are broken in a manner in which order parameters transform non-trivially in the entire symmetry group. In *stripe order* for example, both the translational and spin rotation symmetry are broken to a state which intertwines a charge density wave (CDW) and a spin density wave. Initially proposed in Hartree-Fock studies [453–456], modern numerical techniques have in the last years succeeded in firmly establishing it as the ground state in certain parameter regimes of the strongly correlated repulsive Hubbard model in 2D [457–461]. As such, these orders are relevant to the physics of high-temperature superconductivity where electron-electron interactions in the form of the Hubbard model are understood to play a crucial and likely decisive role [13, 462, 463].

Historically, the competition between superconductivity and stripe order has been discussed thoroughly [464, 465]. Both stripe order and superconductivity have by now been found to be realized in different parameter regimes of the paradigmatic Hubbard and t-J models [380, 457–461, 466–472], and have also been found when further neighbor hopping processes are included [113, 114, 473]. Moreover, numerical studies in the last years have discovered that superconductivity can also be intertwined with CDW order [113, 115, 473–478]. A particular form of intertwined CDW order and superconductivity is the so-called pair-density wave state [474, 479–484], for which recently evidence has been reported in several unconventional superconductors [485, 486]. The coexistence of CDW order, which breaks translational

symmetry, and superconductivity is sometimes also referred to as supersolid order. Fragmentation refers to the phenomenon when fermion pairs condense into not just one, but multiple macroscopic wave functions. The ground state in a certain regime of the t-t'-J model exhibits exactly one fragment per charge stripe of the superconducting condensate, interpreted as an emergent array of coupled Josephson junctions.

The goal of this Chapter, based on [VI], is to strengthen our understanding of this intriguing form of order. Employing density matrix renormalization group (DMRG) [53, 56, 57, 487] simulations, we show the fragmented superconducting stripe order is also realized in the Hubbard model on the square lattice, both with open and cylindrical boundary conditions. Additionally, we investigate the effect of an orbital magnetic field on the fragments of the Cooper condensate. Moreover, we propose a minimalistic macroscopic model to describe the superconducting condensates which is given by an intertwined Ginzburg-Landau theory [4]. Importantly, the mass term is chosen to be position dependent and exactly proportional to the hole-density modulation of the CDW. A one-to-one comparison between the solution of the Ginzburg-Landau equation and the numerical data from DMRG is performed and yields detailed agreement. The fragmentation of the superconducting condensate is then understood as a quantum tunneling between several soliton solutions of the Ginzburg-Landau equation.

We will start by briefly reviewing the physics of the 2D Hubbard model in Section 6.1. We will then introduce the particular model in study and the region we are targeting in Section 6.2. After having described the concept of fragmentation we will then study the properties of the fragmented superconducting phase using two-dimensional DMRG in Section 6.3. We will then propose a Ginzburg-Landau theory to describe the numerical results in Section 6.4.

6.1 Two-dimensional Hubbard model

Compared to the previously discussed 1D Hubbard model, the 2D fermionic Hubbard model [446] shows a much richer physics. For this reason we will introduce it more thoroughly, stating some main theoretical results and experimental realizations. In its more general formulation, the Hamiltonian for spin-1/2 fermions hopping on a lattice interacting with contact interactions can be written as

$$\hat{H} = -\sum_{i,j\in\Lambda,\sigma} t_{ij} c^\dagger_{i,\sigma} c_{j,\sigma} + U \sum_i \hat{n}_{i,\uparrow}\hat{n}_{i,\downarrow}, \tag{6.1}$$

where $c^\dagger_{i,\sigma}$ is the creation operator of a fermion with spin σ on site i and $\hat{n}_{i,\sigma} = c^\dagger_{i,\sigma} c_{i,\sigma}$ is the number operator. The hopping amplitude t_{ij} is often set to non-zero values only for nearest-neighbors sites $\langle ij\rangle$ or next-nearest-neigbor sites $\langle\langle ij\rangle\rangle$ and U is the on-site interaction.

In this formulation the Hamiltonian is symmetric under global unitary transformations $c_{i\sigma} = \mathcal{U}_{\sigma\sigma'} c_{i\sigma'}$, where $\mathcal{U} \in U(2)$. The role of these symmetries become more evident by separating $U(2) = SU(2) \times U(1)$: here the $U(1)$ symmetry generated by the number operator $N = \sum_{i,\sigma} n_{i,\sigma}$ implies the conservation of the total particle number (or charge), while the $SU(2)$ symmetry generated by the spin operator

$$\hat{S} = \sum_{i,\sigma,\sigma'} c^\dagger_{i,\sigma} \boldsymbol{\sigma}_{\sigma\sigma'} c_{i,\sigma'} \tag{6.2}$$

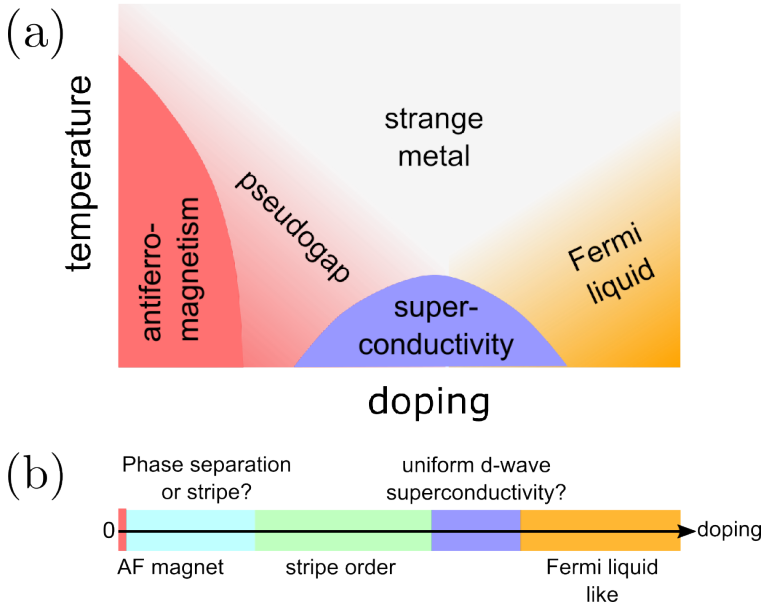

FIGURE 6.1: Sketch of the phase diagram of the 2D Hubbard model (a) at finite temperature and (b) zero temperature. The two proposed diagram are incompatible. Here, we are focusing on the zero-temperature, low-doping region where we expect to see an overlap of the striped and superconducting phases. Figure adapted from [488]

implies the conservation of both the total spin S^2 and the projection on the z-axis S^z. These properties prove particularly useful when studying the model numerically as it allows to reduce the size of the Hilbert space by restricting to sectors with a given quantum number, as explained in Chapter 2.

If the lattice Λ is *bipartite*, meaning that it can be split in two sublattices A and B such that every site in A has only nearest-neighbors in B, the model exhibit several more interesting properties. In particular, at half filling $\nu = 1/2$ Eq. (6.1) shows a further particle-hole symmetry

$$c^\dagger_{i,\sigma} \to (-1)^i c_{i,\sigma}, \tag{6.3}$$

where i is even if it belongs to sublattice A and odd if it belongs to sublattice B. This symmetry implies that the ground state for any choice of t_{ij} and U has uniform density at half filling [489], while it does not exclude the presence of other kind of magnetic ordering. Moreover, if the hopping structure does not break the lattice bipartition, the *Lieb Theorem* states that the ground state of the model at half filling is non-degenerate and is a singlet state with total spin $S = 0$ [490].

This behavior can be understood in the limit of $U \gg t_{ij}$, where the model can be well approximated by the $t - J$ model

$$\hat{H} = -\sum_{\langle ij\rangle,\sigma} t c^\dagger_{i,\sigma} c_{j,\sigma} + J \sum_{\langle ij\rangle} \boldsymbol{S}_i \cdot \boldsymbol{S}_j, \tag{6.4}$$

with $J = 4t^2/U$. In this limit, the model is projected onto the subspace where double occupancy of sites is forbidden, and the repulsive interaction is replaced by an effective antiferromagnetic interaction. If $t/U \to 0$, the system reduces to an antiferromagnetic Heisenberg model, whose ground state on a bipartite lattice is the Néel state.

If, however, we remove *one* electron from the system (still considering the limit $U \to \infty$) the ground state becomes suddenly ferromagnetic with spin $S = 1/2N$, with N the number of electrons, a result usually called *Nagaoka theorem* [491]. This theorem does not generalize to generic fillings. Instead, for fillings $\nu \notin 2\mathbb{Z}$, the *LSMOH* theorem states that no unique, gapless, insulating and featureless ground state can exist [492]. While these results are not directly applicable to the specific problem we are interested in, they give a useful insight on the choice of the ansatz states for the numerical simulations, and readily implementable benchmarks to check for their correctness.

Our main interest lies on the presence of superconductivity in the zero-temperature phase diagram of the model, for intermediate to strong interactions ($U/t \sim 5-10$), and small doping. This is the regime expected to be relevant for the physics of the Cuprates. Experimental results suggest that the Cooper pairing in Cuprates leading to superconductivity forms in the d-wave channnel [493], corresponding to a finite expectation value of the order parameter

$$\Delta_{ij} = \frac{\langle c^\dagger_{i,\uparrow} c^\dagger_{j,\downarrow} - c^\dagger_{i,\downarrow} c^\dagger_{j,\uparrow} \rangle}{\sqrt{2}}, \tag{6.5}$$

where we assumed a singlet pairing of the spins of the pair. While this quantity is necessarily zero in finite-size numerical simulations conserving the $U(1)$ charge conservation symmetry, the presence of superconductivity can be inferred by the presence of long-range order in the pairing-pairing correlation function

$$\lim_{|l-m|\to\infty} \langle \Delta^\dagger_l \Delta_m \rangle \sim |l-m|^{-\eta}, \tag{6.6}$$

for some exponent η, where we grouped together the indices of the lattice sites in a single index l. Using this metric, recent numerical works [461] suggest that the simple Hubbard model on a square lattice does not exhibit any superconducting phase at any doping. This result was obtained by two complementary numerical techniques, Auxiliary Field Quantum Monte Carlo and DMRG.

However, the addition of a next-nearest-neigbor hopping t' introduces frustration in the system that can help stabilize the superconducting phase. This was studied for both the strong-interaction limit $t-t'-J$ model, and the full $t-t'-U$ model. For this latter model there have been encouraging results on the presence of superconductivity in the phase diagram [115], both as a uniform condensate of Cooper pairs or superimposed to a charge density wave background, depending on the doping. Lately the presence of a uniform condensate has been also detected in the full $t-t'-U$ model in both the electron and hole-doped regions.

In the following we will introduce a different method to retrieve the superconducting properties of the doped $t-t'-U$ Hubbard model, that complement and confirms previous results on the matter.

6.2 Model and observables

We study the t-t'-U Hubbard model on a square lattice defined by the Hamiltonian

$$H = -\sum_{ij,\sigma} \left(t_{ij} c^\dagger_{i\sigma} c_{j\sigma} + \text{h.c.} \right) + U \sum_i n_{i\uparrow} n_{i\downarrow}, \tag{6.7}$$

where $t_{ij} = t$ for nearest neighbor lattice sites i and j and $t_{ij} = t'$ for next-nearest neighbor sites. Here, $c^\dagger_{i\sigma}, c_{i\sigma}$ denote the fermionic creation and annihilation operators of spin $\sigma = \uparrow, \downarrow$ and $n_{i\sigma} = c^\dagger_{i\sigma} c_{i\sigma}$ denotes the number operator. We additionally study the effect of a uniform orbital magnetic field $B = \nabla \times \boldsymbol{A}$, orthogonal to the plane of the lattice. We employ the Landau gauge

$$\boldsymbol{A}(\boldsymbol{r}) = (A_x, A_y) = (0, 2\pi\phi x), \tag{6.8}$$

where $\boldsymbol{r} = (x, y)$ denotes a real space coordinate. The total magnetic flux through the simulated system is denoted by $\phi = \int_S \mathrm{d}\boldsymbol{S}\ B$. The Landau gauge is well suited for open and cylindrical boundary conditions, since in the latter case it remains translationally invariant in the y-direction. The coupling of the model to the background magnetic field is implemented via a Peierls substitution

$$t_{ij} \to t_{ij} \exp\left[-i\frac{e}{\hbar}\int_{\boldsymbol{r}_i}^{\boldsymbol{r}_j} \mathrm{d}\boldsymbol{r} \cdot \boldsymbol{A}(\boldsymbol{r})\right], \tag{6.9}$$

where e denotes the elementary charge. In the following, we set $e = 1$, $\hbar = 1$ and focus on the model parameters $U/t = 10$ and $t'/t = 0.2$. For our geometry, the Peierls substitution reduces to

$$t \to t e^{i2\pi\phi x}, \quad t' \to t' e^{i2\pi\phi(x+1/2)}. \tag{6.10}$$

In large orbital magnetic fields, this model has been studied in the context of cold-atoms experiments [494–496]. As worked out extensively in Ref. [474] for $U/t = 12$, on six-leg cylinders this set of parameters stabilizes a superconducting state coexisting with a CDW at small hole-doping. Analogously, the coexistence of CDW and superconducting order has been reported at larger hole-doping by a combination of auxiliary-field quantum Monte Carlo and DMRG [115]. Moreover, the phase diagram at small hole-doping has been found to be in close agreement with the t-t'-J model, where similarly a coexisting CDW and superconducting state have been reported [113, 114, 471, 497]. The findings of this chapter are in full agreement with these previous studies.

Our aim is to elucidate the relation between charge and pairing degrees of freedom. We consider the hole density

$$n_h(\boldsymbol{r}) = 1 - n(\boldsymbol{r}), \tag{6.11}$$

where $\boldsymbol{r}$ denotes the lattice position and $n(\boldsymbol{r})$ the electron density. As the pairing mechanism in the lightly-doped Hubbard model has been diagnosed in previous studies to be of singlet-pairing type, we consider

$$\rho_S(\boldsymbol{r}_i, \boldsymbol{r}_j | \boldsymbol{r}_k, \boldsymbol{r}_l) = \langle \Delta^\dagger_{\boldsymbol{r}_i \boldsymbol{r}_j} \Delta_{\boldsymbol{r}_k \boldsymbol{r}_l} \rangle, \tag{6.12}$$

where the singlet-pairing operators $\Delta_{\boldsymbol{r}_i \boldsymbol{r}_j}$ are defined as

$$\Delta^\dagger_{\boldsymbol{r}_i \boldsymbol{r}_j} = \frac{1}{\sqrt{2}}\left(c^\dagger_{i\uparrow} c^\dagger_{j\downarrow} - c^\dagger_{i\downarrow} c^\dagger_{j\uparrow}\right). \tag{6.13}$$

Moreover, as the pairing in this superconducting phase was established as local in real space [113–115, 473, 475, 497, 498], we restrict ourselves to investigating the

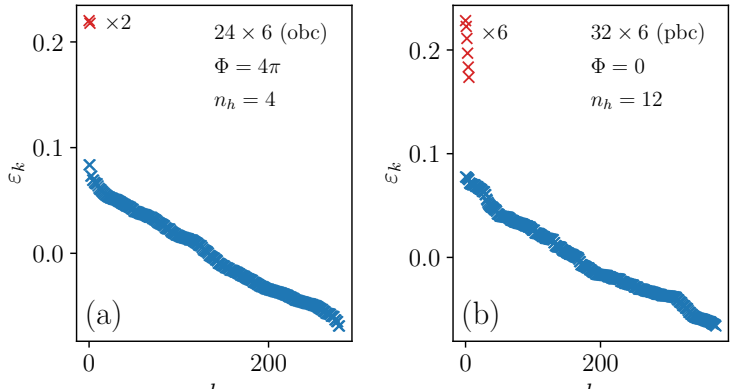

FIGURE 6.2: Fragmentation of the Cooper condensate apparent in the spectrum of the singlet two-particle density matrix of the ground state of the Hubbard model at small doping for $t'/t = 0.2$ and $U/t = 10$. (a) 24×6 square lattice (open boundary conditions) doped with $n_h = 4$ holes away from half-filling and total magnetic flux $\phi = 4\pi$ through the full sample. Two dominant eigenvalues are observed. (b) 32×6 cylinder doped with $n_h = 12$ holes without magnetic flux. We observe six dominant eigenvalues. In both cases, the number of dominant eigenvalues exactly matches the number of CDW maxima.

nearest-neighbor singlet-pairing density matrix

$$\rho_S(\boldsymbol{r}_i, \mu | \boldsymbol{r}_j, \nu) = \rho_S(\boldsymbol{r}_i, (\boldsymbol{r}_i + \mu) | \boldsymbol{r}_j, (\boldsymbol{r}_j + \nu)), \tag{6.14}$$

where $\mu = \hat{\boldsymbol{x}}, \hat{\boldsymbol{y}}$ (resp. ν) denote the vectors connecting nearest-neighbors on the square lattice. We exclude site-local contributions from density and spin correlations by setting $\rho_S(\boldsymbol{r}_i, \mu | \boldsymbol{r}_j, \nu) = 0$ whenever the two links $(\boldsymbol{r}_i, \boldsymbol{r}_i + \mu)$ and $(\boldsymbol{r}_j, \boldsymbol{r}_j + \nu)$ are overlapping. Because of this, $\rho_S(\boldsymbol{r}_i, \mu | \boldsymbol{r}_j, \nu)$ ceases to be positive definite and therefore can have negative eigenvalues. Off-diagonal long-range order occurs whenever

$$\rho_S(\boldsymbol{r}_i, \mu | \boldsymbol{r}_j, \nu) \to C \neq 0 \quad \text{for} \quad |\boldsymbol{r}_i - \boldsymbol{r}_j| \to \infty. \tag{6.15}$$

However, the information contained in $\rho_S(\boldsymbol{r}_i, \mu | \boldsymbol{r}_j, \nu)$ in (6.14) is richer and allows for additional insights beyond diagnosing long-range order. To unveil this hidden properties we have to introduce the concept of *fragmentation* of the Cooper condensate.

6.2.1 Fragmentation and Penrose-Onsager criterion

The starting point of this section is the consideration that the onset of superconductivity can be seen as a pairing of electrons into Cooper pairs. The pairs themselves behave as bosons, and can form a condensate. For non-interacting bosons, the condensation can be described as a situation where a macroscopic portion of the bosons occupies the same single-particle state, with the remaining bosons distributed over the higher-energy state states.

This concept can be extended to interacting bosons using the so-called *Penrose-Onsager criterion* [499]. Consider a system of interacting bosons in a pure state, described by a many-body wavefunction $\Psi(\boldsymbol{r}_1, \boldsymbol{r}_2, \ldots, \boldsymbol{r}_N)$. We can construct the *single-particle* density matrix

$$\rho(\boldsymbol{r}_i, \boldsymbol{r}_j) = \langle b^\dagger_{\boldsymbol{r}_i} b_{\boldsymbol{r}_j} \rangle = \sum \epsilon_n \phi^*_n(\boldsymbol{r}_i) \phi_n(\boldsymbol{r}_j) \tag{6.16}$$

Here we have used the Hermitian nature of the $\rho(\boldsymbol{r}_i, \boldsymbol{r}_j)$ to expand it in terms of its eigenvalues ϵ_n and eigenvectors $\phi_n(\boldsymbol{r})$. The ϵ_n are non-negative and sum to the total number of particles N. The Penrose-Onsager criterion can then be stated in this way:

- if all eigenvalues ϵ_n are of same order ~ 1, the system is in a normal, non-condensed phase;
- if one eigenvalue ϵ_0 is of order $\sim N$, the system is in a *simple* condensate;
- if multiple eigenvalues $\epsilon_1, \ldots, \epsilon_k$ are of order $\sim N$, while the others are of order ~ 1, the system is in a *fragmented* condensate, with k fragments.

In the majority of situations realistic physical systems can only form simple condensates [500]. However, there have been reports of fragmented condensates in experiments, for example in the context of cold atoms [501]. Because of these properties the eigenvalues ϵ_n are often called *condensate fractions*, and the corresponding eigenvectors $\phi_n(\boldsymbol{r})$ *macroscopic wave functions*. This is more evident when considering the non-interacting limit, where the $\phi_n(\boldsymbol{r})$ are the single-particle states of the system, and the ϵ_n are their occupation number. In this case, at zero-temperature, the Bose-Einstein condensation can be stated as $\epsilon_0 = N$.

In our work, following [498], we extend the concept of fragmented condensates to Cooper paired, described by the *two-body density matrix* $\rho_S(\boldsymbol{r}_i, \mu | \boldsymbol{r}_j, \nu)$, where μ, ν are the vectors connecting nearest-neighbor sites. As for bosons, this matrix can be expanded in terms of its eigenvalues ε_n and eigenvectors $\chi_n(\boldsymbol{r}, \mu)$ as

$$\rho_S(\boldsymbol{r}_i, \mu | \boldsymbol{r}_j, \nu) = \sum_n \varepsilon_n \chi_n^*(\boldsymbol{r}_i, \mu) \chi_n(\boldsymbol{r}_j, \nu). \tag{6.17}$$

The onset of Cooper pair condensation can then be inferred by the presence of either one or multiple dominant eigenvalues [499, 500]. Notice that in this case the eigenvectors χ depend on the position of the lattice $\boldsymbol{r}$ as well as the orientation of the bond μ and are, hence, defined on the bonds of the lattice.

6.3 Ground state properties from DMRG

To investigate the onset of intertwined order in the Hubbard model we perform DMRG calculations to obtain the ground state properties of the system. In this scheme, the 2D system is mapped to a 1D chain suitable for DMRG, with the drawback of the x-direction hopping term in the Hamiltonian becoming long-range. This leads to an exponential increase in the computational cost when increasing the width W of the system, limiting the simulations to narrow cylinders. For this reason, in this work, we choose $W = 6$.

We obtain results for systems of length $L = 24$ with open boundary conditions and $L = 32$ with periodic boundary conditions in the y-direction. On a cylindrical geometry the Hamiltonian in Eq. (6.7) is not gauge invariant as a gauge transformation introduces a magnetic flux piercing the cylinder, corresponding to a ground state with a finite momentum k_y along the y-direction. As this is non-physical when looking for ground state properties, we fix the gauge in order to stay in a sector with zero net k_y momentum. Analogously to previous works [113, 115] we restrict to the $S^z_{tot} \equiv \langle \sum_i n_{i\uparrow} - n_{i\downarrow} \rangle = 0$ sector of total spin projection in the z direction. Exploiting this symmetry, together with the conservation of the total charge $N \equiv \langle \sum_i n_{i\uparrow} + n_{i\downarrow} \rangle$ drastically reduces the computational load, allowing us to access larger bond dimensions. For the initial state of DMRG, we choose a physically motivated Néel product

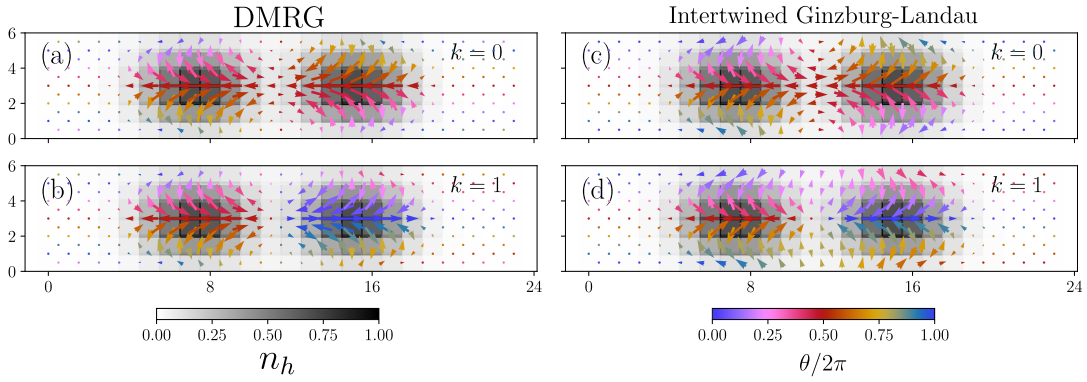

FIGURE 6.3: Comparison between macroscopic wave functions $\chi_k(\boldsymbol{r}, \mu)$ from DMRG simulations and $\psi_k(\boldsymbol{r}, \mu)$ from intertwined Ginzburg-Landau theory. (a,b) Macroscopic wave functions of ground state of the t-t'-U Hubbard model from DMRG with total magnetic flux $\phi = 4\pi$ on a 24×6 lattice with open boundary conditions when doped with $n_h = 4$ holes away from half-filling. Here we take $t'/t = 0.2$, $U/t = 10$. (a) (resp. (b)) shows the values of $\chi_k(\boldsymbol{r}, \mu)$ for the $k = 0$ (resp. $k = 1$) fragment of the condensate. The length of the arrows is proportional to $|\chi_k(\boldsymbol{r}, \mu)|$ and the color indicates the complex angle of $\chi_k(\boldsymbol{r}, \mu)$, where for $\mu = \hat{\boldsymbol{y}}$ we shift the phase by π, to reflect the d-wave nature of the order parameter. The gray scale of the background squares shows the value of the local hole density $n_h(\boldsymbol{r})$. (c,d) Both soliton solutions $\psi_k(\boldsymbol{r}, \mu)$ ($k = 0, 1$) of the intertwined Ginzburg-Landau theory for $\alpha(\boldsymbol{r}) = \alpha n_h(\boldsymbol{r})$, where $n_h(\boldsymbol{r})$ is taken from the values of the DMRG ground state and the free parameters $\alpha = -2.331$, $\beta = 14.465$ are found by matching the DMRG data to Ginzburg-Landau theory. We observe close agreement between both $\chi_k(\boldsymbol{r}, \mu)$ and $\psi_k(\boldsymbol{r}, \mu)$.

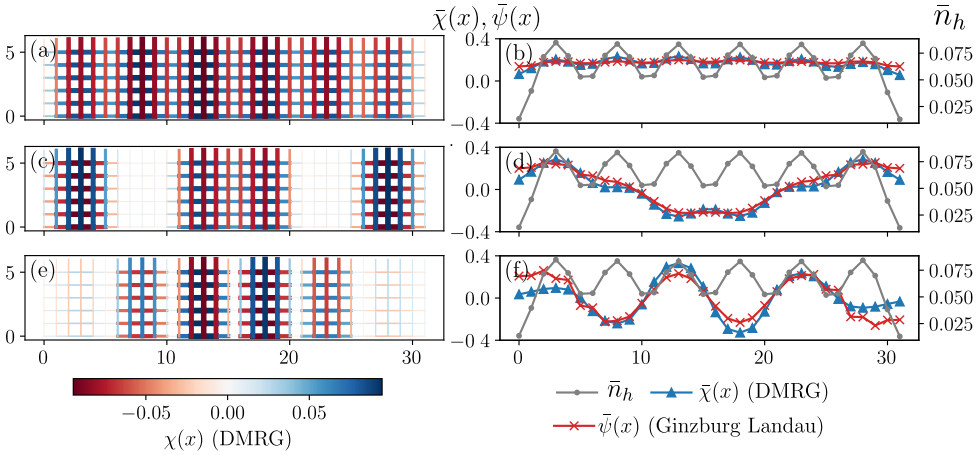

FIGURE 6.4: Selected macroscopic wave functions of the Cooper condensate fragments on a 32×6 cylinder at $t'/t = 0.2$, $U/t = 10$, and doping $p = 1/16$ corresponding to six stripes. (a, c, e) Macroscopic wave functions $\chi_k(\boldsymbol{r}, \mu)$ as in (6.17) with index $k = 0, 2, 5$. The color and width of the bars denote the value of $\chi_k(\boldsymbol{r})$ on the links of the lattice. (b, d, f) y-averaged hole-density $\bar{n}_h = (\sum_y n_h(x, y))/W$ of the ground state (gray, dotted) and comparison between the y-average of the macroscopic wave functions $\bar{\chi}_k(\boldsymbol{r})$ from DMRG and model wave functions $\bar{\psi}_k(\boldsymbol{r})$ from the intertwined Ginzburg-Landau theory with $\alpha = -1.3$ and $\beta = 13$. We report close agreement between the DMRG data and the solutions from Ginzburg-Landau theory.

state with the holes evenly distributed in pairs along the x direction. Special care had to be taken to make sure that this choice of the initial state does not lead to local minima of the DMRG optimization. As the convergence properties are highly dependent on the initial ansatz, we also ran the calculations with different starting states to check that we are converging to a global minimum.

For the $L = 24$ system with open boundary conditions we insert $n_h = \sum_{\boldsymbol{r}} n_h(\boldsymbol{r}) = 4$ holes in the system, corresponding to a hole-doping $p = 1/36$. We start by stabilizing the ground state without any magnetic flux, $\phi = 0$, at a bond dimension $D = 3500$, and then scale up the magnetic flux to $\phi = 4\pi$ at $D = 4000$, using the previously obtained ground state as the initial state for DMRG. For the $L = 32$ system with cylindrical boundary conditions, we insert $n_h = 12$ holes, corresponding to a hole-doping of $p = 1/16$, and we focus on the $\phi = 0$ case only, to better showcase how the different superconducting condensates arrange themselves over the different stripes. For this larger system we show results at a bond dimension $D = 8000$.

We plot the spectrum ε_k of ρ_s as defined in (6.17) in Fig. 6.2 for both parameter sets. In analogy with the previous results on the t-t'-J model [498], we observe multiple dominant eigenvalues above a continuum. Again, the number of dominant eigenvalues matches exactly the number of CDW maxima of the ground state. Thus, the system exhibits the presence of $n_h/2$ fragmented condensates, irrespective of the boundary conditions and the presence or absence of a background magnetic field at these parameter values.

To show the interplay between the CDW and the superconducting order we plot the hole density $n_h(\boldsymbol{r})$ superimposed on the macroscopic wave functions. For the $L = 24$ system with open boundary conditions, we show the macroscopic eigenvectors $\chi_0(\boldsymbol{r}, \mu), \chi_1(\boldsymbol{r}, \mu)$ in Fig. 6.3(a),(b), where the angle and the color of the arrows represent the phase of $\chi_k(\boldsymbol{r}, \mu)$ and the length of its amplitude respectively. We observe the macroscopic wave functions to be supported on the hole-rich regions of the ground state. Compared to an expected d-wave pattern for $\phi = 0$, a finite magnetic field induces rotation in the complex phase that increases by increasing magnetic flux ϕ.

For the $L = 32$ system with cylindrical boundary conditions the three macroscopic eigenvectors $\chi_0(\boldsymbol{r}, \mu), \chi_2(\boldsymbol{r}, \mu), \chi_5(\boldsymbol{r}, \mu)$ are shown in Fig. 6.4, both in the $x - y$ plane and averaged over the y-direction via

$$\bar{\chi}_k(x) = \frac{1}{W} \sum_{y=1}^{W} \chi_k((x, y), \mu). \tag{6.18}$$

Because $\chi_k(\boldsymbol{r}, \mu)$ is real we omit the arrows and only employ the color to define the sign. In all cases, the d-wave pattern of the pairing and the disposition of the superconducting pairing along the density stripes are clearly visible in alternating red and blue colors for $\mu = \hat{\boldsymbol{x}}, \hat{\boldsymbol{y}}$. In particular, for every different condensate, the macroscopic wave function has a different spatial modulation and correspondingly a different number of nodes.

6.3.1 Details on DMRG simulations

To ensure consistent convergence of DMRG for the systems we have studied, some care must be taken in choosing the initial states of the variational optimization. Here we describe our strategy for obtaining initial states. For systems of width $W = 4$, we found that DMRG is not sensitive to the initial starting states, and we use random initial states. Independent of the starting state, we find that the ground

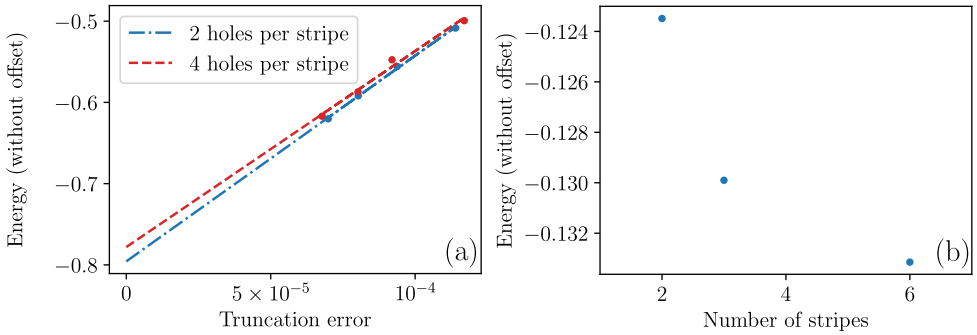

FIGURE 6.5: (a) Scaling of the energy with the truncation error for two different ansätze in a 24×6 system with four holes. (b) Energy behavior for different ansätze at fixed bond dimension $\chi = 4000$ for a 32×6 system with 12 holes

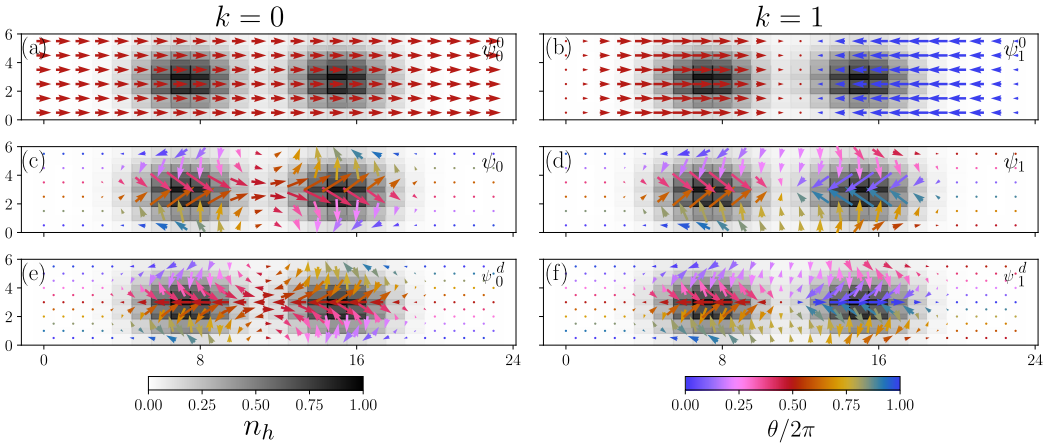

FIGURE 6.6: (a, b) Initial ansatz wave functions $\psi_k^0(\boldsymbol{r})$ used as a starting point in the minimization of the Ginzburg-Landau functional (6.19). (c, d) Obtained local minima $\psi_k(\boldsymbol{r})$ from these initial states after optimization. (e, f) Resulting d-wave order parameters $\psi_k(\boldsymbol{r}, \mu)$ as in (6.26) defined on the links of the lattice.

state is antiferromagnetic with a checkerboard spin pattern, and the holes bind in pairs and distribute evenly along the width of the system.

For width $W = 6$, we use starting states that are inspired by the ground states we find with DMRG at $W = 4$, which we find provide better convergence than random initial states. We have tried different starting states to test that our choice of starting state doesn't lead to a biased result. As an example of this, in Fig. 6.5(a), we show results from DMRG calculations of an $L = 24$ system with open boundary conditions and an equal number of total holes which were biased by the starting states to have different hole configurations (two holes per stripe with more stripes or four holes per stripe fewer stripes). By extrapolating the energy as a function of DMRG truncation error [502], we can conclude that the state with 2 holes per stripe is lower in energy.

In Fig. 6.5(b), for an $L = 32$ system with cylindrical boundary conditions and $n_h = 12$ holes, we compare the variational minimum energy for three different hole configurations (two, four, and six holes per stripe) at fixed bond dimension and as before we see that the energy is lowest for the state with two holes per stripe. Throughout this work, we therefore show results using states that have two holes per stripe.

A finite magnetic field ϕ in the Hamiltonian Eq. (6.7) introduces complex coefficients. In DMRG, this leads to tensors that have complex elements, and therefore the computation time increases by a factor of approximately four compared to the case of zero magnetic field ($\phi = 0$) where tensors with real elements can be used. To improve the convergence time of calculations with finite magnetic field, we first compute the ground state at some fixed bond dimension without a magnetic field and use the state found by DMRG as a starting state for calculations at finite magnetic field.

Care must be taken to efficiently compute the two-body singlet-pairing density matrix ρ_S. Naively, without the use of caching and sparsity, computing every element of a general two-body density matrix on a system of size $N = \mathcal{O}(L)$ (where for simplicity we assume a fixed width W) would scale as $\mathcal{O}(N^5)$ since there are $\mathcal{O}(N^4)$ elements and computing a single element requires $\mathcal{O}(N)$ tensor contractions, which would quickly become impractical. Luckily, there are multiple ways we can reduce this scaling. First, we only need to compute the pairing on neighboring sites, which reduces the scaling to $\mathcal{O}(N^3)$ if no caching is used. If caching of intermediate tensor contractions is used across the computation of different elements, this scaling can be further reduced to $\mathcal{O}(N^2)$. The code we use, which can compute general n-body correlators and automatically cache intermediate tensors involved in computing different elements, can be found at [503].

6.4 Intertwined Ginzburg-Landau theory

In the following, we demonstrate that the macroscopic wave functions $\chi_k(\boldsymbol{r}, \mu)$ of the fragmented Cooper condensates are well described by solutions of an intertwined Ginzburg-Landau functional of the form

$$\mathcal{F}[\psi] = \alpha(\boldsymbol{r})|\psi|^2 + \frac{\beta}{2}|\psi|^4 + \frac{1}{2m^*}\left|\left(-i\hbar\vec{\nabla} + 2e\boldsymbol{A}\right)\psi\right|^2. \tag{6.19}$$

The key aspect in (6.19) is the position dependence of the mass term $\alpha(\boldsymbol{r})$, which is chosen to be

$$\alpha(\boldsymbol{r}) = \alpha n_h(\boldsymbol{r}), \tag{6.20}$$

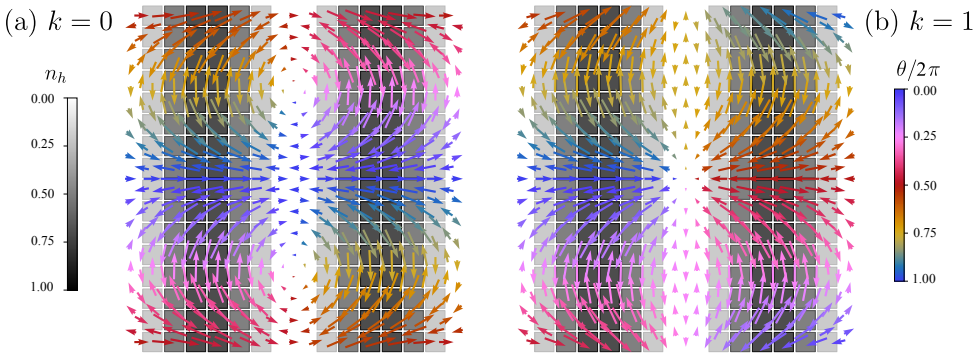

FIGURE 6.7: Both solutions $\psi_k(\boldsymbol{r}, \mu)$ of the intertwined Ginzburg-Landau equation ((6.19)) with $k = 0$ (a) and $k = 1$ (b). We choose $\alpha = -2.331$ and $\beta = 14.465$ on an $L \times L$ lattice with $L = 16$ with a total magnetic flux of $\phi = 1.64 \cdot 2\pi$ through the sample and open boundary conditions. The CDW is assumed to be of the form $n_h(\boldsymbol{r}) = \sin^2(2\pi x/L)$. The gray scale of the background squares is set by the hole density $n_h(\boldsymbol{r})$. The color and length denote the phase and amplitude of $\psi_k(\boldsymbol{r}, \mu)$, where for $\mu = \hat{\boldsymbol{y}}$ we shift the phase by π to reflect the d-wave nature of the order parameter. We observe pinned vortices between the stripes in the $k = 0$ condensate.

so the charge and phase degrees of freedom are intertwined through directly coupling to the hole density $n_h(\boldsymbol{r})$. This action is invariant under a gauge transformation

$$\psi(\boldsymbol{r}) \to e^{2i\phi(\boldsymbol{r})}\psi(\boldsymbol{r}), \quad \boldsymbol{A}(\boldsymbol{r}) \to \boldsymbol{A}(\boldsymbol{r}) - \nabla\phi(\boldsymbol{r}), \tag{6.21}$$

reflecting the transformation rule of Cooper pairs. Minimizing the functional $\mathcal{F}[\psi]$ by solving

$$\frac{\delta\mathcal{F}[\psi]}{\delta\psi} = 0, \tag{6.22}$$

yields the time-independent Ginzburg-Landau equations

$$\frac{1}{2m^*}\left(-i\hbar\vec{\nabla} + 2e\boldsymbol{A}\right)^2\psi = \alpha(\boldsymbol{r})\psi + \beta|\psi|^2\psi. \tag{6.23}$$

Importantly, the criterion (6.22) from which (6.23) is derived is valid for every *local* minimum of the functional (6.19). Hence, whenever there are multiple solutions to (6.23) there are also multiple local minima of (6.19). In the absence of both the nonlinear term ($\beta = 0$) and the vector potential ($\boldsymbol{A} = 0$), the Ginzburg-Landau equation ((6.23)) reduces to the linear time-independent Schrödinger equation. For periodic boundary conditions, in the presence of a periodic modulation of the mass term

$$\alpha(\boldsymbol{r} + \boldsymbol{\lambda}) = \alpha(\boldsymbol{r}), \tag{6.24}$$

Bloch's theorem [504] states that this equation has multiple solutions labeled by the wave number $\boldsymbol{k}$,

$$\psi_k(\boldsymbol{r}) = e^{i\boldsymbol{k}\cdot\boldsymbol{r}}u(\boldsymbol{r}), \tag{6.25}$$

where $u(\boldsymbol{r} + \boldsymbol{\lambda}) = u(\boldsymbol{r})$. Naturally, the question arises whether an analog of Bloch's theorem still holds in the presence of a nonlinearity ($\beta \neq 0$). This has already been addressed in the literature, where generalizations of Bloch's theorem with additional non-linearities have been proven [505–507]. Note that nonlinear Schrödinger equations in periodic potentials naturally occur when describing Bose-Einstein condensates in optical lattices, see e.g. [507–510].

In the presence of both a nonlinearity and the magnetic vector potential in two dimensions, we solve (6.23) numerically. Our approach is to solve the equivalent problem of minimizing $\mathcal{F}[\psi]$ via a local minimization algorithm and verifying that the functional derivative in (6.22) vanishes. Different solutions corresponding to distinct Bloch waves can be obtained by starting the optimization procedure with distinct initial configurations within the basin of attraction of the particular solution, cf. (6.4.1). We employ the BFGS algorithm [511–514] for local optimization and verify the minimization condition (6.22) by monitoring the norm of the Jacobian matrix, which we require to attain a numerical value $< 10^{-7}$ in all studied geometries.

To compare the solutions of the intertwined Ginzburg-Landau equation ((6.23)) to the macroscopic wave functions from DMRG, we solve for $\psi_k(\boldsymbol{r})$ on the vertices of the square lattice. We then define the d-wave order parameter ansatz on the links of the lattice as

$$\psi_k(\boldsymbol{r},\mu) = \begin{cases} +\left[\psi_k(\boldsymbol{r}) + \psi_k(\boldsymbol{r}+\mu)\right]/2 & \text{if} \quad \mu = \hat{\boldsymbol{x}}, \\ -\left[\psi_k(\boldsymbol{r}) + \psi_k(\boldsymbol{r}+\mu)\right]/2 & \text{if} \quad \mu = \hat{\boldsymbol{y}}. \end{cases} \tag{6.26}$$

We compare the intertwined Ginzburg-Landau wave functions with the numerical results in Fig. 6.3(b) for a finite magnetic flux ϕ. At this set of parameters, DMRG yields two fragments of the condensate while the Ginzburg-Landau equation exhibits two distinct solutions, which we find using different initial states when minimizing the Ginzburg-Landau functional, cf. 6.6. Thus, there is a one-to-one correspondence between the superconducting fragments and the distinct solutions of the Ginzburg-Landau theory. Moreover, we observe that both the periodicity in $\chi_0(\boldsymbol{r},\mu)$ and $\chi_1(\boldsymbol{r},\mu)$ and the rotation due to the magnetic field are correctly captured by the Ginzburg-Landau solutions $\psi_0(\boldsymbol{r},\mu)$ and $\psi_1(\boldsymbol{r},\mu)$ and observe accurate agreement in 6.3. To obtain such an agreement, the two model parameters α and β have to be optimized. We performed a full parameter scan to determine optimal values of $\alpha = -2.331$, $\beta = 14.465$, cf. 6.8.

Next, we consider the case of multiple stripes without a magnetic field ($\phi = 0$) on a 32×6 cylinder. As we only obtain DMRG results for open boundary conditions in the x-direction, the corresponding Ginzburg-Landau equation coupling to the hole density from DMRG is not translationally invariant. Thus, we do not immediately expect Bloch waves as solutions. Instead, we find solutions that are localized on the individual stripes and compute their Fourier transform at a momentum k of the superlattice set by the charge density wave which serves as ansatz wave functions $\psi_k(\boldsymbol{r},\mu)$ to compare to DMRG. A detailed discussion of this construction is given in (6.4.1). 6.4 again shows a close agreement between the ansatz wave functions $\psi_k(\boldsymbol{r},\mu)$ from the intertwined Ginzburg-Landau theory and the condensate fragments $\chi_k(\boldsymbol{r},\mu)$. Moreover, this comparison reveals that the different fragments of the condensate can be labeled by the quasi-momentum of the wave function on the superlattice given by the charge density wave. This is the reason we used the label 'k' for both enumerating the fragments $\chi_k(\boldsymbol{r},\mu)$ and model wave functions $\psi_k(\boldsymbol{r},\mu)$. In fact, we observe a 'dispersion', in the sense that the smaller values of k have a larger condensate fraction, i.e. $k' < k$ implies $\varepsilon_{k'} > \varepsilon_k$, reflecting the fact that the uniform condensate is the most dominant condensate.

The intertwined Ginzburg-Landau theory allows us to make predictions for larger systems not accessible by DMRG simulations. As an example, we report in Fig. 6.7 the solutions of (6.19) on a 16×16 grid with a CDW of the form $n_h(\boldsymbol{r}) = \sin^2(2\pi x/L)$. For this larger size we can see how, on the $k = 0$ condensate, vortices are effectively pinned between the stripes for the chosen set of parameters $\alpha = -2.331$ and

$\beta = 14.465$. This set of parameters is the optimal choice when fitting to the DMRG results in 6.3. However, we expect the behavior of the intertwined Ginzburg-Landau equation to be more complex in general.

6.4.1 Details on solving the Ginzburg-Landau equations

We describe how to numerically attain the distinct solutions corresponding to the distinct Bloch wave instanton solutions of (6.23). These are computed by numerically minimizing the parent Ginzburg-Landau functional (6.19) with different initial starting vectors. To obtain a uniform solution we start with a constant initial state ψ_0^0, e.g.

$$\psi_0^0(\boldsymbol{r}) = 1.0, \tag{6.27}$$

as shown in 6.6(a). $\psi(\boldsymbol{r})$ is a function with complex values on the vertices of the lattice. The values of hole-density $n_h(\boldsymbol{r})$ on the lattice are taken from measurements of the ground state from DMRG. We obtain a local minimum of the Ginzburg-Landau functional (6.19) by employing the BFGS algorithm [511–514]. Convergence is tested by postulating the norm of the Jacobian matrix to be of size $< 10^{-7}$. This allows us to obtain the wave function $\psi_0(\boldsymbol{r})$, as shown in 6.6(b). To compare this to the macroscopic wave function from DMRG, we compute the corresponding d-wave order parameter on the links of the lattice by (6.26). The final model wave function $\psi_0(\boldsymbol{r}, \mu)$ is then shown in 6.6(c).

To compute different solutions we initialize the minimization procedure with a starting state of the form

$$\psi_k^0(x, y) = \sin(2\pi k x / L). \tag{6.28}$$

The solution shown in 6.3(d) is obtained when setting $k = 1$. The corresponding initial configuration is shown in 6.6(d). After finding the local minimum associated with this initial solution, we obtain $\psi_1(\boldsymbol{r})$ as shown in 6.6(e), and finally the d-wave order parameter $\psi_1^d(\boldsymbol{r})$ shown in 6.6(f).

Choice of model parameters α and β

The proposed intertwined Ginzburg-Landau functional in (6.19) only has two parameters α and β up to an overall constant factor set by m^*. To obtain good agreement we have investigated the dependence of the solutions on these parameters. These have then been compared to the macroscopic wave functions $\chi_k(\boldsymbol{r}_i, \mu)$ obtained from DMRG. To find the optimal parameters for α and β we consider the following metric comparing both these wave functions:

$$\mathcal{D}_k = \min_\theta \parallel \chi_k(\boldsymbol{r}_i, \mu) - e^{i\theta}\psi_k(\boldsymbol{r}_i, \mu) \parallel^2 . \tag{6.29}$$

The phase θ is introduced due to the freedom of phase in the solution of both the eigenvalue problem to compute $\chi_k(\boldsymbol{r}_i, \mu)$ and the U(1) symmetry of the Ginzburg-Landau functional (6.19). Since only two parameters are involved we can perform a full parameter scan to obtain an optimal fit. The metrics (6.29) when fitting the DMRG ground state with $\phi = 4\pi$ on the 24×6 open boundary sample as in Fig. 6.3 are shown in Fig. 6.8. The combined metric $\mathcal{D}_0 + \mathcal{D}_1$ is minimized for the parameters $\alpha = -2.331$ and $\beta = 14.465$.

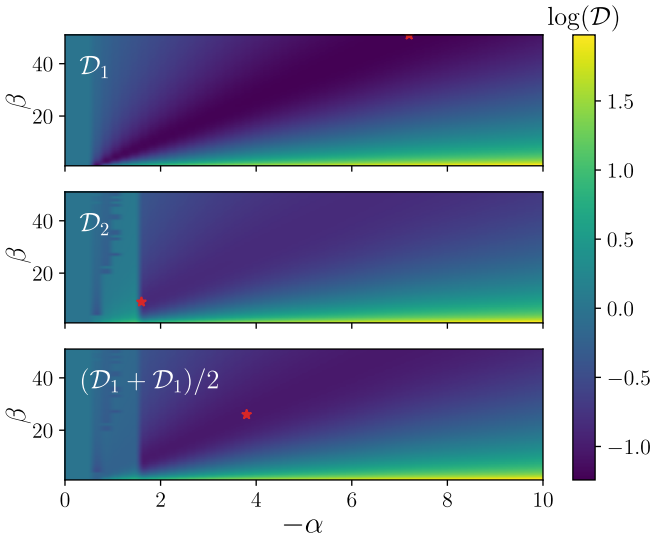

FIGURE 6.8: Full parameter scan for the metric (6.29) for model parameters α and β of the intertwined Ginzburg-Landau equation when comparing to the DMRG ground state shown in 6.3. The red star indicates the minimizing model parameters. Scan performed for a 24×6 sample with beckground flux per plaquette $\phi = 4\pi$.

Bloch waves from solutions of the Ginzburg-Landau equation in the multiple stripe case

In the case of two stripes in the system, we demonstrated in 6.3 that the macroscopic wave functions $\chi_k(\boldsymbol{r}, \mu)$ of the superconducting condensates in (6.17) are well described by solutions $\psi_k(\boldsymbol{r}, \mu)$ of the intertwined Ginzburg-Landau equations (6.23) with two different initial ansatz wave functions, cf. 6.6.

For more than two stripes the situation is slightly complicated by the fact that our DMRG simulations are performed on open boundary conditions in the x-direction. Hence, the solutions to the Ginzburg-Landau equations do not a priori satisfy Bloch's theorem and, hence, momentum is not a good quantum number. We solve the intertwined Ginzburg-Landau equation (6.23) with the hole density given by the ground state from DMRG on the cylindrical boundary conditions. Thereby, we obtain solutions that are either uniform $\psi_{\mathrm{sol},0}(\boldsymbol{r})$ or have a "kink" between stripe i and $i+1$, which we denote by $\psi_{\mathrm{sol},p}(\boldsymbol{r})$, where $p = 1, \ldots, N_{\mathrm{str}} - 1$ and N_{str} denotes the number of stripes in the system. Here, p labels the position of the stripe in the x direction. These direct solutions $\psi_{\mathrm{sol},p}(\boldsymbol{r})$ in the case of the 32×6 cylinder, with $t'/t = 0.2$ and $U/t = 10$, are shown in 6.9(a). In this case, we consider the case of zero magnetic flux, i.e. $\phi = 0$. On an infinitely long cylinder with a perfectly periodic modulation of the charge density, the position of the kink does not impact the value of the free energy functional (6.19) due to translational invariance. Hence, all solutions with only one kink are degenerate and the system can choose to form superpositions of these states. We consider the wave functions

$$\psi_{\mathrm{loc},p}(\boldsymbol{r}) = \psi_{\mathrm{sol},p+1}(\boldsymbol{r}) - \psi_{\mathrm{sol},p}(\boldsymbol{r}), \tag{6.30}$$

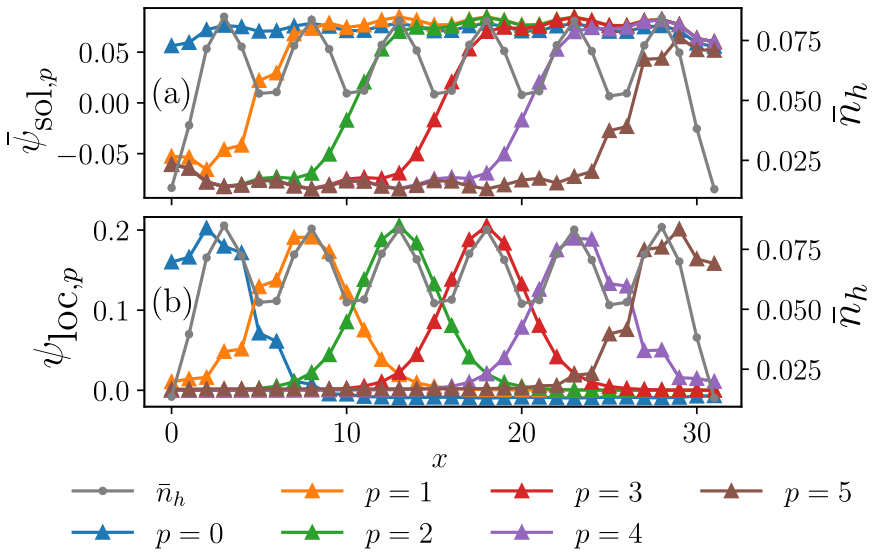

FIGURE 6.9: (a) Solutions of the intertwined Ginzburg-Landau equation in the presence of six stripes on a 32×6 cylinder with open boundary conditions in the x-direction. We show the y-averaged values of $\psi_k(\boldsymbol{r}, \mu)$. For every neighboring pair of stripes a solution exhibiting a "kink" at their interface is found. (b) Corresponding localized wave functions $\psi_{\mathrm{loc},p}$ as defined in (6.30).

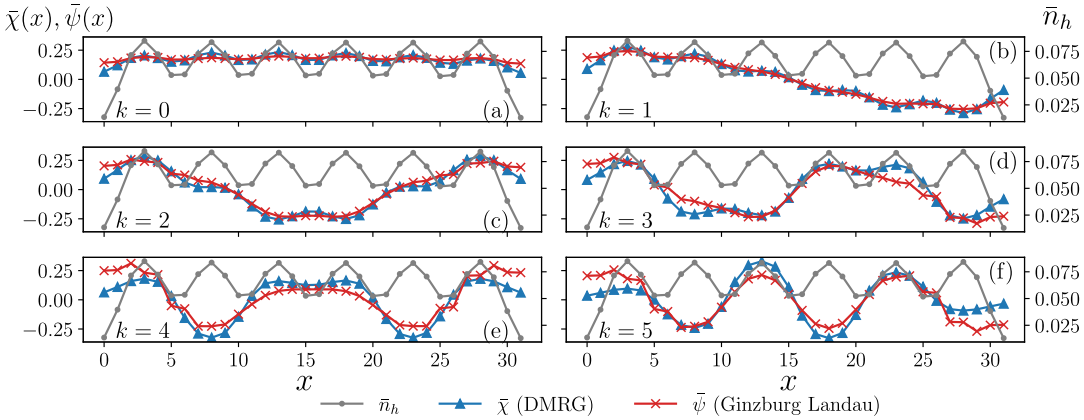

FIGURE 6.10: Complete set of macroscopic wave functions of the ground state of 32×6 cylinder at $t'/t = 0.2$, $U/t = 10$, and doping $p = 1/16$, corresponding to six stripes. Blue lines (triangles) denote wave functions from DMRG of the six fragments of the condensate. Red lines are the corresponding solutions $\psi_k(\boldsymbol{r})$ of the intertwined Ginzburg-Landau theory as specified in (6.31) for $\alpha = -1.3$ and $\beta = 13$. Different panels show the results for different values of the momentum k. We report close agreement between the DMRG data and the Ginzburg-Landau ansatz for every single fragment.

which are localized on stripe p, as shown in 6.9(b). In order to construct Bloch wave functions with a given quasi-momentum k we construct the wave functions

$$\psi_k(\boldsymbol{r}) = \sum_{p=0}^{N_{\text{str}}-1} \cos(\pi\ p \cdot k/(N_{\text{str}}-1))\psi_{\text{loc},p}(\boldsymbol{r}). \tag{6.31}$$

This procedure yields a wave function for $k = 0, \ldots, N_{\text{str}} - 1$, where $k = 0$ corresponds to the uniform solution. The y-averaged solutions $\bar{\psi}_k(x)$ in case of six stripes for the 32×6 cylinder is shown for select values of k in 6.4 and all values of k in 6.10. We report close agreement between the Ginzburg-Landau ansatz wave functions $\psi_k(\boldsymbol{r})$ and the macroscopic wave functions of the dominant condensate fragments from ground state DMRG. Remarkably, the labeling of Bloch states in (6.31) exactly corresponds to the ordering of the fragments by their condensate fraction, i.e. the $k = 0$ is the most dominant eigenvalue, $k = 1$ the second most dominant, etc., until $k = 5$ corresponds to the least dominant eigenvalue.

6.5 Summary

The coexistence of CDWs and superconductivity has by now been reported by numerous numerical studies of doped Hubbard- and t-J-like models [113–115, 473–478]. In this chapter we showed by employing the Penrose-Onsager criterion for superconductivity, that this coexistence yields a fragmentation of the superconducting condensate in the case of the t-t'-U model on the square lattice, generalizing results obtained for the t-t'-J model [498]. This is seen from investigating the eigenvalues and eigenvectors of a suitably chosen two-body density matrix, which correspond to the condensate fractions and the macroscopic wave functions of the Cooper pairs, where more than one dominant eigenvalue is observed. The density matrix itself and the particle density modulations corresponding to a CDW are obtained through two-dimensional DMRG simulations on narrow cylinders or with open boundary conditions. We found that the condensate fragments are localized on the individual stripes of the CDW.

Moreover, we proposed a macroscopic field theory that describes the wave functions of the fragmented condensate with remarkable precision. The key proposition is the intertwined Ginzburg-Landau theory (6.19), where the mass term of the superconducting order parameter is coupled to a static field proportional to the hole density of the system. The CDW is seen as a periodic background potential that leads to the existence of multiple solutions of the Ginzburg-Landau theory, which correspond to Bloch waves at different momenta. These distinct solutions of the intertwined Ginzburg-Landau theory have been shown to precisely describe the individual fragments of the superconducting condensates, see Fig. 6.3 and 6.4. Importantly, the model we proposes only features two parameters α and β (up to an overall constant factor m^*) and can therefore be considered a minimal model coupling the charge density to the superconducting order.

Our findings give rise to an intuitive picture of the behavior of pairs in the stripe-fragmented superconductor. Here, a Cooper pair is in an unequal-weight superposition of the condensate wave functions at different momenta. The individual macroscopic wave functions constitute *local* minima of the Ginzburg-Landau free energy functional (6.19) and do not necessarily yield the same value of the Ginzburg-Landau free energy. Nevertheless, the Cooper pair can "tunnel" between these different minima. An energy difference between these minima is then reflected by a

different occupation number in these modes, just as we observe in our DMRG data. We numerically verified that the uniform condensate solution is a *global* minimum of the Ginzburg-Landau functional, which explains why this mode is populated with the highest condensate fraction, whereas finite momentum solutions have higher values of the Ginzburg-Landau free energy and thus a smaller condensate fraction.

The final question we would like to address is whether a fragmented Cooper condensate could be observed in materials. While our particular choice of parameters in the t-t'-U might not be the set of couplings expected in e.g. the Cuprate superconductors, it is very likely that such supersolid phases with fragmented condensates can occur in more complex scenarios, which then capture the physics of actual materials more accurately. Several studies employing scanning Josephson tunneling spectroscopy have recently reported the emergence of a pair-density wave state [481] in $Bi_2Sr_2CaCu_2O_{8+x}$ [485, 515], in transition metal dichalcogenides [516], or the heavy-fermion superconductor UTe_2 [486]. A peak in the superconducting order parameter at finite momentum has been detected, indicating the emergence of a pair density wave. Besides this finite momentum peak, however, a zero momentum contribution was also measured. We would like to point out that this scenario bears a strong resemblance to our findings, as we propose that the Cooper pairs are in a superposition of condensates with different momentum quantum numbers. Hence, if a fragmented superconductor were to be realized, further peaks at different momenta could indicate this state.

Conclusions and outlook

In this thesis, we explored two of the most active topics in quantum many-body physics, topology and frustration, using two complementary approaches: classical numerical techniques, and the development of schemes to implement such models in quantum simulators.

In Part II of the Thesis we studied topological phases exhibiting excitations with fractional charge and statistics, called anyons, designing and analyzing platforms to experimentally detect them. In Chapter 3, we focused on the anyons present in Fractional Quantum Hall Effect (FQHE) liquids, called quasi-holes. We proposed a scheme considering the insertion of impurities in a FQHE liquid. The impurities interact with the liquid via a repulsive contact potential, leading them to bind to the quasi-holes. Using a mean-field argument, we found that the angular momentum of the impurities is renormalized by a filling-dependent factor due to this interaction with the liquid. We confirmed this by numerical simulations, using exact diagonalization and Monte Carlo sampling of trial wavefunctions. Importantly, for multiple impurities we found that the angular momentum is proportional to the anyonic statistical parameter of the underlying quasi-holes. The anyonic nature of quasi-holes can then be reconstructed by measuring the angular momentum of impurities in FQHE liquids. We studied this scheme for Abelian quasi-holes in a Laughlin Liquid, discussing its robustness when changing the filling, the type of interactions and the nature of the impurities. Finally, we extended the results to non-Abelian anyons in the Moore-Read state, finding that the relations derived for the angular momentum still hold for them. Notably, as this type of anyons the observable statistical parameter is a function of the number of particles in the system, this gives a direct signature of their non-Abelian nature. This protocol opens up a new way to detect Abelian and non-Abelian anyons in FQHE systems realized in quantum simulators, and can possibly be extended to other types of FQHE states.

In Chapter 4 we proposed another technique to detect non-Abelian anyons in another platform, one-dimensional topological superconductors. We focus on a realistic model composed by a semiconducting nanowire on top of an ordinary s-wave superconductor. The interplay of spin-orbit coupling in the wire and proximity-induced superconductivity drives the system in an effective p-wave superconducting phase that can be tuned to be trivial or topological. In the latter, anyons are expected to arise as edge states called Majorana Zero Modes. We developed a protocol to detect their presence through the analysis of the spectrum of the radiation re-emitted by the wire, following an interaction with a pulse of intense light. In this highly non-linear process, called High Harmonic Generation, the system can re-emit light at frequencies up to hundreds of times the one of the incoming pulse. By computing the time dependent electric dipole of the wire during this process numerically solving the time dependent Schrödinger equation, we retrieved this spectrum. We showed that from it, we could infer the full band structure of the system. In particular, we found that in the topological phase there is a sub-bandgap emission plateau related to the presence of zero energy modes, absent in the trivial phase. We used this signature to define a contrast order parameter, that we used to classify the full

topological phase diagram of the system. Moreover, we showed that this plateau is robust against the presence of disorder, confirming the topological protection, and confirmed that it is due to edge states by focusing the pulses on the edge and the bulk of the system and detecting two different behaviors. These results give an alternative to transport techniques to detect Majorana Zero Modes, and it is a general protocol that can be extended to other topological systems to detect their edge states, in one dimension or higher.

In Part III, we studied how frustration can lead to the formation of exotic phases in strongly-correlated lattice systems. In Chapter 5, we started by studying the Bose-Hubbard model on a geometrically frustrated triangular ladder, showing that three different phases can be stabilized with only contact interactions: a Bond Order Wave, a Superfluid and a Chiral Superfluid. We then found that by adding a nearest-neighbor density-density interaction a Density Wave can be stabilized, and the transition between the Bond Order Wave and the Density Wave is compatible with a Deconfined Quantum Critical Point (DQCP). We did so via VUMPS simulations, computing the scaling of the correlation length and the central charge at criticality as a function of the bond dimension. Finally, we proposed an experimental platform for the realization of these phases in optical lattices. By employing a state-dependent potential at the antimagic wavelength we could engineer the hoppings and interactions necessary for the onset of frustration and DQCP, avoiding heating processes that could suppress quantum fluctuations. We then moved to revisiting the phase diagram of the extended Fermi-Hubbard model, where frustration is due to the competing contact and nearest-neighbor interactions. In this case we found using VUMPS that a phase transition between a Bond Order Wave and a Charge Density Wave is also compatible with a DQCP. Furthermore, in presence of a spin-spin interaction another deconfined transition can arise between an Antiferromagnetic phase and the Bond Order Wave. We show that these critical points are associated with the presence of finite non-local order parameters, meaning that these phase transitions are different in nature from the bosonic one. These results give a comprehensive view on deconfined quantum criticality in one dimension and provide a new platform to study these phenomena.

Finally, in Chapter 6 we explored how frustration leads to the onset of Superconductivity intertwined with Charge Density Waves in the two-dimensional Hubbard model on the square lattice. In particular, we studied the system with frustrated next-nearest-neighbor hoppings. By means of large scale DMRG simulations we showed how it is possible to find coexistence between a Superconducting phase and a Charge Density Wave for strong contact interactions and low hole doping. While this confirms previous results, we most importantly showed how this intertwined phase is associated with a fragmentation of the superconducting condensate. To do so we employed the Penrose-Onsager criterion to study the two-body density matrix, finding a number of condensate fragments equal to the number of density stripes in the system. To show the close connection between the density modulations and superconductivity, we developed an effective Ginzburg-Landau theory, finding that a Landau free energy with only two free parameters proportional to the charge density pattern, can reproduce all the macroscopic wavefunctions associated to the fragments. Moreover, we showed that this picture is valid also in presence of a magnetic field, with the phase pattern obtained from the Ginzburg-Landau theory matching the one obtained from the DMRG simulations. These results give a new perspective on the nature of the superconducting condensate in these systems, and a new tool to approach the study of these intertwined phases, with possible extensions to other models and other geometries.

Appendix A

Exact Diagonalization algorithms

In this appendix we will describe the main techniques used to perform exact diagonalization of quantum systems. We will start by introducing the Lanczos method to efficiently compute the lower eigenvalues and eigenvectors of a Hermitian matrix. We will then pass to the description of the dynamics in the ED framework.

Lanczos method for ground state search

In this section we will describe in details the Lanzos method [191], one of the most widespread algorithms in exact diagonalization to find the ground state of a quantum system. This algorithm only computes the k lowest eigenvalues and eigenvectors of a matrix without ever storing the full Hamiltonian in memory. This makes it the most suited for the study of large systems, as it efficiently performs in both CPU and memory.

Following the variational principle, we can write the energy functional as

$$E[\Psi] = \frac{\langle\Psi|\hat{H}||\Psi\rangle}{\langle\Psi|\Psi\rangle}, \tag{A.1}$$

that is minimized for $|\Psi\rangle = |\Psi_0\rangle$, with ground state energy $E_0 = E[\Psi_0]$. Starting from an initial state $|\Psi\rangle$ we can to minimize E by computing the gradient

$$\frac{\delta E[\Psi]}{\delta\langle\Psi|} = \frac{\hat{H}|\Psi\rangle}{\langle\Psi|\Psi\rangle} - \frac{\langle\Psi|\hat{H}|\Psi\rangle}{\langle\Psi|\Psi\rangle^2}|\Psi\rangle \equiv |\Psi_a\rangle, \tag{A.2}$$

and lowering the energy by moving in the opposite direction $E[\Psi - \alpha|\Psi_a\rangle] < E[\Psi]$. To find the optimal value of the real parameter α we can minimize the function $E[\Psi - \alpha|\Psi_a\rangle]$, noting that this corresponds to diagonalizing H in the subspace

$$\mathcal{K}_1 := \text{span}\{|\Psi\rangle, |\Psi_a\rangle\} = \text{span}\{|\Psi\rangle, \hat{H}|\Psi\rangle\}. \tag{A.3}$$

We start by writing an orthonormal basis of $\mathcal{K}_1$ by taking $|v_0\rangle = |\Psi\rangle/\sqrt{\langle\Psi|\Psi\rangle}$ and orthogonalizing $H|\Psi\rangle$ with respect to $|v_0\rangle$:

$$b_1|v_1\rangle := |\tilde{v}_1\rangle = H|v_0\rangle - a_0|v_0\rangle, \tag{A.4}$$

where $a_0 = \langle v_0|H|v_0\rangle$ is the orthogonal projection and $b_1 = \sqrt{\langle\tilde{v}_1|\tilde{v}_1\rangle}$ is a normalizing constant. By defining $a_1 = \langle v_1|H|v_1\rangle$, we can write the Hamiltonian in the subspace $\mathcal{K}_1$ as

$$H_{\mathcal{K}_1} = \begin{pmatrix} a_0 & b_1 \\ b_1 & a_1 \end{pmatrix}. \tag{A.5}$$

The ground state of $H_{\mathcal{K}_1}$ yields the optimal linear combination, that is the optimal value of α that minimizes the energy.

This process can be iterated until convergence to the ground state of H is achieved with the desired precision. We can however perform all the steps at once by constructing the *Krylov subspace* $\mathcal{K}_L$ of dimension L as

$$\mathcal{K}_L := \text{span}\{|v_0\rangle, \hat{H}|v_0\rangle, \hat{H}^2|v_0\rangle, \dots, \hat{H}^{L-1}|v_0\rangle\}. \tag{A.6}$$

Diagonalizing H in $\mathcal{K}_L$ amounts to performing $L-1$ steps of gradient descent. To do this we can construct an orthonormal basis of $\mathcal{K}_L$ by repeatedly orthogonalizing the vectors $|\tilde{v}_i\rangle = \hat{H}^i|v_0\rangle$ with respect to the previous ones:

$$b_{n+1}|v_{n+1}\rangle := |\tilde{v}_{n+1}\rangle = \hat{H}|v_n\rangle - a_n|v_n\rangle - b_n|v_{n-1}\rangle, \tag{A.7}$$

with $a_n = \langle v_n|H|v_n\rangle$ and $b_n = \langle v_n|H|v_{n-1}\rangle$. In this way the projected Hamiltonian $H_{\mathcal{K}_L}$ becomes a tridiagonal matrix

$$H_{\mathcal{K}_L} = \begin{pmatrix} a_0 & b_1 & 0 & \dots & 0 \\ b_1 & a_1 & b_2 & \dots & 0 \\ 0 & b_2 & a_2 & \dots & 0 \\ \vdots & \vdots & \vdots & \ddots & \vdots \\ 0 & 0 & 0 & \dots & a_{L-1} \end{pmatrix}. \tag{A.8}$$

By denoting as Ψ_L and E_L the ground state and the ground state energy of $H_{\mathcal{K}_L}$, we can then write the ground state of H as

$$|\Psi_0\rangle = \sum_{i=0}^{L-1} \Psi_i^L |v_i\rangle. \tag{A.9}$$

Dynamics in the Exact Diagonalization framework

The solution of the time-dependent Schrödinger equation can usually be represented in terms of a unitary time evolution operator $U(t)$ such that

$$|\Psi(t)\rangle = U(t)|\Psi(0)\rangle, \quad i\partial_t U(t) = H(t)U(t). \tag{A.10}$$

The solution of this equation for a time dependent Hamiltonian $H(t)$ is usually obtained by the *time-ordered* exponential

$$U(t) = \mathcal{T} \exp\left(-i \int_0^t H(t')dt'\right). \tag{A.11}$$

The computation of this exponential is numerically infeasible, and we usually resort to a *trotterization* of the time evolution operator. This amounts to approximating the exponential as a product of N infinitesimal evolutions over a time step $\delta t = t/N$ of the form

$$U(t) \approx \prod_{n=0}^{N-1} e^{-iH(n\delta t)\delta t}. \tag{A.12}$$

By using efficient trotterization, usually the error per step compared to the exact solution is of the order of δt^2 [517]. The problem then reduces to computing the infinitesimal evolution operator $e^{-iH(n\delta t)\delta t}$. One way to do that is to use the *Crank-Nicholson* method

$$e^{-iH(n\delta t)\delta t} \sim \frac{1 - iH(n\delta t)\delta t/2}{1 + iH(n\delta t)\delta t/2}, \tag{A.13}$$

where the denominator indicates the inverse of the matrix. This approach, compared to a naive discretization $e^{-iH(n\delta t)\delta t} \sim 1 - iH(n\delta t)\delta t$, has a smaller error of the order of δt^3 and keeps the unitary nature of the evolution operator at any step.

Appendix B

Monte Carlo Integration of ansatz FQHE wavefunctions

For large systems of more than $N \sim 10$ particles, the Exact Diagonalization of the full Hamiltonian of majority particles interacting with impurities in the lowest Landau Level becomes intractable. In this scenario, by assuming that the impurities directly bind to quasi-holes, we can compute the ground state quantities by directly sampling the ansatz wavefunction representing the liquid-impurities mixture. The correctness of this approach has been crosschecked with exact diagonalization results for small sizes. In this Appendix we briefly review the algorithm that we used to perform the Monte Carlo integration.

Our goal is to compute the expectation value of quantities on either the Laughlin state or the Moore-Read state. We will generally call it $\Psi(\{z\},\{w\})$, and it will be a function of the positions of the majority particles and the impurities.

The expectation value of a generic operator $\mathcal{O}$ can be written as

$$\langle \mathcal{O} \rangle = \frac{\langle \Psi | \mathcal{O} | \Psi \rangle}{\langle \Psi | \Psi \rangle} = \frac{\int d^N z d^n w \Psi^*(\{z,w\}) \mathcal{O} \Psi(\{z,w\})}{\int d^N z d^n w \Psi^*(\{z,w\}) \Psi(\{z,w\})}. \tag{B.1}$$

The Monte-Carlo procedure then starts from rewriting this integral in terms of a probability distribution $P(\{z,w\})$:

$$\langle \mathcal{O} \rangle = \int d^N z d^n w P(\{z,w\}) \frac{\mathcal{O}\Psi(\{z,w\})}{\Psi(\{z,w\})}, \quad P(\{z,w\}) = \frac{|\Psi(\{z,w\})|^2}{\int d^N z d^n w |\Psi(\{z,w\})|^2}. \tag{B.2}$$

We can then compute the expectation value $\langle \mathcal{O} \rangle$ by sampling configurations from the probability distribution $P(\{z,w\})$ and computing the average of $\mathcal{O}\Psi(\{z,w\})/\Psi(\{z,w\})$ over the samples

$$\langle \mathcal{O} \rangle \approx \frac{1}{N} \sum_{i=1}^{N} \frac{\mathcal{O}\Psi(\{z_i,w_i\})}{\Psi(\{z_i,w_i\})}, \tag{B.3}$$

where N is the number of samples and $\{z_i,w_i\}$ are the sampled configurations. The error of this estimate scales as $1/\sqrt{N}$. This procedure is particularly efficient for FQH ansatz states and the computation of the angular momentum. We can indeed write the total angular momentum operator as

$$L_z = \sum_{i=1}^{N} z_i \partial_{z_i} + \sum_{j=1}^{n} w_j \partial_{w_j} + h.c., \tag{B.4}$$

or, if we are only interested in the impurities' contribution to the angular momentum, we can sum only over the impurities coordinates. As these are differential

operators, we can write the term to be summed on in (B.3) as

$$\frac{z_i \partial_{z_i} \Psi(\{z,w\})}{\Psi(\{z,w\})} = z_i \partial_{z_i} \log \Psi(\{z,w\}). \tag{B.5}$$

This means that we are only interested in computing the logarithm of the states. As the FQH wavefunctions are polynomials in the coordinates, this amounts to computing the sum of linear terms (plus a quadratic term to account for the exponential decay). For Moore-Read states the Pfaffian can be computed by efficient algorithms [518]. Finally, directly computing the logarithm of the wavefunctions also solves the problem of their magnitude. Indeed, the FQHE wavefunctions are not normalized, and can have values ranging several orders of magnitudes, leading to numerical instabilities.

The algorithm is then structured as follows:

1. Generate a random configuration of particles and impurities coordinates $\{z,w\}$, sampled from a uniform distribution, and compute $\log \Psi(\{z,w\})$.

2. Generate a random *shift* of the particles and impurities positions $\{\delta z, \delta w\}$,, sampled from a uniform distribution. Compute the value of the wavefunction at the shifted position $\log \Psi(\{z',w'\})$.

3. Accept or reject the new configuration using a Metropolis rule. Generate a random number $r \in [0,1)$ from a uniform distribution. If $r < \exp(2\log \Psi(\{z',w'\}) - 2\log \Psi(\{z,w\}))$, accept the new configuration, otherwise keep the old one.

4. Repeat steps number 2. and 3. for a fixed number of times to thermalize the system. In this way the final configuration will be sampled from the probability distribution $P(\{z,w\})$.

5. Compute the values of the total and impurities angular momenta on this configuration.

6. Repeat steps 1. to 5. for N times, and compute the average of the angular momenta over all the samples.

Appendix C

Bosonization analysis of deconfined quantum critical points in the Hubbard model

Interacting spinful one dimensional fermions in the low energy limit are usually well described by a sine-Gordon model [177]

$$\mathcal{H}_\nu^{SG} \doteq \frac{1}{2}\int dx \left[v_\nu K_\nu (\nabla\vartheta_\nu)^2 + \frac{v_\nu}{K_\nu}(\nabla\varphi_\nu)^2 + \frac{g_\nu}{\pi^2 a^2}\cos(\sqrt{8\pi}\varphi_\nu)\right]. \tag{C.1}$$

Here v_ν, K_ν and g_ν are the excitations velocities, Luttinger parameters, and scattering amplitudes respectively while $\varphi_\nu(x)$, $\vartheta_\nu(x)$ ($\nu = c,s$ denote the charge and spin channels respectively) are bosonic fields. While the first two terms in Eq. (C.1) describe free fermions and thus promote fluctuations of the bosonic fields, the last term favors the pinning of $\varphi_\nu(x)$ to specific fixed values. In particular, within a RG analysis the equation

$$2\pi v_\nu (K_\nu - 1) \geq |g_\nu| \tag{C.2}$$

describes the gapless condition for the ν channel. On the other hand, a pinned value of φ_ν signals the presence of a finite gap. Here, we are exactly interested in those phases where the spontaneous breaking of discrete symmetries (SSB), associated with the presence of a local order, gives rise to a finite gap in both the charge and spin channel. This fact is motivated by the possible appearance of continuous phase transitions between different SSB regimes thus representing examples of the recently introduced concept [**roberts2019a**, 173, 174, 383–385, 503] of 1D deconfined quantum critical points (DQCP).

Within the sine-Gordon description above, three possible fully gapped SSB phases can occur: an antiferromagnet (AF) with perfect alternation between fermions with opposite spin associated with the breaking of the spin rotational symmetry; a bond-ordered-wave (BOW) with an effective lattice dimerization induced by the breaking of the site-inversion symmetry; a charge-density-wave (CDW) with perfect alternation between empty sites and fermionic pairs generated by the breaking of the translational symmetry. These phases are captured by the behavior of the relative microscopic order parameters

$$\begin{aligned} \mathcal{O}_{AF}(j) &\equiv (-1)^j (n_{j\uparrow} - n_{j\downarrow}), \\ \mathcal{O}_{BOW}(j) &= (-1)^j \sum_\sigma (c^\dagger_{j\sigma} c_{j+1\sigma} + h.c.), \\ \mathcal{O}_{CDW}(j) &= (-1)^j \sum_\sigma (n_{j\sigma} - 1). \end{aligned} \tag{C.3}$$

The standard field theory treatment of 1D lattice systems of correlated fermions is based on a weak coupling approach in the continuum limit, known as bosonization. Upon replacing the discrete sum over sites j with integrals over the coordinate x, namely: $\sum_j \to \frac{1}{a}\int dx$, with a lattice spacing, the discrete ladder operators $c_{j\sigma}, c^\dagger_{j\sigma}$ are replaced with fermionic fields. Thanks to the peculiar nature of the one dimensional Fermi surface, which consists of just two disconnected points $\pm k_F$, these fields can be conveniently rewritten as a sum of right (R) and left (L) fields $\psi_{\chi\sigma}(x)$ ($\chi = R, L$), each of which acts as ladder operator at one of the two Fermi points. Explicitly:

$$c_{j\sigma} \to \sqrt{a}\left[e^{ik_F x}\psi_{R\sigma}(x) + e^{-ik_F x}\psi_{L\sigma}(x)\right] \tag{C.4}$$

Then, the bosonization procedure amounts to rewrite $\psi_{\chi\sigma}(x)$ in terms of bosonic fields, namely:

$$\psi_{\chi\sigma} = \frac{\eta_{\chi\sigma}}{2\pi\alpha} e^{i\sqrt{\frac{\pi}{2}}[\chi\varphi_c(x)+\vartheta_c(x)+\sigma(\chi\varphi_s(x)+\vartheta_s(x))]} \quad , \tag{C.5}$$

where $\eta_{\chi\sigma}$ are Klein factors preserving the anticommutation rules and $\alpha \sim a$ is an ultraviolet cutoff. In this way, Eqs. (C.3) can be rewritten in terms of the bosonic field appearing in Eq. (C.1)

$$\begin{aligned} \mathcal{O}_{AF}(x) &\sim \cos(\sqrt{2\pi}\varphi_c)\ \sin(\sqrt{2\pi}\varphi_s), \\ \mathcal{O}_{BOW}(x) &\sim \cos(\sqrt{2\pi}\varphi_c)\ \cos(\sqrt{2\pi}\varphi_s), \\ \mathcal{O}_{CDW}(x) &\sim \sin(\sqrt{2\pi}\varphi_c)\ \cos(\sqrt{2\pi}\varphi_s). \end{aligned} \tag{C.6}$$

Within a RG treatment, one can show that in each of the three phases both the charge and spin bosonic field φ_ν are pinned to specific values [519, 520], see the table below

	φ_s	φ_c
AF	$\sqrt{\frac{\pi}{8}}$	0
BOW	0	0
CDW	0	$\sqrt{\frac{\pi}{8}}$

It is now important to relate the behavior of the two possible gaps to the Luttinger constants K_ν. Indeed, one can rigorously show that $K_\nu = 0$ implies the presence of a finite gap in the ν channel. One can now derive the behavior of the two-point correlation functions relative to the order parameters in Eq. (C.6). As demonstrated in the table above, φ_s has the same value for BOW and CDW. This point shows that the spin gap remains open at the transition between these two phases and therefore that $K_s = 0$. On the other hand, this is not the case for φ_c. Crucially, it is possible to demonstrate that at this transition point

$$\langle \mathcal{O}_{BOW}(r)^\dagger \mathcal{O}_{BOW}(0)\rangle \sim r^{-K_c} \sim \langle \mathcal{O}_{CDW}(r)^\dagger \mathcal{O}_{CDW}(0)\rangle \quad . \tag{C.7}$$

Eq. (C.7) thus proves that at this transition point the correlators capturing the BOW and CDW phases vanish algebraically with same critical exponent. This result thus unambiguously rules out a possible first order phase transition and, at the same time, proves the presence of deconfined quantum critical point associated with the closing uniquely in one point of the charge gap. Moreover, we can derive further properties occurring at this DQCP. Specifically, as the spin gap remain open and $\varphi_s = 0$ this implies the presence of an emergent $SU(2)$ symmetry associated with the presence of a Luther-Emery phase captured by the long-range order of the parity operator

$$C_P^{(s)}(r) = \langle \prod_{j\leq r} e^{i\pi(n_{j\uparrow}-n_{j\downarrow})} \rangle \sim \langle [\cos(\sqrt{2\pi}\varphi_s)]^2 \rangle. \tag{C.8}$$

A similar analysis can be performed for the AF-BOW transition. Contrary to the just discussed case, here $\varphi_c = 0$ in both phases while φ_s acquires different values. In this way one can understand that at the BOW-AF transition point the charge gap remains finite so that $K_c = 0$. An analogous analysis as before can prove that at the transition point

$$\langle \mathcal{O}_{AF}(r)^\dagger \mathcal{O}_{AF}(0) \rangle \sim r^{-K_s} \sim \langle \mathcal{O}_{BOW}(r)^\dagger \mathcal{O}_{BOW}(0) \rangle \quad . \tag{C.9}$$

This behavior again proves the presence of a DQCP with emergent $SU(2)$ symmetry this time associated with a charge gapped Mott insulator captured by the long-range behavior of the parity charge operator

$$C_P^{(c)}(r) = \langle \prod_{j\leq r} e^{i\pi(n_j-1)} \rangle \sim \langle [\cos(\sqrt{2\pi}\varphi_c)]^2 \rangle \quad . \tag{C.10}$$

While these results clearly show the presence of DQCPs, special attention has to be devoted to the CDW-AF transition. Specifically, in these two phases φ_s and φ_c have different values, implying the closure of both gaps at the transition point. This scenario is thus compatible uniquely with the presence of fully gapless Luttinger-Liquid (LL) at criticality. In a LL the correlators have to follow the specific decay $r^{-(K_c^*+K_s^*)}$, where K_ν^* are the fixed point of Eq. (C.2). Here, microscopic parameters of specific Hamiltonians can in principle allow for the condition $K_c^* = K_s^* = 1$ to be fulfilled and thus for a continuous phase transition. If we now apply bosonization to the Hubbard model in Eq.(5.33), we can derive the following expressions for the Luttinger parameters, velocities and scattering amplitudes in Eq. (C.1):

$$\begin{aligned} v_\nu &= 2at(2-K_\nu) \quad , \\ K_c &= 1 - \frac{1}{4\pi t}\left(U + 6V + \frac{J_z}{2}\right) \quad , \\ K_s &= 1 - \frac{1}{4\pi t}\left(-U + 2V + 3\frac{J_z}{2}\right) \quad , \\ g_c &= -\left(U - 2V + \frac{J_z}{2}\right)a = -g_s \quad . \end{aligned} \tag{C.11}$$

At first order in the field expansion in Eq. C.5, bosonization predicts the three transitions described above to occur on the same line

$$U + \frac{J_z}{2} = 2V \quad . \tag{C.12}$$

Notice that by including a correlated hopping term as done in [520], the BOW-CDW and AF-BOW become distinct. Apart from this limitation imposed by our approximation, the expressions in Eqs. (C.11) allow observing that the condition $K_c^* = K_s^* = 1$ is never fulfilled. In particular, at the AF-CDW transition we would have $K_c \approx 1 - \frac{2V}{\pi t}$ and $K_s \approx 1 - \frac{J_z}{2\pi t}$, which for any non-vanishing interaction are both lesser than 1. Since bosonization is believed to provide accurate results in the low energy limit, VUMPS calculations as in Chapter 5 are necessary to explore the possible appearance of DQCPs away from this regime.

Bibliography

[I] T. Graß, B. Juliá-Díaz, N. Baldelli, U. Bhattacharya, and M. Lewenstein. "Fractional Angular Momentum and Anyon Statistics of Impurities in Laughlin Liquids". In: *Phys. Rev. Lett.* 125.13 (2020), p. 136801.

[II] N. Baldelli, B. Juliá-Díaz, U. Bhattacharya, M. Lewenstein, and T. Graß. "Tracing Non-Abelian Anyons via Impurity Particles". In: *Phys. Rev. B* 104.3 (2021), p. 035133.

[III] N. Baldelli, U. Bhattacharya, D. González-Cuadra, M. Lewenstein, and T. Graß. "Detecting Majorana Zero Modes via Strong Field Dynamics". In: *ACS Omega* 7.50 (2022), pp. 47424–47430.

[IV] N. Baldelli, C. R. Cabrera, S. Julià-Farré, M. Aidelsburger, and L. Barbiero. *Frustrated Extended Bose-Hubbard Model and Deconfined Quantum Critical Points with Optical Lattices at the Anti-Magic Wavelength*. 2023. arXiv: 2309.03193 [cond-mat].

[V] N. Baldelli, S. Julià-Farré, A. Montorsi, M. Lewenstein, M. Oshikawa, and L. Barbiero. *(In Preparation)*.

[VI] N. Baldelli, B. Kloss, M. Fishman, and A. Wietek. *Fragmented Superconductivity in the Hubbard Model as Solitons in Ginzburg-Landau Theory*. 2023. arXiv: 2307.11820 [cond-mat, physics:quant-ph].

[VII] K. Kottmann, F. Metz, J. Fraxanet, and N. Baldelli. "Variational Quantum Anomaly Detection: Unsupervised Mapping of Phase Diagrams on a Physical Quantum Computer". In: *Phys. Rev. Research* 3.4 (2021), p. 043184.

[VIII] M. Lewenstein et al. *Attosecond Physics and Quantum Information Science*. 2022. arXiv: 2208.14769 [physics, physics:quant-ph].

[1] P. Kapitza. "Viscosity of Liquid Helium below the λ-Point". In: *Nature* 141.3558 (1938), pp. 74–74.

[2] J. F. Allen and A. D. Misener. "Flow of Liquid Helium II". In: *Nature* 141.3558 (1938), pp. 75–75.

[3] L. D. Landau. "On the Theory of Phase Transitions". In: *Zh.Eksp.Teor.Fiz* 7 (1937), pp. 19–32.

[4] V. L. Ginzburg and L. D. Landau. "On the Theory of Superconductivity". In: *Zh.Eksp.Teor.Fiz.* (1950).

[5] K. v. Klitzing, G. Dorda, and M. Pepper. "New Method for High-Accuracy Determination of the Fine-Structure Constant Based on Quantized Hall Resistance". In: *Phys. Rev. Lett.* 45.6 (1980), pp. 494–497.

[6] D. C. Tsui, H. L. Stormer, and A. C. Gossard. "Two-Dimensional Magnetotransport in the Extreme Quantum Limit". In: *Phys. Rev. Lett.* 48.22 (1982), pp. 1559–1562.

[7] J. G. Bednorz and K. A. Müller. "Possible highTc Superconductivity in the Ba-La-Cu-O System". In: *Z. Physik B - Condensed Matter* 64.2 (1986), pp. 189–193.

[8] M. K. Wu, J. R. Ashburn, C. J. Torng, P. H. Hor, R. L. Meng, L. Gao, Z. J. Huang, Y. Q. Wang, and C. W. Chu. "Superconductivity at 93 K in a New Mixed-Phase Y-Ba-Cu-O Compound System at Ambient Pressure". In: *Phys. Rev. Lett.* 58.9 (1987), pp. 908–910.

[9] X. G. Wen. "Vacuum Degeneracy of Chiral Spin States in Compactified Space". In: *Phys. Rev. B* 40.10 (1989), pp. 7387–7390.

[10] X. G. Wen. "Topological Orders In Rigid States". In: *Int. J. Mod. Phys. B* 04.02 (1990), pp. 239–271.

[11] X.-G. Wen. "Zoo of Quantum-Topological Phases of Matter". In: *Rev. Mod. Phys.* 89.4 (2017), p. 041004.

[12] P. W. Anderson. "Resonating Valence Bonds: A New Kind of Insulator?" In: *Mater. Res. Bull.* 8.2 (1973), pp. 153–160.

[13] P. W. Anderson. "The Resonating Valence Bond State in La2CuO4 and Superconductivity". In: *Science* 235.4793 (1987), pp. 1196–1198.

[14] L. Balents. "Spin Liquids in Frustrated Magnets". In: *Nature* 464.7286 (2010), pp. 199–208.

[15] L. Savary and L. Balents. "Quantum Spin Liquids: A Review". In: *Rep. Prog. Phys.* 80.1 (2016), p. 016502.

[16] D. Fausti, R. I. Tobey, N. Dean, S. Kaiser, A. Dienst, M. C. Hoffmann, S. Pyon, T. Takayama, H. Takagi, and A. Cavalleri. "Light-Induced Superconductivity in a Stripe-Ordered Cuprate". In: *Science* 331.6014 (2011), pp. 189–191.

[17] Y. Cao, V. Fatemi, S. Fang, K. Watanabe, T. Taniguchi, E. Kaxiras, and P. Jarillo-Herrero. "Unconventional Superconductivity in Magic-Angle Graphene Superlattices". In: *Nature* 556.7699 (2018), pp. 43–50.

[18] M. König, S. Wiedmann, C. Brüne, A. Roth, H. Buhmann, L. W. Molenkamp, X.-L. Qi, and S.-C. Zhang. "Quantum Spin Hall Insulator State in HgTe Quantum Wells". In: *Science* 318.5851 (2007), pp. 766–770.

[19] T. Hensgens, T. Fujita, L. Janssen, X. Li, C. J. Van Diepen, C. Reichl, W. Wegscheider, S. Das Sarma, and L. M. K. Vandersypen. "Quantum Simulation of a Fermi–Hubbard Model Using a Semiconductor Quantum Dot Array". In: *Nature* 548.7665 (2017), pp. 70–73.

[20] J. W. McIver, B. Schulte, F.-U. Stein, T. Matsuyama, G. Jotzu, G. Meier, and A. Cavalleri. "Light-Induced Anomalous Hall Effect in Graphene". In: *Nat. Phys.* 16.1 (2020), pp. 38–41.

[21] E. Schrödinger. "Are There Quantum Jumps?: Part II". In: *The British Journal for the Philosophy of Science* 3.11 (1952), pp. 233–242.

[22] T. H. Maiman. "Stimulated Optical Radiation in Ruby". In: *Nature* 187.4736 (1960), pp. 493–494.

[23] D. J. Wineland, R. E. Drullinger, and F. L. Walls. "Radiation-Pressure Cooling of Bound Resonant Absorbers". In: *Phys. Rev. Lett.* 40.25 (1978), pp. 1639–1642.

[24] W. Neuhauser, M. Hohenstatt, P. Toschek, and H. Dehmelt. "Optical-Sideband Cooling of Visible Atom Cloud Confined in Parabolic Well". In: *Phys. Rev. Lett.* 41.4 (1978), pp. 233–236.

[25] W. D. Phillips and H. Metcalf. "Laser Deceleration of an Atomic Beam". In: *Phys. Rev. Lett.* 48.9 (1982), pp. 596–599.

[26] A. Ashkin, J. M. Dziedzic, J. E. Bjorkholm, and S. Chu. "Observation of a Single-Beam Gradient Force Optical Trap for Dielectric Particles". In: *Optics letters* 11.5 (1986), pp. 288–290.

[27] E. L. Raab, M. Prentiss, A. Cable, S. Chu, and D. E. Pritchard. "Trapping of Neutral Sodium Atoms with Radiation Pressure". In: *Phys. Rev. Lett.* 59.23 (1987), pp. 2631–2634.

[28] D. E. Pritchard. "Cooling Neutral Atoms in a Magnetic Trap for Precision Spectroscopy". In: *Phys. Rev. Lett.* 51.15 (1983), pp. 1336–1339.

[29] W. Ketterle and N. J. V. Druten. "Evaporative Cooling of Trapped Atoms". In: *Advances In Atomic, Molecular, and Optical Physics*. Ed. by B. Bederson and H. Walther. Vol. 37. Academic Press, 1996, pp. 181–236.

[30] M. H. Anderson, J. R. Ensher, M. R. Matthews, C. E. Wieman, and E. A. Cornell. "Observation of Bose-Einstein Condensation in a Dilute Atomic Vapor". In: *Science* 269.5221 (1995), pp. 198–201.

[31] K. B. Davis, M. Mewes, M. R. Andrews, N. J. van Druten, D. S. Durfee, D. M. Kurn, and W. Ketterle. "Bose-Einstein Condensation in a Gas of Sodium Atoms". In: *Phys. Rev. Lett.* 75.22 (1995), pp. 3969–3973.

[32] I. Bloch, J. Dalibard, and S. Nascimbène. "Quantum Simulations with Ultracold Quantum Gases". In: *Nature Phys* 8.4 (2012), pp. 267–276.

[33] D. Jaksch, C. Bruder, J. I. Cirac, C. W. Gardiner, and P. Zoller. "Cold Bosonic Atoms in Optical Lattices". In: *Phys. Rev. Lett.* 81.15 (1998), pp. 3108–3111.

[34] M. Greiner, O. Mandel, T. Esslinger, T. Hänsch, and I. Bloch. "Quantum Phase Transition from a Superfluid to a Mott Insulator in a Gas of Ultracold Atoms". In: *Nature* 415 (2002), pp. 39–44.

[35] J. Struck, C. Ölschläger, M. Weinberg, P. Hauke, J. Simonet, A. Eckardt, M. Lewenstein, K. Sengstock, and P. Windpassinger. "Tunable Gauge Potential for Neutral and Spinless Particles in Driven Optical Lattices". In: *Phys. Rev. Lett.* 108.22 (2012), p. 225304.

[36] P. Hauke et al. "Non-Abelian Gauge Fields and Topological Insulators in Shaken Optical Lattices". In: *Phys. Rev. Lett.* 109.14 (2012), p. 145301.

[37] A. Celi, P. Massignan, J. Ruseckas, N. Goldman, I. B. Spielman, G. Juzeliūnas, and M. Lewenstein. "Synthetic Gauge Fields in Synthetic Dimensions". In: *Phys. Rev. Lett.* 112.4 (2014), p. 043001.

[38] M. C. Bañuls et al. "Simulating Lattice Gauge Theories within Quantum Technologies". In: *Eur. Phys. J. D* 74.8 (2020), p. 165.

[39] N. R. Cooper, J. Dalibard, and I. B. Spielman. "Topological Bands for Ultracold Atoms". In: *Rev. Mod. Phys.* 91.1 (2019), p. 015005.

[40] J. Argüello-Luengo, A. González-Tudela, T. Shi, P. Zoller, and J. I. Cirac. "Analogue Quantum Chemistry Simulation". In: *Nature* 574.7777 (2019), pp. 215–218.

[41] W. S. Bakr, J. I. Gillen, A. Peng, S. Fölling, and M. Greiner. "A Quantum Gas Microscope for Detecting Single Atoms in a Hubbard-regime Optical Lattice". In: *Nature* 462.7269 (2009), pp. 74–77.

[42] W. S. Bakr, A. Peng, M. E. Tai, R. Ma, J. Simon, J. I. Gillen, S. Fölling, L. Pollet, and M. Greiner. "Probing the Superfluid–to–Mott Insulator Transition at the Single-Atom Level". In: *Science* 329.5991 (2010), pp. 547–550.

[43] J. Choi, S. Hild, J. Zeiher, P. Schauß, A. Rubio-Abadal, T. Yefsah, V. Khemani, D. A. Huse, I. Bloch, and C. Gross. "Exploring the Many-Body Localization Transition in Two Dimensions". In: *Science* 352.6293 (2016), pp. 1547–1552.

[44] L. Barbiero, C. Schweizer, M. Aidelsburger, E. Demler, N. Goldman, and F. Grusdt. "Coupling Ultracold Matter to Dynamical Gauge Fields in Optical Lattices: From Flux Attachment to $\mathbb{Z}_2$ Lattice Gauge Theories". In: *Sci. Adv.* 5.10 (2019), eaav7444.

[45] A. Mazurenko, C. S. Chiu, G. Ji, M. F. Parsons, M. Kanász-Nagy, R. Schmidt, F. Grusdt, E. Demler, D. Greif, and M. Greiner. "A Cold-Atom Fermi–Hubbard Antiferromagnet". In: *Nature* 545.7655 (2017), pp. 462–466.

[46] M. Xu, L. H. Kendrick, A. Kale, Y. Gang, G. Ji, R. T. Scalettar, M. Lebrat, and M. Greiner. "Frustration- and Doping-Induced Magnetism in a Fermi-Hubbard Simulator". In: *Nature* 620.7976 (2023), pp. 971–976.

[47] M. Aidelsburger, M. Atala, M. Lohse, J. T. Barreiro, B. Paredes, and I. Bloch. "Realization of the Hofstadter Hamiltonian with Ultracold Atoms in Optical Lattices". In: *Phys. Rev. Lett.* 111.18 (2013), p. 185301.

[48] M. Aidelsburger, M. Lohse, C. Schweizer, M. Atala, J. T. Barreiro, S. Nascimbène, N. R. Cooper, I. Bloch, and N. Goldman. "Measuring the Chern Number of Hofstadter Bands with Ultracold Bosonic Atoms". In: *Nature Physics* 11.2 (2015), pp. 162–166.

[49] M. Atala, M. Aidelsburger, M. Lohse, J. T. Barreiro, B. Paredes, and I. Bloch. "Observation of Chiral Currents with Ultracold Atoms in Bosonic Ladders (Article) Author". In: *Nat. Phys.* 10.8 (2014), pp. 588–593.

[50] D. Bluvstein et al. "Controlling Quantum Many-Body Dynamics in Driven Rydberg Atom Arrays". In: *Science* 371.6536 (2021), pp. 1355–1359.

[51] G. Semeghini and *et al.* "Probing Topological Spin Liquids on a Programmable Quantum Simulator". In: *Science* 374.6572 (2021), pp. 1242–1247.

[52] D. Wu et al. *Variational Benchmarks for Quantum Many-Body Problems*. 2023. arXiv: 2302.04919 [cond-mat, physics:physics, physics:quant-ph].

[53] U. Schollwoeck. "The Density-Matrix Renormalization Group in the Age of Matrix Product States". In: *Annals of Physics* 326.1 (2011), pp. 96–192.

[54] R. Orús. "A Practical Introduction to Tensor Networks: Matrix Product States and Projected Entangled Pair States". In: *Annals of Physics* 349 (2014), pp. 117–158.

[55] M. C. Bañuls. "Tensor Network Algorithms: A Route Map". In: *Annu. Rev. Condens. Matter Phys.* 14.1 (2023), pp. 173–191.

[56] S. R. White. "Density Matrix Formulation for Quantum Renormalization Groups". In: *Phys. Rev. Lett.* 69.19 (1992), pp. 2863–2866.

[57] S. R. White. "Density-Matrix Algorithms for Quantum Renormalization Groups". In: *Phys. Rev. B* 48.14 (1993), pp. 10345–10356.

[58] J. Dukelsky, M. A. Martín-Delgado, T. Nishino, and G. Sierra. "Equivalence of the Variational Matrix Product Method and the Density Matrix Renormalization Group Applied to Spin Chains". In: *Europhys. Lett.* 43.4 (1998), pp. 457–462.

[59] E. Stoudenmire and S. R. White. "Studying Two-Dimensional Systems with the Density Matrix Renormalization Group". In: *Annual Review of Condensed Matter Physics* 3.1 (2012), pp. 111–128.

[60] G. Vidal. "Efficient Simulation of One-Dimensional Quantum Many-Body Systems". In: *Phys. Rev. Lett.* 93.4 (2004), p. 040502.

[61] A. J. Daley, C. Kollath, U. Schollwöck, and G. Vidal. "Time-Dependent Density-Matrix Renormalization-Group Using Adaptive Effective Hilbert Spaces". In: *J. Stat. Mech.* 2004.04 (2004), P04005.

[62] J. Haegeman, C. Lubich, I. Oseledets, B. Vandereycken, and F. Verstraete. "Unifying Time Evolution and Optimization with Matrix Product States". In: *Phys. Rev. B* 94.16 (2016), p. 165116.

[63] I. P. McCulloch. *Infinite Size Density Matrix Renormalization Group, Revisited*. 2008. arXiv: 0804.2509 [cond-mat].

[64] V. Zauner-Stauber, L. Vanderstraeten, J. Haegeman, I. P. McCulloch, and F. Verstraete. "Topological Nature of Spinons and Holons: Elementary Excitations from Matrix Product States with Conserved Symmetries". In: *Phys. Rev. B* 97.23 (2018), p. 235155.

[65] F. Verstraete, J. J. García-Ripoll, and J. I. Cirac. "Matrix Product Density Operators: Simulation of Finite-Temperature and Dissipative Systems". In: *Phys. Rev. Lett.* 93.20 (2004), p. 207204.

[66] E. M. Stoudenmire and S. R. White. "Minimally Entangled Typical Thermal State Algorithms". In: *New J. Phys.* 12.5 (2010), p. 055026.

[67] G. Vidal. "Efficient Classical Simulation of Slightly Entangled Quantum Computations". In: *Phys. Rev. Lett.* 91.14 (2003), p. 147902.

[68] F. Verstraete and J. I. Cirac. *Renormalization Algorithms for Quantum-Many Body Systems in Two and Higher Dimensions*. 2004. arXiv: cond-mat/0407066.

[69] G. Vidal. "Entanglement Renormalization". In: *Phys. Rev. Lett.* 99.22 (2007), p. 220405.

[70] P. Silvi, F. Tschirsich, M. Gerster, J. Jünemann, D. Jaschke, M. Rizzi, and S. Montangero. "The Tensor Networks Anthology: Simulation Techniques for Many-Body Quantum Lattice Systems". In: *SciPost Physics Lecture Notes* (2019), p. 008.

[71] J. Tindall, M. Fishman, E. M. Stoudenmire, and D. Sels. "Efficient Tensor Network Simulation of IBM's Eagle Kicked Ising Experiment". In: *PRX Quantum* 5.1 (2024), p. 010308.

[72] T. Begušić, J. Gray, and G. K.-L. Chan. "Fast and Converged Classical Simulations of Evidence for the Utility of Quantum Computing before Fault Tolerance". In: *Sci. Adv.* 10.3 (2024), eadk4321.

[73] N. Read. "Order Parameter and Ginzburg-Landau Theory for the Fractional Quantum Hall Effect". In: *Phys. Rev. Lett.* 62.1 (1989), pp. 86–89.

[74] D. J. Thouless, M. Kohmoto, M. P. Nightingale, and M. den Nijs. "Quantized Hall Conductance in a Two-Dimensional Periodic Potential". In: *Phys. Rev. Lett.* 49.6 (1982), pp. 405–408.

[75] B. I. Halperin. “Quantized Hall Conductance, Current-Carrying Edge States, and the Existence of Extended States in a Two-Dimensional Disordered Potential”. In: *Phys. Rev. B* 25.4 (1982), pp. 2185–2190.

[76] F. D. M. Haldane. “Model for a Quantum Hall Effect without Landau Levels: Condensed-Matter Realization of the "Parity Anomaly"”. In: *Phys. Rev. Lett.* 61.18 (1988), pp. 2015–2018.

[77] X.-L. Qi, T. L. Hughes, and S.-C. Zhang. “Topological Field Theory of Time-Reversal Invariant Insulators”. In: *Phys. Rev. B* 78.19 (2008), p. 195424.

[78] C. L. Kane and E. J. Mele. “Quantum Spin Hall Effect in Graphene”. In: *Phys. Rev. Lett.* 95.22 (2005), p. 226801.

[79] B. A. Bernevig and S.-C. Zhang. “Quantum Spin Hall Effect”. In: *Phys. Rev. Lett.* 96.10 (2006), p. 106802.

[80] M. Z. Hasan and C. L. Kane. “Colloquium: Topological Insulators”. In: *Rev. Mod. Phys.* 82.4 (2010), pp. 3045–3067.

[81] R. Jackiw and C. Rebbi. “Solitons with Fermion Number 1/2”. In: *Phys. Rev. D* 13.12 (1976), pp. 3398–3409.

[82] A. P. Schnyder, S. Ryu, A. Furusaki, and A. W. W. Ludwig. “Classification of Topological Insulators and Superconductors”. In: *AIP Conference Proceedings* 1134.1 (2009), pp. 10–21.

[83] A. Kitaev. “Periodic Table for Topological Insulators and Superconductors”. In: *AIP Conference Proceedings* 1134.1 (2009), pp. 22–30.

[84] F. D. M. Haldane. “Continuum Dynamics of the 1-D Heisenberg Antiferromagnet: Identification with the O(3) Nonlinear Sigma Model”. In: *Physics Letters A* 93.9 (1983), pp. 464–468.

[85] I. Affleck, T. Kennedy, E. H. Lieb, and H. Tasaki. “Rigorous Results on Valence-Bond Ground States in Antiferromagnets”. In: *Phys. Rev. Lett.* 59.7 (1987), pp. 799–802.

[86] S. Rachel. “Interacting Topological Insulators: A Review”. In: *Rep. Prog. Phys.* 81.11 (2018), p. 116501.

[87] F. Pollmann, E. Berg, A. M. Turner, and M. Oshikawa. “Entanglement Spectrum of a Topological Phase in One Dimension”. In: *Phys. Rev. B* 81.6 (2010), p. 064439.

[88] T. Senthil. “Symmetry Protected Topological Phases of Quantum Matter”. In: *Annu. Rev. Condens. Matter Phys.* 6.1 (2015), pp. 299–324.

[89] G. Jotzu, M. Messer, R. Desbuquois, M. Lebrat, T. Uehlinger, D. Greif, and T. Esslinger. “Experimental Realization of the Topological Haldane Model with Ultracold Fermions”. In: *Nature* 515.7526 (2014), pp. 237–240.

[90] H. Miyake, G. A. Siviloglou, C. J. Kennedy, W. C. Burton, and W. Ketterle. “Realizing the Harper Hamiltonian with Laser-Assisted Tunneling in Optical Lattices”. In: *Phys. Rev. Lett.* 111.18 (2013), p. 185302.

[91] M. Atala, M. Aidelsburger, J. T. Barreiro, D. Abanin, T. Kitagawa, E. Demler, and I. Bloch. “Direct Measurement of the Zak Phase in Topological Bloch Bands”. In: *Nat. Phys.* 9.12 (2013), pp. 795–800.

[92] S. de Léséleuc, V. Lienhard, P. Scholl, D. Barredo, S. Weber, N. Lang, H. P. Büchler, T. Lahaye, and A. Browaeys. "Observation of a Symmetry-Protected Topological Phase of Interacting Bosons with Rydberg Atoms". In: *Science* 365.6455 (2019), pp. 775–780.

[93] P. Sompet et al. "Realizing the Symmetry-Protected Haldane Phase in Fermi–Hubbard Ladders". In: *Nature* 606 (2022), pp. 484–488.

[94] A. Szasz, J. Motruk, M. P. Zaletel, and J. E. Moore. "Chiral Spin Liquid Phase of the Triangular Lattice Hubbard Model: A Density Matrix Renormalization Group Study". In: *Phys. Rev. X* 10.2 (2020), p. 021042.

[95] F. A. Palm, M. Buser, J. Léonard, M. Aidelsburger, U. Schollwöck, and F. Grusdt. "Bosonic Pfaffian State in the Hofstadter-Bose-Hubbard Model". In: *Phys. Rev. B* 103.16 (2021), p. L161101.

[96] A. Khare. *Fractional Statistics and Quantum Theory*. 2nd ed. World Scientific, 2005. ISBN: 978-981-256-160-2 978-981-256-775-8.

[97] C. Nayak, S. H. Simon, A. Stern, M. Freedman, and S. Das Sarma. "Non-Abelian Anyons and Topological Quantum Computation". In: *Rev. Mod. Phys.* 80.3 (2008), pp. 1083–1159.

[98] A. Kitaev. "Fault-Tolerant Quantum Computation by Anyons". In: *Annals of Physics* 303.1 (2003), pp. 2–30.

[99] S. Bravyi. "Universal Quantum Computation with the Nu=5/2 Fractional Quantum Hall State". In: *Phys. Rev. A* 73.4 (2006), p. 042313.

[100] N. Read and D. Green. "Paired States of Fermions in Two Dimensions with Breaking of Parity and Time-Reversal Symmetries and the Fractional Quantum Hall Effect". In: *Phys. Rev. B* 61.15 (2000), pp. 10267–10297.

[101] D. A. Ivanov. "Non-Abelian Statistics of Half-Quantum Vortices in \mathitp-Wave Superconductors". In: *Phys. Rev. Lett.* 86.2 (2001), pp. 268–271.

[102] A. Y. Kitaev. "Unpaired Majorana Fermions in Quantum Wires". In: *Phys.-Uspekhi* 44.10S (2001), pp. 131–136.

[103] V. Mourik, K. Zuo, S. M. Frolov, S. R. Plissard, E. P. A. M. Bakkers, and L. P. Kouwenhoven. "Signatures of Majorana Fermions in Hybrid Superconductor-Semiconductor Nanowire Devices". In: *Science* 336.6084 (2012), pp. 1003–1007.

[104] J. Léonard, S. Kim, J. Kwan, P. Segura, F. Grusdt, C. Repellin, N. Goldman, and M. Greiner. "Realization of a Fractional Quantum Hall State with Ultracold Atoms". In: *Nature* 619.7970 (2023), pp. 495–499.

[105] L. W. Clark, N. Schine, C. Baum, N. Jia, and J. Simon. "Observation of Laughlin States Made of Light". In: *Nature* 582.7810 (2020), pp. 41–45.

[106] J. Kwan, P. Segura, Y. Li, S. Kim, A. V. Gorshkov, A. Eckardt, B. Bakkali-Hassani, and M. Greiner. *Realization of 1D Anyons with Arbitrary Statistical Phase*. 2023. arXiv: 2306.01737 [cond-mat, physics:physics, physics:quant-ph].

[107] M. Iqbal et al. "Non-Abelian Topological Order and Anyons on a Trapped-Ion Processor". In: *Nature* 626.7999 (2024), pp. 505–511.

[108] M. L. Prichard, B. M. Spar, I. Morera, E. Demler, Z. Z. Yan, and W. S. Bakr. *Directly Imaging Spin Polarons in a Kinetically Frustrated Hubbard System*. 2023. arXiv: 2308.12951 [cond-mat, physics:quant-ph].

[109] M. Lebrat, M. Xu, L. H. Kendrick, A. Kale, Y. Gang, P. Seetharaman, I. Morera, E. Khatami, E. Demler, and M. Greiner. *Observation of Nagaoka Polarons in a Fermi-Hubbard Quantum Simulator*. 2023. arXiv: 2308.12269 [cond-mat, physics:quant-ph].

[110] A. Kitaev. "Anyons in an Exactly Solved Model and Beyond". In: *Annals of Physics* 321.1 (2006), pp. 2–111.

[111] S. T. Bramwell and M. J. P. Gingras. "Spin Ice State in Frustrated Magnetic Pyrochlore Materials". In: *Science* 294.5546 (2001), pp. 1495–1501.

[112] T. W. Lawrence, A. Szöke, and R. B. Laughlin. "Absence of Circular Dichroism in High-Temperature Superconductors". In: *Phys. Rev. Lett.* 69.9 (1992), pp. 1439–1442.

[113] S. Gong, W. Zhu, and D. N. Sheng. "Robust D-Wave Superconductivity in the Square-Lattice t–J Model". In: *Phys. Rev. Lett.* 127.9 (2021), p. 097003.

[114] S. Jiang, D. J. Scalapino, and S. R. White. "Ground State Phase Diagram of the T-t'-J Model". In: *Proc. Natl. Acad. Sci. U.S.A.* 118.44 (2021), e2109978118.

[115] H. Xu, C.-M. Chung, M. Qin, U. Schollwöck, S. R. White, and S. Zhang. *Coexistence of Superconductivity with Partially Filled Stripes in the Hubbard Model*. 2023. arXiv: 2303.08376 [cond-mat, physics:physics].

[116] A. Eckardt, P. Hauke, P. Soltan-Panahi, C. Becker, K. Sengstock, and M. Lewenstein. "Frustrated Quantum Antiferromagnetism with Ultracold Bosons in a Triangular Lattice". In: *EPL* 89.1 (2010), p. 10010.

[117] J. Struck, C. Ölschläger, R. L. Targat, P. Soltan-Panahi, A. Eckardt, M. Lewenstein, P. Windpassinger, and K. Sengstock. "Quantum Simulation of Frustrated Classical Magnetism in Triangular Optical Lattices". In: *Science* 333.6045 (2011), pp. 996–999.

[118] P. W. Anderson. "More Is Different". In: *Science* 177.4047 (1972), pp. 393–396.

[119] J. M. Kosterlitz and D. J. Thouless. "Ordering, Metastability and Phase Transitions in Two-Dimensional Systems". In: *J. Phys. C: Solid State Phys.* 6.7 (1973), p. 1181.

[120] X.-G. Wen. "Topological Orders and Edge Excitations in Fractional Quantum Hall States". In: *Advances in Physics* 44.5 (1995), pp. 405–473.

[121] T. Senthil, A. Vishwanath, L. Balents, S. Sachdev, and M. P. A. Fisher. ""Deconfined" Quantum Critical Points". In: *Science* 303.5663 (2004), pp. 1490–1494.

[122] I. Affleck, T. Kennedy, E. H. Lieb, and H. Tasaki. "Valence Bond Ground States in Isotropic Quantum Antiferromagnets". In: *Commun.Math. Phys.* 115.3 (1988), pp. 477–528.

[123] Z.-C. Gu and X.-G. Wen. "Tensor-Entanglement-Filtering Renormalization Approach and Symmetry Protected Topological Order". In: *Phys. Rev. B* 80.15 (2009), p. 155131.

[124] M. V. Berry. "Quantal Phase Factors Accompanying Adiabatic Changes". In: *Proceedings of the Royal Society of London. A. Mathematical and Physical Sciences* 392.1802 (1997), pp. 45–57.

[125] M. Born and V. Fock. "Beweis des Adiabatensatzes". In: *Z. Physik* 51.3-4 (1928), pp. 165–180.

[126] F. E. Camino, W. Zhou, and V. J. Goldman. "Aharonov-Bohm Superperiod in a Laughlin Quasiparticle Interferometer". In: *Phys. Rev. Lett.* 95.24 (2005), p. 246802.

[127] D. Tong. *Lectures on the Quantum Hall Effect*. 2016. arXiv: 1606.06687 [cond-mat, physics:hep-th].

[128] L. Landau. "Diamagnetismus der Metalle". In: *Z. Physik* 64.9-10 (1930), pp. 629–637.

[129] R. Kubo. "Statistical-Mechanical Theory of Irreversible Processes. I. General Theory and Simple Applications to Magnetic and Conduction Problems". In: *J. Phys. Soc. Jpn.* 12.6 (1957), pp. 570–586.

[130] P. G. Harper. "The General Motion of Conduction Electrons in a Uniform Magnetic Field, with Application to the Diamagnetism of Metals". In: *Proc. Phys. Soc. A* 68.10 (1955), p. 879.

[131] D. R. Hofstadter. "Energy Levels and Wave Functions of Bloch Electrons in Rational and Irrational Magnetic Fields". In: *Phys. Rev. B* 14.6 (1976), pp. 2239–2249.

[132] W. P. Su, J. R. Schrieffer, and A. J. Heeger. "Solitons in Polyacetylene". In: *Phys. Rev. Lett.* 42.25 (1979), pp. 1698–1701.

[133] W. P. Su, J. R. Schrieffer, and A. J. Heeger. "Soliton Excitations in Polyacetylene". In: *Phys. Rev. B* 22.4 (1980), pp. 2099–2111.

[134] A. J. Heeger, S. Kivelson, J. R. Schrieffer, and W. .-. Su. "Solitons in Conducting Polymers". In: *Rev. Mod. Phys.* 60.3 (1988), pp. 781–850.

[135] R. B. Laughlin. "Nobel Lecture: Fractional Quantization". In: *Rev. Mod. Phys.* 71.4 (1999), pp. 863–874.

[136] R. E. Peierls. *Quantum Theory of Solids*. Clarendon Press, 1955. ISBN: 978-0-19-850781-9.

[137] J. Zak. "Berry's Phase for Energy Bands in Solids". In: *Phys. Rev. Lett.* 62.23 (1989), pp. 2747–2750.

[138] J. Bardeen, L. N. Cooper, and J. R. Schrieffer. "Theory of Superconductivity". In: *Phys. Rev.* 108.5 (1957), pp. 1175–1204.

[139] J. Alicea, Y. Oreg, G. Refael, F. von Oppen, and M. P. A. Fisher. "Non-Abelian Statistics and Topological Quantum Information Processing in 1D Wire Networks". In: *Nat. Phys.* 7.5 (2011), pp. 412–417.

[140] J. Alicea. "New Directions in the Pursuit of Majorana Fermions in Solid State Systems". In: *Rep. Prog. Phys.* 75.7 (2012), p. 076501.

[141] E. Majorana. "Teoria Simmetrica Dell'elettrone e Del Positrone". In: *Nuovo Cim.* 14 (1937), p. 171.

[142] F. Wilczek. "Majorana Returns". In: *Nat. Phys.* 5.9 (2009), pp. 614–618.

[143] A. P. Schnyder, S. Ryu, A. Furusaki, and A. W. W. Ludwig. "Classification of Topological Insulators and Superconductors in Three Spatial Dimensions". In: *Phys. Rev. B* 78.19 (2008), p. 195125.

[144] A. Altland and M. R. Zirnbauer. "Nonstandard Symmetry Classes in Mesoscopic Normal-Superconducting Hybrid Structures". In: *Phys. Rev. B* 55.2 (1997), pp. 1142–1161.

[145] S. Ryu, A. P. Schnyder, A. Furusaki, and A. W. W. Ludwig. "Topological Insulators and Superconductors: Tenfold Way and Dimensional Hierarchy". In: *New J. Phys.* 12.6 (2010), p. 065010.

[146] T. Kennedy. "Exact Diagonalisations of Open Spin-1 Chains". In: *J. Phys.: Condens. Matter* 2.26 (1990), p. 5737.

[147] F. Pollmann, E. Berg, A. M. Turner, and M. Oshikawa. "Symmetry Protection of Topological Order in One-Dimensional Quantum Spin Systems". In: *Phys. Rev. B* 85.7 (2012), p. 075125.

[148] M. Oshikawa. "Hidden Z2*Z2 Symmetry in Quantum Spin Chains with Arbitrary Integer Spin". In: *J. Phys.: Condens. Matter* 4.36 (1992), p. 7469.

[149] M. den Nijs and K. Rommelse. "Preroughening Transitions in Crystal Surfaces and Valence-Bond Phases in Quantum Spin Chains". In: *Phys. Rev. B* 40.7 (1989), pp. 4709–4734.

[150] H. Li and F. D. M. Haldane. "Entanglement Spectrum as a Generalization of Entanglement Entropy: Identification of Topological Order in Non-Abelian Fractional Quantum Hall Effect States". In: *Phys. Rev. Lett.* 101.1 (2008), p. 010504.

[151] V. Kalmeyer and R. B. Laughlin. "Equivalence of the Resonating-Valence-Bond and Fractional Quantum Hall States". In: *Phys. Rev. Lett.* 59.18 (1987), pp. 2095–2098.

[152] R. B. Laughlin. "Anomalous Quantum Hall Effect: An Incompressible Quantum Fluid with Fractionally Charged Excitations". In: *Phys. Rev. Lett.* 50.18 (1983), pp. 1395–1398.

[153] R. Willett, J. P. Eisenstein, H. L. Störmer, D. C. Tsui, A. C. Gossard, and J. H. English. "Observation of an Even-Denominator Quantum Number in the Fractional Quantum Hall Effect". In: *Phys. Rev. Lett.* 59.15 (1987), pp. 1776–1779.

[154] B. I. Halperin. "Theory of the Quantized Hall Conductance". In: (1983).

[155] G. Moore and N. Read. "Nonabelions in the Fractional Quantum Hall Effect". In: *Nuclear Physics B* 360.2 (1991), pp. 362–396.

[156] N. Read and E. Rezayi. "Beyond Paired Quantum Hall States: Parafermions and Incompressible States in the First Excited Landau Level". In: *Phys. Rev. B* 59.12 (1999), pp. 8084–8092.

[157] F. D. M. Haldane. "Fractional Quantization of the Hall Effect: A Hierarchy of Incompressible Quantum Fluid States". In: *Phys. Rev. Lett.* 51.7 (1983), pp. 605–608.

[158] M. Dolev, M. Heiblum, V. Umansky, A. Stern, and D. Mahalu. "Observation of a Quarter of an Electron Charge at the ν=5/2 Quantum Hall State". In: *Nature* 452.7189 (2008), pp. 829–834.

[159] C. Nayak and F. Wilczek. "$2n$ Quasihole States Realize 2^{n-1}-Dimensional Spinor Braiding Statistics in Paired Quantum Hall States". In: *Nuclear Physics B* 479.3 (1996), pp. 529–553.

[160] A. Stern. "Anyons and the Quantum Hall Effect - a Pedagogical Review". In: *Annals of Physics* 323.1 (2008), pp. 204–249.

[161] W. Pauli. "The Connection Between Spin and Statistics". In: *Phys. Rev.* 58.8 (1940), pp. 716–722.

[162] M. G. G. Laidlaw and C. M. DeWitt. "Feynman Functional Integrals for Systems of Indistinguishable Particles". In: *Phys. Rev. D* 3.6 (1971), pp. 1375–1378.

[163] J. M. Leinaas and J. Myrheim. "On the Theory of Identical Particles". In: *Il Nuovo Cimento B* 37.1 (1977), pp. 1–23.

[164] F. Wilczek. "Magnetic Flux, Angular Momentum, and Statistics". In: *Phys. Rev. Lett.* 48.17 (1982), pp. 1144–1146.

[165] V. Lahtinen and J. K. Pachos. "A Short Introduction to Topological Quantum Computation". In: *SciPost Phys.* 3.3 (2017), p. 021.

[166] D. Arovas, J. R. Schrieffer, and F. Wilczek. "Fractional Statistics and the Quantum Hall Effect". In: *Phys. Rev. Lett.* 53.7 (1984), pp. 722–723.

[167] P. Bonderson, V. Gurarie, and C. Nayak. "Plasma Analogy and Non-Abelian Statistics for Ising-type Quantum Hall States". In: *Phys. Rev. B* 83.7 (2011), p. 075303.

[168] T. Senthil, L. Balents, S. Sachdev, A. Vishwanath, and M. P. A. Fisher. "Quantum Criticality beyond the Landau-Ginzburg-Wilson Paradigm". In: *Phys. Rev. B* 70.14 (2004), p. 144407.

[169] A. Vishwanath and T. Senthil. "Physics of Three-Dimensional Bosonic Topological Insulators: Surface-Deconfined Criticality and Quantized Magnetoelectric Effect". In: *Phys. Rev. X* 3.1 (2013), p. 011016.

[170] T. Grover and T. Senthil. "Topological Spin Hall States, Charged Skyrmions, and Superconductivity in Two Dimensions". In: *Phys. Rev. Lett.* 100.15 (2008), p. 156804.

[171] K. Slagle, Y.-Z. You, and C. Xu. "Exotic Quantum Phase Transitions of Strongly Interacting Topological Insulators". In: *Phys. Rev. B* 91.11 (2015), p. 115121.

[172] Y.-Y. He, H.-Q. Wu, Y.-Z. You, C. Xu, Z. Y. Meng, and Z.-Y. Lu. "Bona Fide Interaction-Driven Topological Phase Transition in Correlated Symmetry-Protected Topological States". In: *Phys. Rev. B* 93.11 (2016), p. 115150.

[173] S. Jiang and O. Motrunich. "Ising Ferromagnet to Valence Bond Solid Transition in a One-Dimensional Spin Chain: Analogies to Deconfined Quantum Critical Points". In: *Phys. Rev. B* 99.7 (2019), p. 075103.

[174] R.-Z. Huang, D.-C. Lu, Y.-Z. You, Z. Y. Meng, and T. Xiang. "Emergent Symmetry and Conserved Current at a One-Dimensional Incarnation of Deconfined Quantum Critical Point". In: *Phys. Rev. B* 100.12 (2019), p. 125137.

[175] C. Zhang and M. Levin. "Exactly Solvable Model for a Deconfined Quantum Critical Point in 1D". In: *Phys. Rev. Lett.* 130.2 (2023), p. 026801.

[176] P. Coleman. *Introduction to Many-Body Physics*. 1st ed. Cambridge University Press, 2015. ISBN: 978-0-521-86488-6 978-1-139-02091-6.

[177] T. Giamarchi. *Quantum Physics in One Dimension*. Oxford University Press, 2004. ISBN: 0-19-852500-1.

[178] E. Y. Loh, J. E. Gubernatis, R. T. Scalettar, S. R. White, D. J. Scalapino, and R. L. Sugar. "Sign Problem in the Numerical Simulation of Many-Electron Systems". In: *Phys. Rev. B* 41.13 (1990), pp. 9301–9307.

[179] M. Troyer and U.-J. Wiese. "Computational Complexity and Fundamental Limitations to Fermionic Quantum Monte Carlo Simulations". In: *Phys. Rev. Lett.* 94.17 (2005), p. 170201.

[180] J. I. Cirac, D. Pérez-García, N. Schuch, and F. Verstraete. "Matrix Product States and Projected Entangled Pair States: Concepts, Symmetries, Theorems". In: *Rev. Mod. Phys.* 93.4 (2021), p. 045003.

[181] A. Aspuru-Guzik and P. Walther. "Photonic Quantum Simulators". In: *Nature Phys* 8.4 (2012), pp. 285–291.

[182] R. Blatt and C. F. Roos. "Quantum Simulations with Trapped Ions". In: *Nature Phys* 8.4 (2012), pp. 277–284.

[183] C. Monroe et al. "Programmable Quantum Simulations of Spin Systems with Trapped Ions". In: *Rev. Mod. Phys.* 93.2 (2021), p. 025001.

[184] A. Browaeys and T. Lahaye. "Many-Body Physics with Individually Controlled Rydberg Atoms". In: *Nat. Phys.* 16.2 (2020), pp. 132–142.

[185] M. Lewenstein, A. Sanpera, V. Ahufinger, B. Damski, A. Sen(De), and U. Sen. "Ultracold Atomic Gases in Optical Lattices: Mimicking Condensed Matter Physics and Beyond". In: *Adv. Phys.* 56.2 (2007), pp. 243–379.

[186] M. Lewenstein, A. Sanpera, and V. Ahufinger. *Ultracold Atoms in Optical Lattices: Simulating Quantum Many-Body Systems*. OUP Oxford, 2012. ISBN: 978-0-19-162743-9.

[187] A. J. Daley, I. Bloch, C. Kokail, S. Flannigan, N. Pearson, M. Troyer, and P. Zoller. "Practical Quantum Advantage in Quantum Simulation". In: *Nature* 607.7920 (2022), pp. 667–676.

[188] S. He, S. H. Simon, and B. I. Halperin. "Response Function of the Fractional Quantized Hall State on a Sphere. II. Exact Diagonalization". In: *Phys. Rev. B* 50.3 (1994), pp. 1823–1831.

[189] T. Neupert, L. Santos, C. Chamon, and C. Mudry. "Fractional Quantum Hall States at Zero Magnetic Field". In: *Phys. Rev. Lett.* 106.23 (2011), p. 236804.

[190] A. Wietek and A. M. Läuchli. "Sublattice Coding Algorithm and Distributed Memory Parallelization for Large-Scale Exact Diagonalizations of Quantum Many-Body Systems". In: *Phys. Rev. E* 98.3 (2018), p. 033309.

[191] C. Lanczos. "An Iteration Method for the Solution of the Eigenvalue Problem of Linear Differential and Integral Operators". In: *J. RES. NATL. BUR. STAN.* 45.4 (1950), p. 255.

[192] A. Klümper, A. Schadschneider, and J. Zittartz. "Matrix Product Ground States for One-Dimensional Spin-1 Quantum Antiferromagnets". In: *EPL* 24.4 (1993), p. 293.

[193] M. Fannes, B. Nachtergaele, and R. F. Werner. "Finitely Correlated States on Quantum Spin Chains". In: *Communications in Mathematical Physics* 144.3 (1992), pp. 443–490.

[194] S. Östlund and S. Rommer. "Thermodynamic Limit of Density Matrix Renormalization". In: *Phys. Rev. Lett.* 75.19 (1995), pp. 3537–3540.

[195] F. Verstraete, D. Porras, and J. I. Cirac. "Density Matrix Renormalization Group and Periodic Boundary Conditions: A Quantum Information Perspective". In: *Phys. Rev. Lett.* 93.22 (2004), p. 227205.

[196] J. Eisert, M. Cramer, and M. B. Plenio. "Colloquium: Area Laws for the Entanglement Entropy". In: *Rev. Mod. Phys.* 82.1 (2010), pp. 277–306.

[197] C. Eckart and G. Young. "The Approximation of One Matrix by Another of Lower Rank". In: *Psychometrika* 1.3 (1936), pp. 211–218.

[198] L. Mirsky. "Symmetric Gauge Functions And Unitarily Invariant Norms". In: *Q J Math* 11.1 (1960), pp. 50–59.

[199] G. M. Crosswhite and D. Bacon. "Finite Automata for Caching in Matrix Product Algorithms". In: *Phys. Rev. A* 78.1 (2008), p. 012356.

[200] J. Motruk, M. P. Zaletel, R. S. K. Mong, and F. Pollmann. "Density Matrix Renormalization Group on a Cylinder in Mixed Real and Momentum Space". In: *Phys. Rev. B* 93.15 (2016), p. 155139.

[201] L. Vanderstraeten, J. Haegeman, and F. Verstraete. "Tangent-Space Methods for Uniform Matrix Product States". In: *SciPost Phys. Lect. Notes* (2019), p. 7.

[202] C. Hubig, I. P. McCulloch, U. Schollwöck, and F. A. Wolf. "A Strictly Single-Site DMRG Algorithm with Subspace Expansion". In: *Phys. Rev. B* 91.15 (2015), p. 155115.

[203] J. Jordan, R. Orús, G. Vidal, F. Verstraete, and J. I. Cirac. "Classical Simulation of Infinite-Size Quantum Lattice Systems in Two Spatial Dimensions". In: *Phys. Rev. Lett.* 101.25 (2008), p. 250602.

[204] M. Lubasch, J. I. Cirac, and M.-C. Bañuls. "Unifying Projected Entangled Pair State Contractions". In: *New J. Phys.* 16.3 (2014), p. 033014.

[205] R. Orús and G. Vidal. "Simulation of Two-Dimensional Quantum Systems on an Infinite Lattice Revisited: Corner Transfer Matrix for Tensor Contraction". In: *Phys. Rev. B* 80.9 (2009), p. 094403.

[206] M. Gerster, M. Rizzi, P. Silvi, M. Dalmonte, and S. Montangero. "Fractional Quantum Hall Effect in the Interacting Hofstadter Model via Tensor Networks". In: *Phys. Rev. B* 96.19 (2017), p. 195123.

[207] G. Magnifico, T. Felser, P. Silvi, and S. Montangero. "Lattice Quantum Electrodynamics in (3+1)-Dimensions at Finite Density with Tensor Networks". In: *Nat Commun* 12.1 (2021), p. 3600.

[208] M. Olshanii. "Atomic Scattering in the Presence of an External Confinement and a Gas of Impenetrable Bosons". In: *Phys. Rev. Lett.* 81.5 (1998), pp. 938–941.

[209] M.-O. Mewes, M. R. Andrews, N. J. van Druten, D. M. Kurn, D. S. Durfee, and W. Ketterle. "Bose-Einstein Condensation in a Tightly Confining Dc Magnetic Trap". In: *Phys. Rev. Lett.* 77.3 (1996), pp. 416–419.

[210] I. Bloch, J. Dalibard, and W. Zwerger. "Many-Body Physics with Ultracold Gases". In: *Rev. Mod. Phys.* 80.3 (2008), pp. 885–964.

[211] P. Hauke, M. Lewenstein, and A. Eckardt. "Tomography of Band Insulators from Quench Dynamics". In: *Phys. Rev. Lett.* 113.4 (2014), p. 045303.

[212] N. Fläschner, B. S. Rem, M. Tarnowski, D. Vogel, D.-S. Lühmann, K. Sengstock, and C. Weitenberg. "Experimental Reconstruction of the Berry Curvature in a Floquet Bloch Band". In: *Science* 352.6289 (2016), pp. 1091–1094.

[213] M. Endres et al. "Observation of Correlated Particle-Hole Pairs and String Order in Low-Dimensional Mott Insulators". In: *Science* 334.6053 (2011), pp. 200–203.

[214] L. Saminadayar, D. C. Glattli, Y. Jin, and B. Etienne. "Observation of the e/3 Fractionally Charged Laughlin Quasiparticle". In: *Phys. Rev. Lett.* 79.13 (1997), pp. 2526–2529.

[215] H. Bartolomei et al. “Fractional Statistics in Anyon Collisions”. In: *Science* 368.6487 (2020), pp. 173–177.

[216] F. E. Camino, W. Zhou, and V. J. Goldman. “e/3 Laughlin Quasiparticle Primary-Filling ν=1/3 Interferometer”. In: *Phys. Rev. Lett.* 98.7 (2007), p. 076805.

[217] R. L. Willett, L. N. Pfeiffer, and K. W. West. “Measurement of Filling Factor 5/2 Quasiparticle Interference with Observation of Charge e/4 and e/2 Period Oscillations”. In: *Proceedings of the National Academy of Sciences* 106.22 (2009), pp. 8853–8858.

[218] N. Ofek, A. Bid, M. Heiblum, A. Stern, V. Umansky, and D. Mahalu. “Role of Interactions in an Electronic Fabry–Perot Interferometer Operating in the Quantum Hall Effect Regime”. In: *Proceedings of the National Academy of Sciences* 107.12 (2010), pp. 5276–5281.

[219] J. Nakamura, S. Liang, G. C. Gardner, and M. J. Manfra. “Direct Observation of Anyonic Braiding Statistics”. In: *Nature Physics* 16.9 (2020), pp. 931–936.

[220] M. Greiter, X.-G. Wen, and F. Wilczek. “Paired Hall State at Half Filling”. In: *Phys. Rev. Lett.* 66.24 (1991), pp. 3205–3208.

[221] N. Read. “Paired Fractional Quantum Hall States and the ν=5/2 Puzzle”. In: *Physica B: Condensed Matter* 298.1 (2001), pp. 121–128.

[222] L. Tiemann, G. Gamez, N. Kumada, and K. Muraki. “Unraveling the Spin Polarization of the ν=5/2Fractional Quantum Hall State”. In: *Science* 335.6070 (2012), pp. 828–831.

[223] I. P. Radu, J. B. Miller, C. M. Marcus, M. A. Kastner, L. N. Pfeiffer, and K. W. West. “Quasi-Particle Properties from Tunneling in the \nu=5/2 Fractional Quantum Hall State”. In: *Science* 320.5878 (2008), pp. 899–902.

[224] M. Banerjee, M. Heiblum, V. Umansky, D. E. Feldman, Y. Oreg, and A. Stern. “Observation of Half-Integer Thermal Hall Conductance”. In: *Nature* 559.7713 (2018), pp. 205–210.

[225] S. Baer, C. Rössler, T. Ihn, K. Ensslin, C. Reichl, and W. Wegscheider. “Experimental Probe of Topological Orders and Edge Excitations in the Second Landau Level”. In: *Phys. Rev. B* 90.7 (2014), p. 075403.

[226] N. Gemelke, E. Sarajlic, and S. Chu. *Rotating Few-body Atomic Systems in the Fractional Quantum Hall Regime*. 2010. arXiv: 1007.2677 [cond-mat, physics:quant-ph].

[227] N. Goldman, G. Juzeliūnas, P. Öhberg, and I. B. Spielman. “Light-Induced Gauge Fields for Ultracold Atoms”. In: *Reports on Progress in Physics* 77.12 (2014), p. 126401.

[228] M. Hafezi, S. Mittal, J. Fan, A. Migdall, and J. M. Taylor. “Imaging Topological Edge States in Silicon Photonics”. In: *Nature Photonics* 7.12 (2013), pp. 1001–1005.

[229] M. C. Rechtsman, J. M. Zeuner, Y. Plotnik, Y. Lumer, D. Podolsky, F. Dreisow, S. Nolte, M. Segev, and A. Szameit. “Photonic Floquet Topological Insulators”. In: *Nature* 496.7444 (2013), pp. 196–200.

[230] S. Mittal, S. Ganeshan, J. Fan, A. Vaezi, and M. Hafezi. “Measurement of Topological Invariants in a 2D Photonic System”. In: *Nature Photonics* 10.3 (2016), pp. 180–183.

[231] F. Baboux, E. Levy, A. Lemaître, C. Gómez, E. Galopin, L. Le Gratiet, I. Sagnes, A. Amo, J. Bloch, and E. Akkermans. "Measuring Topological Invariants from Generalized Edge States in Polaritonic Quasicrystals". In: *Phys. Rev. B* 95.16 (2017), p. 161114.

[232] L. Asteria, D. T. Tran, T. Ozawa, M. Tarnowski, B. S. Rem, N. Fläschner, K. Sengstock, N. Goldman, and C. Weitenberg. "Measuring Quantized Circular Dichroism in Ultracold Topological Matter". In: *Nature Physics* 15.5 (2019), pp. 449–454.

[233] M. Tarnowski, F. N. Ünal, N. Fläschner, B. S. Rem, A. Eckardt, K. Sengstock, and C. Weitenberg. "Measuring Topology from Dynamics by Obtaining the Chern Number from a Linking Number". In: *Nature Communications* 10.1 (2019), p. 1728.

[234] S. Mittal, J. Fan, S. Faez, A. Migdall, J. M. Taylor, and M. Hafezi. "Topologically Robust Transport of Photons in a Synthetic Gauge Field". In: *Phys. Rev. Lett.* 113.8 (2014), p. 087403.

[235] M. A. Bandres, M. C. Rechtsman, and M. Segev. "Topological Photonic Quasicrystals: Fractal Topological Spectrum and Protected Transport". In: *Phys. Rev. X* 6.1 (2016), p. 011016.

[236] P. Lunt, P. Hill, J. Reiter, P. M. Preiss, M. Gałka, and S. Jochim. *Realization of a Laughlin State of Two Rapidly Rotating Fermions*. 2024. arXiv: 2402.14814 [cond-mat, physics:physics, physics:quant-ph].

[237] N. R. Cooper, N. K. Wilkin, and J. M. F. Gunn. "Quantum Phases of Vortices in Rotating Bose-Einstein Condensates". In: *Phys. Rev. Lett.* 87.12 (2001), p. 120405.

[238] T. Graß, B. Juliá-Díaz, N. Barberán, and M. Lewenstein. "Non-Abelian Spin-Singlet States of Two-Component Bose Gases in Artificial Gauge Fields". In: *Phys. Rev. A* 86.2 (2012), p. 021603.

[239] S. Furukawa and M. Ueda. "Quantum Hall States in Rapidly Rotating Two-Component Bose Gases". In: *Phys. Rev. A* 86.3 (2012), p. 031604.

[240] B. Paredes, P. Fedichev, J. I. Cirac, and P. Zoller. "1/2-Anyons in Small Atomic Bose-Einstein Condensates". In: *Phys. Rev. Lett.* 87.1 (2001), p. 010402.

[241] E. Kapit, P. Ginsparg, and E. Mueller. "Non-Abelian Braiding of Lattice Bosons". In: *Phys. Rev. Lett.* 108.6 (2012), p. 066802.

[242] T. Graß, B. Juliá-Díaz, and M. Lewenstein. "Topological Phases in Small Quantum Hall Samples". In: *Phys. Rev. A* 89.1 (2014), p. 013623.

[243] S. Dutta and E. J. Mueller. "Coherent Generation of Photonic Fractional Quantum Hall States in a Cavity and the Search for Anyonic Quasiparticles". In: *Phys. Rev. A* 97.3 (2018), p. 033825.

[244] T. Graß, M. Gullans, P. Bienias, G. Zhu, A. Ghazaryan, P. Ghaemi, and M. Hafezi. "Optical Control over Bulk Excitations in Fractional Quantum Hall Systems". In: *Phys. Rev. B* 98.15 (2018), p. 155124.

[245] R. O. Umucalılar, E. Macaluso, T. Comparin, and I. Carusotto. "Time-of-Flight Measurements as a Possible Method to Observe Anyonic Statistics". In: *Phys. Rev. Lett.* 120.23 (2018), p. 230403.

[246] N. R. Cooper and S. H. Simon. "Signatures of Fractional Exclusion Statistics in the Spectroscopy of Quantum Hall Droplets". In: *Phys. Rev. Lett.* 114.10 (2015), p. 106802.

[247] Z. Papić, R. S. K. Mong, A. Yazdani, and M. P. Zaletel. "Imaging Anyons with Scanning Tunneling Microscopy". In: *Phys. Rev. X* 8.1 (2018), p. 011037.

[248] S. C. Morampudi, A. M. Turner, F. Pollmann, and F. Wilczek. "Statistics of Fractionalized Excitations through Threshold Spectroscopy". In: *Phys. Rev. Lett.* 118.22 (2017), p. 227201.

[249] Y. Zhang, G. J. Sreejith, N. D. Gemelke, and J. K. Jain. "Fractional Angular Momentum in Cold-Atom Systems". In: *Phys. Rev. Lett.* 113.16 (2014), p. 160404.

[250] Y. Zhang, G. J. Sreejith, and J. K. Jain. "Creating and Manipulating Non-Abelian Anyons in Cold Atom Systems Using Auxiliary Bosons". In: *Phys. Rev. B* 92.7 (2015), p. 075116.

[251] D. Lundholm and N. Rougerie. "Emergence of Fractional Statistics for Tracer Particles in a Laughlin Liquid". In: *Phys. Rev. Lett.* 116.17 (2016), p. 170401.

[252] F. Grusdt, N. Y. Yao, D. Abanin, M. Fleischhauer, and E. Demler. "Interferometric Measurements of Many-Body Topological Invariants Using Mobile Impurities". In: *Nature Communications* 7.1 (2016), p. 11994.

[253] A. Camacho-Guardian, N. Goldman, P. Massignan, and G. M. Bruun. "Dropping an Impurity into a Chern Insulator: A Polaron View on Topological Matter". In: *Phys. Rev. B* 99.8 (2019), p. 081105.

[254] A. Muñoz de las Heras, E. Macaluso, and I. Carusotto. "Anyonic Molecules in Atomic Fractional Quantum Hall Liquids: A Quantitative Probe of Fractional Charge and Anyonic Statistics". In: *Phys. Rev. X* 10.4 (2020), p. 041058.

[255] C. G. Darwin. "The Diamagnetism of the Free Electron". In: *Mathematical Proceedings of the Cambridge Philosophical Society* 27.1 (1931), pp. 86–90.

[256] B. Juliá-Díaz, T. Graß, N. Barberán, and M. Lewenstein. "Fractional Quantum Hall States of a Few Bosonic Atoms in Geometric Gauge Fields". In: *New J. Phys.* 14.5 (2012), p. 055003.

[257] T. Scharf, J. Thibon, and B. G. Wybourne. "Powers of the Vandermonde Determinant and the Quantum Hall Effect". In: *J. Phys. A: Math. Gen.* 27.12 (1994), p. 4211.

[258] N. Rougerie. *Some Contributions to Many-Body Quantum Mathematics*. 2016. arXiv: 1607.03833 [cond-mat, physics:math-ph, physics:quant-ph].

[259] D. Lundholm. "Many-Anyon Trial States". In: *Phys. Rev. A* 96.1 (2017), p. 012116.

[260] Z. Papić, R. Thomale, and D. A. Abanin. "Tunable Electron Interactions and Fractional Quantum Hall States in Graphene". In: *Phys. Rev. Lett.* 107.17 (2011), p. 176602.

[261] C. Fey, P. Schmelcher, A. Imamoglu, and R. Schmidt. "Theory of Exciton-Electron Scattering in Atomically Thin Semiconductors". In: *Phys. Rev. B* 101.19 (2020), p. 195417.

[262] A. H. MacDonald, G. C. Aers, and M. W. C. Dharma-wardana. "Hierarchy of Plasmas for Fractional Quantum Hall States". In: *Phys. Rev. B* 31.8 (1985), pp. 5529–5532.

[263] X. Wan, Z.-X. Hu, E. H. Rezayi, and K. Yang. "Fractional Quantum Hall Effect at N=5/2: Ground States, Non-Abelian Quasiholes, and Edge Modes in a Microscopic Model". In: *Phys. Rev. B* 77.16 (2008), p. 165316.

[264] E. Macaluso, T. Comparin, L. Mazza, and I. Carusotto. "Fusion Channels of Non-Abelian Anyons from Angular-Momentum and Density-Profile Measurements". In: *Phys. Rev. Lett.* 123.26 (2019), p. 266801.

[265] Y. Tserkovnyak and S. H. Simon. "Monte Carlo Evaluation of Non-Abelian Statistics". In: *Phys. Rev. Lett.* 90.1 (2003), p. 016802.

[266] M. Baraban, G. Zikos, N. Bonesteel, and S. H. Simon. "Numerical Analysis of Quasiholes of the Moore-Read Wave Function". In: *Phys. Rev. Lett.* 103.7 (2009), p. 076801.

[267] M. Byszewski et al. "Optical Probing of Composite Fermions in a Two-Dimensional Electron Gas". In: *Nat. Phys.* 2 (2006), 239 EP–.

[268] H. C. Nerl, K. T. Winther, F. S. Hage, K. S. Thygesen, L. Houben, C. Backes, J. N. Coleman, Q. M. Ramasse, and V. Nicolosi. "Probing the Local Nature of Excitons and Plasmons in Few-Layer MoS2". In: *npj 2D Materials and Applications* 1.1 (2017), p. 2.

[269] S. Manna, J. Wildeboer, G. Sierra, and A. E. B. Nielsen. "Non-Abelian Quasiholes in Lattice Moore-Read States and Parent Hamiltonians". In: *Phys. Rev. B* 98.16 (2018), p. 165147.

[270] A. Stern. "Non-Abelian States of Matter". In: *Nature* 464.7286 (2010), pp. 187–193.

[271] S. D. Sarma, M. Freedman, and C. Nayak. "Majorana Zero Modes and Topological Quantum Computation". In: *npj Quantum Inf.* 1.1 (2015), p. 15001.

[272] L. Fu and C. L. Kane. "Superconducting Proximity Effect and Majorana Fermions at the Surface of a Topological Insulator". In: *Phys. Rev. Lett.* 100.9 (2008), p. 096407.

[273] L. Fu and C. L. Kane. "Josephson Current and Noise at a Superconductor/Quantum-Spin-Hall-insulator/Superconductor Junction". In: *Phys. Rev. B* 79.16 (2009), p. 161408.

[274] Y. Oreg, G. Refael, and F. von Oppen. "Helical Liquids and Majorana Bound States in Quantum Wires". In: *Phys. Rev. Lett.* 105.17 (2010), p. 177002.

[275] R. M. Lutchyn, J. D. Sau, and S. Das Sarma. "Majorana Fermions and a Topological Phase Transition in Semiconductor-Superconductor Heterostructures". In: *Phys. Rev. Lett.* 105.7 (2010), p. 077001.

[276] A. Cook and M. Franz. "Majorana Fermions in a Topological-Insulator Nanowire Proximity-Coupled to an s-Wave Superconductor". In: *Phys. Rev. B* 84.20 (2011), p. 201105.

[277] J. Kemp, N. Y. Yao, C. R. Laumann, and P. Fendley. "Long Coherence Times for Edge Spins". In: *Journal of Statistical Mechanics: Theory and Experiment* 2017.6 (2017), p. 063105.

[278] Y. Wang. "Detecting Topological Phases via Survival Probabilities of Edge Majorana Fermions". In: *Phys. Rev. E* 98.4 (2018), p. 042128.

[279] F. J. Gómez-Ruiz, J. J. Mendoza-Arenas, F. J. Rodríguez, C. Tejedor, and L. Quiroga. "Universal Two-Time Correlations, out-of-Time-Ordered Correlators, and Leggett-Garg Inequality Violation by Edge Majorana Fermion Qubits". In: *Phys. Rev. B* 97.23 (2018), p. 235134.

[280] C. B. Daıfmmode \breveg\else ğ\fi, L.-M. Duan, and K. Sun. "Topologically Induced Prescrambling and Dynamical Detection of Topological Phase Transitions at Infinite Temperature". In: *Phys. Rev. B* 101.10 (2020), p. 104415.

[281] J. Bjerlin, A. S. Sørensen, and S. Haas. "Probing Majorana Modes via Local Spin Dynamics". In: *Phys. Rev. B* 106.3 (2022), p. 035414.

[282] K. T. Law, P. A. Lee, and T. K. Ng. "Majorana Fermion Induced Resonant Andreev Reflection". In: *Phys. Rev. Lett.* 103.23 (2009), p. 237001.

[283] K. Flensberg. "Tunneling Characteristics of a Chain of Majorana Bound States". In: *Phys. Rev. B* 82.18 (2010), p. 180516.

[284] T. D. Stanescu, R. M. Lutchyn, and S. Das Sarma. "Majorana Fermions in Semiconductor Nanowires". In: *Phys. Rev. B* 84.14 (2011), p. 144522.

[285] M. T. Deng, C. L. Yu, G. Y. Huang, M. Larsson, P. Caroff, and H. Q. Xu. "Anomalous Zero-Bias Conductance Peak in a Nb–InSb Nanowire–Nb Hybrid Device". In: *Nano Lett.* 12.12 (2012), pp. 6414–6419.

[286] A. Das, Y. Ronen, Y. Most, Y. Oreg, M. Heiblum, and H. Shtrikman. "Zero-Bias Peaks and Splitting in an Al–InAs Nanowire Topological Superconductor as a Signature of Majorana Fermions". In: *Nat. Phys.* 8.12 (2012), pp. 887–895.

[287] P. Yu, J. Chen, M. Gomanko, G. Badawy, E. P. A. M. Bakkers, K. Zuo, V. Mourik, and S. M. Frolov. "Non-Majorana States Yield Nearly Quantized Conductance in Proximatized Nanowires". In: *Nat. Phys.* 17.4 (2021), pp. 482–488.

[288] A. Andreev. "Thermal Conductivity of the Intermediate State in Superconductors". In: *Sov. Phys. JETP* 19 (1964), p. 1228.

[289] J. Liu, A. C. Potter, K. T. Law, and P. A. Lee. "Zero-Bias Peaks in the Tunneling Conductance of Spin-Orbit-Coupled Superconducting Wires with and without Majorana End-States". In: *Phys. Rev. Lett.* 109.26 (2012), p. 267002.

[290] E. J. H. Lee, X. Jiang, R. Aguado, G. Katsaros, C. M. Lieber, and S. De Franceschi. "Zero-Bias Anomaly in a Nanowire Quantum Dot Coupled to Superconductors". In: *Phys. Rev. Lett.* 109.18 (2012), p. 186802.

[291] S. Das Sarma and H. Pan. "Disorder-Induced Zero-Bias Peaks in Majorana Nanowires". In: *Phys. Rev. B* 103.19 (2021), p. 195158.

[292] H. A. Hafez, S. Kovalev, J.-C. Deinert, Z. Mics, B. Green, N. Awari, M. Chen, S. Germanskiy, U. Lehnert, J. Teichert, et al. "Extremely Efficient Terahertz High-Harmonic Generation in Graphene by Hot Dirac Fermions". In: *Nature* 561.7724 (2018), pp. 507–511.

[293] J. L. Krause, K. J. Schafer, and K. C. Kulander. "High-Order Harmonic Generation from Atoms and Ions in the High Intensity Regime". In: *Phys. Rev. Lett.* 68.24 (1992), pp. 3535–3538.

[294] F. Krausz and M. Ivanov. "Attosecond Physics". In: *Rev. Mod. Phys.* 81.1 (2009), pp. 163–234.

[295] S. Baker, J. S. Robinson, C. A. Haworth, H. Teng, R. A. Smith, C. C. Chirilă, M. Lein, J. W. G. Tisch, and J. P. Marangos. "Probing Proton Dynamics in Molecules on an Attosecond Time Scale". In: *Science* 312.5772 (2006), pp. 424–427.

[296] D. Shafir, H. Soifer, B. D. Bruner, M. Dagan, Y. Mairesse, S. Patchkovskii, M. Y. Ivanov, O. Smirnova, and N. Dudovich. "Resolving the Time When an Electron Exits a Tunnelling Barrier". In: *Nature* 485.7398 (2012), pp. 343–346.

[297] M. Hohenleutner, F. Langer, O. Schubert, M. Knorr, U. Huttner, S. W. Koch, M. Kira, and R. Huber. "Real-Time Observation of Interfering Crystal Electrons in High-Harmonic Generation". In: *Nature* 523.7562 (2015), pp. 572–575.

[298] S. Ghimire and D. A. Reis. "High-Harmonic Generation from Solids". In: *Nat. Phys.* 15.1 (2019), pp. 10–16.

[299] J. Alcalà et al. "High Harmonic Spectroscopy of Quantum Phase Transitions in a High-Tc Superconductor". In: *Proc. Natl. Acad. Sci. U.S.A.* 119.40 (2022), e2207766119.

[300] J. Reimann, S. Schlauderer, C. Schmid, F. Langer, S. Baierl, K. Kokh, O. Tereshchenko, A. Kimura, C. Lange, J. Güdde, et al. "Subcycle Observation of Lightwave-Driven Dirac Currents in a Topological Surface Band". In: *Nature* 562.7727 (2018), pp. 396–400.

[301] D. Bauer and K. K. Hansen. "High-Harmonic Generation in Solids with and without Topological Edge States". In: *Phys. Rev. Lett.* 120.17 (2018), p. 177401.

[302] C. Jürß and D. Bauer. "High-Harmonic Generation in Su-Schrieffer-Heeger Chains". In: *Phys. Rev. B* 99.19 (2019), p. 195428.

[303] R. E. F. Silva, Á. Jiménez-Galán, B. Amorim, O. Smirnova, and M. Ivanov. "Topological Strong-Field Physics on Sub-Laser-Cycle Timescale". In: *Nat. Photon.* 13.12 (2019), pp. 849–854.

[304] A. Chacón et al. "Circular Dichroism in Higher-Order Harmonic Generation: Heralding Topological Phases and Transitions in Chern Insulators". In: *Phys. Rev. B* 102.13 (2020), p. 134115.

[305] C. Shao, H. Lu, X. Zhang, C. Yu, T. Tohyama, and R. Lu. "High-Harmonic Generation Approaching the Quantum Critical Point of Strongly Correlated Systems". In: *Phys. Rev. Lett.* 128.4 (2022), p. 047401.

[306] A. Pattanayak, S. Pujari, and G. Dixit. "Role of Majorana Fermions in High-Harmonic Generation from Kitaev Chain". In: *Scientific Reports* 12.1 (2022), p. 6722.

[307] M. L. Bera, J. O. de Almeida, M. Dziurawiec, M. Płodzień, M. M. Maśka, M. Lewenstein, T. Grass, and U. Bhattacharya. "Topological Phase Detection through High-Harmonic Spectroscopy in Extended Su-Schrieffer-Heeger Chains". In: *Phys. Rev. B* 108.21 (2023), p. 214104.

[308] M. Lewenstein, P. Balcou, M. Y. Ivanov, A. L'Huillier, and P. B. Corkum. "Theory of High-Harmonic Generation by Low-Frequency Laser Fields". In: *Phys. Rev. A* 49.3 (1994), pp. 2117–2132.

[309] G. Vampa, C. R. McDonald, G. Orlando, D. D. Klug, P. B. Corkum, and T. Brabec. "Theoretical Analysis of High-Harmonic Generation in Solids". In: *Phys. Rev. Lett.* 113.7 (2014), p. 073901.

[310] Y.-J. Doh, J. A. van Dam, A. L. Roest, E. P. A. M. Bakkers, L. P. Kouwenhoven, and S. De Franceschi. "Tunable Supercurrent Through Semiconductor Nanowires". In: *Science* 309.5732 (2005), pp. 272–275.

[311] M. Leijnse and K. Flensberg. "Introduction to Topological Superconductivity and Majorana Fermions". In: *Semicond. Sci. Technol.* 27.12 (2012), p. 124003.

[312] M. Kanega, T. N. Ikeda, and M. Sato. "Linear and Nonlinear Optical Responses in Kitaev Spin Liquids". In: *Phys. Rev. Res.* 3.3 (2021), p. L032024.

[313] J.-Y. Guan et al. “Experimental Evidence of Anomalously Large Superconducting Gap on Topological Surface State of β-Bi_2Pd Film”. In: *Sci. Bull.* 64.17 (2019), pp. 1215–1221.

[314] K. Hagiwara et al. “Superconducting Gap and Pseudogap in the Surface States of the Iron-Based Superconductor PrFeAsO1-y Studied by Angle-Resolved Photoemission Spectroscopy”. In: *Phys. Rev. Res.* 3.4 (2021), p. 043151.

[315] J. C. Baggesen and L. B. Madsen. “On the Dipole, Velocity and Acceleration Forms in High-Order Harmonic Generation from a Single Atom or Molecule”. In: *J. Phys. B At. Mol. Opt.* 44.11 (2011), p. 115601.

[316] M. Dziurawiec, J. O. de Almeida, M. L. Bera, M. Płodzień, M. M. Maśka, M. Lewenstein, T. Grass, and U. Bhattacharya. *Unraveling Multifractality and Mobility Edges in Quasiperiodic Aubry-André-Harper Chains through High-Harmonic Generation*. 2023. arXiv: 2310.02757 [cond-mat].

[317] J. Sauls. “Andreev Bound States and Their Signatures”. In: *Philos. Trans. R. Soc. A* 376.2125 (2018), p. 20180140.

[318] R. Tuovinen, E. Perfetto, R. van Leeuwen, G. Stefanucci, and M. A. Sentef. “Distinguishing Majorana Zero Modes from Impurity States through Time-Resolved Transport”. In: *New Journal of Physics* 21.10 (2019), p. 103038.

[319] E. Prada, P. San-Jose, M. W. A. de Moor, A. Geresdi, E. J. H. Lee, J. Klinovaja, D. Loss, J. Nygård, R. Aguado, and L. P. Kouwenhoven. “From Andreev to Majorana Bound States in Hybrid Superconductor–Semiconductor Nanowires”. In: *Nat. Rev. Phys.* 2.10 (2020), pp. 575–594.

[320] Y. Tanaka and S. Tamura. “Theory of Surface Andreev Bound States and Odd-Frequency Pairing in Superconductor Junctions”. In: *Journal of Superconductivity and Novel Magnetism* 34.6 (2021), pp. 1677–1694.

[321] D. T. Tran, A. Dauphin, A. G. Grushin, P. Zoller, and N. Goldman. “Probing Topology by "Heating": Quantized Circular Dichroism in Ultracold Atoms”. In: *Sci. Adv.* 3.8 (2017), e1701207.

[322] J. Argüello-Luengo, J. Rivera-Dean, P. Stammer, A. S. Maxwell, D. M. Weld, M. F. Ciappina, and M. Lewenstein. *Analog Simulation of High Harmonic Generation in Atoms*. 2023. arXiv: 2308.10223 [physics, physics:quant-ph].

[323] C. Lhuillier and G. Misguich. “Frustrated Quantum Magnets”. In: *High Magnetic Fields: Applications in Condensed Matter Physics and Spectroscopy*. Ed. by C. Berthier, L. P. Lévy, and G. Martinez. Berlin, Heidelberg: Springer Berlin Heidelberg, 2001, pp. 161–190. ISBN: 978-3-540-45649-0.

[324] C. Lacroix, P. Mendels, and F. Mila. *Introduction to Frustrated Magnetism*. Springer Ser. Solid-State Sci, 2011.

[325] S. Fujimoto. “Hall Effect of Spin Waves in Frustrated Magnets”. In: *Phys. Rev. Lett.* 103.4 (2009), p. 047203.

[326] X.-Q. Wang, G.-Q. Luo, J.-Y. Liu, W. V. Liu, A. Hemmerich, and Z.-F. Xu. “Evidence for an Atomic Chiral Superfluid with Topological Excitations”. In: *Nature* 596.7871 (2011), pp. 227–231.

[327] Y.-F. Wang, H. Yao, Z.-C. Gu, C.-D. Gong, and D. N. Sheng. “Non-Abelian Quantum Hall Effect in Topological Flat Bands”. In: *Phys. Rev. Lett.* 108.12 (2012), p. 126805.

[328] X.-L. Qi and S.-C. Zhang. “Topological Insulators and Superconductors”. In: *Rev. Mod. Phys.* 83.4 (2011), pp. 1057–1110.

[329] M. Sato and Y. Ando. "Topological Superconductors: A Review". In: *Rep. Prog. Phys.* 80.7 (2017), p. 076501.

[330] Y. Zhou, K. Kanoda, and T.-K. Ng. "Quantum Spin Liquid States". In: *Rev. Mod. Phys.* 89.2 (2017), p. 025003.

[331] C. K. Majumdar and D. K. Ghosh. "On Next,ÄêNearest,ÄêNeighbor Interaction in Linear Chain. I". In: *J. Math. Phys* 10.8 (1969), pp. 1388–1398.

[332] F. D. M. Haldane. "Spontaneous Dimerization in the S=\frac12 Heisenberg Antiferromagnetic Chain with Competing Interactions". In: *Phys. Rev. B* 25.7 (1982), pp. 4925–4928.

[333] A. M. Läuchli. "Numerical Simulations of Frustrated Systems". In: *Introduction to Frustrated Magnetism: Materials, Experiments, Theory*. Ed. by C. Lacroix, P. Mendels, and F. Mila. Berlin, Heidelberg: Springer Berlin Heidelberg, 2011, pp. 481–511. ISBN: 978-3-642-10589-0.

[334] A. P. Ramirez. "Strongly Geometrically Frustrated Magnets". In: *Annu. rev. mater. sci.* 24.1 (1994), pp. 453–480.

[335] O. A. Starykh. "Unusual Ordered Phases of Highly Frustrated Magnets: A Review". In: *Rep. Prog. Phys.* 78.5 (2015), p. 052502.

[336] C. Gross and I. Bloch. "Quantum Simulations with Ultracold Atoms in Optical Lattices". In: *Science* 357.6355 (2017), pp. 995–1001.

[337] B. Damski, H. Fehrmann, H.-U. Everts, M. Baranov, L. Santos, and M. Lewenstein. "Quantum Gases in Trimerized Kagomé Lattices". In: *Phys. Rev. A* 72.5 (2005), p. 053612.

[338] A. W. Glaetzle, M. Dalmonte, R. Nath, C. Gross, I. Bloch, and P. Zoller. "Designing Frustrated Quantum Magnets with Laser-Dressed Rydberg Atoms". In: *Phys. Rev. Lett.* 114.17 (2015), p. 173002.

[339] T. Zhang and G.-B. Jo. "One-Dimensional Sawtooth and Zigzag Lattices for Ultracold Atoms". In: *Sci. Rep.* 5.1 (2015), p. 16044.

[340] D. Yamamoto, T. Fukuhara, and I. Danshita. "Frustrated Quantum Magnetism with Bose Gases in Triangular Optical Lattices at Negative Absolute Temperatures". In: *Commun. Phys.* 3.1 (2020).

[341] E. Anisimovas, M. Raččiūūnas, C. Sträter, A. Eckardt, I. B. Spielman, and G. Juzeliūūnas. "Semisynthetic Zigzag Optical Lattice for Ultracold Bosons". In: *Phys. Rev. A* 94.6 (2016), p. 063632.

[342] J. Cabedo, J. Claramunt, J. Mompart, V. Ahufinger, and A. Celi. "Effective Triangular Ladders with Staggered Flux from Spin-Orbit Coupling in 1D Optical Lattices". In: *Eur. Phys. J. D* 74.6 (2020), p. 123.

[343] L. Barbiero, J. Cabedo, M. Lewenstein, L. Tarruell, and A. Celi. "Frustrated Magnets without Geometrical Frustration in Bosonic Flux Ladders". In: *Phys. Rev. Res.* 5.4 (2023), p. L042008.

[344] F. A. An, E. J. Meier, and B. Gadway. "Engineering a Flux-Dependent Mobility Edge in Disordered Zigzag Chains". In: *Phys. Rev. X* 8.3 (2018), p. 031045.

[345] T.-H. Leung, M. N. Schwarz, S.-W. Chang, C. D. Brown, G. Unnikrishnan, and D. Stamper-Kurn. "Interaction-Enhanced Group Velocity of Bosons in the Flat Band of an Optical Kagome Lattice". In: *Phys. Rev. Lett.* 125.13 (2020), p. 133001.

[346] C. D. Brown, S.-W. Chang, M. N. Schwarz, T.-H. Leung, V. Kozii, A. Avdoshkin, J. E. Moore, and D. Stamper-Kurn. "Direct Geometric Probe of Singularities in Band Structure". In: *Science* 377.6612 (2022), pp. 1319–1322.

[347] J. Struck et al. "Engineering Ising-XY Spin-Models in a Triangular Lattice Using Tunable Artificial Gauge Fields". In: *Nat. Phys.* 9.11 (2013), pp. 738–743.

[348] P. Saugmann, J. Vargas, Y. Kiefer, M. Hachman, R. Eichberger, A. Hemmerich, and J. Larson. "Route toward Classical Frustration and Band Flattening via Optical Lattice Distortion". In: *Phys. Rev. A* 106.4 (2022), p. L041302.

[349] J. Yang, L. Liu, J. Mongkolkiattichai, and P. Schauss. "Site-Resolved Imaging of Ultracold Fermions in a Triangular-Lattice Quantum Gas Microscope". In: *PRX Quantum* 2.2 (2021), p. 020344.

[350] J. Mongkolkiattichai, L. Liu, D. Garwood, J. Yang, and P. Schauss. "Quantum Gas Microscopy of a Geometrically Frustrated Hubbard System". In: *Phys. Rev. A* 108.6 (2023), p. L061301.

[351] M. Xu, L. H. Kendrick, A. Kale, Y. Gang, G. Ji, R. T. Scalettar, M. Lebrat, and M. Greiner. *Doping a Frustrated Fermi-Hubbard Magnet*. 2022.

[352] G. Grüner. "The Dynamics of Charge-Density Waves". In: *Rev. Mod. Phys.* 60.4 (1988), pp. 1129–1181.

[353] G. V. Chester. "Speculations on Bose-Einstein Condensation and Quantum Crystals". In: *Phys. Rev. A* 2.1 (1970), pp. 256–258.

[354] N. K. Glendenning. "Phase Transitions and Crystalline Structures in Neutron Star Cores". In: *Phys. Rep.* 342.6 (2001), pp. 393–447.

[355] R. Landig, L. Hruby, N. Dogra, M. Landini, R. Mottl, T. Donner, and T. Esslinger. "Quantum Phases from Competing Short- and Long-Range Interactions in an Optical Lattice". In: *Nature* 532.7600 (2016), pp. 476–479.

[356] V. Helson, T. Zwettler, F. Mivehvar, E. Colella, K. Roux, H. Konishi, H. Ritsch, and J.-P. Brantut. "Density-Wave Ordering in a Unitary Fermi Gas with Photon-Mediated Interactions". In: *Nature* 618.7966 (2023), pp. 716–720.

[357] L. Tanzi, S. M. Roccuzzo, E. Lucioni, F. Famà, A. Fioretti, C. Gabbanini, G. Modugno, A. Recati, and S. Stringari. "Supersolid Symmetry Breaking from Compressional Oscillations in a Dipolar Quantum Gas". In: *Nature* 574.7778 (2019), pp. 382–385.

[358] M. Guo, F. Böttcher, J. Hertkorn, J.-N. Schmidt, M. Wenzel, H. P. Büchler, T. Langen, and T. Pfau. "The Low-Energy Goldstone Mode in a Trapped Dipolar Supersolid". In: *Nature* 574.7778 (2019), pp. 386–389.

[359] L. Chomaz et al. "Long-Lived and Transient Supersolid Behaviors in Dipolar Quantum Gases". In: *Phys. Rev. X* 9.2 (2019), p. 021012.

[360] L. Su et al. "Dipolar Quantum Solids Emerging in a Hubbard Quantum Simulator". In: *Nature* 622.7984 (2023), pp. 724–729.

[361] E. Guardado-Sanchez, B. M. Spar, P. Schauss, R. Belyansky, J. T. Young, P. Bienias, A. V. Gorshkov, T. Iadecola, and W. S. Bakr. "Quench Dynamics of a Fermi Gas with Strong Nonlocal Interactions". In: *Phys. Rev. X* 11.2 (2021), p. 021036.

[362] H. P. Zahn, V. P. Singh, M. N. Kosch, L. Asteria, L. Freystatzky, K. Sengstock, L. Mathey, and C. Weitenberg. "Formation of Spontaneous Density-Wave Patterns in Dc Driven Lattices". In: *Phys. Rev. X* 12.2 (2022), p. 021014.

[363] P. Scholl et al. "Quantum Simulation of 2D Antiferromagnets with Hundreds of Rydberg Atoms". In: *Nature* 595.7866 (2021).

[364] L. Christakis, J. S. Rosenberg, R. Raj, S. Chi, A. Morningstar, D. A. Huse, Z. Z. Yan, and W. S. Bakr. "Probing Site-Resolved Correlations in a Spin System of Ultracold Molecules". In: *Nature* 614 (2023), pp. 64–69.

[365] A. W. Sandvik. "Evidence for Deconfined Quantum Criticality in a Two-Dimensional Heisenberg Model with Four-Spin Interactions". In: *Phys. Rev. Lett.* 98.22 (2007), p. 227202.

[366] F.-J. Jiang, M. Nyfeler, S. Chandrasekharan, and U.-J. Wiese. "From an Antiferromagnet to a Valence Bond Solid: Evidence for a First-Order Phase Transition". In: *J. Stat. Mech.: Theory Exp* 2008.02 (2008), P02009.

[367] O. I. Motrunich and A. Vishwanath. *Comparative Study of Higgs Transition in One-Component and Two-Component Lattice Superconductor Models*. 2008. arXiv: 0805.1494 [cond-mat].

[368] J. Lou, A. W. Sandvik, and N. Kawashima. "Antiferromagnetic to Valence-Bond-Solid Transitions in Two-Dimensional \textSU(N) Heisenberg Models with Multispin Interactions". In: *Phys. Rev. B* 80.18 (2009), p. 180414.

[369] A. Banerjee, K. Damle, and F. Alet. "Impurity Spin Texture at a Deconfined Quantum Critical Point". In: *Phys. Rev. B* 82.15 (2010), p. 155139.

[370] A. W. Sandvik. "Continuous Quantum Phase Transition between an Antiferromagnet and a Valence-Bond Solid in Two Dimensions: Evidence for Logarithmic Corrections to Scaling". In: *Phys. Rev. Lett.* 104.17 (2010), p. 177201.

[371] K. Harada, T. Suzuki, T. Okubo, H. Matsuo, J. Lou, H. Watanabe, S. Todo, and N. Kawashima. "Possibility of Deconfined Criticality in SU(N) Heisenberg Models at Small N". In: *Phys. Rev. B* 88.22 (2013), p. 220408.

[372] K. Chen, Y. Huang, Y. Deng, A. B. Kuklov, N. V. Prokof'ev, and B. V. Svistunov. "Deconfined Criticality Flow in the Heisenberg Model with Ring-Exchange Interactions". In: *Phys. Rev. Lett.* 110.18 (2013), p. 185701.

[373] A. Nahum, J. T. Chalker, P. Serna, M. Ortuño, and A. M. Somoza. "Deconfined Quantum Criticality, Scaling Violations, and Classical Loop Models". In: *Phys. Rev. X* 5.4 (2015), p. 041048.

[374] H. Shao, W. Guo, and A. W. Sandvik. "Quantum Criticality with Two Length Scales". In: *Science* 352.6282 (2016), pp. 213–216.

[375] J. Y. Lee, Y.-Z. You, S. Sachdev, and A. Vishwanath. "Signatures of a Deconfined Phase Transition on the Shastry-Sutherland Lattice: Applications to Quantum Critical SrCu2(BO3)2". In: *Phys. Rev. X* 9.4 (2019), p. 041037.

[376] M. Song, J. Zhao, L. Janssen, M. M. Scherer, and Z. Y. Meng. *Deconfined Quantum Criticality Lost*. 2023. arXiv: 2307.02547 [cond-mat, physics:hep-lat, physics:hep-ph, physics:hep-th].

[377] Z.-X. Li, S.-K. Jian, and H. Yao. *Deconfined Quantum Criticality and Emergent SO(5) Symmetry in Fermionic Systems*. 2019. arXiv: 1904.10975 [cond-mat].

[378] F. F. Assaad and T. Grover. "Simple Fermionic Model of Deconfined Phases and Phase Transitions". In: *Phys. Rev. X* 6.4 (2016), p. 041049.

[379] Z. H. Liu, W. Jiang, B.-B. Chen, J. Rong, M. Cheng, K. Sun, Z. Y. Meng, and F. F. Assaad. *Fermion Disorder Operator at Gross-Neveu and Deconfined Quantum Criticalities*. 2022.

[380] E. W. Huang, T. Liu, W. O. Wang, H.-C. Jiang, P. Mai, T. A. Maier, S. Johnston, B. Moritz, and T. P. Devereaux. "Fluctuating Intertwined Stripes in the Strange Metal Regime of the Hubbard Model". In: *Phys. Rev. B* 107.8 (2023), p. 085126.

[381] D. Charrier, F. Alet, and P. Pujol. "Gauge Theory Picture of an Ordering Transition in a Dimer Model". In: *Phys. Rev. Lett.* 101.16 (2008), p. 167205.

[382] G. J. Sreejith and S. Powell. "Scaling Dimensions of Higher-Charge Monopoles at Deconfined Critical Points". In: *Phys. Rev. B* 92.18 (2015), p. 184413.

[383] C. Mudry, A. Furusaki, T. Morimoto, and T. Hikihara. "Quantum Phase Transitions beyond Landau-Ginzburg Theory in One-Dimensional Space Revisited". In: *Phys. Rev. B* 99.20 (2019), p. 205153.

[384] B. Roberts, S. Jiang, and O. I. Motrunich. "One-Dimensional Model for Deconfined Criticality with Z3×Z3 Symmetry". In: *Phys. Rev. B* 103.15 (2021), p. 155143.

[385] J. Y. Lee, J. Ramette, M. A. Metlitski, V. Vuletic, W. W. Ho, and S. Choi. "Landau-Forbidden Quantum Criticality in Rydberg Quantum Simulators". In: *Phys. Rev. Lett.* 131.8 (2023), p. 083601.

[386] S. Prembabu, R. Thorngren, and R. Verresen. *Boundary Deconfined Quantum Criticality at Transitions between Symmetry-Protected Topological Chains*. 2022. arXiv: 2208.12258 [cond-mat, physics:quant-ph].

[387] M. E. Zayed et al. "4-Spin Plaquette Singlet State in the Shastry–Sutherland Compound SrCu2(BO3)2". In: *Nat. Commun.* 13.10 (2017), pp. 962–966.

[388] J. Guo et al. "Quantum Phases of SrCu2(BO3)2 from High-Pressure Thermodynamics". In: *Phys. Rev. Lett.* 124.20 (2020), p. 206602.

[389] Y. Cui et al. "Proximate Deconfined Quantum Critical Point in SrCu2(BO3)2". In: *Science* 380.6650 (2023), pp. 1179–1184.

[390] T. Hong et al. "Evidence for Pressure Induced Unconventional Quantum Criticality in the Coupled Spin Ladder Antiferromagnet C9H18N2CuBr4". In: *Nat. Commun.* 13.1 (2022), p. 3073.

[391] V. Zauner-Stauber, L. Vanderstraeten, M. T. Fishman, F. Verstraete, and J. Haegeman. "Variational Optimization Algorithms for Uniform Matrix Product States". In: *Phys. Rev. B* 97.4 (2018), p. 045145.

[392] S.-L. Drechsler et al. "Frustrated Cuprate Route from Antiferromagnetic to Ferromagnetic Spin-1/2 Heisenberg Chains: Li2ZrCuO4 as a Missing Link near the Quantum Critical Point". In: *Phys. Rev. Lett.* 98.7 (2007), p. 077202.

[393] M. Sato, S. Furukawa, S. Onoda, and A. Furusaki. "Competing Phases In Spin-1/2 J1-J2 Chain with Easy-Plane Anisotropy". In: *Mod. Phys. Lett. B* 25.12n13 (2011), pp. 901–908.

[394] S. Furukawa, M. Sato, S. Onoda, and A. Furusaki. "Ground-State Phase Diagram of a Spin-1/2 Frustrated Ferromagnetic XXZ Chain: Haldane Dimer Phase and Gapped/Gapless Chiral Phases". In: *Phys. Rev. B* 86.9 (2012), p. 094417.

[395] A. U. B. Wolter et al. "Magnetic Properties and Exchange Integrals of the Frustrated Chain Cuprate Linarite PbCuSO4(OH)2". In: *Phys. Rev. B* 85.1 (2012), p. 014407.

[396] A. Orlova, E. L. Green, J. M. Law, D. I. Gorbunov, G. Chanda, S. Krämer, M. Horvatić, R. K. Kremer, J. Wosnitza, and G. L. J. A. Rikken. "Nuclear Magnetic Resonance Signature of the Spin-Nematic Phase in LiCuVO4 at High Magnetic Fields". In: *Phys. Rev. Lett.* 118.24 (2017), p. 247201.

[397] C. P. Grams, D. Brüning, S. Kopatz, T. Lorenz, P. Becker, L. Bohatý, and J. Hemberger. "Observation of Chiral Solitons in LiCuVO4". In: *Commun. Phys.* 5.1 (2022).

[398] E. H. Lieb and F. Y. Wu. "Absence of Mott Transition in an Exact Solution of the Short-Range, One-Band Model in One Dimension". In: *Phys. Rev. Lett.* 20.25 (1968), pp. 1445–1448.

[399] A. W. Sandvik, L. Balents, and D. K. Campbell. "Ground State Phases of the Half-Filled One-Dimensional Extended Hubbard Model". In: *Phys. Rev. Lett.* 92.23 (2004), p. 236401.

[400] S. Ejima and S. Nishimoto. "Phase Diagram of the One-Dimensional Half-Filled Extended Hubbard Model". In: *Phys. Rev. Lett.* 99.21 (2007), p. 216403.

[401] M. Di Dio, L. Barbiero, A. Recati, and M. Dalmonte. "Spontaneous Peierls Dimerization and Emergent Bond Order in One-Dimensional Dipolar Gases". In: *Phys. Rev. A* 90.6 (2014), p. 063608.

[402] C. Trefzger, C. Menotti, B. Capogrosso-Sansone, and M. Lewenstein. "Ultracold Dipolar Gases in Optical Lattices". In: *J. Phys. B: At. Mol. Opt. Phys.* 44.19 (2011), p. 193001.

[403] O. Dutta, M. Gajda, P. Hauke, M. Lewenstein, D.-S. Lühmann, B. A. Malomed, T. Sowiński, and J. Zakrzewski. "Non-Standard Hubbard Models in Optical Lattices: A Review". In: *Rep. Prog. Phys.* 78.6 (2015), p. 066001.

[404] S. Baier, M. J. Mark, D. Petter, K. Aikawa, L. Chomaz, Z. Cai, M. Baranov, P. Zoller, and F. Ferlaino. "Extended Bose-Hubbard Models with Ultracold Magnetic Atoms". In: *Science* 352.6282 (2016), pp. 201–205.

[405] T. D. Kuehner and H. Monien. "Phases of the One-Dimensional Bose-Hubbard Model". In: *Phys. Rev. B* 58.22 (1998), R14741–R14744.

[406] D. Rossini and R. Fazio. "Phase Diagram of the Extended Bose–Hubbard Model". In: *New J. Phys.* 14.6 (2012), p. 065012.

[407] M. P. A. Fisher, P. B. Weichman, G. Grinstein, and D. S. Fisher. "Boson Localization and the Superfluid-Insulator Transition". In: *Phys. Rev. B* 40.1 (1989), pp. 546–570.

[408] W. Metzner and D. Vollhardt. "Correlated Lattice Fermions in D=∞ Dimensions". In: *Phys. Rev. Lett.* 62.3 (1989), pp. 324–327.

[409] N. D. Mermin and H. Wagner. "Absence of Ferromagnetism or Antiferromagnetism in One- or Two-Dimensional Isotropic Heisenberg Models". In: *Phys. Rev. Lett.* 17.22 (1966), pp. 1133–1136.

[410] J. Fraxanet, D. González-Cuadra, T. Pfau, M. Lewenstein, T. Langen, and L. Barbiero. "Topological Quantum Critical Points in the Extended Bose-Hubbard Model". In: *Phys. Rev. Lett.* 128.4 (2022), p. 043402.

[411] A. Montorsi and M. Roncaglia. "Nonlocal Order Parameters for the 1D Hubbard Model". In: *Phys. Rev. Lett.* 109.23 (2012), p. 236404.

[412] S. Julià-Farré, D. González-Cuadra, A. Patscheider, M. J. Mark, F. Ferlaino, M. Lewenstein, L. Barbiero, and A. Dauphin. "Revealing the Topological Nature of the Bond Order Wave in a Strongly Correlated Quantum System". In: *Phys. Rev. Res.* 4.3 (2022), p. L032005.

[413] E. G. Dalla Torre, E. Berg, and E. Altman. "Hidden Order in 1D Bose Insulators". In: *Phys. Rev. Lett.* 97.26 (2006), p. 260401.

[414] A. Dhar, M. Maji, T. Mishra, R. V. Pai, S. Mukerjee, and A. Paramekanti. "Bose-Hubbard Model in a Strong Effective Magnetic Field: Emergence of a Chiral Mott Insulator Ground State". In: *Phys. Rev. A* 85.4 (2012), p. 041602.

[415] S. Greschner, L. Santos, and T. Vekua. "Ultracold Bosons in Zig-Zag Optical Lattices". In: *Phys. Rev. A* 87.3 (2013), p. 033609.

[416] M. P. Zaletel, S. A. Parameswaran, A. Rüegg, and E. Altman. "Chiral Bosonic Mott Insulator on the Frustrated Triangular Lattice". In: *Phys. Rev. B* 89.15 (2014), p. 155142.

[417] T. Mishra, S. Greschner, and L. Santos. "Polar Molecules in Frustrated Triangular Ladders". In: *Phys. Rev. A* 91.4 (2015), p. 043614.

[418] C. Romen and A. M. Läuchli. "Chiral Mott Insulators in Frustrated Bose-Hubbard Models on Ladders and Two-Dimensional Lattices: A Combined Perturbative and Density Matrix Renormalization Group Study". In: *Phys. Rev. B* 98.5 (2018), p. 054519.

[419] S. Singha Roy, L. Carl, and P. Hauke. "Genuine Multipartite Entanglement in a One-Dimensional Bose-Hubbard Model with Frustrated Hopping". In: *Phys. Rev. B* 106.19 (2022), p. 195158.

[420] C.-M. Halati and T. Giamarchi. "Bose-Hubbard Triangular Ladder in an Artificial Gauge Field". In: *Phys. Rev. Res.* 5.1 (2023), p. 013126.

[421] J. Haegeman, T. J. Osborne, and F. Verstraete. "Post-Matrix Product State Methods: To Tangent Space and Beyond". In: *Phys. Rev. B* 88.7 (2013), p. 075133.

[422] J. Fraxanet, A. Dauphin, M. Lewenstein, L. Barbiero, and D. González-Cuadra. *Higher-Order Topological Peierls Insulator in a Two-Dimensional Atom-Cavity System*. 2023. arXiv: 2305.03409 [cond-mat, physics:quant-ph].

[423] T. Holstein and H. Primakoff. "Field Dependence of the Intrinsic Domain Magnetization of a Ferromagnet". In: *Phys. Rev.* 58.12 (1940), pp. 1098–1113.

[424] C. Gross and W. S. Bakr. "Quantum Gas Microscopy for Single Atom and Spin Detection". In: *Nat. Phys.* 17.12 (2021), pp. 1316–1323.

[425] K. G. Wilson and J. Kogut. "The Renormalization Group and the ϵ Expansion". In: *Phys. Rep.* 12.2 (1974), pp. 75–199.

[426] M. Karski, L. Fürster, J.-M. Choi, A. Steffen, W. Alt, D. Meschede, and A. Widera. "Quantum Walk in Position Space with Single Optically Trapped Atoms". In: *Science* 325.5937 (2009), pp. 174–177.

[427] T. Groh, S. Brakhane, W. Alt, D. Meschede, J. K. Asbóth, and A. Alberti. "Robustness of Topologically Protected Edge States in Quantum Walk Experiments with Neutral Atoms". In: *Phys. Rev. A* 94.1 (2016), p. 013620.

[428] O. Mandel, M. Greiner, A. Widera, T. Rom, T. W. Hänsch, and I. Bloch. "Controlled Collisions for Multi-Particle Entanglement of Optically Trapped Atoms". In: *Nature* 425 (2003), pp. 937–940.

[429] L. Förster et al. “Microwave Control of Atomic Motion in Optical Lattices”. In: *Phys. Rev. Lett.* 103.23 (2009), p. 233001.

[430] N. Belmechri, L. Förster, W. Alt, A. Widera, D. Meschede, and A. Alberti. “Microwave Control of Atomic Motional States in a Spin-Dependent Optical Lattice”. In: *J. Phys. B: At. Mol. Opt. Phys.* 46.10 (2013), p. 104006.

[431] L. Riegger, N. Darkwah Oppong, M. Höfer, D. R. Fernandes, I. Bloch, and S. Fölling. “Localized Magnetic Moments with Tunable Spin Exchange in a Gas of Ultracold Fermions”. In: *Phys. Rev. Lett.* 120.14 (2018), p. 143601.

[432] N. Darkwah Oppong, G. Pasqualetti, O. Bettermann, P. Zechmann, M. Knap, I. Bloch, and S. Fölling. “Probing Transport and Slow Relaxation in the Mass-Imbalanced Fermi-Hubbard Model”. In: *Phys. Rev. X* 12.3 (2022), p. 031026.

[433] A. Heinz, A. J. Park, N. Šantić, J. Trautmann, S. G. Porsev, M. S. Safronova, I. Bloch, and S. Blatt. “State-Dependent Optical Lattices for the Strontium Optical Qubit”. In: *Phys. Rev. Lett.* 124 (2020), p. 203201.

[434] T. O. Höhn, E. Staub, G. Brochier, N. D. Oppong, and M. Aidelsburger. *State-Dependent Potentials for the $^1S_0$ and $^3P_0$ Clock States of Neutral Ytterbium Atoms*. 2023. arXiv: 2305.20084 [cond-mat.quant-gas].

[435] M. D. Frye, B. C. Yang, and J. M. Hutson. “Ultracold Collisions of Cs Atoms in Excited Zeeman and Hyperfine States”. In: *Phys. Rev. A* 100.2 (2019), p. 022702.

[436] D. Jaksch and P. Zoller. “Creation of Effective Magnetic Fields in Optical Lattices: The Hofstadter Butterfly for Cold Neutral Atoms”. In: *New J. Phys.* 5 (2003), pp. 56–56.

[437] F. Gerbier and J. Dalibard. “Gauge Fields for Ultracold Atoms in Optical Superlattices”. In: *New J. Phys.* 12.3 (2010), p. 033007.

[438] A. Impertro, J. F. Wienand, S. Häfele, H. von Raven, S. Hubele, T. Klostermann, C. R. Cabrera, I. Bloch, and M. Aidelsburger. “An Unsupervised Deep Learning Algorithm for Single-Site Reconstruction in Quantum Gas Microscopes”. In: *Commun Phys* 6.1 (2023), p. 166.

[439] C. Chin, V. Vuletiıfmmode \acutec\else ć\fi, A. J. Kerman, S. Chu, E. Tiesinga, P. J. Leo, and C. J. Williams. “Precision Feshbach Spectroscopy of Ultracold \mathrmCs_2”. In: *Phys. Rev. A* 70.3 (2004), p. 032701.

[440] S. Keßler and F. Marquardt. “Single-Site-Resolved Measurement of the Current Statistics in Optical Lattices”. In: *Phys. Rev. A* 89.6 (2014), p. 061601.

[441] P. A. Murthy, D. Kedar, T. Lompe, M. Neidig, M. G. Ries, A. N. Wenz, G. Zürn, and S. Jochim. “Matter-Wave Fourier Optics with a Strongly Interacting Two-Dimensional Fermi Gas”. In: *Phys. Rev. A* 90.4 (2014), p. 043611.

[442] K. Hueck, N. Luick, L. Sobirey, J. Siegl, T. Lompe, and H. Moritz. “Two-Dimensional Homogeneous Fermi Gases”. In: *Phys. Rev. Lett.* 120.6 (2018), p. 060402.

[443] A. Bohrdt, D. Greif, E. Demler, M. Knap, and F. Grusdt. “Angle-Resolved Photoemission Spectroscopy with Quantum Gas Microscopes”. In: *Phys. Rev. B* 97.12 (2018), p. 125117.

[444] P. T. Brown, E. Guardado-Sanchez, B. M. Spar, E. W. Huang, T. P. Devereaux, and W. S. Bakr. “Angle-Resolved Photoemission Spectroscopy of a Fermi–Hubbard System”. In: *Nat. Phys.* 16.1 (2020), pp. 26–31.

[445] L. Barbiero, A. Montorsi, and M. Roncaglia. "How Hidden Orders Generate Gaps in One-Dimensional Fermionic Systems". In: *Phys. Rev. B* 88.3 (2013), p. 035109.

[446] J. Hubbard and B. H. Flowers. "Electron Correlations in Narrow Energy Bands". In: *Proceedings of the Royal Society of London. Series A. Mathematical and Physical Sciences* 276.1365 (1997), pp. 238–257.

[447] J. Kanamori. "Electron Correlation and Ferromagnetism of Transition Metals". In: *Progress of Theoretical Physics* 30.3 (1963), pp. 275–289.

[448] V. J. Emery. "Theory of High-${\mathrm{T}}_{\mathrm{c}}$ Superconductivity in Oxides". In: *Phys. Rev. Lett.* 58.26 (1987), pp. 2794–2797.

[449] S. Hirthe, T. Chalopin, D. Bourgund, P. Bojović, A. Bohrdt, E. Demler, F. Grusdt, I. Bloch, and T. A. Hilker. "Magnetically Mediated Hole Pairing in Fermionic Ladders of Ultracold Atoms". In: *Nature* 613.7944 (2023), pp. 463–467.

[450] E. Fradkin, S. A. Kivelson, and J. M. Tranquada. "Colloquium: Theory of Intertwined Orders in High Temperature Superconductors". In: *Rev. Mod. Phys.* 87.2 (2015), pp. 457–482.

[451] R. M. Fernandes, P. P. Orth, and J. Schmalian. "Intertwined Vestigial Order in Quantum Materials: Nematicity and Beyond". In: *Annu. Rev. Condens. Matter Phys.* 10.1 (2019), pp. 133–154.

[452] M. Vojta. "Lattice Symmetry Breaking in Cuprate Superconductors: Stripes, Nematics, and Superconductivity". In: *Adv. Phys.* 58.6 (2009), pp. 699–820.

[453] J. Zaanen and O. Gunnarsson. "Charged Magnetic Domain Lines and the Magnetism of High-T_c Oxides". In: *Phys. Rev. B* 40.10 (1989), pp. 7391–7394.

[454] D. Poilblanc and T. M. Rice. "Charged Solitons in the Hartree-Fock Approximation to the Large-U Hubbard Model". In: *Phys. Rev. B* 39.13 (1989), pp. 9749–9752.

[455] K. Machida. "Magnetism in La2CuO4 Based Compounds". In: *Phys. C: Supercond. Appl* 158.1 (1989), pp. 192–196.

[456] M. Kato, K. Machida, H. Nakanishi, and M. Fujita. "Soliton Lattice Modulation of Incommensurate Spin Density Wave in Two Dimensional Hubbard Model –A Mean Field Study–". In: *J. Phys. Soc. Japan* 59.3 (1990), pp. 1047–1058.

[457] J. P. F. LeBlanc et al. "Solutions of the Two-Dimensional Hubbard Model: Benchmarks and Results from a Wide Range of Numerical Algorithms". In: *Phys. Rev. X* 5.4 (2015), p. 041041.

[458] B.-X. Zheng, C.-M. Chung, P. Corboz, G. Ehlers, M.-P. Qin, R. M. Noack, H. Shi, S. R. White, S. Zhang, and G. K.-L. Chan. "Stripe Order in the Underdoped Region of the Two-Dimensional Hubbard Model". In: *Science* 358.6367 (2017), pp. 1155–1160.

[459] E. W. Huang, C. B. Mendl, S. Liu, S. Johnston, H.-C. Jiang, B. Moritz, and T. P. Devereaux. "Numerical Evidence of Fluctuating Stripes in the Normal State of High-T_c Cuprate Superconductors". In: *Science* 358.6367 (2017), pp. 1161–1164.

[460] E. W. Huang, C. B. Mendl, H.-C. Jiang, B. Moritz, and T. P. Devereaux. "Stripe Order from the Perspective of the Hubbard Model". In: *npj Quantum Mater.* 3.1 (2018), p. 22.

[461] Simons Collaboration on the Many-Electron Problem, M. Qin, C.-M. Chung, H. Shi, E. Vitali, C. Hubig, U. Schollwöck, S. R. White, and S. Zhang. "Absence of Superconductivity in the Pure Two-Dimensional Hubbard Model". In: *Phys. Rev. X* 10.3 (2020), p. 031016.

[462] F. C. Zhang and T. M. Rice. "Effective Hamiltonian for the Superconducting Cu Oxides". In: *Phys. Rev. B* 37.7 (1988), pp. 3759–3761.

[463] V. J. Emery and G. Reiter. "Mechanism for High-Temperature Superconductivity". In: *Phys. Rev. B* 38.7 (1988), pp. 4547–4556.

[464] S. A. Kivelson, I. P. Bindloss, E. Fradkin, V. Oganesyan, J. M. Tranquada, A. Kapitulnik, and C. Howald. "How to Detect Fluctuating Stripes in the High-Temperature Superconductors". In: *Rev. Mod. Phys.* 75.4 (2003), pp. 1201–1241.

[465] J.-J. Wen et al. "Observation of Two Types of Charge-Density-Wave Orders in Superconducting La2-xSrxCuO4". In: *Nat. Commun.* 10.1 (2019), p. 3269.

[466] P. Mai, S. Karakuzu, G. Balduzzi, S. Johnston, and T. A. Maier. "Intertwined Spin, Charge, and Pair Correlations in the Two-Dimensional Hubbard Model in the Thermodynamic Limit". In: *Proc. Natl. Acad. Sci. U.S.A.* 119.7 (2022), e2112806119.

[467] P. Mai, N. S. Nichols, S. Karakuzu, F. Bao, A. Del Maestro, T. A. Maier, and S. Johnston. "Robust Charge-Density-Wave Correlations in the Electron-Doped Single-Band Hubbard Model". In: *Nat. Commun.* 14.1 (2023), p. 2889.

[468] H. Xu, H. Shi, E. Vitali, M. Qin, and S. Zhang. "Stripes and Spin-Density Waves in the Doped Two-Dimensional Hubbard Model: Ground State Phase Diagram". In: *Phys. Rev. Res.* 4.1 (2022), p. 013239.

[469] B. Xiao, Y.-Y. He, A. Georges, and S. Zhang. "Temperature Dependence of Spin and Charge Orders in the Doped Two-Dimensional Hubbard Model". In: *Phys. Rev. X* 13.1 (2023), p. 011007.

[470] F. Šimkovic, R. Rossi, and M. Ferrero. "Two-Dimensional Hubbard Model at Finite Temperature: Weak, Strong, and Long Correlation Regimes". In: *Phys. Rev. Res.* 4.4 (2022), p. 043201.

[471] A. Wietek, J. Wang, J. Zang, J. Cano, A. Georges, and A. Millis. "Tunable Stripe Order and Weak Superconductivity in the Moiré Hubbard Model". In: *Phys. Rev. Res.* 4.4 (2022), p. 043048.

[472] A. Wietek, Y.-Y. He, S. R. White, A. Georges, and E. M. Stoudenmire. "Stripes, Antiferromagnetism, and the Pseudogap in the Doped Hubbard Model at Finite Temperature". In: *Phys. Rev. X* 11.3 (2021), p. 031007.

[473] H.-C. Jiang and S. A. Kivelson. "High Temperature Superconductivity in a Lightly Doped Quantum Spin Liquid". In: *Phys. Rev. Lett.* 127.9 (2021), p. 097002.

[474] H.-C. Jiang. "Pair Density Wave in the Doped Three-Band Hubbard Model on Two-Leg Square Cylinders". In: *Phys. Rev. B* 107.21 (2023), p. 214504.

[475] Y.-F. Jiang, T. P. Devereaux, and H.-C. Jiang. *Ground State Phase Diagram and Superconductivity of the Doped Hubbard Model on Six-Leg Square Cylinders*. 2023. arXiv: 2303.15541 [cond-mat].

[476] X. Lu, F. Chen, W. Zhu, D. N. Sheng, and S.-S. Gong. *Emergent Superconductivity and Competing Charge Orders in Hole-Doped Square-Lattice t–J Model*. 2023. eprint: arXiv:2304.03963.

[477] H.-X. Wang, Y.-F. Jiang, and H. Yao. *Robust D-Wave Superconductivity from the Su-Schrieffer-Heeger-Hubbard Model: Possible Route to High-Temperature Superconductivity*. 2022. arXiv: 2211.09143 [cond-mat].

[478] B. Ponsioen, S. S. Chung, and P. Corboz. "Superconducting Stripes in the Hole-Doped Three-Band Hubbard Model". In: *Phys. Rev. B* 108.20 (2023), p. 205154.

[479] D. F. Agterberg and H. Tsunetsugu. "Dislocations and Vortices in Pair-Density-Wave Superconductors". In: *Nat. Phys.* 4.8 (2008), pp. 639–642.

[480] Z. Dai, Y.-H. Zhang, T. Senthil, and P. A. Lee. "Pair-Density Waves, Charge-Density Waves, and Vortices in High-T_c Cuprates". In: *Phys. Rev. B* 97.17 (2018), p. 174511.

[481] D. F. Agterberg, J. S. Davis, S. D. Edkins, E. Fradkin, D. J. Van Harlingen, S. A. Kivelson, P. A. Lee, L. Radzihovsky, J. M. Tranquada, and Y. Wang. "The Physics of Pair-Density Waves: Cuprate Superconductors and Beyond". In: *Annual Review of Condensed Matter Physics* 11.1 (2020), pp. 231–270.

[482] K. S. Huang, Z. Han, S. A. Kivelson, and H. Yao. "Pair-Density-Wave in the Strong Coupling Limit of the Holstein-Hubbard Model". In: *npj Quantum Mater.* 7.1 (2022), p. 17.

[483] C. Setty, L. Fanfarillo, and P. J. Hirschfeld. "Mechanism for Fluctuating Pair Density Wave". In: *Nat. Commun.* 14.1 (2023), p. 3181.

[484] Y. Wang, S. D. Edkins, M. H. Hamidian, J. C. S. Davis, E. Fradkin, and S. A. Kivelson. "Pair Density Waves in Superconducting Vortex Halos". In: *Phys. Rev. B* 97.17 (2018), p. 174510.

[485] M. H. Hamidian et al. "Detection of a Cooper-pair Density Wave in \chemBi_2 Sr_2 CaCu_2 O_8+x". In: *Nature* 532.7599 (2016), pp. 343–347.

[486] Q. Gu et al. "Detection of a Pair Density Wave State in UTe2". In: *Nature* 618.7967 (2023), pp. 921–927.

[487] U. Schollwöck. "The Density-Matrix Renormalization Group". In: *Rev. Mod. Phys.* 77.1 (2005), pp. 259–315.

[488] M. Qin, T. Schäfer, S. Andergassen, P. Corboz, and E. Gull. "The Hubbard Model: A Computational Perspective". In: *Annu. Rev. Condens. Matter Phys.* 13.1 (2022), pp. 275–302.

[489] D. P. Arovas, E. Berg, S. Kivelson, and S. Raghu. "The Hubbard Model". In: *Annu. Rev. Condens. Matter Phys.* 13.1 (2022), pp. 239–274.

[490] E. H. Lieb. "Two Theorems on the Hubbard Model". In: *Phys. Rev. Lett.* 62.10 (1989), pp. 1201–1204.

[491] H. Tasaki. "Extension of Nagaoka's Theorem on the Large-U Hubbard Model". In: *Phys. Rev. B* 40.13 (1989), pp. 9192–9193.

[492] E. Lieb, T. Schultz, and D. Mattis. "Two Soluble Models of an Antiferromagnetic Chain". In: *Annals of Physics* 16.3 (1961), pp. 407–466.

[493] D. J. Scalapino. "A Common Thread: The Pairing Interaction for Unconventional Superconductors". In: *Rev. Mod. Phys.* 84.4 (2012), pp. 1383–1417.

[494] D. Cocks, P. P. Orth, S. Rachel, M. Buchhold, K. Le Hur, and W. Hofstetter. "Time-Reversal-Invariant Hofstadter-Hubbard Model with Ultracold Fermions". In: *Phys. Rev. Lett.* 109.20 (2012), p. 205303.

[495] L. Stenzel, A. L. C. Hayward, U. Schollwöck, and F. Heidrich-Meisner. "Topological Phases in the Fermi-Hofstadter-Hubbard Model on Hybrid-Space Ladders". In: *Phys. Rev. A* 102.2 (2020), p. 023315.

[496] F. A. Palm, M. Kurttutan, A. Bohrdt, U. Schollwöck, and F. Grusdt. "Ferromagnetism and Skyrmions in the Hofstadter–Fermi–Hubbard Model". In: *New Journal of Physics* 25.2 (2023), p. 023021.

[497] Y.-F. Jiang, J. Zaanen, T. P. Devereaux, and H.-C. Jiang. "Ground State Phase Diagram of the Doped Hubbard Model on the Four-Leg Cylinder". In: *Phys. Rev. Research* 2.3 (2020), p. 033073.

[498] A. Wietek. "Fragmented Cooper Pair Condensation in Striped Superconductors". In: *Phys. Rev. Lett.* 129.17 (2022), p. 177001.

[499] O. Penrose and L. Onsager. "Bose-Einstein Condensation and Liquid Helium". In: *Phys. Rev.* 104.3 (1956), pp. 576–584.

[500] A. J. Leggett. *Quantum Liquids*. Great Clarendon Street Oxford: Oxford University Press, 2006. ISBN: 978-0-19-852643-8.

[501] B. Evrard, A. Qu, J. Dalibard, and F. Gerbier. "Observation of Fragmentation of a Spinor Bose-Einstein Condensate". In: *Science* 373.6561 (2021), pp. 1340–1343.

[502] C. Hubig, J. Haegeman, and U. Schollwöck. "Error Estimates for Extrapolations with Matrix-Product States". In: *Phys. Rev. B* 97.4 (2018), p. 045125.

[503] N. Baldelli and M. Fishman. *ITensorCorrelators.Jl*. 2023.

[504] F. Bloch. "Über Die Quantenmechanik Der Elektronen in Kristallgittern". In: *Z. Phys.* 52.7 (1929), pp. 555–600.

[505] V. N. Serkin, M. Matsumoto, and T. L. Belyaeva. "Bright and Dark Solitary Nonlinear Bloch Waves in Dispersion Managed Fiber Systems and Soliton Lasers". In: *Opt. Commun.* 196.1 (2001), pp. 159–171.

[506] H. A. Haus and Y. Chen. "Dispersion-Managed Solitons as Nonlinear Bloch Waves". In: *J. Opt. Soc. Am. B* 16.6 (1999), pp. 889–894.

[507] P. J. Y. Louis, E. A. Ostrovskaya, C. M. Savage, and Y. S. Kivshar. "Bose-Einstein Condensates in Optical Lattices: Band-gap Structure and Solitons". In: *Phys. Rev. A* 67.1 (2003), p. 013602.

[508] D.-I. Choi and Q. Niu. "Bose-Einstein Condensates in an Optical Lattice". In: *Phys. Rev. Lett.* 82.10 (1999), pp. 2022–2025.

[509] J. H. Denschlag, J. E. Simsarian, H. Häffner, C. McKenzie, A. Browaeys, D. Cho, K. Helmerson, S. L. Rolston, and W. D. Phillips. "A Bose-Einstein Condensate in an Optical Lattice". In: *J. Phys. B* 35.14 (2002), pp. 3095–3110.

[510] I. Bloch. "Ultracold Quantum Gases in Optical Lattices". In: *Nat. Phys.* 1.1 (2005), pp. 23–30.

[511] C. G. Broyden. "The Convergence of a Class of Double-rank Minimization Algorithms 1. General Considerations". In: *IMA J. Appl. Math.* 6.1 (1970), pp. 76–90.

[512] R. Fletcher. "A New Approach to Variable Metric Algorithms". In: *Comput. J.* 13.3 (1970), pp. 317–322.

[513] D. Goldfarb. "A Family of Variable-Metric Methods Derived by Variational Means". In: *Math. Comput.* 24.109 (1970), pp. 23–26.

[514] D. F. Shanno. “Conditioning of Quasi-Newton Methods for Function Minimization”. In: *Math. Comput.* 24.111 (1970), pp. 647–656.

[515] S. D. Edkins et al. “Magnetic Field–Induced Pair Density Wave State in the Cuprate Vortex Halo”. In: *Science* 364.6444 (2019), pp. 976–980.

[516] X. Liu, Y. X. Chong, R. Sharma, and J. C. S. Davis. “Discovery of a Cooper-pair Density Wave State in a Transition-Metal Dichalcogenide”. In: *Science* 372.6549 (2021), pp. 1447–1452.

[517] S. Paeckel, T. Köhler, A. Swoboda, S. R. Manmana, U. Schollwöck, and C. Hubig. “Time-Evolution Methods for Matrix-Product States”. In: *Annals of Physics* 411 (2019), p. 167998.

[518] M. Wimmer. “Efficient Numerical Computation of the Pfaffian for Dense and Banded Skew-Symmetric Matrices”. In: *ACM Trans. Math. Softw.* 38.4 (2012), pp. 1–17.

[519] M. Nakamura. “Mechanism of CDW-SDW Transition in One Dimension”. In: *J. Phys. Soc. Japan* 68.10 (1999), pp. 3123–3126.

[520] M. Nakamura. “Tricritical Behavior in the Extended Hubbard Chains”. In: *Phys. Rev. B* 61.24 (2000), pp. 16377–16392.